

Optimization of composition and structure of cemented carbide cutting tools

Présentée le 19 mars 2021

Faculté des sciences de base
Laboratoire de physique de la matière complexe
Programme doctoral en physique

pour l'obtention du grade de Docteur ès Sciences

par

Samy ADJAM

Acceptée sur proposition du jury

Prof. F. Mila, président du jury
Dr D. Mari, directeur de thèse
Prof. G. Fantozzi, rapporteur
Dr J. Böhlmark, rapporteur
Dr T. La Grange, rapporteur

All we have to decide is what to do
with the time that is given us.
— Gandalf the Grey

To my beloved wife Neda
To my parents, sister and my whole family
To my friends



Non-disclosure agreement

This document presents a doctoral thesis, which was conducted jointly by the research group of mechanical spectroscopy (GSM) at EPFL and the industrial manufacturer Lamina Technologies SA. This project is funded by the Swiss Innovation Agency InnoSuisse and referred under No. 18396.1 PFIW-IW.

This work is subject to a confidentiality clause. No information contained in this document may be used, disclosed or communicated unless having received prior written authorization from Lamina Technologies SA.

Ce document présente une thèse de doctorat, qui a été menée conjointement entre le groupe de recherche sur la spectroscopie mécanique (GSM) à l'EPFL et le fabricant industriel Lamina Technologies SA. Ce projet est soutenu par InnoSuisse, l'agence suisse pour l'encouragement de l'innovation, et enregistré sous la référence No. 18396.1 PFIW-IW.

Ce travail fait l'objet d'une clause de confidentialité. Aucune information contenue dans le présent document ne saurait être utilisée, divulguée ou communiquée à moins d'en avoir reçu l'autorisation préalable écrite de Lamina Technologies SA.

Abstract

WC-Co cemented carbides are composites, which combine a hard phase consisting of WC grains and a metallic ductile phase as a binder. Their excellent mechanical properties, combining high hardness, toughness and refractory properties, make them excellent materials for cutting processes such as turning, drilling and milling. For such applications, cemented carbides are coated with thin ceramic films that increase their resistance to thermal stress as well as to the mechanical and chemical wear inherent in extreme machining conditions. Three main characteristics determine the performance and wear resistance of cutting tools: the cohesion of the hard phase above 1200 K, the ductility of the cobalt binder, and the mechanical and thermal resistance of the coatings.

This work focuses on the impact of the microstructural behaviour of the cobalt binder on the tool-life of the cutting tools. The aim is to develop new binders for cemented carbides with improved impact resistance.

The techniques of transmission electron microscopy at room temperature and in-situ at high temperature, as well as mechanical spectroscopy in a forced torsion pendulum have proved to be essential for the identification of the microstructure of cobalt and for the study of the relaxation phenomena occurring therein.

Mechanical spectroscopy has evidenced the presence of two relaxation peaks, P1 and P2 in the cobalt phase and a peak (P3) related to WC-WC grain boundary sliding. The peak P1 appears to be correlated with the cutting tool life measured in interrupted cutting tests.

In this work, the role of the binder is highlighted in particular by the identification of a glass-type transition observed for cobalt. The thermodynamics of the transition is evidenced by the behavior of P1 whose relaxation time diverges according to a Vogel-Fulcher-Tammann model, which is characteristic of glass transitions. The state of the material corresponding to temperatures below this transition shows a strong dependence on its thermomechanical history. This dependence is confirmed by a divergence in plastic deformations over two identical temperature cycles with different thermomechanical histories. Such a divergence on a standard protocol, called (ZFC/FC), seems to indicate a break in the thermodynamic hypothesis of ergodicity, even though it could not be attributed solely to the behaviour of cobalt.

Abstract

Transmission electron microscopy at room temperature has determined that the low temperature phase of the cobalt binder has a face-centred cubic structure and is composed of twinned nanodomains containing nanotwins. This state is therefore characterised by a short-range order without the long-range order that is characteristic of glassy materials. In-situ observations have highlighted a detwinning process corresponding to the temperatures of the cobalt relaxation peak identified by mechanical spectroscopy. This detwinning process continues until the appearance of a long-range ordered face-centred cubic phase above 1050K, which is favourable to deformation.

Mechanically, this transition is similar to a brittle-to-ductile transition, greatly influencing the properties of the material and its toughness. The cutting tool life could benefit from lowering the brittle to ductile transition temperature.

WC-Co cemented carbides; Mechanical Spectroscopy; Internal Friction; cutting tools; strain glass; non-ergodicity; glass-like transition; Vogel-Fulcher-Tammann relaxation process; cobalt nanodomains; nanotwins

Résumé

Les carbures cémentés WC-Co sont des composites qui associent une phase dure composée de grains de WC et une phase ductile métallique servant de liant. Leurs excellentes propriétés mécaniques, alliant haute dureté, ténacité et un caractère réfractaire élevé, en font d'excellents matériaux pour des processus de coupe tels que le tournage, perçage et fraisage. Pour de telles applications, les carbures cémentés sont revêtus de couches minces céramiques qui augmentent leur résistance aux contraintes thermiques ainsi qu'à l'usure mécanique et chimique inhérentes aux conditions extrêmes d'usinage. Trois caractéristiques principales déterminent les performances et la résistance à l'usure des outils de coupe : la cohésion de la phase dure au-dessus de 1200 K, le caractère déformable du liant cobalt, et la résistance mécanique et thermique des revêtements.

Ce travail s'intéresse à l'impact de la microstructure du cobalt sur la durée de vie des outils de coupes. Le but est de développer de nouveaux liants pour carbures cémentés dont la résistance aux chocs serait améliorée.

Les observations par microscopie électronique à transmission à température ambiante et in-situ à haute température, ainsi que la spectroscopie mécanique se sont révélées essentielles pour l'identification de la microstructure du cobalt et pour l'études des phénomènes de relaxation qui s'y produisent.

La spectroscopie mécanique a mis en évidence deux pics de relaxation P1 et P2 dans le cobalt et un pic (P3) relatif au glissement des joints de grain WC-WC. Le pic P1 est corrélé avec la durée de vie des outils de coupe mesurée par test de coupe interrompue.

Dans ce travail, le rôle du liant est notamment mis en lumière par l'identification d'une transition de type vitreux observée au sein du cobalt. La thermodynamique de cette transition est mise en évidence par le comportement du pic P1, dont le temps de relaxation diverge suivant un modèle de Vogel-Fulcher-Tammann qui caractérise les transitions vitreuses. L'état du matériau correspondant aux températures inférieures à cette transition démontre une forte dépendance à son historique thermomécanique. Cette dépendance est vérifiée par une disparité des déformations plastiques sur deux cycles en température identiques mais dont l'historique thermomécanique varie. Une telle disparité observée sur un protocole standard, dit (ZFC/FC), semble désigner une brisure d'ergodicité, sans pouvoir l'attribuer pour autant au seul comportement du cobalt.

Les études par microscopie électronique à transmission à température ambiante ont déterminé que la phase basse température du liant cobalt possède la structure cubique à faces centrées et qu'elle se compose de nanodomains maclés contenant des nano-macles. Cet état est donc caractérisé par un ordre à courte distance sans ordre à longue portée ce qui est typique des matériaux vitreux. Des observations in-situ ont mis en évidence un processus de dé-maclage correspondant aux températures du pic de relaxation du cobalt identifié par spectroscopie mécanique. Ce processus de dé-maclage se poursuit jusqu'à l'apparition d'une phase cubique à faces centrées à longue distance au-dessus de 1050K, favorable à la déformation.

Mécaniquement, cette transition s'apparente à une transition fragile-ductile influençant grandement les propriétés du matériau et sa ténacité. La durée de vie de l'outil pourrait bénéficier d'un abaissement de la température de transition fragile-ductile.

Contents

Abstract (English/Français)	i
WC-Co Cutting Tools : An Introduction	1
Technology and Industry	2
WC-Co cemented carbide	4
High-temperature mechanical behaviour and deformation	6
Novel research approach and objectives	8
1 Physical and experimental principles	9
1.1 Thermodynamics	9
1.2 Matter Structures and Change of State	10
1.2.1 Non-crystalline material transformations	12
1.2.2 Application fields of glass transition	16
1.3 Mechanical spectroscopy	18
1.3.1 Phenomenology of anelasticity	18
1.3.2 Thermodynamic approach of anelasticity	20
2 Experimental techniques	25
2.1 Machining tests and Tool-life	26
2.1.1 Failures mechanisms in machining	27
2.1.2 Shock test	28
2.1.3 Rapid wear test	28
2.2 Thin film coating	29
2.2.1 Deposition techniques in the hardmetals industry	29
2.2.2 Coatings material and techniques in this work	31
2.3 Hardness and nanohardness tests	32
2.3.1 Microhardness	33
2.3.2 Nanohardness	33
2.4 Friction tests	36
2.5 Electron microscopy	37
2.5.1 Scanning Electron Microscopy	37
2.5.2 Transmission Electron Microscopy	38
2.5.3 Sample preparation	39
2.6 X-ray diffraction and Residual stresses in thin films	40
2.6.1 X-ray diffraction	40
2.6.2 Residual stress measured by X-Ray diffraction	40
2.6.3 Measurement conditions	43

2.7	Mechanical spectroscopy	43
2.7.1	Internal Friction and Debye Peak	45
2.7.2	Thermally activated relaxations	47
2.7.3	Internal friction measuring technique	48
2.7.4	Reference internal friction measurements	49
3	Experimental Results and Observations	53
3.1	Durability and Tool-life	54
3.2	Comparative study	55
3.2.1	Friction tests	55
3.2.2	Mechanical properties and characteristics of the coatings	58
3.2.3	WC-Co bulk mechanical characteristics	61
3.3	Microstructural defects dynamics in the cobalt phase	62
3.3.1	Reference Internal Friction Spectra for different Cobalt Contents	62
3.3.2	Stabilisation processes	65
3.3.3	Measurements in isothermal conditions and T-point effect	68
3.3.4	Thermal activation of cobalt-related relaxation processes in the WC-Co	69
3.3.5	Thermal activation of the Cobalt relaxation peak P1	71
3.3.6	Thermal activation of the Cobalt relaxation peak P2	74
3.4	Investigations on ergodicity	76
3.5	Magnetic study	80
3.5.1	Magnetization transition and Curie temperature of WC-Co	82
3.5.2	Effect of magnetisation on microstructural relaxation	83
3.6	Transmission Electron Microscopy Study	85
3.6.1	Microscopic study at room temperature	85
3.6.2	In-situ microscopic study at high temperature	89
4	Discussion	95
4.1	Essential concepts of this study	95
4.1.1	Evidence from the initial comparative study	97
4.1.2	Overview	98
4.2	Cobalt microstructure in cemented carbides	98
4.3	Properties and characteristics of cemented carbides as a function of temperature	99
4.3.1	Microscopic characteristics	99
4.3.2	Microstructural defects dynamics	100
4.3.3	Magnetic properties	103
4.4	Cobalt in cemented carbides as a strain glass	103
4.4.1	Coating effect	105
4.4.2	Origin of cobalt glassy state	106
4.5	Perspectives	107
	Conclusion	109
	Bibliography	113

Appendices	129
Appendix A: Shock test	129
Appendix B: Facing until the center test	130
Appendix C: Friction test	131
Appendix D: Nanoindentation test	132
Appendix E: Frequency internal friction spectra	133
Remerciements (Français)	135
Scientific publications and conferences contributions	137
Contact informations	139
Curriculum Vitae	141

WC-Co Cutting Tools : An Introduction

Facing the need to manufacture faster, in large quantities and at lower cost, modern industry is confronted to ever-increasing demand and constraints. For the manufacture of functional metal-based products, the industry has numerous techniques¹ at its disposal. The most important techniques are undoubtedly the machining processes, the main ones being turning, drilling and milling. These operations are based on the use of cutting inserts mounted on various machine tools, as illustrated in Figure 1. Due to their extreme conditions of use, the hardness, toughness and wear resistance of the cutting tool material are of great importance. The cutting materials are therefore mainly high speed steel, hardmetals, aluminium oxide (Al_2O_3), cubic boron nitride (CBN), or diamond [1].

This work focuses on tungsten cemented carbides (WC-Co) and aims at modeling the high-temperature mechanical behaviour in order to optimise the microstructure and elementary constituents of these hardmetals. This chapter introduces the studied material and various compositions used in industry. Its manufacturing process is briefly presented. The structure of the composite, the various phases that composes it and the microstructure of its components are also presented. The framework of this project is then described in greater detail.

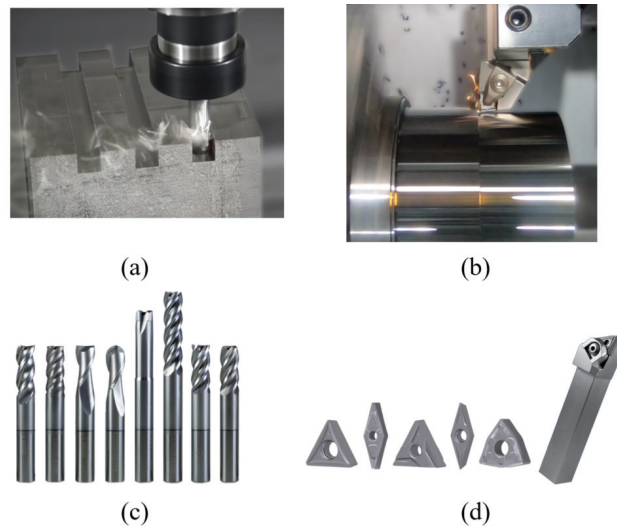


Figure 1: Examples of different cutting tools and the machining processes using them. (a) Milling process using Lamina's Solid Carbide Multi-Mat tool [2]. (b) Turning process with Lamina's Magia Pro insert [3]. (c) General purpose solid carbide end mills [4]. (d) Turning inserts [4].

¹For metal manufacturing, the main techniques employed are casting, moulding and sintering of metal powders, metal forming (by rolling or extrusion), metal assembly processes (such as joining), machining or the rapidly evolving field of additive manufacturing [5, 6].

Technology and Industry

Hard materials are one of the cornerstones of modern manufacturing. They are indispensable tools for the transformation of raw materials into advanced products for metal components. Among hard materials, cemented carbide are certainly the most successful composites ever discovered. They were developed by a study group from the OSRAM Study Company ² in the 1920s in Berlin, Germany. The outstanding combination of hardness and toughness of tungsten cemented carbides make them the perfect material for machining processes in industries as diverse as automotive, aerospace and mining. A limitation exists however for steel machining applications due to the high solubility of WC in steel [7]. This characteristic leads to wear by diffusion of the tool material into the workpiece, implying the need to add a diffusion barrier on cemented carbides to extend their range of application.

Several strategies exist to ensure better resistance of the tools to wear and deformation. For instance, the addition of cubic carbides (e.g. TiC, TaC, NbC) and carbonitrides (e.g. TiCN) are used to ensure increased hardness of the material. Excessive hardness, however, reduces the ductility of the material, which is crucial. Another widely used strategy is to coat the cutting inserts with thin ceramic layers to ensure high wear and heat resistance [8].

Classification of hardmetals

There are two main groups of materials for the so-called hardmetal cutting applications: composites whose hard phase is composed of tungsten carbide grains (WC) and those made out of titanium carbonitrides (TiCN). Cemented carbides refer to composites made of a ceramic matrix with a majority of WC tungsten carbide and a metallic binder. The name cemented carbides originates from the fact that the metal binder is used as a cement for the composite. Cermet are the second group of materials. Such composites consist of at least a ceramic phases and a metallic phase (hence the origin of the word "cer-met"). The uses of one or the other composite type varies according to their specific properties, for instance the higher hardness of cermet materials or the high toughness and resistance to thermal and mechanical shocks of cemented carbides. It is also possible to combine these two families of materials to form a mixed cermet with customised mechanical properties, such as TiCN-WC-Mo-(Co,Ni) [9].

Fabrication method

Liquid phase sintering is a technique of powder metallurgy for manufacturing composite materials. It is this method which is used for the production of hard metals. Starting from a mixture of powders, composed of the various components of the desired composite and the addition of an organic binder, the cutting inserts are pressed into the desired compact form and then densified by sintering at high temperature and high neutral gas pressure.

This process does not require all of the components to go through a liquid phase, it is sufficient to overcome the eutectic point of the binary system at the appropriate concen-

²This invention is today referred as the patent of K. Schröter DRP 420.689 (1923) [10] compaigny to produce hard materials by pressing and sintering.

tration. In the case of WC-Co cemented carbides, the temperature of the eutectic is at $1590K$ [11] while the melting point of cobalt is at $1768K$. These high temperatures easily induce important diffusions of W and C elements into the Co binder. It is important to avoid the formation of a graphite phase (excess of C) or a η phase W_3Co_3C (deficiency of C), which both lower the mechanical properties of the composite. The carbon content is therefore an important parameter, which also happens to be very sensitive: the ternary Co-W-C diagram shows only a limited range ensuring the formation of a two-phase Co-WC composite [12, 13, 14]. For these reasons, the sintering temperature of WC-Co is generally approximately at $1720K$ with an appropriate C content. The advantage of using cobalt as a binder for cemented carbides is its high wettability with respect to WC grains [15, 16]. This ensures a low porosity of the composite and provides high cohesion between carbides and metal.

The final grain size of the composite plays an important role in the mechanical properties of the material, in particular on hardness [17, 18] and on strength and creep deformation resistance with a high temperature dependency [19]. The final grain size is mainly determined by the type of powder used (see Table 1). Finer WC grains are generally preferred for milling, shank tools and all applications requiring sharp edges, as fine-grained materials generally offer better edge toughness [20, 21]. If a higher bulk toughness is required, a coarser-grained WC/Co is used.

Powder Nomenclature	Grain Size [μm]
Nano	<0.2
Ultrafine	0.2-0.5
Submicron	0.5-0.8
Fine	0.8-1.3
Medium	1.3-2.5
Coarse	2.5-6.0
Extra coarse	>6.0

Table 1: Classification of powder types for hardmetals sintering, from [17].

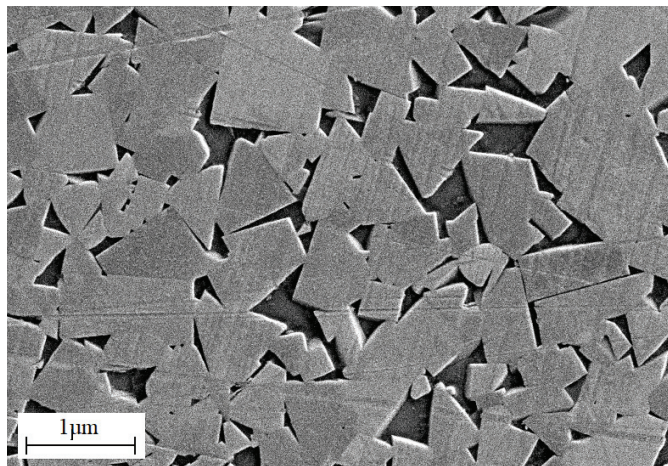


Figure 2: Metallography of the polished surface of a cemented carbide obtained by scanning electron microscopy performed on a ZEISS GeminiSEM 300 microscope with an acceleration voltage of 5 keV. The metallic binder is shown in dark contrast, while the tungsten carbide grains are shown in light contrast.

WC-Co cemented carbide

With the adequate sintering parameters, the WC-Co composite consists of a two-phase alloy: a hard phase composed by the WC grains, which have a highly faceted shape, and a ductile phase composed by the metallic binder. The typical morphology of such a composite is presented in Figure 2. This arrangement combines the mechanical advantages of carbides with the ductility of metallic materials and exhibits a unique combination of mechanical properties and great wear resistance as shown in Table 2.

Mechanical properties	Value range
Vickers Hardness H_V [$kg_f \cdot mm^{-2}$]	1000 - 2300
Fracture toughness K_{IC} [$MPa \cdot m^{1/2}$]	9 - 20
High elastic modulus [GPa]	300 - 700
Transverse rupture strength [GPa]	2 - 4
Wear resistance	High
Impact resistance	Moderate

Table 2: Mechanical properties of typical WC-Co composite, considering cobalt contents from 3 to 30% by weight. From [17, 22].

The characteristic shape of the WC grains found in cemented carbide is highly faceted, as seen in Figures 2 and 3(a). This shape results from the sintering and the cristallographic structure of the WC, which is simple hexagonal [23] and forms stoichiometric crystals with one tungsten and one carbon atom per unit cell with a ratio of its lattice parameters close to one (see Table 3).

The cobalt is mostly found in a face centered cubic (α) structure at room temperature in cemented carbides [24, 25]. However, the structre of pure cobalt is normally hexagonal at room temperature and undergoes a first order phase transition from hcp to fcc at around 700 K [26], as illustrated in Figure 3(b). The mismatch between the low-temperature states of pure cobalt and cobalt bound in a WC-Co induces the formation of a stacking fault network in the cobalt that highly increases its yield stress [27, 28].

Two hypotheses exist on the origin of the cubic phase in cobalt. Either it is the presence of dissolved carbon and tungsten atoms, which blocks the structure of cobalt. Or it is due to the influence of enormous residual stresses within the cemented carbides, which have been reported by many studies [25, 24]. The high thermal residual stresses are of the order of 2 GPa in the cobalt phase and of the order of -0.4 GPa for the WC skeleton for conventional grades [25]. This residual stress arises during the cooling from the sintering process temperature between the binder and hard phases. It depends on the constituents and their expansion coefficient, on the binder content and on the carbide size.

Cobalt is known to be the element that controls the ductility of the WC-Co composite. However it also controls a significant proportion of the overall hardness of the composite. Hardening strategies focus on controlling the structural defects contained by the binder, either by the presence of W elements in solution or by the dislocations it contains [29]. In

the latter case, the maximum free length of the dislocations is controlled by the average distance between the Co/carbide interfaces. One of the important parameter for controlling the performance of cutting tools is therefore their binder phase content.

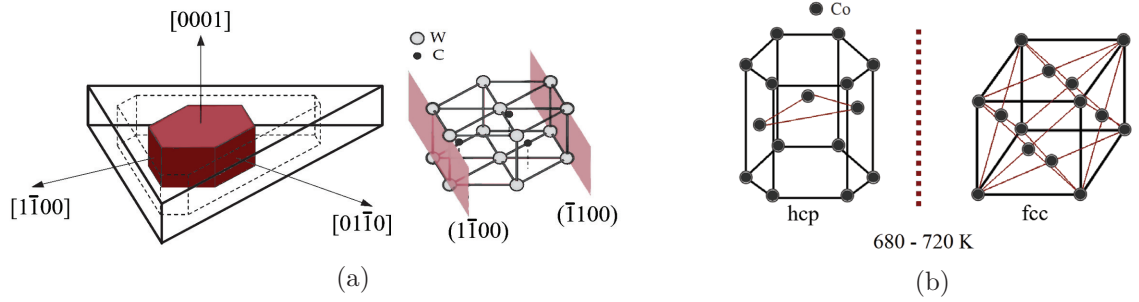


Figure 3: Structure and morphology of the cobalt and WC grains in cemented carbides (a) WC grains have a simple hexagonal crystalline structure, and are observed with a shape of a triangular prism in cemented carbides. Arranged from [23]. (b) Pure cobalt is found in a hcp crystalline structure at room temperature and undergoes a phase transition at about 700K [26].

The main physical, structural and mechanical properties of the constituents of WC-Co composites are presented in the Table 3 below.

Properties	Element / Constituent			
	WC	Co	Ni	Fe
Atomique Number	-	27	28	26
Periodic Table Group	-	(VIII-B)	(VIII-B)	(VIII-B)
Structure	h	(hc)/cfc	cfc	cc(/cfc)
Transition temperature [K]	-	700	-	1170
Lattice parameter [nm]	a:0.290 c:0.283	0.354	0.352	0.286
Young modulus E [GPa]	710	211	199.5	211.4
Poisson's ratio ν []	0.2	0.32	0.312	0.293
Melting point [K]	3050	1768	1723	1809
Self-diffusion activation energy [eV/atom]	-	2.78	2.91	2.65/2.91
Activation energy for W Diffusion [eV/atom]	-	2.47	3.08	2.9
Activation energy for C Diffusion [eV/atom]	-	1.67	1.43	0.82/1.39

Table 3: Physical properties of the constituents of cemented carbides [30, 31, 11].

High-temperature mechanical behaviour and deformation

This section focuses on the description of the high-temperature behaviour and deformation characteristics of hardmetals in order to outline certain directions for industrial research and development. In the case of coated cemented carbides, and due to the high temperatures and high pressures experienced during machining, the performance and lifespan of cutting tools can be impaired by multiple wear processes [32, 33], by plastic deformation [34, 35], or by coating cracking or flaking [36], eventually leading to tool breakage. The deformation behaviour of WC-Co is well established for the working temperatures reached during machining. Three temperature domains have been identified [37, 27, 38]:

- (I) Low temperature domain with approximately $T < 800K$. Elastic deformations followed by brittle fractures are observed.
- (II) Medium temperature domain with approximately $800K < T < 1100K - 1200K$. This region corresponds to a tough behaviour, and limited plastic deformation occurs.
- (III) High temperature domain with approximately $T > 1100K - 1200K$. In this region, extended plastic deformation is observed. It corresponds to creep.

These domains delimit the behaviour observed for cemented carbides. Globally the same pattern can be obtained for cermets with some adjustments of the temperature values according to their composition [27]. The activation of these various mechanical behaviour domains is achieved by setting specific microstructure defects into motion, depending on the temperature and the applied stresses. The microstructure defects in WC-Co consists of dissolved point defects (W,C) in the cobalt phase, and dislocations both in the binder and in the WC grains [27, 28, 39].

The first **domain (I)** representing a brittle material is essentially characterised by the microstructure of the cobalt phase, the hard phase remaining as a continuous skeleton of interconnected WC grains. In this low-temperature domain, the α phase cobalt contains a cross-connected network of stacking faults, which are bordered by partial dislocations [27]. The blocking of this partial dislocation movement by the stacking faults have a hardening effect on the binder.

As the temperature increases, the partial dislocations become more mobile in the metallic binder and the material enters into the **domain (II)**. Although their movement remains limited by the presence of the network of stacking faults, the mobility of partial dislocations increases the bulk material toughness. Limited plastic deformation was therefore observed in the study of the yield stress behaviour as function of the temperature [37].

The microstructure of cemented carbides still evolves in the high temperature range of **domain (III)**. Microscopic observations of WC-Co samples deformed above 1270K show that the binder mainly contains perfect dislocations recombined from the partials. Along with the microstructure, the material behaviour evolves to exhibit high plastic deformation and creep through grain boundary sliding [40].

Generally, diffusion and dislocation movement are regarded as the mechanisms inducing grain boundary sliding [41]. For cemented carbides, WC grain boundary sliding is also attributed to dislocation movement in the grain boundary regions [39]. It is considered that the dislocation movement are due to high tensile stresses localized at the grain boundary

during the deformation of the material [42, 36]. Grain boundary sliding is accompanied by the infiltration and lamella formation of cobalt between the WC grains. The binder phase lamellae form 10 to 50 nm wide bands between the grains [39, 43] and are shown to be related to the applied stress [44]. The infiltration of cobalt under tensile stress would result from the energetically favourable formation of WC/Co boundaries instead of WC/WC boundaries, with the exception for the $\Sigma 2$ WC/WC boundaries [45].

It has been shown that the deformation results also in the generation of cavitation at the WC grain boundaries and by the decohesion of certain grains forming the skeleton [27, 44]. It has been found that cavities increase in size and number with increasing temperature and deformation [44]. One of the materials fracture mechanisms at very high temperatures is therefore the decohesion of WC grains.

Temperature variation and applied external stress can have a significant impact on the binder residual stress. It has been proven that the binder experiences high tensile residual stress that are temperature dependent [25]. Starting from a value of approximately -400 MPa at room temperature, the compressive stresses in the WC grains are cancelled out at approximately 1075K and continue to increase in the tensile range after. For a cobalt binder, it is estimated that thermal stresses should start at about 1850 MPa and also be relaxed around 1075K [24]. The internal residual stresses and their evolution may play a significant role in the plastic deformation by influencing the microstructure of the cutting tool at high temperature.

It is thus clear that the performance of cutting bulk materials is essentially limited by the evolution of their microstructure under their conditions of use at high temperatures and stresses. Among the constituents of cemented carbides, it seems that the binder plays the the most important role. Cobalt remains the most widely used element for the manufacture of cemented carbide. There are, however, alternatives, notably iron (Fe) and nickel (Ni), both of which are transition metals of group (VIII-B) close to cobalt in the periodic table of elements. Although very few studies exist on this subject [36, 46, 47, 48], alloys formed with these elements are generally used for the development of new binders to replace cobalt, and not the pure elements [47].

Novel research approach and objectives

The intent of this project is to determine the factors influencing the tool-life of the cutting inserts. A specific methodology is used, which is conducted through a comparative study confronting the tool-life measured in real machining conditions with a broad variety of properties. Each of those properties are related to several regions of the cutting tool material. Coatings mechanical properties (i.e. hardness, elastic modulus, and residual stress), coating features (i.e. roughness, thickness, and friction coefficient), bulk mechanical properties (i.e. hardness and fracture toughness) and bulk mechanical characteristics (i.e. porosity, granulometry, crystal structure and defects microstructure, bulk defects dynamics) are investigated. An extensive analysis of the binder of the studied cemented carbide samples was then carried out on its microstructure, its transformations and the dynamics of its defects.

In this thesis, **Chapter 1** will introduce the fundamental principles used for the different studies and measurements conducted during this work. These same fundamental concepts serve as a basis for understanding the different phenomena observed during this work and will therefore also be important for the discussion of the obtained results. The physical theories presented here are well-established principles and are therefore not an original work.

Chapter 2 presents the experimental techniques, setups and specifications used in this study. As this is a collaborative work between the GSM mechanical spectroscopy group at EPFL and the industrial manufacturer Lamina Technologies SA, the experimental methods were partly carried out in various EPFL laboratories or directly with the industrial partner.

Experimental results are reported in the **Chapter 3**. The first part of this section presents important early results and observations in the form of a comparative study. These findings were the basis for the investigation strategy and the conception of modified cutting materials. A second part presents further analyses, in particular on the dynamics of microstructure defects and electron microscopy studies, in an attempt to clearly explain these early stage observations.

A further analysis of these results is presented in **Chapter 4** and allows us to define a physical model of the essential role of the metallic binder within cemented carbides and the influence of its constituent phases. A feasibility study on the development of new binders for cemented carbides is also discussed.

Finally, the **Conclusion** of this project briefly reports the general observations and findings of this project.

1 Physical and experimental principles

This chapter focuses on the physical principles essential to the understanding of this thesis work. It begins with a brief introduction to the thermodynamics of phase transformations leading to the concept of glass transition in materials. Then, the principles surrounding materials transforming into a glassy state called strain-glass with particular behaviours are discussed. This point happens to be central to the Results Chapter 3 and the Discussion Chapter 4. Finally the anelasticity in materials will be discussed. This principle is at the basis of the mechanical spectroscopy technique, which has proved essential for the study of the microstructural evolution of WC-Co materials, and which is presented in detail in the Chapter 2 on Experimental Methods.

1.1 Thermodynamics

Phenomenological thermodynamics studies, from simple macroscopic quantities such as temperature, heat and entropy, the evolution of the properties of bodies where thermal exchanges such as transformations between thermal and mechanical energy occur. These considerations make thermodynamics the indispensable discipline of metallurgy for the study of deformations, structural and diffusion defects, as well as for the study of phase transformations.

In view of the importance of thermodynamic concepts, this section provides a brief summary of the basic of thermodynamics for metallurgy. In this context, one generally wishes to find the equilibrium of a system from its state variables through the expression of a state function. The choice of the state function depends on the situation under consideration (system with constant volume, pressure or temperature).

Thermodynamic considerations are based on the variation of internal energy of a given system by :

$$dE = \delta Q + \delta W$$

This relates the reversible variation in energy E to the irreversible variations in heat Q and work W on a given system. By considering reversible processes, it is possible to relate the internal energy E to the thermodynamic variables P , V , S and T by :

$$dE = T \cdot dS - P \cdot dV$$

It is therefore possible to retrieve appropriate state functions for different situations:

- For a constant volume system, there can be found simply $dE = dQ$.
- For a constant pressure system, one can define the enthalpy H starting from the heat exchanged with the system $dQ = dE + P \cdot dV = d(E + P \cdot V) = dH$. Enthalpy $dH = T \cdot dS + V \cdot dP$ thus expresses an exchanged heat.
- For a constant temperature system, it is possible to consider the work of a reversible process through Helmholtz free energy, expressing a work, $F = E - T \cdot S$ per:
 $\delta W = dE - \delta Q = dE - T \cdot dS = d(E - T \cdot S) = dF$
- For usual experimental conditions at constant pressure and temperature, Gibbs G free energy is used, with $dG = -S \cdot dT + V \cdot dP + \mu dN$. Under the conditions of constant pressure and temperature of a N particles system, Gibbs free energy is directly related to the chemical potential μ of a particle by $G = \mu \cdot N$.

Due to the conditions it is related to, the main thermodynamic concept used in metallurgy is the Gibbs free energy. In thermodynamics, it will determine whether a process will take place or not. For a more detailed view of the implications of thermodynamics in materials science, the reader is invited to refer to more detailed discussions provided by [49, 50].

1.2 Matter Structures and Change of State

Thermodynamic systems experience states in which their physical properties, atomic arrangement and composition are homogeneous; these are referred to as thermodynamic phases. Within condensed matter, atoms can arrange themselves in many different ways depending on the bonds linking these atoms (Van der Waals interactions, ionic, covalent or metallic bonds). These configurations are generally regular and can create crystalline or non-crystalline arrangements. One concept is particularly interesting to characterize the arrangement of condensed matter: it is the notion of order. Whether for geometric order or chemical order, there exist two types:

- The **short-distance order** takes into account atoms in the first neighbor position (atomic dimension), by the existence or not of arrangements of neighboring atoms in polyhedron.
- The **long-distance order** deals with atoms whose distance is greater than the atomic spacing, by the existence or not of arrangements of the polyhedra formed by neighbouring atoms.

This notion of order makes it possible to establish the characteristics of condensed solids, for instance:

- Liquids have a short range order, but no long range order.
- Crystals have a long-distance order.
- Metal alloys, which all have a geometrical order, are considered to be disordered or not, if they have a chemical order or not, respectively.
- Materials such as glass, polymers, wood, cement and granular material do not have long-range order. These are referred to as non-crystalline solids.

It should be considered that these systems may undergo **phase transformations** due to temperature variations, that can be for example a change in the atomic configuration of the system or a change in the phase composition of a composite. The designation of **phase transition** is preferred when only one property differs between initial and final phase, for example a order-disorder transition. The denomination **phase change** encompasses the other two designations of phase transformation and phase transition. The tendency of matter to tend towards a more structured form at low temperature is based on the reduction of entropy as explained by the third law of thermodynamics [49]. A phase transformation involving a change in crystalline structure is given for example by the martensitic phase transformation in cobalt from a high temperature face centered cubic (f.c.c.) structure to an hexagonal close packed (h.c.p.) structure at 700K [26]. On the other hand, disorder–order transitions refers to ordering of physical quantities such as magnetic moment, electric dipole or lattice strain [51].

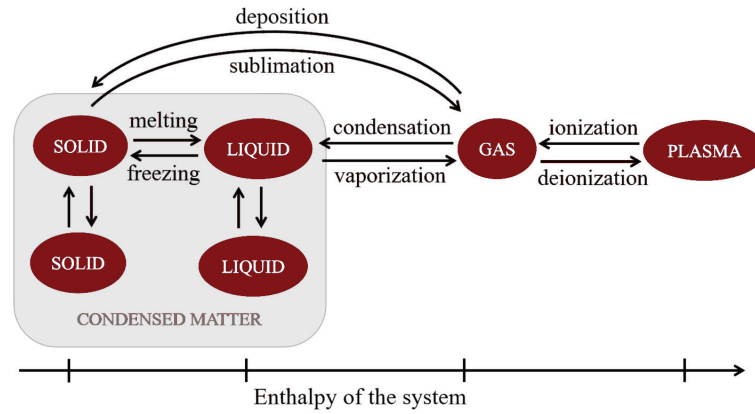


Figure 1.1: Schematic illustration of the phase transformations between the four fundamental states of matter and the corresponding enthalpy H evolution.

A classification given by Ehrenfest [49, 50, 52] exists for the transformations, which classifies first-order and second-order transformations on the basis of the behavior of the Gibbs free energy G :

- **First-order transformations** involve transformations from a phase A to B whose Gibbs free energy function G remains continuous all along, but whose state functions involving G derivatives are discontinuous. This is the case for the functions of enthalpy $H = G - T \cdot \delta G / \delta T$, and entropy $S = \delta G / \delta T$, but also for other physical quantities such as specific heat C_P or volume V . The discontinuity of the enthalpy, expressing a heat exchange, implies the formation of a heat over the transformation called the latent heat $L_C = H_A - H_B$. An up-to-date classification defines as first-order any transformation involving latent heat [52]. The martensitic phase transition mentioned above is for instance a first-order transition, as well as the liquid-solid transformation.
- **Second-order transformations** concern transformations where the G function and all its first derivatives with respect to thermodynamic variables remain continuous while the second derivatives of G contain a discontinuity. In the modern classification, second order transformations are those that have no associated latent heat [52]. The order-disorder transformations of some metal alloys as well as the ferro/paramagnetic and ferro/paraelectric transitions are, for example, of the second order [49].

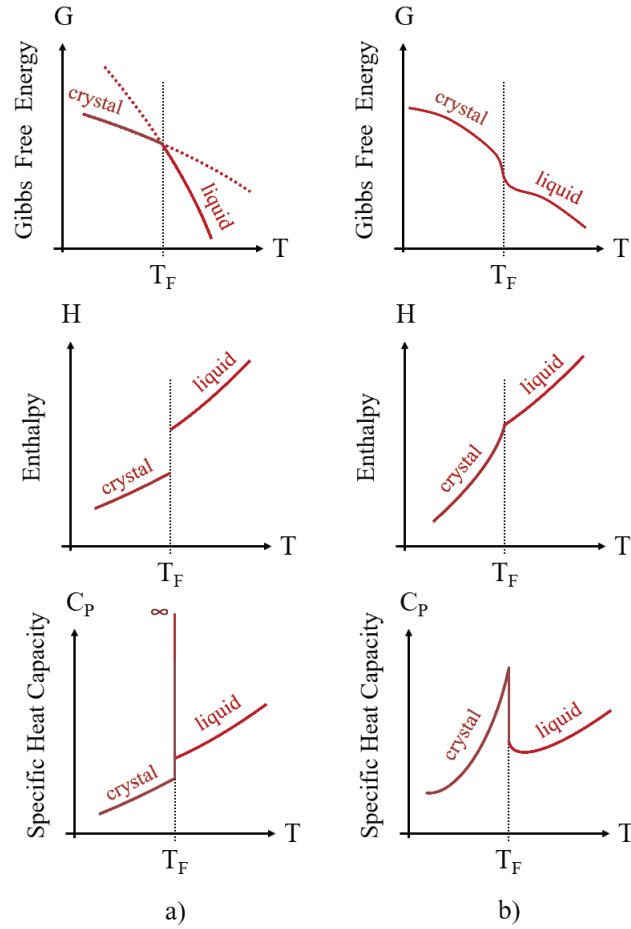


Figure 1.2: First (a) and second (b) order phase transition classification according to their thermodynamic characteristics.

1.2.1 Non-crystalline material transformations

First, let's consider the formation of a crystalline solid. For a usual liquid-solid transition, the system remains constantly at thermodynamic equilibrium during the cooling of the liquid until it reaches the melting temperature T_F . Then, when the system passes below the melting point and remains in thermodynamic equilibrium, the material crystallizes. The evolution from liquid to solid follows the functions of the Gibbs free energy G as schematized in the Figure 1.3 below. The transformation temperatures are given by the intersections between the lines of G of the different states: here the melting point between the liquid and solid states. The entropy of each state is given by the slope of the Gibbs free energy functions for each state. However, it is necessary to consider the fact that the liquid-solid transformation is not abrupt. There are in fact two mechanisms for the formation of an ordered structure from a disordered solution [50]:

1. Crystallization can occur homogeneously due to local rearrangements, thereby increasing the short-range order leading to a long-range order.
2. The material crystallizes through the formation of localized crystal nuclei, which tend to increase their size. This is the process of nucleation and growth. This mechanism is considered to be the most common, and it reveals the existence of an energy barrier to the formation of an ordered domain [49]. This last point has to be kept in mind.

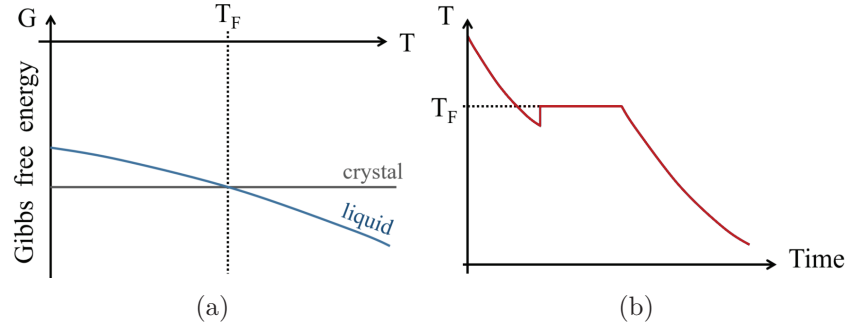


Figure 1.3: Phenomenology of the liquid-solid transformation (a) Evolution of the Gibbs Free Energy G for the condensed states of matter. The minimum Gibbs Free Energy indicates the most favorable state. (b) Dynamics of the crystallization of a pure body observed by calorimetry techniques [49].

The next step is to consider the case where a system does not remain constantly at thermodynamic equilibrium while it is cooled. Indeed, it is possible for a system to remain in the liquid state below the freezing/melting point. It then finds itself in a metastable state, called the supercooled liquid state [49]. In fact, the formation of a crystal or glass depends on the ability of a material to overcome the thermodynamic nucleation barrier it contains. If the nucleation barrier is surpassed within the material while cooling below the liquidus temperature, the material will rearrange easily and undergo a phase transformation into a crystal. If, on the other hand, the material is cooled too rapidly, the liquid remains in metastable equilibrium under the liquidus as illustrated in Figure 1.4. Here, the fact that this state corresponds to an out-of-equilibrium state is clearly visible since it does not correspond to the global minimum of the Gibbs free energy G . It increases its viscosity until it reaches a glass transition temperature where it exhibits mechanical properties similar to those of a solid [49]. A glass is then created. The glass transition temperature is not necessarily unique. This characteristic is related to the fact that the system is in an out-of-equilibrium state and may therefore be related to the cooling rate [53].

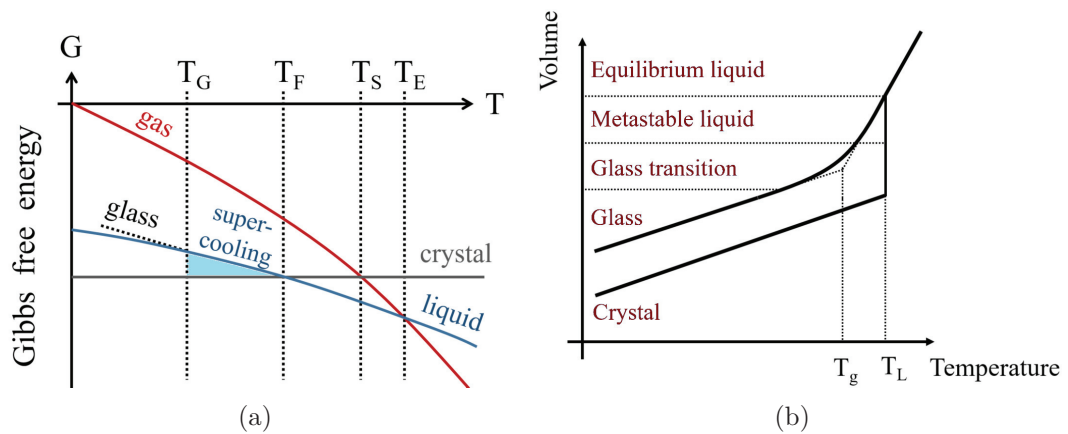


Figure 1.4: Phenomenology of the liquid-glass transformation (a) Evolution of the Gibbs Free Energy G for the condensed states of matter. The minimum Gibbs Free Energy indicates the most favorable state. (b) Schematic diagram of the volume change during the cooling of a liquid. The difference between the formation of glasses and crystals is highlighted. The cooling rate is of critical importance, since it controls the nucleation of crystals.

Formal description of glass transition

Without having fully presented it, it has just been seen that the glass transition is strongly dependent on the conditions of the evolution of a system and therefore on the rearrangements of its structure. We can define the average time τ_{mob} which a structural unit of a system takes to move by a distance comparable to its dimension by translation. By considering any molecule in a viscous environment under constraint σ , it is possible to determine the frequency of jumps from a site occupied by a molecule to a neighbouring empty site as Eyring formulated it [49, 54, 55]:

$$\nu_{\pm} = \nu_0 \cdot \exp\left(-\frac{\Delta g \mp \sigma v_a}{k_B T}\right) \quad (1.1)$$

This obviously takes into account the work done by the strain during the jump. The frequency constant is $\nu_0 = cte \cdot \nu_D \approx 10^{-13} s^{-1}$ with ν_D being the Debye frequency for atom vibration in their potential. The Gibbs free energy variation of the particle in the jump to reach its activated position is given by Δg , and v_a represents the activation volume (proportional to the cube of the jump dimension). This expression leads easily to the actual jumping time:

$$\tau_{mob} = (v_+ - v_-)^{-1} = \nu_0^{-1} \cdot \exp\left(\frac{\Delta g}{k_B T}\right) \quad (1.2)$$

Therefore, the formulation by Eyring lead to temperature effects similar to the **Arrhenius law**. This law describes the temperature dependence of a reaction or relaxation rate, where the natural logarithm of the rate constant of a reaction is proportional to its activation energy and inversely proportional to the Boltzmann thermal energy $k_B T$. It is noticeable that a decrease in temperature induces an increase in the characteristic time of structural rearrangement. Two cases can now be examined:

- For a state out of thermodynamic equilibrium, if sufficient experimental time t_{exp} is allocated to the material to rearrange (i.e. $t_{exp} > \tau_{mob}$), the system can reach the thermodynamic equilibrium configuration. This is obviously true if a stable or metastable thermodynamic equilibrium is considered, and it is the latter that interests us here. These conditions satisfy the hypothesis of ergodicity for thermodynamic systems. For the situation where sufficient experimental time is allocated, it is possible to express the dynamic viscosity of the supercooled system by taking Equation 1.1 [49] as:

$$\eta = \eta_0 \exp\left(\frac{\Delta g}{k_B T}\right)$$

- As soon as the characteristic rearrangement time becomes too long for the experimentally allocated time (i.e. $t_{exp} < \tau_{mob}$), changes can no longer take place within the system. The system can no longer reach its equilibrium configuration and remains frozen in an out-of-equilibrium state called the glassy state. It is then considered that the system is no longer ergodic. The corresponding transition can therefore be classified as a non-thermodynamic transition [51]. In such a situation, there is a peculiarity in the viscosity of the system, which increases drastically over a small temperature range as shown in the Figure 1.5. This thus deviates from a behaviour compatible with the Arrhenius law. The empirical law of Vogel-Fulcher-Tamman is therefore generally evoked [56, 57, 58, 59, 49]:

$$\eta = \eta_0 \exp\left(\frac{\Delta g}{k_B (T - T_0)}\right) \quad (1.3)$$

In the Vogel-Fulcher-Tammann expression, T_0 is the "Vogel temperature" at which the viscosity or relaxation time diverges.

When a system in metastable equilibrium is cooled, its structural organisation increases. This is due to the fact that the number of structural units with at least one degree of freedom of translation and at least one free neighbouring site decreases [49]. The **glass transition temperature** T_g is therefore defined by the condition where the system is sufficiently cooled so that $t_{\text{exp}} = \tau_{\text{mob}}$. It should be noted that the Vogel temperature is not the same as the glass transition temperature even if they remain close. It is, however, possible to estimate the value of T_0 in relation to the glass transition temperature T_g . T_0 is generally found to be close to $T_g - 50\text{K}$ (see page 51 of [49]).

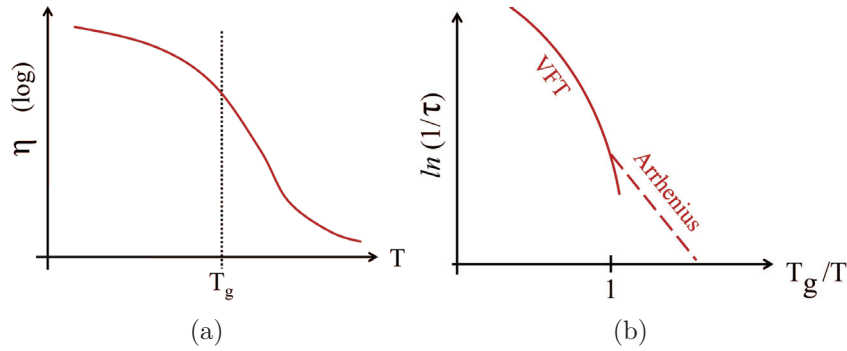


Figure 1.5: Two glass transition characteristics (a) Viscosity variation around the glass transition temperature T_g . (b) Relaxation time variation showing two different behaviours: one following the Vogel-Fulcher-Tammann law (VFT) and one following the Arrhenius law.

There is a lot of confusion around the term glass. Some people refer to glass as all types of amorphous materials [60] otherwise to non-crystalline materials [61]. In common parlance, a glass is the material obtained by fusing silica with metal oxides, commonly Sodium (Na) and Calcium (Ca). The mixing is carried out at high temperatures, usually around 1400-1600 Celsius, which is then rapidly cooled to prevent the material to crystallize. However, many other materials can exist in a non-crystalline form, or more specifically in a glassy state of matter or "Glaszustand" in German as defined by Tamman in 1933 [62]. To avoid any ambiguity, glasses should be referred to non-crystalline materials undergoing a glass transition.

1.2.2 Application fields of glass transition

The interest in glass transition now goes far beyond the study of glass such as silicate glasses [63] or polymers [64]. There are a number of situations indicating that glass transition plays a fundamental role in many aspects of condensed matter physics. The essential point of these considerations is the order parameter of the system (e.g. atomic configuration, density, magnetic moment, dipole moment) when the latter varies with temperature to maintain thermodynamic equilibrium. As a matter of fact, any thermodynamic system tends from an unordered high-temperature state to an ordered low-temperature state. This occurs in an attempt to reduce entropy, as assured by the third law of thermodynamics.

For instance, in the case of magnetisation, the order-disorder magnetic moment transition corresponds to the ferromagnetic transition. In the case of the electric dipole, this refers to the ferroelectric transition. And for the lattice strain it corresponds to the martensitic transition between a high temperature parent phase (or austenite or ferroelastic phase) and a low temperature martensitic phase. A parallel can therefore be drawn between these three systems as shown in Figure 1.6. For the transitions mentioned above, the thermodynamic equilibrium is kept.

Maintaining thermodynamic equilibrium implies the need for various degrees of freedom during a characteristic rearrangement time. As this characteristic time increases with decreasing temperature, there may be situations where this characteristic time becomes larger than the time scale of any reasonable observation. The system then freezes in a glassy state that is a disordered phase with local order only (see Figure 1.6). This is why these transitions are also referred to as glass transitions [49, 65].

One may therefore wonder whether there is a counterpart to the disorder-order ferromagnetic, ferroelectric and martensitic transitions. The latter should be of the disorder-frozen disorder type. For the magnetic system, there is indeed a conjugate glass transition to the classic ferromagnetic transition for spin glasses. This is called the cluster-spin glass transition and is present in ferromagnetic materials doped with non-magnetic elements [66]. This also applies to ferroelectric systems, where by sufficiently doping such a system with point defects a conjugated glass transition can be induced which is called a relaxor transition [67]. The existence of a glass transition conjugated to the martensitic transition was also theorised [68, 69, 70] and finally observed by Ren et al. for instance in doped TiNiFe systems [51, 65, 71, 72, 73, 74]. It is understood that doping plays an essential role in the formation of a glassy phase, since the frozen state appears only at high concentrations of defects [51]. Thus, it is possible to suspect a disorder-frozen disorder transition for various materials undergoing a martensitic transition, as is the case with pure cobalt. It would therefore be the formation of a strain glass through a glass transition that could be of interest for this work.

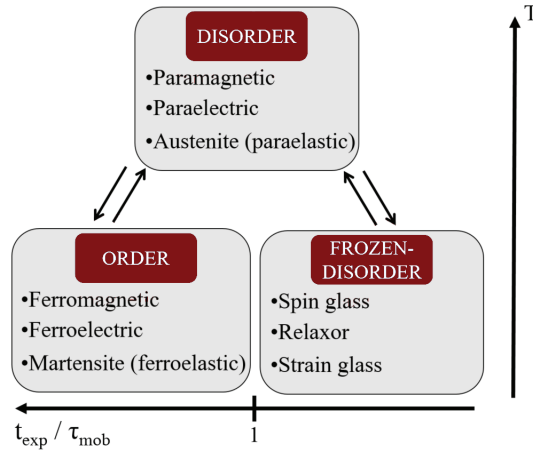


Figure 1.6: Diagram showing the possible symmetry between thermodynamic and non-thermodynamic transitions. The non-thermodynamic transitions are due to the breaking of the ergodicity hypothesis, which is ensured in conventional thermodynamics. The occurrence of a glass transition depends on whether the time allocated to the experiment t_{exp} is sufficient for the rearrangement time of the system τ_{mob} . If this is not the case, the system is unable to order itself and becomes frozen. Each ferromagnetic, ferroelectric and ferroelastic transition thus finds its conjugated transition. A transition from a high-temperature disordered state to a low-temperature ordered state is replaced by a transition from a high-temperature disordered state to a low-temperature frozen-disordered state.

Whichever physical system is considered, the attribution of a strain-glass behaviour requires several characteristics [65] :

1. The relaxation time related to the transition process should follow the Vogel-Fulcher-Tammann (VFT) model (or equivalent). This means that the relaxation process associated with a glass transition is thermally activated, but the relaxation time diverges towards a temperature. The relaxation time can be measured by any type of spectroscopy suitable for the system under investigation.
2. The system studied must demonstrate a break in the hypothesis of ergodicity and must therefore depend on its thermomechanical history. The hypothesis of ergodicity is, in most cases, difficult to demonstrate for a system, but a standard method is nonetheless used experimentally; it is the zero-field-cooling(ZFC-FH)/fieldcooling(FC-FH) measurement [65].
3. The low-temperature crystalline state exhibits a short-range order and is characterized by the same average structure as the high-temperature disordered crystalline state.

1.3 Mechanical spectroscopy

The damping capacity of a material is defined by its ability to dissipate mechanical energy into heat. While the mechanical energy is induced by external mechanical stresses, the heat is generated by internal friction. Generally it is referred to as relaxation phenomena caused by the movement of structural defects. The experimental method for measuring internal friction is called mechanical spectroscopy. Through this technique, dissipative mechanisms are activated within a solid under cyclic stresses at specific temperatures and cyclic stress frequencies. Such dissipative mechanisms are the key to deeply investigate the microstructural evolution of a material, since the internal friction originates from the movement of crystal lattice defects.

The formalism of internal friction is developed in this section first through a phenomenological approach describing the origins of internal friction and is illustrated by a creep experiment. As it will become apparent, the origins of these phenomena can be explained through the concept of the anelasticity of solids. A thermodynamic approach is then used to fully develop the formalism of internal friction, that is a model describing the relaxation phenomena occurring within a solid. Other approaches, such as the phenomenological and rheological approaches [75, 76, 11], allow us to explain that same formalism.

1.3.1 Phenomenology of anelasticity

Consider an ideal anelastic solid, i.e. a solid the total strain of which ε induced by a stress σ composed of the sum of an elastic term ε_{el} and an anelastic term ε_{an} . We omit any term related to a plastic and therefore irreversible strain ε_{pl} :

$$\varepsilon = \varepsilon_{el} + \varepsilon_{an} \quad (1.4)$$

The elastic strain ε_{el} immediately follows the stress and is reversible. It is expressed linearly as a function of the stress σ (Hooke's law) through the modulus of compliance J (or commonly the compliance) i.e. the reciprocal of the modulus of elasticity M . A non-relaxed term J_N is considered for the elastic part:

$$\varepsilon_{el} = J_N \cdot \sigma \quad (1.5)$$

The anelastic deformation is also reversible, but it is time-dependent and follows the stress until it reaches an equilibrium value ε_{an}^∞ . The temporal evolution of the anelastic deformation ε_{an} is characterized by a relaxation time τ . Once an equilibrium position has been reached, the deformation of an ideal anelastic solid can be expressed through the stress σ and the relaxed compliance J_R (relaxed term):

$$\varepsilon = \varepsilon_{el} + \varepsilon_{an}^\infty = J_R \cdot \sigma \quad (1.6)$$

For an arbitrary deformation, the generalization of the Hooke's law would be expressed as function of second-order tensor through a set of linear equations [75, 76]. The rudimentary Hooke's law remains however valid for simple cases such as uniaxial deformation or pure shear. Following equations 1.5 and 1.6, the application of a stress on an ideal anelastic solid induces a deformation of the solid over time. This phenomenon is illustrated by the creep and creep recovery experiment as shown in Figure 1.7.

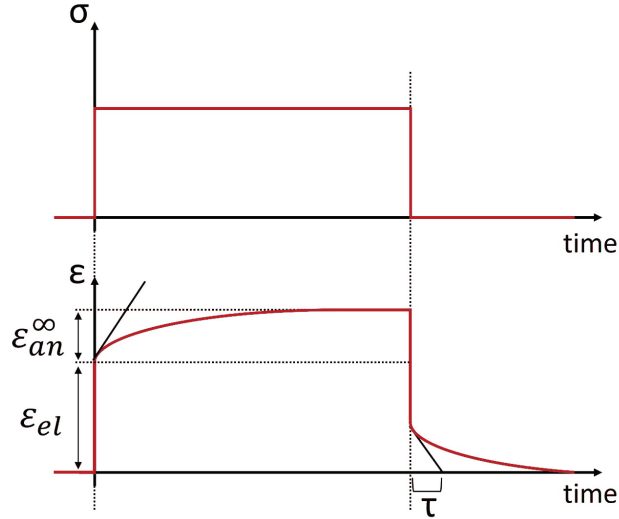


Figure 1.7: Creep and creep recovery experiment - Time evolution of the elastic and anelastic deformation of an ideal anelastic solid following the application of a stress σ . The anelastic deformation is described by its relaxed strain amplitude $\varepsilon_{an}^{\infty}$ and relaxation time τ . The elastic strain amplitude ε_{el} is not time-dependent and is generally greater than the anelastic relaxed strain amplitude $\varepsilon_{an}^{\infty}$.

This temporal evolution is called anelastic relaxation and is described by the two parameters of relaxation time τ and relaxation intensity Δ defined as:

$$\Delta = \frac{\varepsilon_{an}^{\infty}}{\varepsilon_{el}} = \frac{J_R - J_N}{J_N} = \frac{\delta J}{J_N} \quad (1.7)$$

$$\tau(T) = \tau_0 \cdot \exp\left(\frac{E_{act}}{k_B \cdot T}\right) \quad (1.8)$$

The equation 1.8 refers to the specific case of a thermally activated relaxation process (as explained in the section 2.7.2 at the page 47), where the relaxation time τ is expressed with a limit relaxation time τ_0 and varies exponentially with the thermal energy $k_b \cdot T$ and an activation energy E_{act} corresponding to the observed relaxation process.

The microscopic origin of anelasticity is explained by the movement of defects in the internal structure of the solid. These defects move from an equilibrium position without stress to another equilibrium position under stress. In most cases, the higher the density of defects, the greater the relaxation intensity Δ ¹. Moreover, it would be irrelevant to conduct an experiment over the entire period of anelastic relaxation. Experimentally, the investigations on anelastic solid systems are made in quasi-static or dynamic experiments.

Quasi-static measures correspond to creep and creep recovery experiments or to stress relaxation experiments. For these techniques, either the stress or the strain is held constant for periods of a few seconds or more. Dynamic experiments study the anelastic behavior during much shorter times. For these techniques, a periodic stress or strain is applied on a solid and the phase lag between stress and strain is measured. For more details, section 2.7 will specifically develop and discuss the dynamic measurement of anelasticity.

¹This is not the case for grain boundary sliding.

1.3.2 Thermodynamic approach of anelasticity

This section aims at developing the ideal linear solid equation through the formalism of thermodynamics. In thermodynamics, to describe a solid system and its evolution a set of state variables ξ_i is necessary. Such variables set should be defined by a minimum number of parameter while describing the system. These variables can be internal and external state variables.

In the case of an equilibrium system, the state variables are not independent. They are linked by a system state equation $U = U(\xi_1, \xi_2, \xi_3, \dots)$. For a system undergoing a transformation, the state variables must be independent of each other. Equilibrium thermodynamics satisfies the fact that for each infinitesimal change in an external variable the solid evolves to unique equilibrium states in a continuous way. With the later remark, it can be understood that viscoelastic or plastic materials cannot be completely described as an equilibrium thermodynamic solid. Indeed, such materials do not induce a unique equilibrium strain value for each applied stress and strain is not reversible. The equilibrium states through which these materials pass can demonstrate discontinuities. A material that satisfies a linear relationship between stress and strain, as well as the ability to recover after the release of an applied stress, is a thermodynamic solid. Of course, these conditions are assured for anelastic materials after a long enough relaxation time.

For this case study, the external state variables include temperature, stress and strain. Instead, internal state variables may be short-range or long-range order parameters, and are for example the variation in the concentration of point defects (zero dimensional defects), the mean displacement of dislocations (one dimensional defects) or the sliding distance of grain boundaries (two dimensional defects).

To describe an ideal linear solid system, the first step is to understand whether it is a thermodynamic system in equilibrium or out of equilibrium. In fact, considering an anelastic relaxation, the system has to be evaluated as being in pseudo equilibrium (a process close to equilibrium), as proven hereafter.

Let's consider a stress-free anelastic solid at equilibrium. The structural defects it contains are also at equilibrium. These can then become mobile under the action of an external stress σ , and induce a process of anelastic relaxation (deformation) ε_{an} to reach a new equilibrium point under stress ε_{an}^∞ (relaxed). Let's note ξ the internal variable associated with the displacement of these defects, evolving from the initial value $\xi = 0$ to the final value $\xi = \xi_R$. One can reasonably estimate that the relation between the anelastic deformation and the internal variable is linear: $\varepsilon_{an} = \kappa \cdot \xi$ with κ a coupling constant. During deformation, the state variables σ and ξ are independent, and thus the total deformation of the solid corresponds to the combination of the contributions of the two state variables :

$$\varepsilon(\sigma, \xi) = J_N \cdot \sigma + \kappa \cdot \xi \quad (1.9)$$

The initial state is given by $\varepsilon = 0$, $\sigma = 0$ and $\xi = 0$; the state variables are therefore interdependent. The final state is given by $\varepsilon = J_N \cdot \sigma + \varepsilon_{an}^\infty = J_N \cdot \sigma + \kappa \cdot \xi_R$. However, it can be reasonably supposed that the relaxed internal variable ξ_R is uniquely defined by the applied constraint σ , and can thus be related by:

$$\xi_R = \rho \cdot \sigma \quad (1.10)$$

Consequently, the state variables become dependent again at equilibrium under constraint $\varepsilon(\sigma, \xi_R) = J_N \cdot \sigma + \kappa \cdot \rho \cdot \sigma$. Considering equilibrium systems, the study of phenomena related to anelasticity would become trivial, all internal variables becoming interdependent. The laws of linear elasticity would suffice to study solids. For that reason, the anelasticity is studied experimentally in quasi-static or dynamical methods. Although it is now clear that the state must be out of equilibrium, it is necessary to study states for which sufficient time has been allocated in order to achieve a so-called pseudo-equilibrium (named *Gleichgewichtsnähe* by Meixner [77]). In such a state, the solid does not have enough time for each of its internal variables to reach their equilibrium value, the system is in a transient state close to equilibrium, allowing the system to be described by independant external and internal state variables.

Anelastic solids standard equation

As described above, an anelastic relaxation is a thermodynamic phenomenon where an equilibrium is found through the coupling of a mechanical stress with a pure elastic response and internal variables. Those internal variable are physically related with the structural defects in solids evolving through kinetic processes.

For each internal variable ξ , it is possible to develop its temporal evolution when it tends towards its equilibrium value ξ_R . The ideal anelastic materials studied only take into account reversible behaviors. Thus, only a linear theory is developed and only a first-order development of the time differential equation of the internal variables is necessary. In this regard, the variation with time of an internal variable ξ is proportional to the difference between ξ and its equilibrium point ξ_R with a proportionality constant having the reciprocal of time as a unit:

$$\frac{d\xi}{dt} = -\frac{1}{\tau} (\xi - \xi_R) \quad (1.11)$$

$(1/\tau)$ is used as it is the characteristic time of the relaxation. Following the example of the creep experiment of Figure 1.7 where a constant strain is applied at $t = 0$, the solution of the time differential equation is then:

$$\xi(t) = \xi_R [1 - \exp(-t/\tau)] \quad (1.12)$$

Combining Equations 1.9 and 1.11 with the expression of the internal variable relaxed under stress $\xi_R = \rho \cdot \sigma$, one can find an equation for anelastic solids $(J_N + \kappa \cdot \rho) \cdot \sigma + \tau \cdot J_N \cdot \dot{\sigma} = \varepsilon + \tau \cdot \dot{\varepsilon}$. Finally this relation can be generalized to the standard equation for anelastic solids, considering Equations 1.5 and 1.6 with $\varepsilon_{an}^\infty = \kappa \cdot \varepsilon_R = \kappa \cdot \rho \sigma$:

$$\boxed{J_R \cdot \sigma + \tau \cdot J_N \cdot \dot{\sigma} = \varepsilon + \tau \cdot \dot{\varepsilon}} \quad (1.13)$$

It is concluded, that the change in one internal variable inducing anelastic behaviours can be described as a set of two constant parameters including the anelastic relaxation time and amplitude $\{\tau, \delta J\}$, where the term δJ has been introduced. It corresponds to the amplitude of the purely anelastic relaxation $\delta J = J_R - J_N = \varepsilon_{an}^\infty / \sigma = \kappa \cdot \rho$.

Generalized thermodynamic considerations

A generalized description of ideal anelastic solids with n different relaxing microstructural defects should consider external variables such as stress σ and temperature T , and n internal variables ξ_i with $i=(1,...,n)$. While the generalization to the case with n internal variables ξ_i for the Equations 1.10 and 1.9 is direct, that of their temporal evolution (Equation 1.11) presents several crucial questions. During their transition to a new equilibrium, the evolution's rate of the internal variables depends not only on their deviation from their equilibrium position but also on the deviation of the set of all internal variables from their equilibrium. Each internal variable is therefore not only coupled to stress and strain, but also to all other internal variables. However, it is possible to demonstrate [75, 77, 78] that, for such systems, it is possible to define a linear transformation from n coupled linear differential equations to n decoupled linear differential equations. The linear transformation defines a new set of internal variables (ξ'_i) called "normal internal variables", where anelastic relaxation behaviours appear to be independent from each other. The previously presented solution of Equation 1.12 is therefore valid for each internal variable. The spectrum of relaxation behaviours occurring in a solid is then completely described by a set of (at most) n pairs of relaxation time and amplitude $\{\tau'_i, \delta J'_i\}$. It should be noted, however, that internal variables corresponding to one same relaxation time will then be associated to one single set of parameters $\{\tau'_i, \delta J'_i\}$. Accordingly, the total magnitude of anelastic relaxation is given by the following relation where $n' \leq n$.

$$\delta J = \sum_{i=1}^{n'} \kappa'_i \cdot \rho'_i = \sum_{i=1}^{n'} \delta J'_i \quad (1.14)$$

Thermodynamic functions

The considerations presented above allow to fully describe behaviours of anelastic solids through thermodynamic functions (e.g. free energy, internal energy). The anelastic deformation relationships can be developed through Gibbs free energy. One can start by developing its differential form per unit volume $g = g(T, \sigma, \xi)$ considering one internal variable ξ (all quantities defined per unit volume prior to deformation will be denoted by lower case letters hereafter).

$$dg = -s \cdot dT - \varepsilon \cdot d\sigma - A \cdot d\xi \quad (1.15)$$

Where the quantity A is named the affinity and is the conjugated variable of ξ given by:

$$A = - \left(\frac{\partial g}{\partial \xi} \right)_{\sigma, T, \xi} \quad (1.16)$$

The affinities represent the driving forces towards equilibrium when their conjugate variable are not in equilibrium. Following the same approach, we find the well-known relationships, where the entropy per unit volume is the conjugate variable of the temperature, and where the strain is the conjugate variable of the stress :

$$s = - \left(\frac{\partial g}{\partial T} \right)_{\sigma, \xi} \quad \text{and} \quad \varepsilon = - \left(\frac{\partial g}{\partial \sigma} \right)_{T, \xi} \quad (1.17)$$

Carrying out Taylor's series to quadratic terms of the Gibbs function around the value where the solid is under no stress and at equilibrium $g_0 = g(T = T_0, \sigma = 0, \xi = 0)$ leads to [75] :

$$g(T, \sigma, \xi) = g_0 - \frac{1}{2} \cdot \frac{C_\sigma}{T} \cdot \Delta T^2 - \frac{1}{2} \cdot J_N \cdot \sigma^2 - \sigma \cdot \kappa \cdot \xi - \alpha \cdot \sigma \cdot \Delta T - \Delta T \cdot \varkappa \cdot \xi + \frac{1}{2} \beta \cdot \xi^2 \quad (1.18)$$

Where α is the thermal expansion coefficient, c_σ is the specific heat at constant stress per unit volume, and $\Delta T = (T - T_0)$. From Equation 1.18, it is then possible to find the strain and the affinity in isothermal conditions :

$$\varepsilon(\sigma, \xi) = - \left. \frac{\partial g}{\partial \sigma} \right|_{\Delta T=0} = J_N \cdot \sigma + \kappa \cdot \xi \quad (1.19)$$

$$A(\sigma, \xi) = - \left. \frac{\partial g}{\partial \xi} \right|_{\Delta T=0} = -\sigma \cdot \kappa + \beta \cdot \xi \quad (1.20)$$

The anelastic deformation relationship is then given by Equation 1.19 and is composed by an anelastic and an elastic part as observed in the creep experiment of Figure 1.7. Equation 1.19 is in line with the developments presented around Equations 1.9 and 1.10.

2 Experimental techniques

This thesis work is defined by the need to correlate tool-life with other mechanical characteristics and properties that would be easier to control from an industrial point of view. The durability of cutting tools is indeed a macroscopic property, which may be influenced by multiple factors. In order to ensure the discrimination capability of the insert's tool-life measurement, it was decided to perform tests under extreme operating conditions on industrial cutting machines. Wear and shock resistance were evaluated.

The intent of this chapter is to present all the measurement techniques used to carry out the comparative study between the durability of the tools produced by Lamina-tech and a broad variety of properties, which may impact it. In particular, techniques such as micro- and nano-indentation, X-ray diffraction, tribology, mechanical spectroscopy or advanced microscopy (SEM, TEM) are introduced. Each of the properties under consideration are related to several regions of the coated cemented carbide composite material. Coatings mechanical properties (i.e. hardness, elastic modulus, and residual stress), coating characteristics (i.e. roughness, thickness, and friction coefficient), bulk mechanical properties (i.e. hardness and fracture toughness) and bulk mechanical characteristics (i.e. porosity, granulometry, crystal structure and defects microstructure, bulk defects dynamics) are investigated.

2.1 Machining tests and Tool-life

In the machining industry, hardmetal cutting tools are used to shape workpieces by removing gradually some of their surface material. Cutting tools are mostly produced in small pieces in the form of squares, rhombuses, triangles or drills called inserts, where their edges form the active cutting parts. The main machining techniques are milling, turning or drilling ¹, and each of them operates according to a specific geometry as shown in Figure 2.1. Tool wear mechanisms in machining are reported in Figure 2.2.

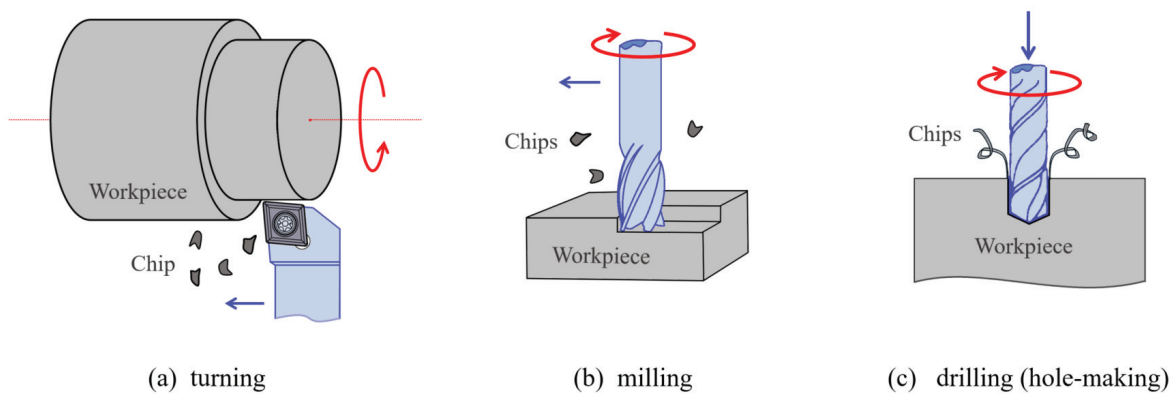


Figure 2.1: Main machining processes with cutting tools where small chips are removed from the workpiece material. The cutting operation is ensured by the relative movement between the cutting tools and the workpiece, controlled by the feed motion (blue arrow) and the cutting rotation (red arrow) : (a) Turning corresponds to the removal of material from a rotating workpiece (cutting motion) with the progression of a tool's cutting edge (feed motion). (b) In milling, a tool with multiple cutting edges spins (cutting motion) and is moved in relation to the surface of the sample (feed motion) to remove material. (c) The drilling process corresponds to the formation of a round hole by inserting a rotating tool (cutting motion) with several cutting edges into the workpiece (feed motion).

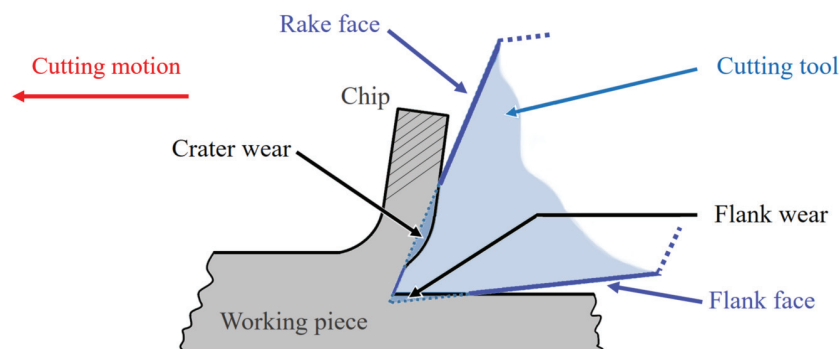


Figure 2.2: Wear mechanisms during the machining of a workpiece.

¹In french the corresponding terms are: fraiseage (milling), chariotage (turning) and perçage (drilling).

2.1.1 Failures mechanisms in machining

Cutting tools undergo to severe friction conditions with large temperature gradients near the tool surface and extreme stresses [79]. These working conditions lead to cutting tool failures during their use. A change in the shape of the tool resulting from the progressive loss of tool material is referred to as wear [80, 81]. These failures include flank wear and crater wear, as shown in the Figure 2.3. These wear mechanisms are normal failures, i.e. they are unavoidable but must be controlled and minimised.

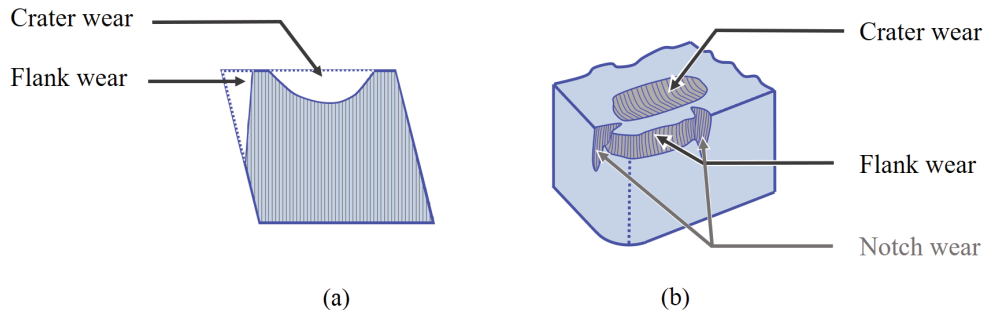


Figure 2.3: Wear failures phenomena on inserts (a) Sectional view of a flank and crater wear. (b) Side view of a flank, a crater and notch wear.

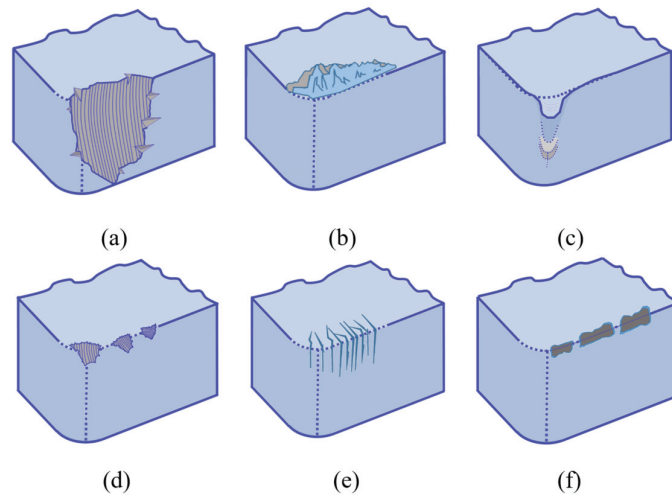


Figure 2.4: Abnormal failures phenomena on inserts (a) Insert breakage. (b) Built-up edge formation. (c) Plastic deformation. (d) Edge chipping or frittering. (e) Comb (thermal) cracks. (f) coating flaking.

However, abnormal failures can also occur. Such mechanisms are insert breakage, built-up edge formation, plastic deformation, edge chipping or frittering, comb (thermal) cracks or notch wear. These phenomena are shown in the Figure 2.4 and Figure 2.3(b). For inserts without conception or manufacturing defects, these failure mechanisms are the consequence of avoidable causes and better machining conditions must be used. The failure mechanisms of cutting tools are dependent on several physical properties and behaviour of the composite materials. Not exhaustively, these include hardness and elastic moduli, deformation behaviours, fracture toughness and strength.

As cemented carbides are multiphase materials, insert fractures can occur in several stages and depend on crack propagation modes. Crack are initiated by the fracture of a material defect or of one of its microstructure elements, and it occurs when stresses and strains reach

a critical level. This maximum stress level defines the strength of the material. However, micro-fractures can occur without propagating into critical cracks. In order to avoid such critical issues, it is essential to be able to model and control the crack propagation. Nonetheless, these aspects will not be discussed in this section. For more information on fracture modes and crack propagation, the reader may refer to other works [82, 83].

In practice, if the surface state of an insert has no obvious defects, its wear is assessed during its use. A polymechanic learns how to recognise wear and defects on his cutting tools by the surface state of the parts he is working on, by the appearance of the cutting chips (size, shape, colors), and through the use of the machine-tool (noise, necessary machining efforts, and vibrations in turning, milling or drilling).

For the manufacturer of cemented carbide cutting tools, however, it is necessary to define quantitative tests to ensure the quality and durability of his products. For this purpose, tests under extreme conditions are conducted. These are irreversible destructive tests where the final criteria are catastrophic breakage or excessive wear induced on the cutting tools. In this work, two tests were conducted under controlled conditions to evaluate the performance of coated cutting tools: a shock test and a rapid wear test (also called cratering).

2.1.2 Shock test

The tool-life is measured during a turning shock-test on a 42CrMo4 steel workpiece. The workpiece mounted on the lathe is notched along its length by two slots, which induces interrupted cuts during the shock test (see Figure 2.5). To avoid discrepancy the workpiece material comes from the same production batch. The turning is performed without coolant with a depth of cut of $DOC = 2.00mm$ and a feed rate of $F = 0.23mm/rev$ using $V_c = 160m/min$ as a cutting speed. The service life during a cutting process is determined until tool breakage by repeated measurements. The observed failure mechanisms of the inserts were flaking, chipping and breakage.

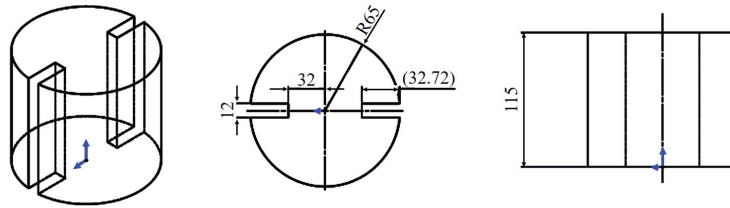


Figure 2.5: Diagram of the part used to evaluate the impact resistance of the insert.

2.1.3 Rapid wear test

The crater wear test, also called "facing until the center test", is performed to determine the resistance to tool wear and tool toughness. It is executed in turning a 42CrMo4 steel workpiece with coolant. Since the wear resistance is measured and not breakage, the test is stopped each 2.5 minutes to observe the wear evolution. The cratering tests are made under the two different following conditions : depth of cut of $DOC = 2.00mm$ or $1.00mm$, a feed rate of $F = 0.3mm/rev$ or $0.25mm/rev$, and cutting speed $V_c = 270m/min$ or $200m/min$. Times of machining until critical wear or failure are measured during repeated measurements. Critical failure mechanisms of the inserts were built-up edge, coating flaking and insert breakage.

2.2 Thin film coating

In the field of the cutting tools industry, thin films coatings prevent cracks, delamination and tool failure. Thin films are synthesized materials with a thickness ranging from a few angstroms to tens of micrometers. Their applications for hardmetals date back to the 1970s with the introduction of chemical vapor deposition (CVD) methods, to which were added the physical vapor deposition (PVD) methods in the 1980s. In the coated tools industry, the most commonly used coating materials are TiC, TiCN, TiN, TiAlN, Al₂O₃, and to a lesser extent CrN, CrAlN, TiB₂, ZrN and carbon coatings (diamond or DLC). As reported by [8], this is mainly due to their excellent properties for machining conditions. These characteristics are listed in the Table 2.1 below:

Characteristic Improvement	Hardness at RT	Hot Hardness (T° >800 °C)	Chemical Stability	Oxidation Stability
↑	TiC	Al ₂ O ₃	Al ₂ O ₃	Al ₂ O ₃
	TiCN	TiAlN	TiAlN	TiAlN
	Al ₂ O ₃	TiN	TiN	TiN
	TiAlN	TiCN	TiCN	TiCN
	TiN	TiC	TiC	TiC

Table 2.1: Classification of the main PVD and CVD coatings for hardmetals depending on their advantages for machining conditions, according to [8].

It is clear from the Table 2.1 that the coatings with the best advantages for most cutting operations are the coating materials TiAlN and Al₂O₃. This may, however, differ for certain machining processes. Along with the composition of coatings, there are many characteristics that are involved in the durability of thin films. Their architecture [84], hardness and toughness [85, 86], residual stresses [87, 88, 86], grain structure (grain refinement) [86, 89] or texture [90] must also be taken into account. These last points are essentially controlled by the way they are produced.

2.2.1 Deposition techniques in the hardmetals industry

The two main types of thin film coating techniques are chemical and physical depositions. The first set of techniques is based on precursors that undergo a chemical transformation on the surface of a solid, creating the thin films. They include chemical vapor deposition (CVD), electroplating and chemical solution deposition (CSD). Physical deposition consists in transforming a solid of the chosen material into a pulverized gas phase (physical phase change), which will be deposited with a defined composition and architecture on a target. Those methods include cathodic arc deposition (CAD), Electron Beam Physical Vapor Deposition (EBPVD), sputtering techniques (PVD), and Pulsed Laser Deposition (PLD). In the hardmetals industry, CVD techniques are used to synthesize alpha-phase alumina coatings, while TiAlN thin films are deposited by PVD techniques [8]. Even if the CVD alpha-phase alumina coatings are the best-selling products for turning operations, PVD techniques have considerable advantages. Thanks to PVD, it is easy to obtain high quality ceramic coatings with high hardness, wear resistance and sharper cutting edges. The thickness of PVD films is also easily controllable. Typically CVD coatings have thicknesses in the range of 10 to 20 microns, whereas PVD can easily be applied in the micron range.

This control is tremendously useful for the preparation of multilayer or nanolaminate coatings. Another disadvantage of CVD is the process temperature. In a CVD furnace, the temperature can rise between 800 and 1000°C, which can have a negative impact since tensile stress can be induced on the surface during cooling to form fine cracks. In contrast, the process temperatures of PVD generally do not exceed 500°C and the produced surfaces have residual compressive stresses. Therefore, CVD coated tools are used for turning applications, where the cutting force is uniform and continuous during the process. On the contrary, the compressive stresses of PVD coatings make them the best candidates for interrupted cutting or multipurpose tools, where preventing crack formation and expansion is a key parameter. Milling is a typical interrupted cutting process.

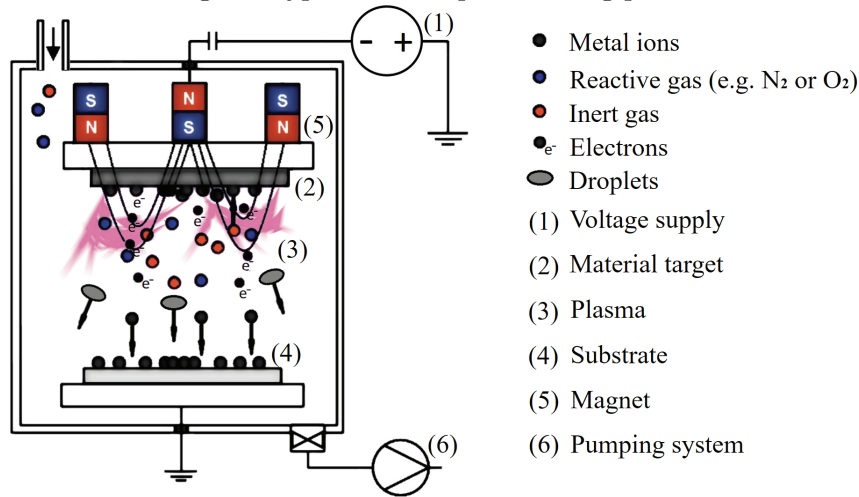


Figure 2.6: Schematic diagram of a cathodic arc evaporation (CAE) system

The coatings used in this study are applied with PVD techniques either on WC-6wt.%Co or WC-10wt.%Co grades materials. The composition of the thin films is based on CrN, TiN and TiAlN (or AlTiN). Their arrangement has been chosen to be multilayer or bilayer, with CrN or TiN as the subcoating.

TiN is an extremely versatile material when used in industrial deposition. It is stable and inert, i.e. it will not corrode and has excellent chemical resistance. Above all, it has high temperature tolerance [91] and high hardness [92].

CrN is also an excellent industrial coating. It is a tough material with high hardness [93], good oxidation and temperature resistance [94], which gives it corrosion resistance.

TiAlN is known to be a coating with excellent performance in high temperature applications. It has better high temperature resistance than TiN or TiC [91]. It also has higher hardness and especially higher hot hardness [95]. The idea of alloying Al and TiN emerged [96, 97, 98] in order to form coatings with increased resistance to oxidation and to wear. TiAlN coatings have quite a complex structure, since it is not composed of a single phase. It is known for $Ti_xAl_{1-x}N$ with $x < 0.7$ that two sublattices are observed, one occupied by randomly distributed Al and Ti atoms and the other being composed of N atoms [99]. Since this system is not thermodynamically stable, a decomposition into AlN, TiN or titanium-rich TiAlN elements may occur. The main advantage of this coating is its resistance to high temperatures, which is essentially ensured by the formation of a thin protective film of amorphous Al₂O₃ [91, 96]. This has the property of being hard, providing low friction and resisting oxidation. In addition to this, Al₂O₃ elements are constantly recreated at high temperatures as wear progresses.

2.2.2 Coatings material and techniques in this work

The deposition method used by the industrial partner of this project for coating production is a cathodic arc evaporation (CAE) method (or Arc-PVD) [100]. The cathodic arc deposition process consists of producing a low-voltage, high-current plasma discharge over a target made up of the material to be evaporated. This coating process is generated in a high vacuum reactor as shown in the Figure 2.6. The target forms the cathode, and the substrate and the reaction chamber represent the anode. Usually a magnetic field is applied to the cathode in order to control the dynamics of the arc spots. The evaporation of the solid material from the target into a metal plasma vapour is achieved by the high energy density plasma arcs. However, this process also produces droplets that tend to cluster into macroparticles (MPs). These droplets are the biggest disadvantage of the Arc-PVD technique since they can eventually be deposited on the coating surface or be embedded inside the coating. Such phenomenon would result in rough surface and reduce the overall performance of the coating. In order to control droplet generation, there exist various techniques for optimizing cathode target power supply and magnetron configuration (such as the arc splitting technology from swiss-PVD [101]).

The sputtering technique available in the EPFL laboratories consists of Direct Current Magnetron Sputtering (DC-MS). Its basic principle is simple, a target source of the desired material is bombarded with plasma-derived energetic ions. When the kinetic energy of the ions is greater than the binding energy of the surface atoms, these latest are torn off. To form the thin film, these atoms are then condensed on the surface of the chosen substrate. Although there are several possible methods of ion bombardment, the one commonly used is magnetron sputtering. The diagram in the figure 2.7 illustrates the basic setup of such a sputtering deposition system.

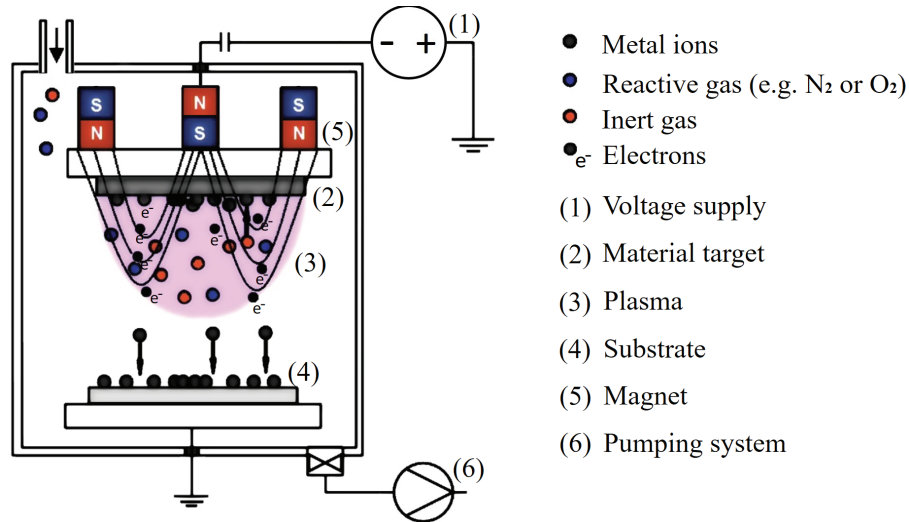


Figure 2.7: Schematic diagram of a magnetron sputtering system

A plasma is used as a source of ion bombardment for sputtering. This plasma is obtained by means of two electrodes, where the first is brought to a high potential (direct current (DC), high power pulses (HiPIMS) or radio frequency (RF) potential) and the second is connected to ground. This plasma is created by discharge at the cathode and is fueled by

a mixture of gases. First of all, a noble gas (e.g. Argon) is needed to stabilize the plasma. Then a reactive gas is required, the nature of which depends on the coating material required.

Considering the example of titanium nitride (TiN) deposition, the source element is a titanium metal target, and the source gases are argon (Ar) and dinitrogen (N_2). When free electrons from the plasma collide with argon atoms, these atoms lose electrons and become positively charged. These argon cations are then attracted to the target source and bombard the surface, transferring their kinetic energy to it. When this bombardment energy is sufficient, the targeted atoms are ejected and form the sputter. The free electrons in the plasma also ionize the sputtered material (Ti^+ for example), and the plasma dissociates the gaseous particles of N_2 . The titanium cations Ti^+ are accelerated towards the substrate by means of a bias affixed to the substrate. Finally, titanium ions then combine with excited nitrogen particles to form a deposit of TiN on the substrate.

Usually, a magnetic field source is added to this type of system, which is then called magnetron sputtering. This configuration implies that the plasma components move in a superposition of electric and magnetic fields. This imposes a helical trajectory on the electrons, the light elements of the plasma, thus lengthening their travel over the surface of the source and thereby increasing the number of collisions. The concentration of electrons is the highest in regions where the magnetic field is parallel to the surface of the source. Heavy elements resulting from ionization are attracted directly to the source, as the magnetic field has little effect on them. Because the efficiency of electron ionization is higher, the sputtering rate increases in magnetron configurations.

2.3 Hardness and nanohardness tests

In the field of hardmetals, hardness is an essential parameter since the tool must be harder than the workpiece. Hardness is the property of a material that characterizes its resistance to permanent shape change induced by an applied compressive force. Describing the hardness properties for composite materials as complex as coated tungsten cemented carbides as a whole can be hazardous or even completely inadequate. This section covers therefore different hardness characterization techniques, each of them more appropriate for different parts of the studied specimens. In this study the following aspects of the materials were tested :

- coating nanohardness measurements,
- bulk average microhardness measurements,
- and in some cases bulk fracture toughness assessments.

For characterizing each of these properties, the instruments that were used and the measurement protocol are presented in the paragraphs that follow and the results of the analyses will be discussed in Section 3.2.2.

2.3.1 Microhardness

In conventional hardness testing, hardness of materials is defined through the well-known relation introduced by R. L. Smith and G. E. Sandly [102, 103] as the ratio between the applied load P and the contact area between the indenter and the material A . This corresponds to the following relationship for Vickers indenters:

$$H_v = \frac{P}{A} = P \cdot \frac{2\sin(136^\circ/2)}{D^2} \simeq \frac{1.8544 \cdot P}{D^2} \quad (2.1)$$

where P represents the load (in kilogram-force kg_f), and where D is the average of the two diagonals of the imprint in mm . The hardness HV is here given in Vickers (kg_f/mm^2). For Vickers hardness reported with units of GPa, it is determined as $HV \simeq 0.0018544 \cdot P/D$, with the load in N , and the mean diagonal of the indentations in mm .

The microhardness was measured using a SHIMADZU HNV-G Series Micro Vickers Hardness Tester [104] illustrated in Figure 2.8. The load of 19.61N was applied (in HV2.0 mode equivalent to approx. 2.0 kg_f) during 30 seconds and the hardness values were calculated by measuring the diameters of the indent using a Keyence VHX-5000 Digital Microscope [105]. For preparation, the samples were cut in half and mirror polished on trays using diamond pastes.

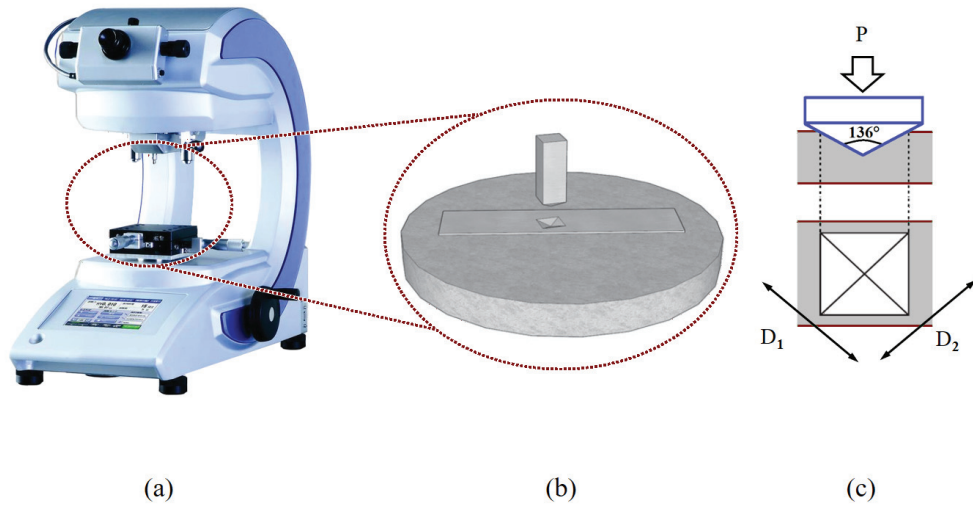


Figure 2.8: Principles and instrument for microindentation. (a) Vickers microhardness tester with pyramidal diamond indenter. (b) Indentation process. (c) The hardness value is calculated from the applied load P and the size of the resulting indentation (mean value of indentation diagonals D_1 and D_2).

2.3.2 Nanohardness

With the need to discriminate the small-scale mechanical properties for each component of a composite or multiphase material, depth-sensitive nanoindentation instruments were developed in the 1980s [106, 107]. This led to the development of standard methods for measuring hardness and modulus of elasticity calculated from data along the load-displacement curves of Berkovich indentations [107, 108, 109]. Because of their resolution

and repeatability, these techniques are now widely used, especially for the investigation of thin films. The Figure 2.9 below presents the principles of measurement by nanoindentation and illustrates the measured quantities.

The Oliver-Pharr method used in this work consists in analyzing the load-unloading curve produced during indentation. A typical curve is given in the Figure 2.9(c). The slope of the unload curve S can be used to calculate the elastic modulus in Pascals:

$$E = \frac{1 - \nu_{sample}^2}{\frac{1}{E_r} - \frac{1 - \nu_{ind}^2}{E_{ind}}} \quad (2.2)$$

with ν_{sample} the Poisson ratio of the sample's material, E_r the reduced modulus (a combination of the sample material and indenter elastic deformations), and ν_{ind} and E_{ind} the elastic modulus and Poisson's ratio of the indenter, respectively. Typical values for the Poisson ratio are from 0.1 to 0.3 for ceramics and from 0.2 to 0.4 for metals. For the diamond indenter, elastic modulus and Poisson ratio values are 1141 GPa and 0.07 [110], respectively. The reduced modulus E_r is obtained from the Hertzian theory of contact mechanics [111], with:

$$E_r = \frac{\sqrt{\pi}}{2} \cdot \frac{S}{\sqrt{A_p}} \quad (2.3)$$

where the value A_p is the projected area of indenter's contact and the slope of the unload curve S is determined from the tangent at the maximum penetration point (see h_{max} on Figure 2.9(c)). Following the developments presented in [111], one finally finds the function of the ideal projected surface A_p for a Berkovich indenter as well as the slope S at maximum displacement. It allows to calculate the modulus of elasticity E of the sample:

$$E = \frac{1 - \nu_{sample}^2}{\frac{2\sqrt{C_0 \cdot h_c^2 + C_1 \cdot h_c}}{\alpha \cdot m (h_{max} - h_p)^{m-1} \cdot \sqrt{\pi}} - \frac{1 - \nu_{ind}^2}{E_{ind}}} \quad (2.4)$$

Here, C_0 and C_1 are two fitting coefficients to express the projected area function A_p as function of the penetration depth h_c . The terms *alpha* and *m* are power law fitting constants (see [109]) to connect load P and displacement depth h . The value of the projected area of the Berkovich indenter A_p allows to determine the hardness in Pascals from:

$$H = \frac{P_{max}}{A_p} \quad (2.5)$$

Note that this definition of hardness is based on the contact area under load.

In this study, the nanoindentation technique was used to test the small-scale mechanical properties of the PVD coatings developed by our industrial partner. It is known that the substrate of a thin film can have an impact on the nanoindentation measurement. To avoid this pitfall, it is generally accepted that a depth of indentation penetration of less than 10 percent of the coating thickness avoids an influence of the substrate on the measurement [112]. As the surface roughness has a great impact on the nanoindentation measurement, a polishing step is necessary in the sample preparation. In order to apply the same type of polishing to all the samples and because some samples are only a few microns

thick, it is essential to remove as little material as possible thanks to a soft polishing (polishing paste of 1 microns and manual polishing). For that purpose, the polishing is interrupted approximately every 2 minutes to check the surface state by optical microscopy (magnification between 500x and 1000x). The polishing is stopped once enough areas begin to appear smooth under the microscope.

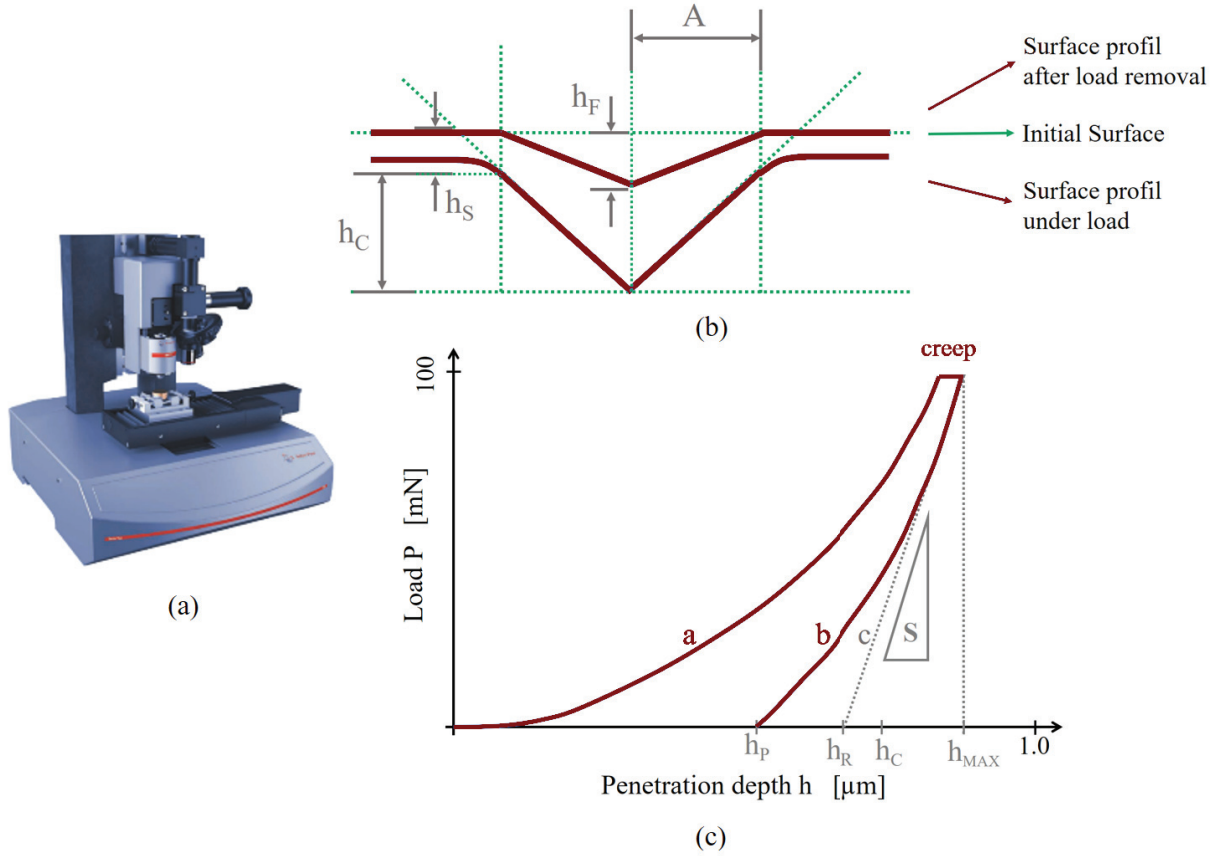


Figure 2.9: Principles and instrument for nanoindentation. (a) NanoIndenter NHT3 from the manufacturer Anton Paar. (b) sectional representation for a nanoindentation process showing the different quantities determined for the analysis. (c) Typical loading and unloading curves plotting force vs. displacement during nanoindentation test.

The nanoindentations were performed for each coatings on a nanoindenter NHT3 from Anton Paar in depth control mode with linear loading. The values of each mechanical property are averaged from at least ten imprints.

2.4 Friction tests

A tribological approach is carried out in order to provide additional informations to that obtained by conventional mechanical properties tests for hardmetals. The aim of these tests is not to model the wear of the cutting inserts as a function of different applied stresses, but to develop a basis for discriminating the direct influence of coatings characteristics on the durability of the tools. The parameter of interest presented in this section is the coefficient of friction (COF). This is studied as a function of different PVD coatings. The coefficient of friction and its evolution serves as basis to study the energy dissipation and also the wear mechanisms at the tool surface.

The consequences on friction of wear mechanisms were investigated using a linear tribometer illustrated in Figure 2.10. Short term wear tests were conducted during 500 seconds with 3 mm diameter 100Cr6 steel ball on coated inserts. The effect of the normal force and friction speed were not investigated. The tests were performed with a fixed applied force of 2N and without lubricant. The load corresponds to an average Hertzian contact pressure of 1030 MPa with a contact radius of approximately $30\text{ }\mu\text{m}$, whichever PVD coating is studied (see [113]).

It is important to note here that these conditions are far away from the machining conditions and that they do not cause damage to the coating and WC-Co similar to that observed on cutting tools after machining. This is in line with our interest to discriminate only the behaviour of the coatings studied. For a broader perspective on the tribological behaviour of contact interfaces in machining for cutting tools, a study of interest can be found elsewhere [35].

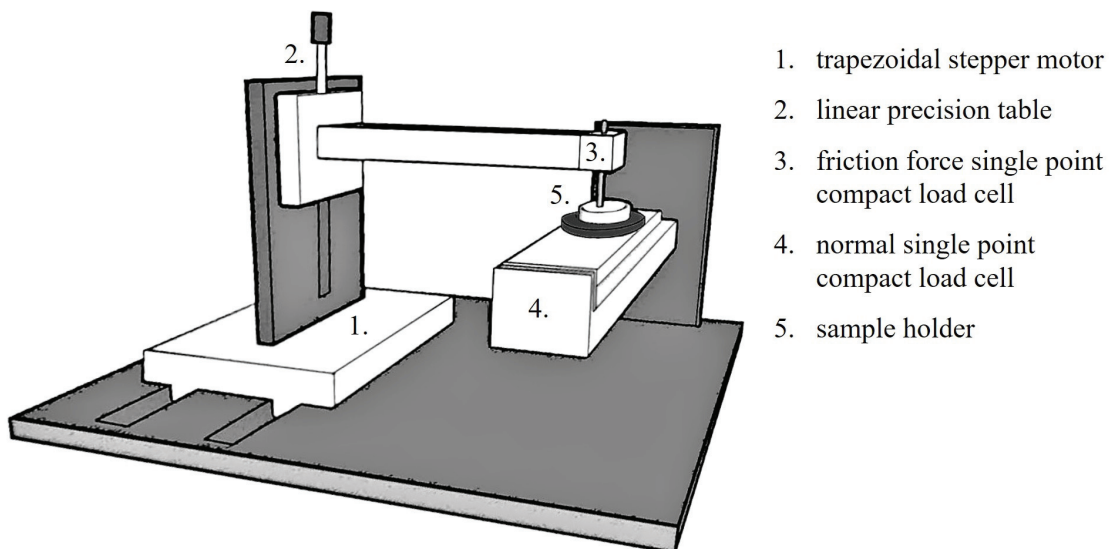


Figure 2.10: Linear Tribometer for the measurements of the friction coefficient against steel (dry measurement).

2.5 Electron microscopy

This section is intended to describe a technique that is complementary to the internal friction techniques, namely electron microscopy. Such imaging techniques are crucial for interpreting the observations of damping phenomena related to the dynamics of solid defects. The aim is to identify the structure, microstructures and metallurgical defects of the materials studied, either statically at room temperature, or dynamically by varying the temperature in the case of this study. For this purpose, scanning and transmission electron microscopy techniques have been used for the direct observation of WC-Co cemented carbide materials.

2.5.1 Scanning Electron Microscopy

Scanning Electron Microscopy (SEM) uses an electron beam to make its images. Specifically, the electron beam is focused on a small probe and scanned over the surface of the sample. Upon contact with the sample, different signals are emitted by the electron beam/matter interaction. After detection of these signals, various images are generated by correlating the signal intensity with the position of the probe. The typical signals types detected in scanning electron microscopy are illustrated in Figure 2.11. Those are:

- secondary electrons (SE), used for imaging surface morphology
- backscattered electrons (BSE), used for compositional imaging
- X-rays, used for compositional analysis (EDX or EDS).

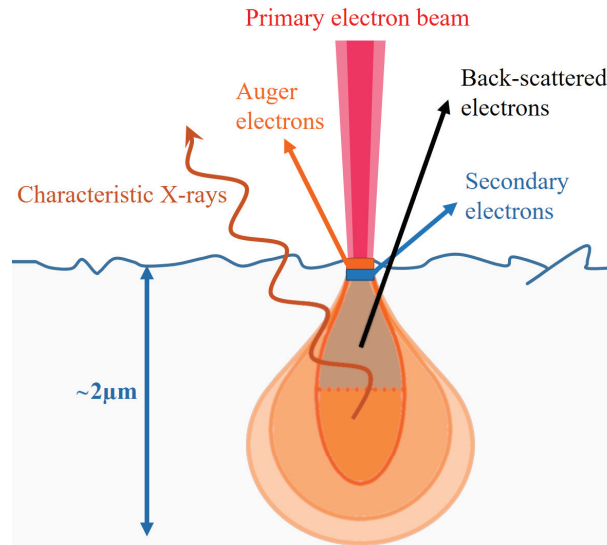


Figure 2.11: Electron–matter interactions and the different types of signals generated in Scanning Electron Microscopy (SEM).

In this study, scanning electron microscopy was performed primarily to characterize the grain size of WC-Co composite samples. These observations were performed on a ZEISS Gemini SEM 300 microscope [114] generally working around 5 keV for conventional examinations (otherwise between 1-30 keV). This instrument is equipped with a standard Everhart-Thornley detector for secondary electrons (SE), a Gemini II column equipped with the Inlens (SE) and EsB (Energy selective BSE) detectors, 4 quadrant backscattered electron detector (BSE), variable pressure secondary electron (VPSE) detector and a EDX detector from Oxford Instruments [115].

2.5.2 Transmission Electron Microscopy

Like a SEM, a transmission electron microscope (TEM) uses an electron beam as a primary source to illuminate the sample. However, much higher energy electrons are used for transmission microscopy, typically around 80-300 keV. As suggested by its name, the transmission electron microscopy uses transmitted electrons (electrons that are passing through the sample) and collects them to create an image. The latter part is provided by an objective lens, that focuses the transmitted electrons, and by imaging lenses (intermediate and projective), that magnifies the image and project it on to a recording device (see Figure 2.12). Care must be taken, however, that the sample must be sufficiently thin (generally <200 nm to be "electron-transparent") to allow electrons to pass through. As a result, transmission electron microscopy offers important information on the inner structure of the sample, such as crystal structure and orientation, defects or morphology.

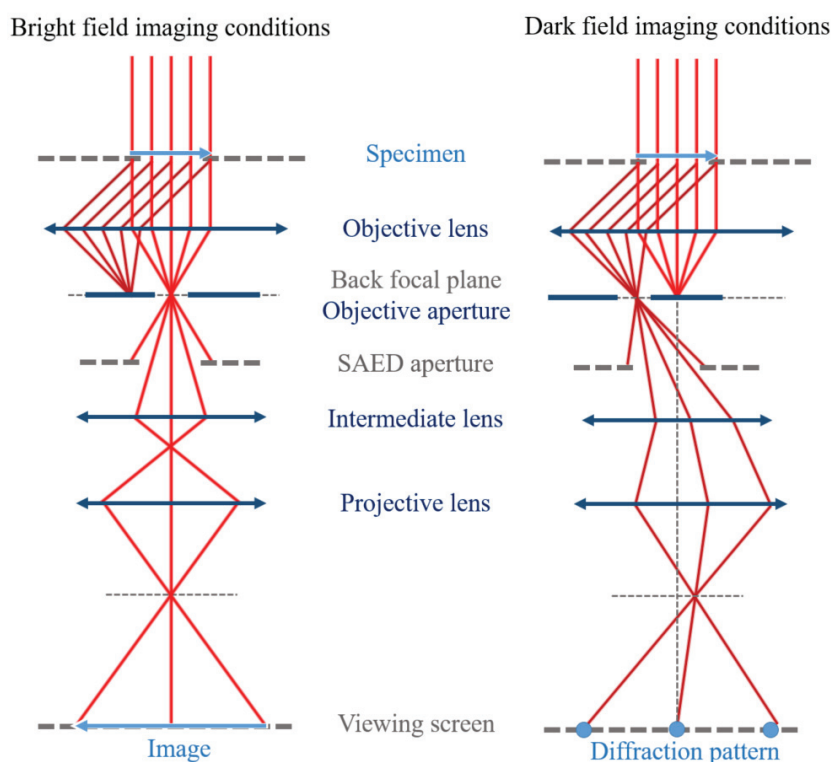


Figure 2.12: Schematic diagram of bright-field and dark-field TEM imaging modes.

In transmission electron microscopy, the images are obtained from the contrast created by the thickness of the sample, by the density of the atomic number or by electron diffraction from the sample. Direct transmitted beams or diffracted transmitted beams are the fundamental principles for TEM imaging. The origin of diffracted beams can be explained for instance by the elastic scattering (diffraction) induced from the atomic planes of crystalline materials. The diffraction pattern thus obtained can give informations of the crystal structure and orientation of the sample. Selected diffracted beams can be used for dark-field imaging conditions. It is a very suitable technique used for discriminating elements that do not fulfill the diffraction condition (defects do not form a perfect crystal). Such elements would appear as dark objects on the image. They can be crystalline defects, twins, and second phase precipitates (see Figure 2.12).

Another imaging condition is the bright-field imaging. By using an objective aperture, it is possible to select only the non-diffracted electrons to form an image. The image created in bright-field conditions contains mass-thickness and diffraction contrasts [116]. Grain boundaries and crystalline defects such as dislocations can be observed in bright-field imaging contrast (see Figure 2.12). The same applies for dark-field imaging as well. Dark field has lower intensity but can show better contrast.

In this study, scanning transmission electron microscopy was performed for WC-Co samples to characterize their microstructure and microstructure-evolution as function of the temperature. All TEM observations were performed on a Talos F200S G2 TEM and STEM microscope from ThermoFisher [117, 118], with a 200 keV acceleration voltage. The TEM experiments were carried out both statically at room temperature and in situ from 600 to 1100 Kelvin.

2.5.3 Sample preparation

Samples to be studied by electron microscopy must necessarily go through a preparation step. A distinction must be made between those sent to the SEM and those sent to the TEM. Since the interest is focused on the surface region of the sample, the SEM specimens must be mirror polished. They are first cut by electro-erosion and then polished using diamond pastes. The example of a WC-Co sample prepared for scanning microscopy is shown in Figure 2.13(a). For those intended for the TEM, there are two possibilities to make them "electron-transparent". TEM lamella can be directly prepared with the Focused-Ion-Beam (FIB) technique. The principle of a FIB instrument is the same as the SEM technique, except that it is equipped with a second column providing an ion beam (usually gallium ions). Ions having higher mass and higher momentum than electrons, FIB can be used to mill material with an outstanding precision, as shown in Figure 2.13(b). Another way to prepare TEM specimens is to machine a bowl dip in a disc of the material (by dimpling and then electropolishing or ion milling) or to prepare a sample with a taper (tripod mounting). An example of a WC-Co disc thinned to electron transparency is shown in Figure 2.13(c). All of the above techniques were used in the preparation of the TEM samples for this study. During sample preparation, a special effort was made to minimize disturbance to the microstructure of the WC-Co samples and their internal stresses. Since WC-Co is a composite manufactured by sintering, this material is known to contain high internal stresses [24] which have an obvious impact on its microstructure, and in particular on the cobalt phase.

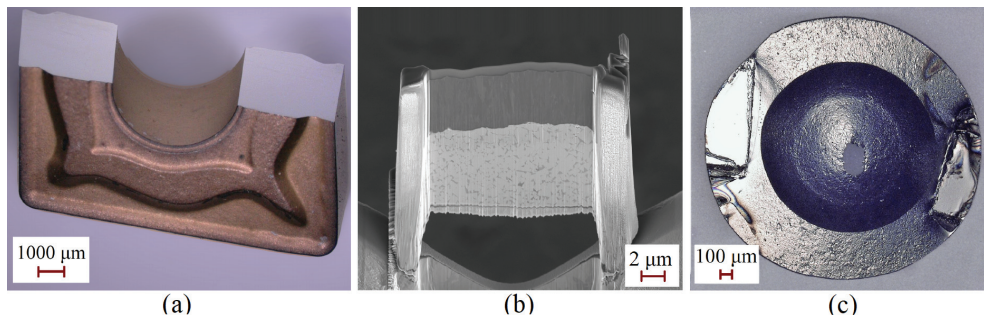


Figure 2.13: Sample preparations for electron microscopy. (a) WC-Co cutting tools cut in half and mirror polished for SEM observations. (b) WC-Co TEM lamella prepared by FIB. (c) 3mm WC-Co disc dimpled and finished by ion-milling for TEM observations.

2.6 X-ray diffraction and Residual stresses in thin films

During their production, coated cemented carbide cutting tools go through various thermal and mechanical processes such as sintering, hot pressing or high temperature coating. These production steps may result in significant residual stresses both in the bulk WC-Co material or at the surface coating. Those residual stresses affect largely the tool performances [119, 120, 121].

This section focuses on residual stresses in the thin films of cutting tools. Compressive residual stresses are believed to be more beneficial for reducing a crack initiation and propagation [122], therefore the final steps in the coating process must be chosen carefully in order to create desirable residual stresses in the surface of the cutting tool.

2.6.1 X-ray diffraction

X-ray diffraction (XRD) is a very useful technique for characterizing the crystal structure of a material. X-rays have a wavelength on the order of the atomic scale (\AA), and when they illuminate a material they are elastically scattered on the electron clouds of the atoms it contains. The re-emitted X-rays interfere constructively or destructively in certain directions. Such a phenomenon induces a diffracted beam (or reflected beam with respect to the diffracting planes), which relates the diffraction angle θ (the diffraction peak position), the interplanar space d and any integer value n of the wavelength λ of the radiation [123]. This principle is well-known as the Bragg's law 2.6 and is illustrated by the Figure 2.14.

$$n \cdot \lambda = 2 \cdot d_{hkl} \cdot \sin(\theta_{hkl}) \quad (2.6)$$

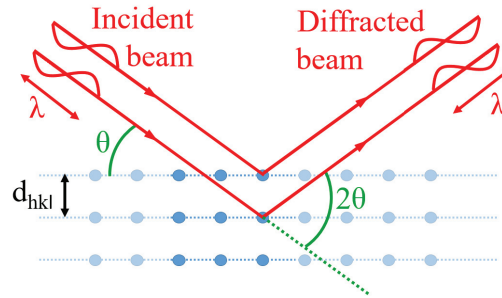


Figure 2.14: Geometry for derivation of the Bragg conditions in real space.

2.6.2 Residual stress measured by X-Ray diffraction

In this work, X-ray diffraction (XRD) were performed for measuring the residual stresses on coated samples. It is possible to determine the residual tensile or compressive stress using the $\sin^2\Psi$ method [122, 123]. The basis of its principle is illustrated in Figure 2.15. When considering a material that contains several randomly oriented crystallites, the interplanar spacing of each crystallite depends on the overall residual static stress and on their orientation with respect to the stress. For the crystallites in a stress-free material, the distances of the lattice spacing of the hkl lattice planes are the same for all crystallite, regardless of their orientation. For the crystallite for which the lattice planes are under

the influence of a residual stress (tensile or compressive), the lattice planes d-spacing depends on the stress (increases for tensions and decreases for compressions). Regarding the orientation dependency, the lattice planes perpendicular to the static stress experience the maximum influence and their d-spacing changes, while the ones parallel to the static stress remain unchanged.

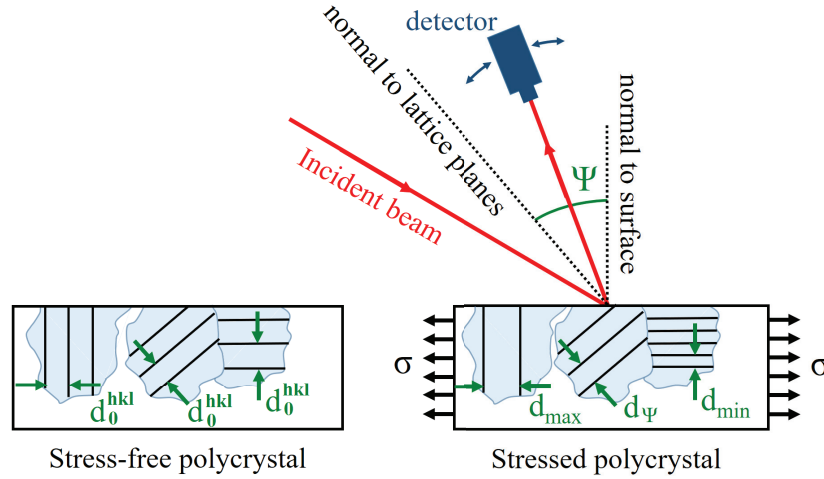


Figure 2.15: Schematic representation of the direction-dependent lattice strain by residual stress. A tensile stress is or is not applied on a polycrystalline specimen. For stress-free specimens, the spacing of the lattice plane d_0^{hkl} is independent of the crystallite orientation. For specimens under static stress, the d-spacing of the lattice planes are dependent on the crystallites orientation; due to the influence of the residual stress, the more the lattice planes are perpendicular to the static stress the more the d-spacing is enhanced.

It is thus possible by X-ray diffraction to determine a variation of the interplanar spacing from d_0^{hkl} to d_{Ψ}^{hkl} , corresponding respectively to a crystallite without constraint to a crystallite under constraint. In terms of diffraction peaks, this corresponds to the measurement of a shift of the same diffraction peak from θ_0^{hkl} to θ_{Ψ}^{hkl} as function of a tilt angle Ψ , as it can be understood through Bragg's law.

Then it is possible to determine the elastic strain of the hkl planes from the following relation 2.7.

$$\varepsilon_{\Psi,\Phi}^{hkl} = \frac{d_{\Psi,\Phi}^{hkl} - d_0^{hkl}}{d_0^{hkl}} \quad (2.7)$$

where d_0^{hkl} is the d-spacing of the $\{hkl\}$ lattice planes for the strain-free crystallite, and where Ψ is the inclination angle of the surface normal with respect to the diffraction vector, which identifies the direction of the strain measurement. Φ represents the rotation angle of the specimen around its surface normal (see Figure 2.16b). Biaxial stresses are the most appropriate for the analyses of surface phenomena or for coatings studies. By considering only the biaxial stresses (according to the plane formed by \vec{x}_1 and \vec{x}_2 in the Figure 2.16b), it is possible to demonstrate [123] that the deformation $\varepsilon_{\Psi,\Phi}^{hkl}$ can be rewritten through the targeted value of the residual stress, as written in the Equation 2.8. This relation is expressed with the help of the isotropic elastic parameters of the studied material, which are Young's modulus E and Poisson's ratio ν , and with the introduction of the stress σ_{Φ} according to the angle Φ .

These elements are shown together with the geometry for surface residual stress measurements in the Figure 2.16b.

$$\varepsilon_{\Psi,\Phi}^{hkl} = \frac{d_{\Psi,\Phi}^{hkl} - d_0^{hkl}}{d_0^{hkl}} = \frac{1+\nu}{E} \cdot \sigma_{\Phi} \cdot \sin^2 \Psi - \frac{\nu}{E} \cdot (\sigma_{11} + \sigma_{22}) \quad (2.8)$$

This expression can be rewritten as :

$$d_{\Psi,\Phi}^{hkl} = d_0 \cdot \frac{1+\nu}{E} \cdot \sigma_{\Phi} \cdot \sin^2 \Psi - d_0 \cdot \frac{\nu}{E} \cdot (\sigma_{11} + \sigma_{22}) + d_0 \quad (2.9)$$

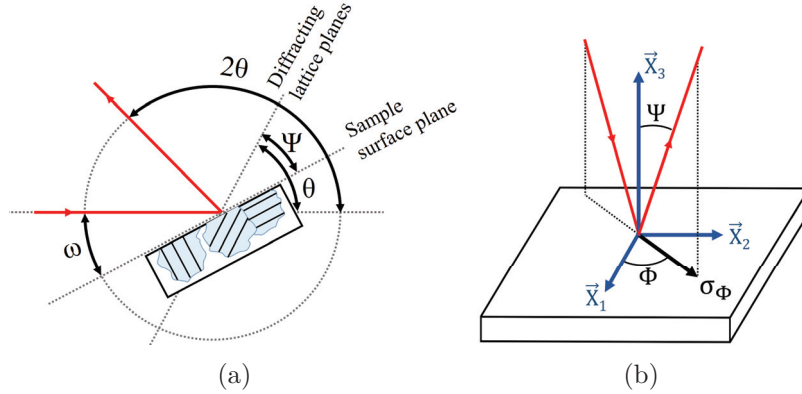


Figure 2.16: Geometric representations for thin films residual stress measurement by mean of X-ray diffraction (a) Geometry of the diffractometer. It brings the following relation for the diffraction angles $\Psi = \theta - \omega$. (b) Geometry for biaxial stress measurements.

The latter relation 2.9 expresses the linear variation of the interplanar spacing $d_{\Psi,\Phi}^{hkl}$ with respect to $\sin^2 \Psi$. By relating to $\sin^2 \Psi$ the interplane space d measured for a series of Ψ tilts, it is therefore possible to determine the stress σ_{Φ} . As a reminder d_0 is the stress-free interplanar distance. This parameter can be approximated by $d_{33} = d_{\Psi=0}$, with a very small induced error on the final residual stress value.

The $\sin^2 \Psi$ method therefore refers to a series of measurements, as function of the tilted angle Ψ , of the d-spacing d corresponding to one diffraction peak. The variation of d is reported as a function of $\sin^2 \Psi$, and the slope of this plot is used to identify the residual stress. A positive slope corresponds to a stress in tension, while a negative slope corresponds to a stress in compression.

$$Slope = d_0 \cdot \frac{1+\nu}{E} \cdot \sigma_{\Phi} \approx d_{\Psi=0} \cdot \frac{1+\nu}{E} \cdot \sigma_{\Phi} \quad (2.10)$$

2.6.3 Measurement conditions

Preliminary DRX measurements were conducted in standard ($\theta - 2\theta$) mode on all of the coated cutting tools included in this study. These diffractograms were taken with the help of Julien CHAUVET on an ARL Equinox 2000 device from Thermo-Scientific [124]. Figure 2.17 the X-ray diffractograms of a reference sample with their identified peaks.

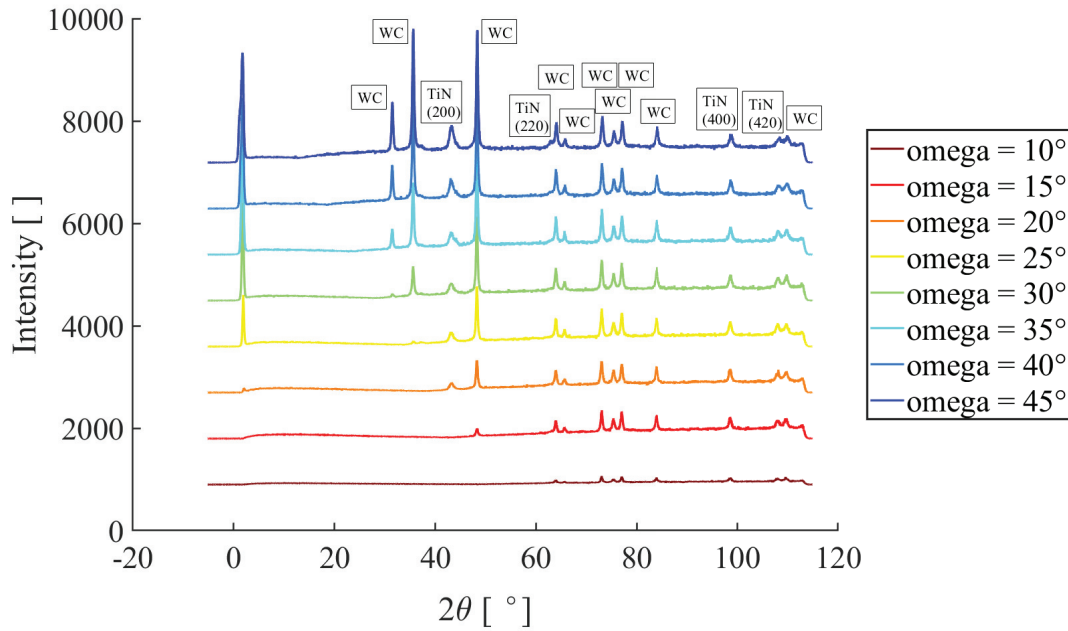


Figure 2.17: Reference X-ray diffractograms as function of different diffraction angles ω . Their main peaks are identified for WC and for the Coating.

For XRD residual stress measurements, a Panalytical Empyrean diffractometer was used working in the Bragg-Brentano geometry ($\theta - 2\theta$) with Cu $K\alpha_1$ radiation (1.5405980 \AA). The high power X-Ray tube, working at 45 kV for 40 mA, was mounted for measurements in point focus. Residual stress measurements were performed at room temperature on coated samples with the standard X-ray $\sin^2\Phi$ method. All coatings are of CrN/AlTiN type. The stresses were measured in the coatings using $\{420\}$ reflections at around $2\theta = 108^\circ$ and at the diffraction angles ω of values 10° , 15° , 20° , 25° , 30° , 35° , 40° and 45° .

2.7 Mechanical spectroscopy

As explained in the section 1.3, the underlying principle of mechanical spectroscopy is the anelasticity of materials. Anelastic relaxation occurring inside materials are driven by the kinetic of crystalline solids defects. The external manifestation of such internal relaxation phenomenon is the time dependence of the strain response of a material to an external applied stress. The quasi-static method has been illustrated in Figure 1.7 of section 1.3 with the creep and creep recovery experiment. Quasi-static methods have however two major drawbacks. Firstly, the time required to carry out the observation of anelastic behaviour may extend over periods of several seconds or longer, which makes it difficult to apply in extensive study such as measurements over a whole temperature range.

Secondly, the precision required to observe anelastic phenomena is considerable; for elastic deformations of the order of 10^{-6} , the needed accuracy is of the order of 10^{-9} to 10^{-8} . The anelasticity is better investigated through dynamic methods, and this techniques are the object of this section.

In general, mechanical spectroscopy can use any techniques capable of creating vibrations within a material and measuring strain responses. Depending on the frequency range of interest, several techniques exist such as forced torsion pendulum (mHz-Hz) or longitudinal excitation waves (KHz-MHz) [26]. The principle behind dynamic methods is always the same and is conveniently described through the complex notation. Consider an harmonic stress excitation of the material as :

$$\sigma = \sigma_0 \cdot \exp(i\omega t) \quad (2.11)$$

As ideal elastic and anelastic behaviours are examined, only recoverable and linear relationships are considered. The induced deformation is then a cyclic strain with the same frequency ω but delayed by a phase lag δ [] due to the anelastic behaviour. From the perspective of dimensional analysis, the unit of the frequency ω is kept in Hertz.

$$\varepsilon = \varepsilon_0 \cdot \exp(i(\omega t - \delta)) \quad (2.12)$$

Following the standard equation for anelastic solids 1.13, the cyclic stresses 2.11 and strains 2.12 lead to the relation :

$$\varepsilon = J^*(\omega) \cdot \sigma = [J_1(\omega) - i \cdot J_2(\omega)] \cdot \sigma$$

Which is the response relation of anelastic solids in dynamical mode. Recalling $\delta J = J_R - J_N$ (1.7) and the standard equation for anelastic solids (1.13), one finds the expression for J_1 and J_2 , respectively the real and imaginary parts of the complex compliance $J^*(\omega)$:

$$\boxed{J_1 = J_N + \frac{\delta J}{1 + \omega^2 \tau^2}} \quad \boxed{J_2 = \delta J \cdot \frac{\omega \tau}{1 + \omega^2 \tau^2}} \quad (2.13)$$

The above relations are called **Debye equations**. The phase lag δ can be illustrated in two ways: by the stress-strain versus time in the dynamic mode as in Figure 2.18(a), and by the complex compliance representation in a vector diagram that revolves around its origin at an frequency ω as in Figure 2.18(b).

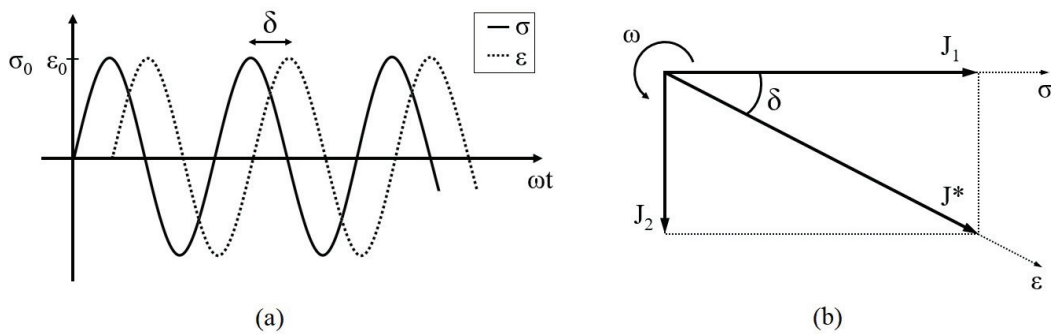


Figure 2.18: Dynamic excitation and response. (a) Loss angle δ between the applied cyclic stress σ and measured cyclic strain ε . (b) Complex diagram linking stress σ , strain ε and compliance J . This diagram revolves around its origin at an frequency ω .

2.7.1 Internal Friction and Debye Peak

The phase lag between stress and strain is the key parameter for the dynamic measurement method. Indeed, there is a direct relationship between the phase shift δ and Internal Friction IF . As explained in the section 1.3, the anelasticity of solids originates from the movement of defects in the structure of crystalline materials. Their movement involves a loss of energy within the material, which is defined as Internal Friction IF . During one deformation cycle, energy is dissipated in the form of heat $\Delta W_{lost,fric}$ and energy is stored elastically $W_{stored,el}$. The ratio of the dissipated energy over the maxmial stored energy defines the Internal Friction.

$$IF = \frac{1}{2\pi} \cdot \frac{\Delta W_{lost,fric}}{W_{stored,el}} \quad (2.14)$$

Applying Equations 2.11 and 2.12, the lost energy $\Delta W_{lost,fric}$ is calculated by:

$$W_{lost,fric} = \oint_{cycle} \sigma d\varepsilon = \sigma_0 \cdot \varepsilon_0 \cdot \pi \cdot \sin \delta$$

To calculate the maximum elastic energy supplied to the system $W_{stored,el}$, one should notice that it corresponds to the maximum of the positive integral between 0 and $\pi/2$.

$$\Delta W_{stored,el} = \int_{\omega t=0}^{\omega t=\pi/2} \sigma d\varepsilon = \frac{1}{2} \sigma_0 \cdot \varepsilon_0 \cdot (\cos \delta + \frac{\pi}{2} \sin \delta) \approx \frac{1}{2} \sigma_0 \cdot \varepsilon_0 \cdot \cos \delta \quad , \delta \ll 1$$

The direct result is that the internal friction IF and the phase shift δ are connected by :

$$IF = \tan \delta = \frac{J_2}{J_1} \quad (2.15)$$

Where the last part of the equation is directly taken from the complex compliance definition (see Figure 2.18(b)). Given the internal friction obtained for cyclic stress and deformation on an ideal anelastic solid 2.15 with the complex compliances obtained in dynamic mode 2.13 and using the fact that the anelastic deformation is much smaller than the elastic deformation 1.7 ($\delta J = J_R - J_N \ll J_N$), the shape of the Internal Friction as well as the compliance variation, as function of the deformation frequency can be calculated. It is found that the Internal Friction function of frequency is a **Debye peak** with the relaxation amplitude Δ (1.7):

$$IF = \Delta \frac{\omega \tau}{1 + \omega^2 \tau^2} \quad (2.16)$$

One can also express the compliance (or modulus) variation by looking at the relative relaxation of compliance δJ over its norm $|J(\omega)|$. By considering small relative anelastic amplitude $\delta J \ll J_N$, one finds $J_1 \approx J_N$, which leads to:

$$\frac{\delta J(\omega)}{|J^*(\omega)|} = \frac{Re(J(\omega)) - J_N}{J_N} = \frac{J_1(\omega) - J_N}{J_N} = \Delta \frac{1}{1 + \omega^2 \tau^2} \quad (2.17)$$

One can show that the compliance variation is equivalent to the dynamic modulus variation (see [75]), and therefore:

$$|\delta J|/|J| = |\Delta E|/|E|$$

Internal Friction peaks of Debye form and modulus variations are shown in Figure 2.19. It can be seen that the Debye peak has its maximum at $\Delta/2$ at $\omega_p\tau_p=1$. The values are indicated with a p-index to emphasize that they are defining the maximum of the peak. Internal Friction allows finding the set of parameters defining each anelastic relaxation which are the amplitude of relaxation and its characteristic time $\{\tau_i, \delta J_i\} \sim \{\tau_i, \Delta_i\}$.

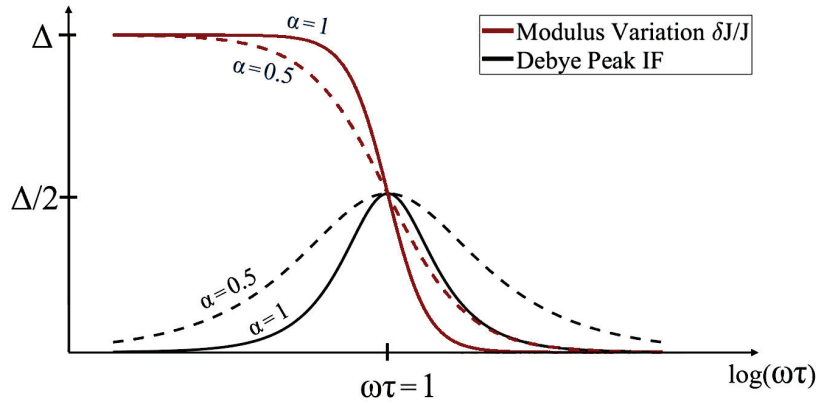


Figure 2.19: The Internal Friction function as function of the frequency forming a Debye Peak. The curve presents a maximum at $\omega\tau=1$. It is plotted with its corresponding modulus (or compliance) variation. A broader Internal Friction peak and its related modulus variation are also presented with one $\alpha < 1$.

When several relaxation phenomena take place within the same material, it was described in subsection 1.3.2 that there is a linear transformation allowing to define internal variables independent from each other and thus to use the principle of superposition 1.14. It is therefore possible to use the following relations:

$$IF = \sum_i \Delta_i \frac{\omega\tau_i}{1 + \omega^2\tau_i^2} \quad \frac{\Delta E}{E} = \sum_i \Delta_i \frac{1}{1 + \omega^2\tau_i^2}$$

In practice, pure Debye peaks are rarely observed for crystalline materials. Debye peak sare broadened, corresponding to a continuous distribution of the same relaxation mechanism, as for example the length distribution of dislocation defects. For this matter, a convenient approach is to use the substitution $x = \ln(\omega\tau)$ which can be used to rewrite a Debye form into an hyperbolic secant $\omega\tau/(1 + \omega^2\tau^2) = 1/2 \cdot \text{sech}(x)$. Using this substitution on J_2 , it is possible [75, 125] to find an analogous form $J_2(x) = J_2(x_0) \cdot \text{sech}[\alpha(x - x_0)]$. It finally leads to the generalized relations for broadened Internal Friction peaks and for modulus variations, with $0 < \alpha \leq 1$ as a broadening factor. The value $\alpha = 1$ corresponds to a pure Debye peak, while values of $\alpha < 1$ define broad Debye relaxations as shown in Figure 2.19.

$$IF = \sum_i \Delta_i \frac{(\omega\tau_i)^\alpha}{1 + (\omega\tau_i)^{2\alpha}} \quad \frac{\Delta E}{E} = \sum_i \Delta_i \frac{1}{1 + (\omega\tau_i)^{2\alpha}} \quad , \alpha \leq 1 \quad (2.18)$$

2.7.2 Thermally activated relaxations

In the previous developpements , we considered the analysis of phenomena at constant temperature where the relaxation time τ remains constant. In many cases, however, the movement of microstructural defects are thermally activated. For such cases, a correction has to be applied for the jump rate between equilibrium position of specific defects. For a jump rate ν this modification takes a regular Maxwell-Boltzmann form. Considering the probability of a defect to overcome an energy barrier per atom ΔG_0 thanks to thermal energy $k_B T$, we get:

$$\nu = \nu_0 \cdot \exp\left(\frac{-\Delta G_0}{k_B T}\right)$$

The quantity ν_0 is a frequency factor of the order of $10^{13}[s^{-1}]$. The frequency ν_0 is related to the vibration frequency of an atom in its crystal lattice ν_D (called the Debye frequency) by $\nu_0 = cst \cdot \nu_D$ [49]. The Boltzmann constant is defined to be $1.38 \cdot 10^{-23}[J \cdot K^{-1}]$ or $8.64 \cdot 10^{-5}[eV \cdot K^{-1}]$. The energy barrier ΔG_0 is defined by the defect mechanisms the jump is related to. For instance, typical energy barriers for the motion of dislocations are of the order of $1[eV/atom]$ [126]. The anelastic relaxation time is defined by the time available to a defect between two successive jumps, that is $\nu = \tau^{-1}$:

$$\tau = \tau_0 \cdot \exp\left(\frac{\Delta G_0}{k_B T}\right) \quad (2.19)$$

It is therefore also possible to analyse relaxation phenomena by varying the temperature. For that, we simply introduce Equation 2.19 in $\omega_p \cdot \tau_p = 1$, which is the condition for the maximum of a Debye peak :

$$\omega \tau_0 \cdot \exp\left(\frac{E_{act}}{k_B T}\right) = 1 \quad (2.20)$$

Where E_{act} is the activation energy of an atomic jump sufficient to overcome the energy barrier ΔG_0 . A difference between the activation energy and the energy barrier is set, since the cyclic stress σ applied to the material during a dynamic measurement will favour the atomic jump by a work $W(\sigma^*)$ as $E_{act} \equiv \Delta G = \Delta G_0 - W(\sigma^*)$. The quantity σ^* is the mean effective stress working on a defect over its activation area. The relation 2.20 allows therefore to investigate relaxation processes within material and express the corresponding limit relaxation time τ_0 and activation energy E_{act} :

- In isothermal condition, the measurement of the Internal Friction is performed as function of the frequency.
- At constant frequency, the measurement of the Internal Friction is performed as function of the temperature.

Assuming a stable microstructure, several measurements on the same relaxation process will bring as many internal friction peak positions in temperature and frequency $\{T_p, \omega_p\}$. By reporting the peak positions in an Arrhenius diagram as $\ln(\omega_p)$ as a function of $1/T_p$, it is possible to determine the activation energy of this relaxation process as well as the corresponding relaxation limit time. Equation 2.20 just leads to:

$$\ln(\omega_p) = \ln(\tau_0^{-1}) - \frac{E_{act}}{k_B} \cdot \frac{1}{T_p} \quad (2.21)$$

In most cases, the physical observations are congruent with the Arrhenius law. However, there are situations where this relation is not verified. And for such cases, there exists a proper parallel with the condensed matter physics for metastable materials known as glass-forming materials. Although glasses behave macroscopically like conventional solids, their structure does not have the long-range periodicity characteristic of crystals. They are therefore long-range disordered solids. Glass-like material formation is associated with the transition of condensed phases that are liquid, glassy and crystalline. Starting from the viscous liquid phase, a sufficiently fast cooling rate induces an increase of the viscosity η or of the relaxation time τ of the liquid which leads to a glass transition, preventing any transition to an ordered crystalline phase. For such situations, the empirical law of Vogel-Fulcher-Tammann is generally employed as stated in Section 1.2.1 and Equation 1.3 [56, 57, 58, 59, 49]:

$$\tau = \tau_0 \cdot \exp\left(\frac{\Delta E}{k_B \cdot (T - T_0)}\right) \quad (2.22)$$

Here, ΔE is the activation barrier and T_0 is the "Vogel temperature" or "ideal glass transition temperature" at which the viscosity or relaxation time diverges.

2.7.3 Internal friction measuring technique

An experimental facility, called Lyra, was used for the measurement of internal friction. It is an inverted torsion pendulum operating in subresonant mode with forced oscillations in a wide frequency range (from 0.1 mHz to 10 Hz). The installation is shown in Figure 2.20.

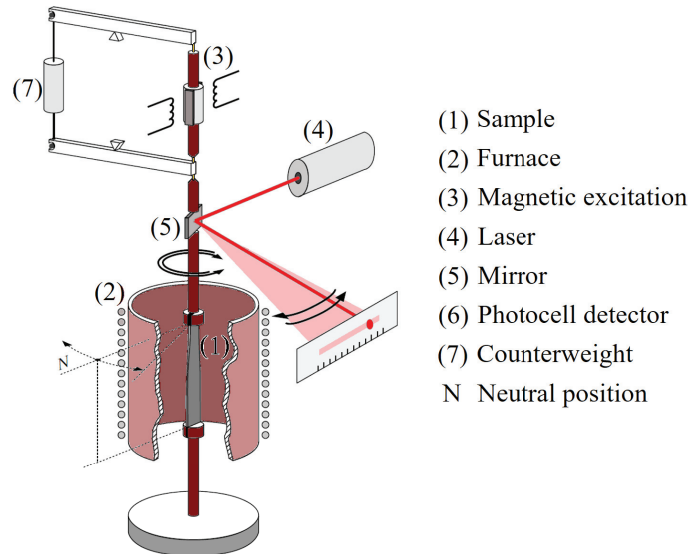


Figure 2.20: Principle of the inverted forced torsion pendulum Lyra. Illustration adapted from [127] with the permission of the EPFL Mechanical Spectroscopy Group.

This installation is particularly well suited to the study of WC-Co cemented carbides, as it operates over a wide temperature range from 300 K to 1600 K, which corresponds to the high temperatures to which cutting tools can be subjected during machining [79]. During the measurements, typical heating and cooling rates were set at 1K/min. The induced strains were all fixed at $5 \cdot 10^{-5}$ (operating range: 10^{-6} and 10^{-5}). The sample sizes of WC-6wt.%Co and WC-10wt.%Co are typically $0.8 \times 3 \times 30 \text{ mm}^3$. These lamella-shaped samples were produced by the industrial partner of this project by sintering and then PVD coating together with the corresponding industrial inserts.

2.7.4 Reference internal friction measurements

The main results of measurements on cemented carbide materials carried out by mechanical spectroscopy are presented. These will serve as reference for the continuation of the study project.

For WC-6wt.%Co and WC-10wt.%Co tungsten cemented carbide materials, the characteristic internal friction spectrum measured between 700-1400 K and in the 1Hz frequency range exhibits three peaks as shown in the Figure 2.21, which will subsequently be referred as P1, P2 and P3 in their temperature position order. In addition to these relaxation peaks, an exponential background is added to the spectrum and is associated with the presence of a peak at very high temperature. These observations are in excellent agreement with previous studies carried out by Ammann and Schaller [128, 129] on a material of the same composition, but with different production features. With the addition of Mari's work in electron microscopy and high temperature deformation techniques [130], these initial studies have made it possible to model the dynamics of the microstructural defects of WC-Co and its mechanical properties in high temperature ranges [131].

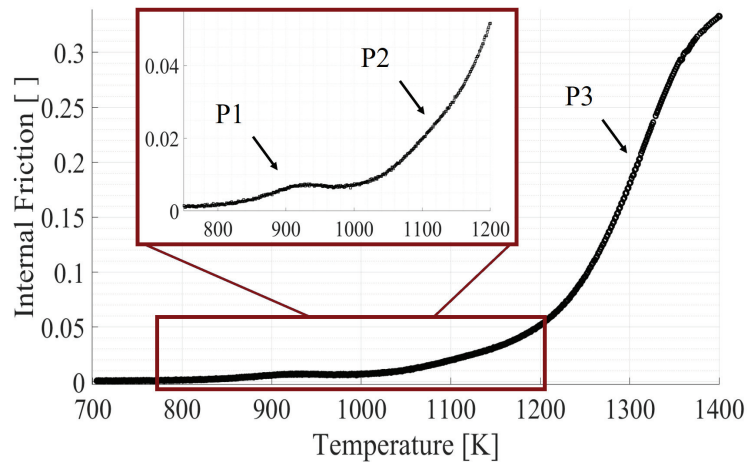


Figure 2.21: Internal friction curve as function of temperature in the 1 Hz frequency range for a WC-6wt.%Co sample. Three relaxation peaks and an exponential high-temperature background are observed. This spectrum is obtained after the microstructure thermomechanical stabilisation process described above.

Although the presence of the P1, P2 and P3 Internal Friction peaks can be observed for each measurement obtained by mechanical spectroscopy, the spectra reported in this study always correspond (except when indicated) to materials which have undergone "thermomechanical stabilisation" processes (i.e. several phases of high-temperature annealing under cyclic stresses in a torsion pendulum). These annealing processes, hereinafter referred to as *material microstructure thermomechanical stabilisation*, consist of the following steps:

1. Temperature cycle between 700K and 1050K, with a torsional oscillation frequency of 1Hz, a ramp of 1K/min, a torsional strain amplitude of $5 \cdot 10^{-5}$, with a high temperature dwell of 360minutes.
2. Temperature cycle between 700K and 1050K, with a torsional oscillation frequency of 1Hz, a ramp of 1K/min, a torsional strain amplitude of $5 \cdot 10^{-5}$, with a high temperature dwell of 120minutes.

3. Temperature cycle between $700K$ and $1050K$, with a torsional oscillation frequency of $1Hz$, a ramp of $1K/min$, a torsional strain amplitude of $5 \cdot 10^{-5}$, with a high temperature dwell of *60minutes*.

Once this thermal treatment was carried out on the material, the internal friction spectra are found to be repeatable for the same specimen as well as reproducible with other identical specimens. The reasons for these thermomechanical stabilisation steps are of physical origin and will be explained in greater details in the results Section 3.3.2 and 3.4. In accordance with the observations of Mari [37, 131] and with complementary results presented in the Introduction page 6, the internal friction spectra of WC-Co can be interpreted as a function of three temperature domains:

- I The first domain is between $800K$ and $1050K$ and is related to the first relaxation peak. The first internal friction peak P1 is at approximately $920K$ and $945K$ in the $1Hz$ frequency range, for materials composed of WC-6wt.%Co and WC-10wt.%Co respectively. In previous research [132], this relaxation peak was attributed to the cobalt phase. To demonstrate this point, two types of samples were tested by mechanical spectroscopy: a pure WC sample sintered without cobalt, and a sample of WC-Co from which the cobalt metallic binder had been removed from the composite by chemical etching in boiling hydrochloric acid (HCl). Both specimen showed mechanical spectra with low internal friction intensity below $1000K$ and no relaxation peak P1. This latter attribution of the relaxation peak P1 to the cobalt phase has also been confirmed in the present study by results presented in Section 3.3.1. In the previous studies [11, 131], the peak P1 was observed to disappear after annealing above $1200K$. Some studies seem to show that this peak shifts to higher temperature and gives rise to the peak P2 [28]. The peak P1 could only be restored after a long annealing of 72 hours at $1000K$. Surprisingly, this behaviour of the peak P1 is not observed in the samples used for this study. After annealing above $1050K$, a slight shift of this relaxation peak towards higher temperatures can be observed but it remains always present.
- II The second domain is between $1050K$ and $1200K$ and is related to the second relaxation peak. For the relaxation peak P2, the temperature position of the peak P2 at $1Hz$ and for WC-6wt.%Co and WC-10wt.%Co compositions is $1125K$ and $1160K$ respectively. As the peak P1, the peak P2 is attributed to the cobalt phase of WC-Co. Samples consisting solely of the WC tungsten carbide skeleton (either by sintering or chemical etching) do not produce a relaxation peak in the temperature range mentioned. The studies conducted by Mari [28] have shown that the peak P1 may turn into a higher temperature peak. That is the peak P2 of this study (same temperature and frequency range for a similar composition). The transition between these two relaxation peaks indicated therefore that both should be attributed to the same type of defect.
- III The last domain starts above $1200K$ and is related to the third relaxation peak P3. This third peak is located at approximately $1300K$ for measurements at $1Hz$ and does not seem to depend on the cobalt content. It is associated with grain boundary sliding of the WC hard phase [130].

It is then possible to link these different temperature domains to the mechanical behaviours of tungsten cemented carbides cutting tools. During cutting, the different damping phenomena highlighted before and attributed to the peaks P1, P2 and P3 will be activated due to the temperature and they will control the mechanical properties of the WC-Co material. Thanks to three point bending tests [37], it has been shown that WC-Co exhibits three specific mechanical behaviour domains related to the temperature:

- Elastic and brittle behaviour (up to $775K$), corresponding to low internal friction values before the peak P1.
- Tough and limited plasticity behaviour (between $775K$ and $1075K$), related to the region of the peak P1.
- Creep behaviour (above $1075K$), corresponding to temperature beyond the peak P2 where the values of internal friction increase strongly.

By comparing the model of mechanical behaviour with that of internal friction (linked to the microstructure of the material), it can be seen that the transition temperatures between the different domains are linked to the microstructure and the composition of the cobalt binder. This observation provides a solid foundation to base the search for improved cemented carbide cutting tools on the composition and microstructure of the cobalt binder.

3 Experimental Results and Observations

In this chapter, the experimental observations are reported. First, the preliminary results that defines the main lines of study for this work are presented. Those first results consist on a comparative study highlighting the most influential parameters for the durability of cutting tools. The internal friction spectra of the cemented carbides are then presented. Particular emphasis is placed on the study of the properties of the cobalt binder. A complementary analysis by internal friction of the effects of the magnetic field is also shown. As the analysis of the internal friction spectra of cemented carbides can be difficult, it is essential to associate complementary studies to mechanical spectroscopy. The choice of electron microscopy in this case proves to be judicious since it allows direct characterization of the materials and their evolution.

The materials studied in this work are based on already existing cutting tools produced by Lamina-tech. A first matrix of experiments (Table 3.1) has been developed to explore different grades of cutting inserts. This samples matrix allows probing their different characteristics (matrix grades, and architecture, composition and thickness of the coatings).

			Coating properties					Cutting inserts		
			Architecture		Composition				Thickness	
			Bi-layers	Multi-layers	Comp.1 of type TiAlN	Comp.2 of type TiAlN	Comp.3 of type TiAlN			
Matrix properties	Grades	WC-6wt.%Co	X		X			Thick.1		Sample 1
			X		X			Thick.2		Sample 2
			X		X			Thick.3		Sample 3
				X	X			Thick.4		Sample 4
				X	X			Thick.5		Sample 5
		WC-10wt.%Co	X		X			Thick.6		Sample 6
			X			X		Thick.7		Sample 7
			X				X	Thick.8		Sample 8

Table 3.1: Samples matrix of the cutting inserts produced by Lamina-tech and used in this work. This study, aiming at enhancing the durability of the cutting inserts manufactured by Lamina-tech, focuses on all the parameters that can intervene in the tool-life, i.e. bulk properties of various grades, coating architecture, coating composition or coating thickness (n.b. the informations are encoded to insure confidentiality).

3.1 Durability and Tool-life

A first measurement campaign, based on the experience matrix of Table 3.1, was conducted to test the tool-life of the corresponding cutting inserts in real machining conditions. Two tests were developed by our industrial partner. They consist in a shock test and a rapid wear test conducted on 42CrMo4 chromium-molybdenum steel workpieces. The exact conditions of these tests are presented in sections 2.1.2 and 2.1.3 respectively, and are briefly recalled below.

The cutting tool-life is determined by the shock test until the tools break, by repeated measurements. The observed failure mechanisms of the inserts were flaking, chipping and breaking. All shock resistance performances for turning inserts are presented in the Figure 3.1. Some of the corresponding inserts evolution images and failure images are presented in the Appendix 4.5.

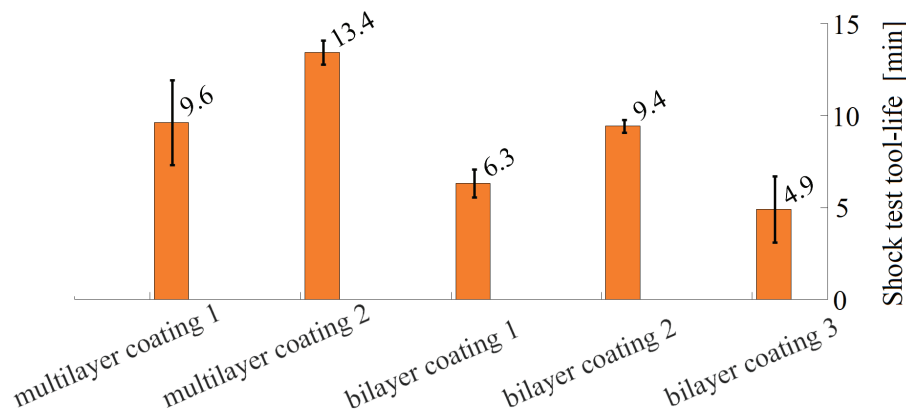


Figure 3.1: Machining performance in shock test consisting on turning with interrupted cuts for turning samples. All values correspond to mean behaviours and their reported errors to one standard deviation.

The resistance to tool wear of the cutting inserts were determined by the "facing until the center test" until the tools break, by repeated measurements. This consists of the inserts rapid wear under extreme machining conditions and at high speed. The observed failure mechanisms of the inserts were built-up edge, coating flaking and insert breakage, as reported in the Appendix 4.5. As it can be seen on the wear resistance results on the Figure 3.2, there is limited discrepancy between the resistance time to rapid wear. These results do not make it possible to determine the parameters influencing wear resistance, and were therefore not used in the comparative study presented below.

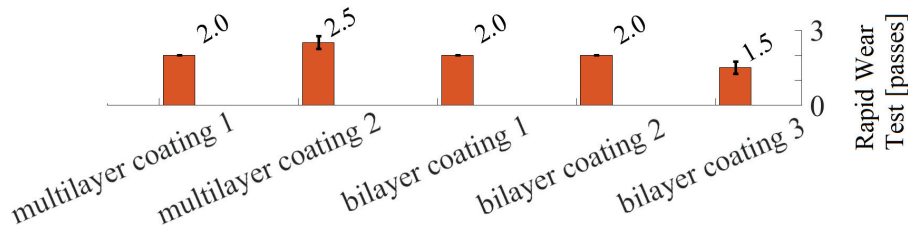


Figure 3.2: Machining performance in rapid wear test consisting on turning a workpiece at high cutting speed. All values correspond to mean behaviours and their reported errors to one standard deviation.

3.2 Comparative study

A first part of this work consists into a comparative study between the tool-life of the cutting inserts and various properties. The interest is to test coatings properties, bulk characteristics and mechanical properties and compare them to the tool-life of the cutting inserts. This step aims at defining the most influential parameters in machining performance. It serves then as an indicator for further investigations and development on cutting insert quality improvement.

Hereafter the influences of coating hardness, coating residual stress, coating friction coefficient, coating thickness and bulk defects microstructure dynamics are compared with the tool-life presented above in Figure 3.1.

3.2.1 Friction tests

A tribological study was carried out in order to determine the evolution over time of the coefficient of friction (COF) of the inserts as a function of their PVD coatings. By finding patterns of behaviour in the COF evolution and by comparing these results with those of the tool life, it is possible to determine whether the surface parameters influencing tool friction also have an influence on the durability of cutting tools. Parameters such as texture and roughness, the composition of interacting surfaces and other tribological and environmental properties could thus reveal their importance for the durability of coated tools.

The first part of this tribological study thus consists in analyzing the evolution of the coefficients of friction for all the available samples. The example of a COF vs. time curve for a low load of 2 N and a test duration of 500 seconds is shown below in the Figure 3.3.

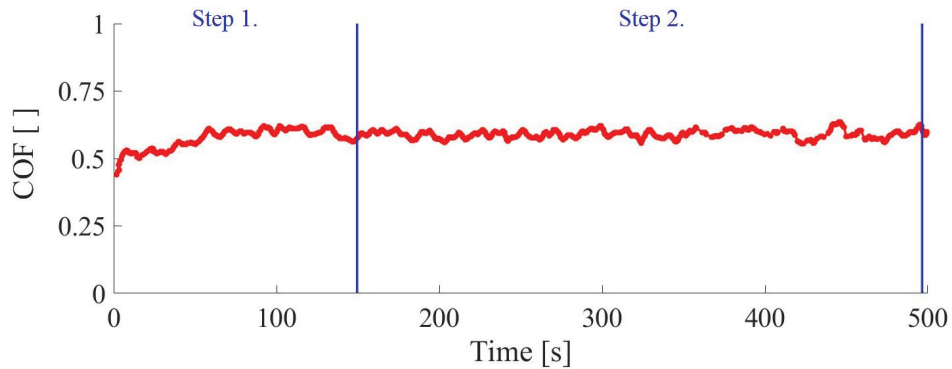


Figure 3.3: Evolution of the friction coefficient as a function of time measured on a linear tribometer. The ball used as sliding material is a 3 mm diameter 100Cr6 steel ball. The applied force is 2N. The samples are industrially produced cutting tools with different PVD coatings.

Through the evolution of the coefficient of friction as a function of time, two to three distinct steps were highlighted for all the coated inserts:

1. A first step corresponds to the sudden evolution of the friction coefficient during the first moments of friction. This mainly consists in an increase in friction. It can be explained by shocks between the asperities of both surfaces. This process ends when the surfaces in contact are more homogeneous in terms of surface roughness.

2. In a second step, the coefficient of friction stabilises as a result of the adjustment of the friction interface. This is the stationary behavior.
3. A third step sometimes occurs. This corresponds to a strong perturbation of the friction coefficient curve over time, which can be caused by changes in contact conditions at the interface through debris flow. This step is not taken into account in the comparative analysis.

The second part of this tribological study aims at comparing the patterns of COF behaviour with the tool-life for all the different coated inserts. Only the values that are useful for the comparative study of tool durability are reported below in the Table 3.2. The corresponding curves can be found in the Appendix 4.5.

	Coefficient Of Friction (COF)		
	COF []	COF evolution over time [s^{-1}] (**)	COF []
Sample	Unsteady behaviour (early begining Step 1.*)	Unsteady behaviour (Step 1.)	Stationary behaviour (Step 2.)
Multilayer coating 1	0.47 ± 0.05	$(0.74 \pm 0.31) \cdot 10^{-3}$	0.53 ± 0.05
Multilayer coating 2	0.48 ± 0.02	$(1.87 \pm 0.95) \cdot 10^{-3}$	0.60 ± 0.06
Bilayer coating 1	0.53 ± 0.04	$(3.23 \pm 3.12) \cdot 10^{-3}$	0.53 ± 0.03
Bilayer coating 2	0.47 ± 0.05	$(2.28 \pm 1.03) \cdot 10^{-3}$	0.46 ± 0.02
Bilayer coating 3	0.51 ± 0.07	$(-0.83 \pm 1.25) \cdot 10^{-3}$	0.55 ± 0.09

Table 3.2: Coatings friction coefficient values for turning samples as function of their coating. All samples are made out of WC-6wt.%Co. Their coating is of CrN/AlTiN type and were produced by an Arc-PVD technique with various thicknesses between 4 and 12 μm . The PVD coatings are either multilayer or bilayer. All values correspond to mean behaviours and are reported with one standard deviation. (*)The unsteady behaviour of step 1 corresponds to the initial evolution of the COF over less than 10 seconds. (**) The COF evolution in the step 1 represents the slope of the coefficient in the unsteady behaviour. The higher the value, the greater the increase in the coefficient of friction over time.

It is generally reported [17] that coated hardmetals have a relatively low coefficient of friction of about 0.2 in tribological test against steel without lubricant, while typical steel against steel values of about 0.4. Kagnaya [35] reported medium values for coefficient of friction of about 0.5 in tribological test of uncoated WC-6wt.%Co against steel without lubricant. In this study, it was suprisingly observed that the values of coefficients of friction were equivalent to the one of uncoated cemented carbides. The values observed in stationary behavior for the different coatings are between 0.4 and 0.6. These medium values correspond to the observations of other works [133, 134] for $Ti_{35}Al_{65}N$ or ZrN coatings, respectively. Therefore, this seems to indicate a particular condition of the surface states of the studied cutting-tools.

A potential approach to increasing the durability of cutting tools would therefore be to investigate the surface condition of the PVD coatings used by improving their resistance to wear and their induced friction. In particular, it is known that the HiPIMS physical vapour deposition technique produces coatings with finer grains than conventional cathode

arc-evaporation method [135, 136]. However, such techniques implementation goes beyond the scope of this study.

The results of the comparison of COF behaviour models with tool life did not show any direct correlation between the coefficient of friction induced by the different coatings and the overall tool-life of the cutting inserts. These comparisons are shown in Figures 3.4, 3.5 and 3.6, for the stationary behaviour of step 2, for the initial COF evolution in step 1 and for the average COF value in step 1, respectively.

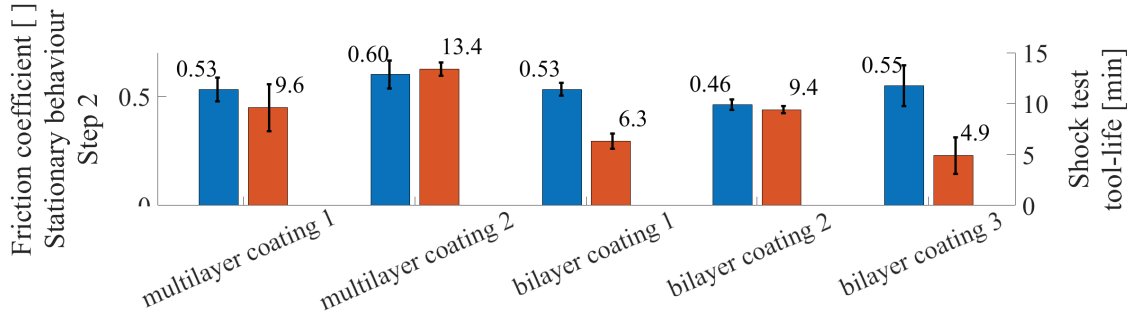


Figure 3.4: Comparison for turning samples of the machining performance with the coatings friction coefficient for the stationary behaviour of step 2 reported in Table 3.2. No direct correlation highlighted. All values correspond to mean behaviours and their reported errors to one standard deviation.

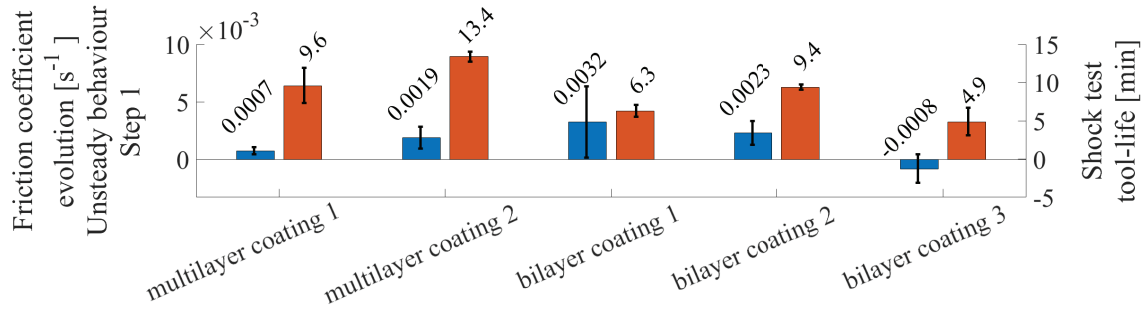


Figure 3.5: Comparison for turning samples of the machining performance with the evolution of the coatings friction coefficient for the unsteady behaviour of step 1 reported in Table 3.2. No direct correlation highlighted. All values correspond to mean behaviours and their reported errors to one standard deviation.

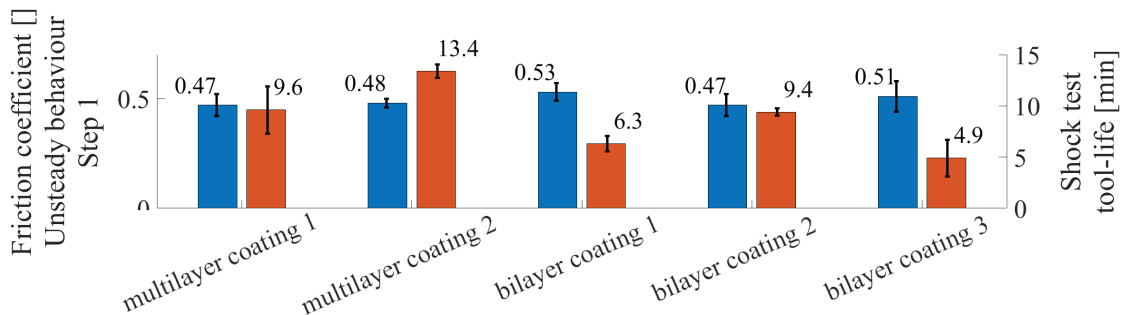


Figure 3.6: Comparison for turning samples of the machining performance with the mean value of the coatings friction coefficient for the unsteady behaviour of step 1 reported in Table 3.2. No direct correlation highlighted. All values correspond to mean behaviours and their reported errors to one standard deviation.

3.2.2 Mechanical properties and characteristics of the coatings

In this Section, coatings mechanical properties (i.e. hardness, elastic modulus, and residual stress), and coating characteristics (i.e. architecture, thickness) are investigated. Each studied properties is then compared with the durability of the cutting inserts defined by the tool-life in extreme shock tests reported in Sections 2.1.2 and 3.1 above. This makes it possible to highlight (or not) the influence of each parameter on the tools durability and thus to motivate further investigations.

Hardness and Elastic modulus

Transition metal carbides and nitrides as TiN, or even more TiAlN, show excellent properties such as high hardness or high melting point, making them excellent coatings for cutting applications [8, 99]. Hard and wear-resistant thin films are essential for the carbide and cemented carbide industry to ensure the quality of the cutting tools they produce. Nanoindentation tests allowed to determine the values of elastic moduli and hardness of the various CrN/TiAlN-type PVD coatings. The method used for the analysis of nanoindentation curves (i.e. force applied by the Berkovich Diamond indenter vs. penetration depth) is the standard Oliver and Pharr method reported in the Section 2.3.2. In order not to affect the nano-hardness measurement with the properties of the bulk material underneath the coating, practice requires that the indentation does not exceed 10 percent of the total thickness of the layer. Also, due to the high roughness of the PVD coatings on the studied samples, it was necessary to ensure a uniform and smooth surface finish on surface portions large enough to perform an indentation. Before each nanoindentation a soft polishing process was conducted (c.f. Section 2.3.2 for the experimental methodology). Ten indentations at arbitrary locations on the adequately homogeneous and smooth coated surface were made and averaged. Appendix 4.5 illustrates some surface states marked by Berkovich indentations and the corresponding nano-indentation curves.

As shown in Figure 3.7, the nanohardness values are not directly correlated to the values of the tool-life measured in shock-tests and reported the Figure 3.1. The obtained nanohardness are of the same order of magnitude for the different studied PVD layers. The same lack of correlation is observed for the elastic moduli of the different coatings, as illustrated in the Figure 3.8 below.

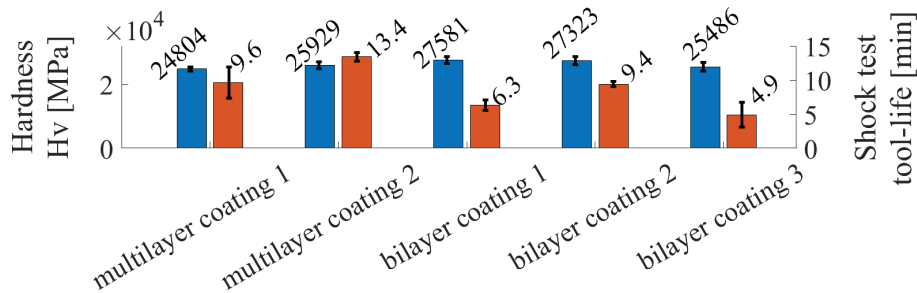


Figure 3.7: Comparison for turning samples of the machining performance with the coatings hardness. No direct correlation highlighted. All values correspond to mean behaviours and their reported errors represent one standard deviation.

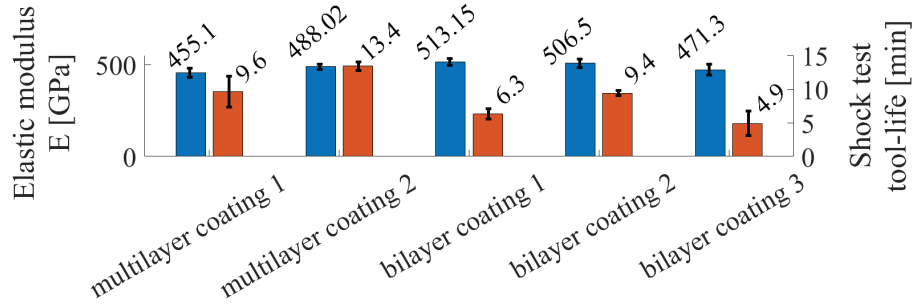


Figure 3.8: Comparison of the machining performance with the coatings elastic moduli for turning samples. No direct correlation highlighted. All values correspond to mean behaviours and their reported errors represent one standard deviation.

Thickness and Architecture

For coatings, the characteristics of the architecture and thickness are also studied in Figure 3.9. It can be noticed that multilayer coatings induce better overall performance. Taking this last factor into account, it can also be noted that the thinner the coatings are, the better their tool-life in shock-tests.

The observations in the Figure 3.9 below clearly show the advantages of multilayer coatings compared to bilayers, as also reported in the literature [84, 137, 138, 139]. It is known that multilayer and multicomponent coating systems offer improved performance in tribological applications such as cutting tools, and especially when these coatings contain multiple layers with thicknesses in the nanometre range. The use of different compositions as well as multiple layers for coatings is a natural step induced by the need for compatibility between the different systems considered and sometimes their contradictory requirements. First, there is the interface between the coating and the workpiece, where adhesive or abrasive wear, corrosion and oxidation can be observed. Then there is the coating and its physical characteristics with its hardness, fatigue resistance, internal stresses and toughness. Finally, there is the interface between the coating and the substrate material, where layer adhesion, substrate/layer interactions and inadequate thermal expansion must be taken into account. The use of a single coating therefore quickly becomes an insoluble problem for cemented carbide tools with regard to their extreme and highly variable operating conditions. The design of multilayer coatings makes it possible to meet each of these requirements, mainly considering the coefficients of chemical bonding and thermal expansion between each system.

Surprisingly, it can be seen from the results in the Figure 3.9 that the performance of the cutting tools decreases as the thickness of the PVD layers increases. These observations suggest that increasing the thickness of thin layers induces a more brittle coating material, which would imply a boundary on the coatings thickness. This is contrary to the results of other research [140, 141, 142], which observes an increase in tool life with an increase in layer thickness, often correlated with a slight increase in hardness. However, an optimum layer thickness for tool life can exist as reported by [143], which may explain the latter observations.

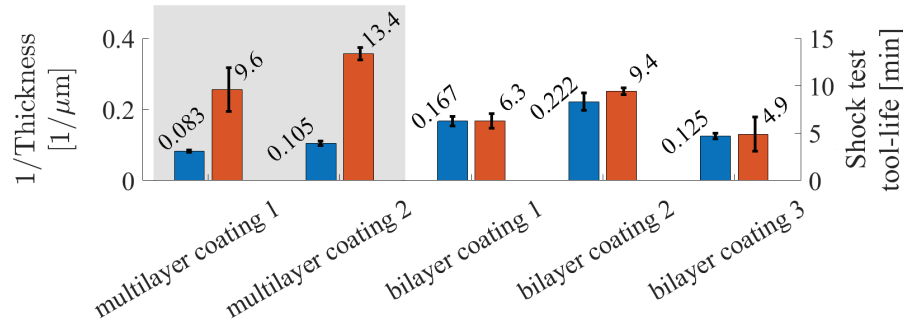


Figure 3.9: Comparison for turning samples of the machining performance with the coatings thickness and its architecture. Multilayer samples are highlighted in grey, while bilayer samples are left uncoloured. An indirect correlation between thickness and tool life can be observed by taking into account the fact that multilayer coatings have better overall performance. All values correspond to mean behaviours. The reported errors represent one standard deviation for the tool-life measurements. For the thickness, the errors correspond to overestimations taking into account half of the precision given by the manufacturer. (n.b. the informations are encoded to insure the confidentiality of the production of Lamina-tech).

Residual stresses in coatings

The residual stress state of a coated cutting tool greatly influences its fatigue resistance, performance and tool-life [87]. The stresses in a thin layer can be either compressive or tensile. In the case of thin PVD layers for the cutting tools industry, the residual stresses originate from various sources [144]:

- Residual stresses induced directly during deposition. This is known as intrinsic growth stress, which can result from defects induced by the energy of the particles bombarded by the PVD plasma, or from phase transformations or chemical reactions during deposition.
- Thermally induced stresses resulting from temperature changes and differences in the coefficient of thermal expansion between the PVD coating material and its substrate.
- Residual stresses induced during the use of cutting tools due to differences in thermal and mechanical properties between the substrate and the PVD coating material.

Due to the important mechanical external stresses and the high thermal loads induced by the machining processes, it is known that compressive residual stresses are advantageous for cutting tools. Compressive stresses inhibit the nucleation and propagation of cracks, which is the opposite of tensile stresses that facilitate crack initiation, stress corrosion and decrease fatigue life [144, 145, 146]. There is, however, an upper limit where excessive residual compressive stress would lead to embrittlement of the coating [145, 147].

The residual stress of the different coatings is determined by the Sinus-Square-Psi method (Equation 2.10) through an X-ray diffraction technique and their values are reported in the Figure 3.10 below. All measurements take into account the diffraction peak of TiN (420) at $2\theta \approx 108.2$ degrees for different omega inclinations. The omega angles range from 10 to 45 degrees each 5 degrees increment. Diffractograms fitting and analysis are performed with the help of the HighScore Plus Panalytical software. The evolution of the d-spacings as a function of the different omegas can be analysed by linear regression to determine the residual stresses of the layers. The reader is invited to refer to the Section 2.6.2 for the

presentation of the used techniques and notations. All tested coatings exhibit compressive stresses and are therefore well suited to their intended use. However, no direct correlation could be determined between the measured residual stress values and the tool-life of the cutting tools.

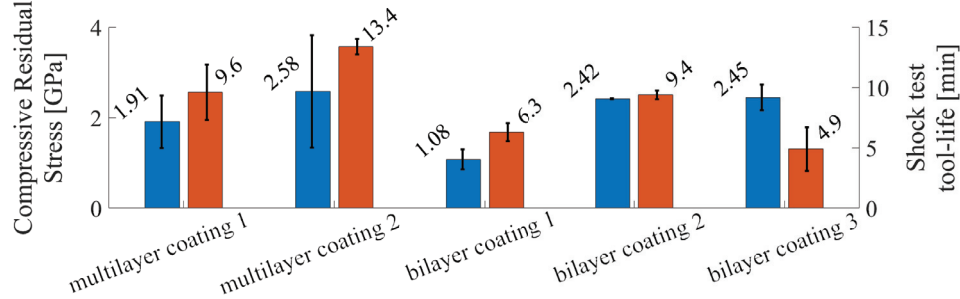


Figure 3.10: Comparison for turning samples of the machining performance with the coatings residual stress. No direct correlation highlighted. All values are determined through formula 2.10 and by linear regression of the evolution of the d-spacing as a function of the omega inclinations. The reported errors represent the combined uncertainties resulting from the equation 2.10. (n.b. the informations are encoded to insure the confidentiality of the production of Lamina-tech).

3.2.3 WC-Co bulk mechanical characteristics

Cobalt microstructure properties

The analysis of the spectra obtained by mechanical spectroscopy gave some unexpected results. In the 1 Hz frequency range, a mechanical damping peak P1 is detected between 900K and 920K for all samples as illustrated in the Figure 3.11. The relaxation peak P1 is related to the properties of cobalt and the dynamics of the defects it contains. Therefore, the addition of a coating to the surface of the material should not impact the characteristics of this peak. However, it was observed that the P1 peak is systematically shifted to lower temperature for samples where the thin film is deposited.

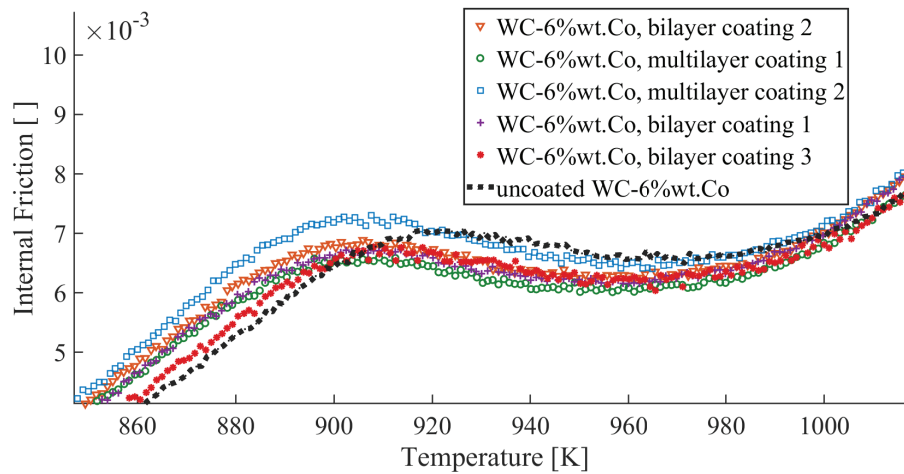


Figure 3.11: (Comparison of IF measurements between coated and uncoated WC-6wt.%Co specimens.

The comparison between the tool lifetime and the cobalt properties studied by mechanical spectroscopy was made by defining the variation of the peak P1 position between a coated sample and its uncoated reference. This gives the temperature position shift of the peak P1 induced by each of the coatings. In the figure 3.12 below are reported all the variations in the positions of the P1 peaks as a function of their coating. These values are compared with those of the tool-life of the corresponding cutting tools. Interestingly, this peak shift is correlated to the tool-life: the greater the peak shift, the longer the tool-life. It demonstrates a direct link between the tool-life, a macroscopic property, and the damping capacity of the material, a microscopic property.

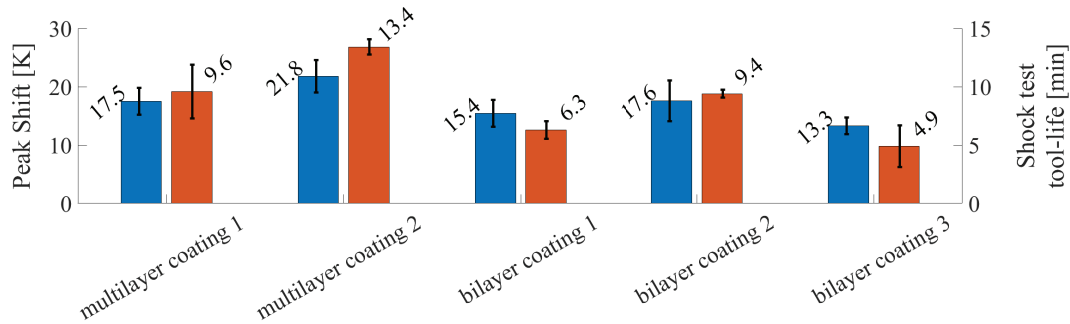


Figure 3.12: (Comparison of the variation of the position of peak P1 for various PVD coating grades (according to their WC-Co reference) with the lifetime of cutting tools measured on a test bench. A direct correlation between a macroscopic property (the tool-life) and a microscopic property (the Cobalt microstructure properties corresponding to the peak P1) could be highlighted. The errors reported for the temperature shift of the P1 peaks are estimated on the difference between several numerical fitting models, i.e. between a fitting according to the Debye model and a fitting according to a Lorentzian model. (n.b. the informations are encoded to insure the confidentiality of the production of Lamina-tech).

3.3 Microstructural defects dynamics in the cobalt phase

The various comparative studies presented above show that the performances of the cutting tools might be determined by the cobalt microstructure. Therefore, most of the following part of this study is dedicated to the investigation of the cobalt microstructure by mechanical spectroscopy and by transmission electron microscopy.

3.3.1 Reference Internal Friction Spectra for different Cobalt Contents

The phases which constitute the WC-Co composites regulate their anelastic properties through the relaxation mechanisms which occur inside each phase. The initial cobalt content defines the dimensions of the binder areas of the composite but also the thickness of the metallic binder between the WC grains [127]. The cobalt content should therefore play a role in the defects dynamic.

As explained in the Section 2.7.4, for all WC-6wt.%Co and WC-10wt.%Co specimens, the characteristic IF spectra measured in the 700K–1350K temperature range exhibit three peaks: P1, P2 and P3. The spectra were deconvoluted with three Debye peaks and an exponential background. The presence of a high temperature/low frequency exponential

background reflects the presence of at least one relaxation peak at very high temperatures. The IF peaks P1 and P2 show a dependence on the cobalt content of the samples as visible on the Figure 3.13. The higher the cobalt content, the greater the intensity of the peaks. Compared to the spectrum of the WC-6wt.%Co sample, the amplitude of the internal friction at high temperature of WC-10wt.%Co is decreased after the second peak P2.

For the uncoated reference samples, at 1 Hz, the intensity of the peak P1 increases from $5.7 \cdot 10^{-3}$ to $8.5 \cdot 10^{-3}$ for the samples with 6wt.% Co and 10wt.% Co, respectively. It increases from $1.1 \cdot 10^{-2}$ to $2.1 \cdot 10^{-2}$ for the peak P2. For the uncoated reference samples, at 1 Hz, the peak P1 appears at about 920 K and P2 at about 1130 K for specimens with 6wt.% Co (Figure 3.14) and respectively at about 945 K and 1165 K for samples with 10wt.% Co (Figure 3.15). The third peak P3, partially visible on IF spectra, can be fitted at 1300 K for WC-6wt.% Co and at 1350 K for WC-10wt.% Co specimens. There is a relative uncertainty about the temperature position of the relaxation peak P3, especially for the 6 weight percent cobalt sample. The 1300K position option is an extrapolation from the Arrhenius diagram of the peak position for a frequency of 1Hz for an uncoated WC-6wt.%Co. The Arrhenius diagram concerned is obtained after several frequency scan measurements of the internal friction and after annealing at 1350K. An ageing effect with cobalt infiltration between the WC grain boundaries is therefore not excluded. It can also be noted that the position at 1350K is satisfactory for the measurements on WC-10wt.%Co and a similar fitting was found for other similar samples.

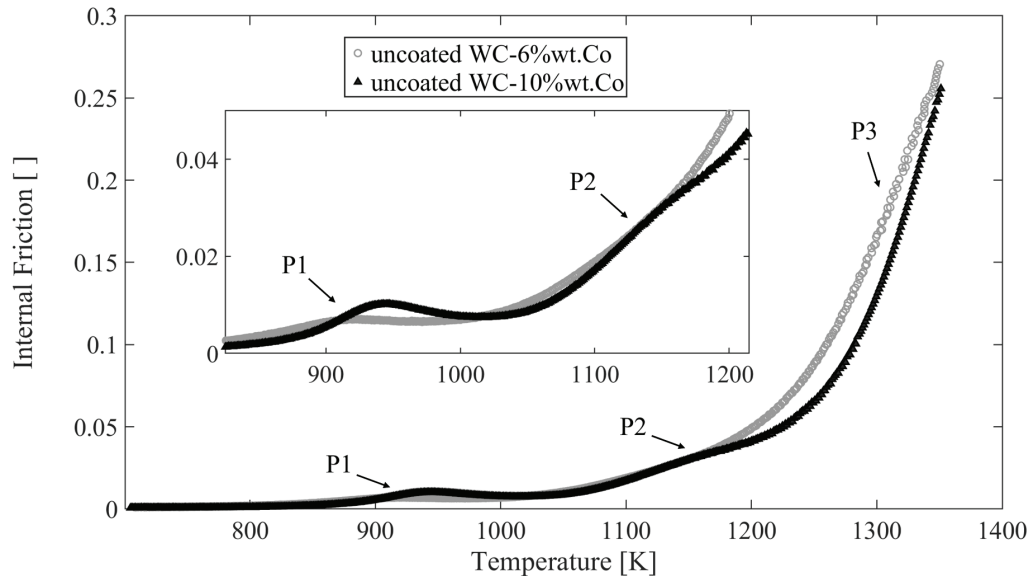


Figure 3.13: Internal Friction spectra of WC-Co samples with different binder contents, respectively 6 and 10 weight percent cobalt. The Internal Friction is measured as function of the temperature for periodic stresses at 1Hz. Three relaxation peaks and one exponential background are observed.

Spectra obtained at lower frequencies (see Figure 3.23) indicate that P3 is a well-defined peak. It has been observed that the peak P1 is sensitive to heat treatments; this may indicate a metastable nature. Thereby, all analyses of this peak have been carried out after three annealing processes at 1050 K of several hours inside the torsion pendulum. This stabilisation process presented in Section 2.7.4 will be fully discussed hereafter.

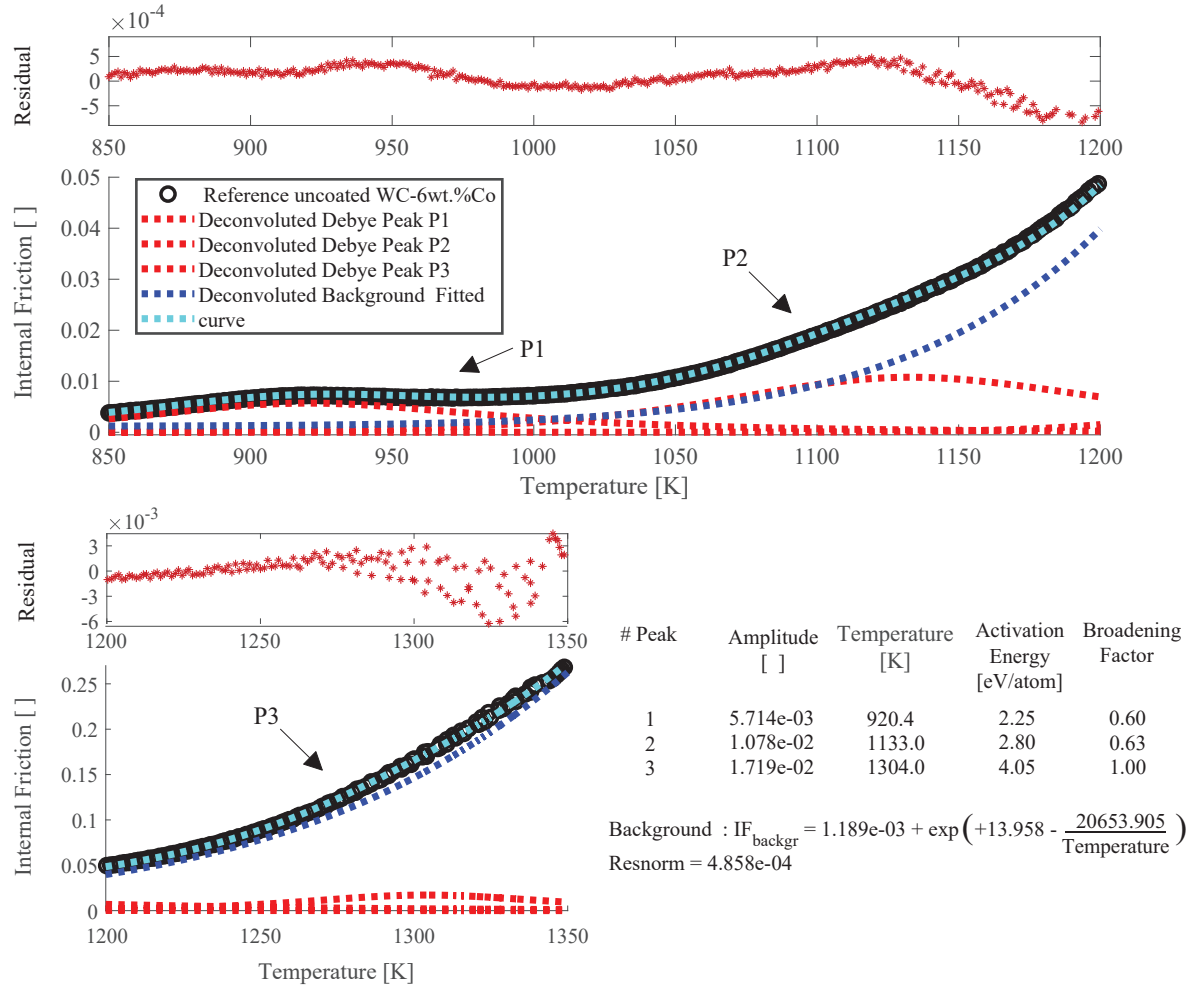


Figure 3.14: Internal friction spectrum of an uncoated WC-6wt.%Co sample measured between 700K and 1350K at 1Hz in a torsion pendulum in forced mode. The measurement was performed with a torsional strain of $5 \cdot 10^{-5}$ with a ramp of 1 K/min. The spectrum deconvolution by three Debye relaxation peaks and an exponential background is presented. This reference IF spectrum is established during a temperature heating ramp, after a so-called stabilisation process defined in Section 3.3.2. After these annealing stabilisation steps, the observed relaxation peaks are fully repeatable within the same test temperature ranges.

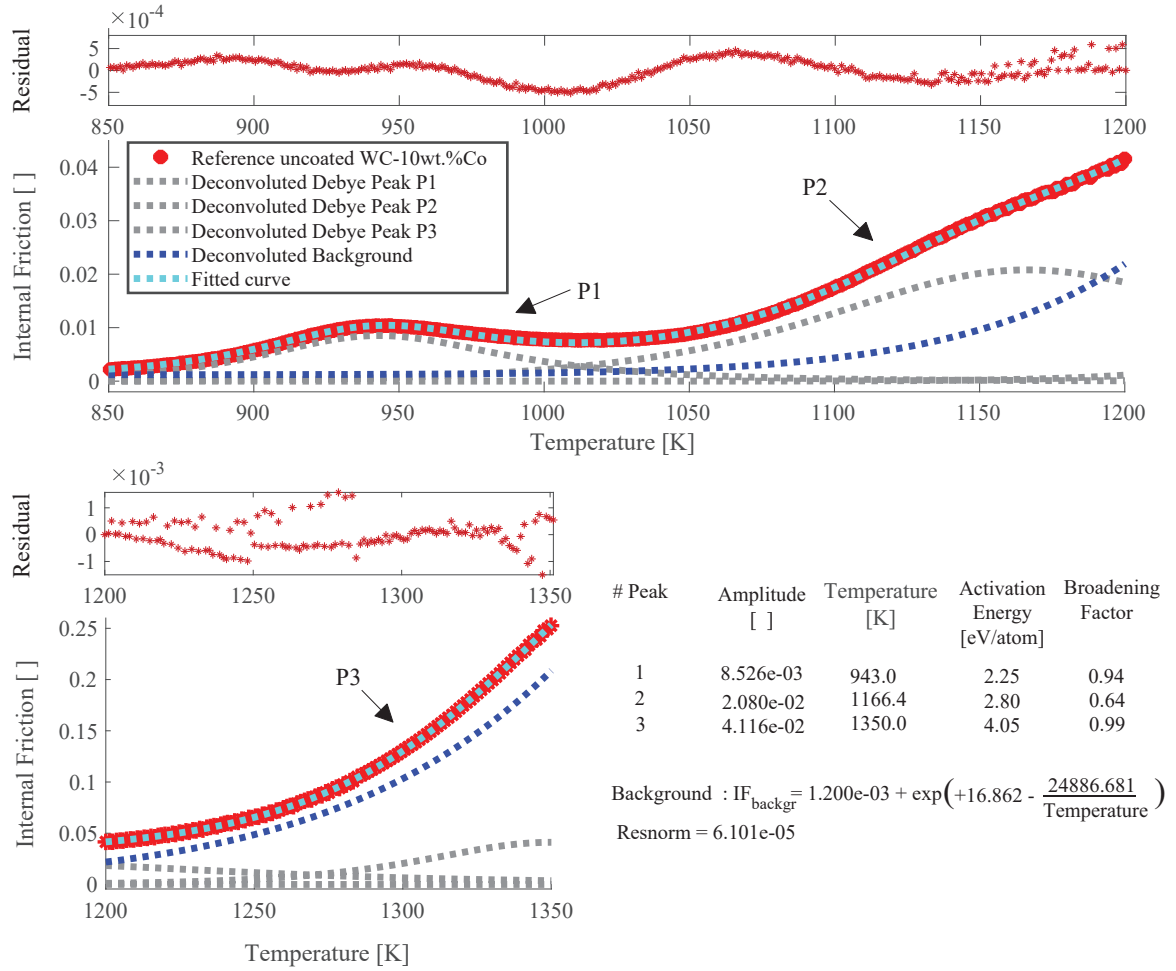


Figure 3.15: Internal friction spectrum of an uncoated WC-10wt.%Co sample measured between 700K and 1350K at 1Hz in a torsion pendulum in forced mode. The measurement was performed with a torsional strain of $5 \cdot 10^{-5}$ with a ramp of 1 K/min. The spectrum deconvolution by three Debye relaxation peaks and an exponential background is presented. This reference IF spectrum is established during a temperature heating ramp, after a so-called stabilisation process defined in Section 3.3.2. After these annealing stabilisation steps, the observed relaxation peaks are fully repeatable within the same test temperature ranges.

3.3.2 Stabilisation processes

An ideal composite material for cutting tool applications in machining should have its different phases as stable as possible over the entire temperature and pressure ranges it passes through. However, one can observe that the microstructure changes rapidly over a wide temperature range. The stability of the WC-Co microstructure is ensured by carrying out several anneals in specific temperature ranges such as 700 K to 1050 K, defining the range of limited toughness and plasticity of WC-Co composites. In the present section, the stability of the microstructure of the composite for temperature ranges corresponding to the relaxation phenomena observed in cobalt are examined.

First Cobalt relaxation process below 1050 K

As presented in Section 2.7.4, the microstructure thermomechanical stabilisation process for the peak P1 consists of three annealing at 1050K followed by a spectrum measurement upon cooling and heating. The following conditions were used: a torsional oscillation frequency of $1Hz$, a ramp of 1 K/min , a torsional strain amplitude of $5 \cdot 10^{-5}$, first with a high temperature dwell of 360 minutes, then of 120 minutes, and finally of 60 minutes.

The effects of these stabilisation phases on the internal friction and the modulus of the WC-Co are shown in Figure 3.16. We observe several effects of annealing at 1050K. First of all it can be seen that the P1 peak shifts towards low temperatures (from 950K to 920K) after the first annealing. A decrease in the amplitude of internal friction above 900K is also observed after annealing. Similar observations can be made on a WC-10wt.%Co grade.

In the set of relative shear modulus curves (Figure 3.16) two inflection points can be seen at approximately 920 – 930K and 975K – 1000K (depending on whether the curve is before or after annealing). By studying the relative shear modulus of the material, a generalized hardening of the material can be seen with the increase in modulus after an initial annealing at 1050K. This hardening corresponds to an increase in modulus of $\Delta G/G = 3.0\%$ at 700K and $\Delta G/G = 2.2\%$ at 1000K for a sample of WC-6wt.%Co. For a cobalt content of 10wt.%, the hardening is then 3.9% and 2.7% at 700K and 1000K respectively.

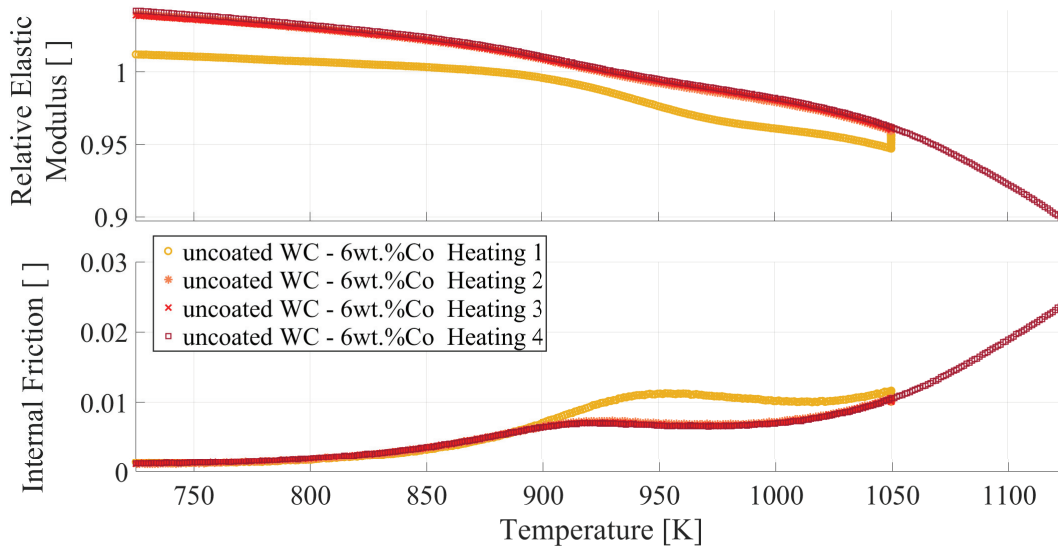


Figure 3.16: Evolution of the Internal Friction Spectra and the material relative modulus for reference uncoated WC-6wt.%Co sample over a whole process of thermomechanical stabilisation of the Cobalt microstructure at 1050K. The curves for "Heating 1" correspond to the material as received. Note that the curves of the annealing 2, 3 and 4 overlap.

After these thermomechanical stabilisation processes, the internal friction spectra for WC-Co samples showed high reproducibility and repeatability. The three anneals of the thermomechanical stabilisation process (Heating 1, 2 and 3) are necessary to restore the microstructure as observed on the reference Internal Friction spectra after various treatments of the material (annealing at very high temperatures, etc.). These processes provide thus a reliable basis for the results comparison of this study. It is interesting to

note that the full repeatability of internal friction spectra has not been observed in previous studies [28]. Stable characteristic states were also observed for annealing below 1100K, but after 1200K the P1 peak disappeared and a higher temperature peak similar to the P2 peak observed in the present work appeared.

Second Cobalt relaxation process below 1200 K

The entire observation of the relaxation peak P2 requires to deviate from the conditions defined for the thermomechanical stabilisation of the peak P1. A rise in the annealing temperatures of the WC-Co, however, causes the relaxation peaks to shift. This cannot be avoided, but a limitation of the measuring temperatures is necessary. It is possible to ensure that the relaxation peak P2 can be measured completely without attaining temperatures above 1200K. Since thermal activation shifts a relaxation peak to lower temperatures by lowering the frequency, a frequency of 50 mHz was set to analyse P2 instead of 1Hz.

The figure 3.17 below shows the evolution of the internal friction and relative modulus curves for a WC-10wt.%Co sample, after it has been treated by the thermomechanical stabilisation process at 1050K described above. However, an important point should be noted here: the WC-10wt.%Co material used here is slightly different from the materials used in the rest of this study as it corresponds to a different production batch. The Internal Friction Spectra observed for this batch are similar in shape to those of the reference material but their cobalt relaxation peaks are slightly shifted towards low temperatures (approx. 15K).

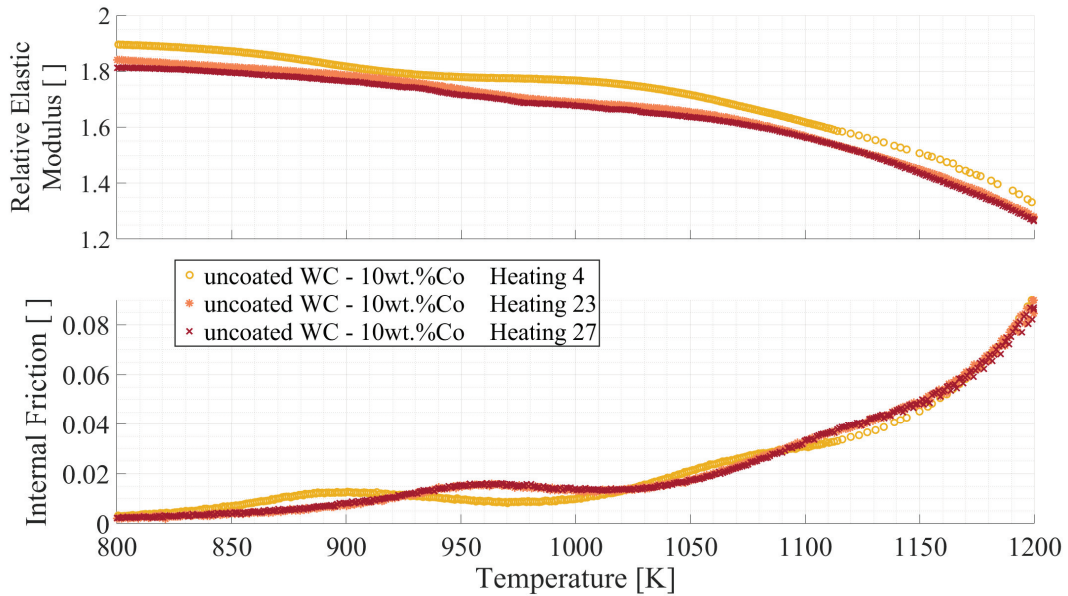


Figure 3.17: Evolution of the Internal Friction Spectra and the material relative modulus for reference uncoated WC-10wt.%Co sample after several annealing at 1200K. Note that the curves of the annealing 23 and 27 overlap. Measurements are taken at 50 mHz.

A first annealing up to 1200K called "Heating 4" is presented in Figure 3.17. It follows the thermomechanical stabilisation treatments at 1050K. The relaxation peaks P1 and P2 are at 900K and 1078K respectively for measurements at 50mHz, while P1 was at 930K for 1Hz measurements. After a series of anneals at 1200K (here the anneals between "Heating 4" and "Heating 23" for measurements at different frequencies), we observe a shift of the relaxation peaks P1 and P2 towards higher temperatures. The temperature position of P1 passes from 900K to 956K, while its amplitude slightly increases from $1.127 \cdot 10^{-2}$ to $1.228 \cdot 10^{-2}$.

Relative shear modulus curves of Figure 3.17, show two inflection points can be seen at approximately 885–950K and 965K–1020K (depending on whether the curve is before or after annealing at 1200K). By studying the relative shear modulus of the material, a general softening of the material can be seen with the decrease in modulus after several annealing at 1200K. This softening corresponds to an decrease in modulus of $\Delta G/G = 2.9\%$ at 700K and $\Delta G/G = 4.4\%$ at 1000K for the new batch sample of WC-10wt.%Co.

These observations make it possible to define two measurement procedures for the P2 peak:

- Single measurement carried out directly after a thermomechanical stabilisation process consisting of three anneals at 1050K.
- Several observations of the P2 peak, after thermomechanical stabilisation of several anneals at 1200K and low frequency.

3.3.3 Measurements in isothermal conditions and T-point effect

Damping phenomenon in matter can also occur at constant temperature and frequency. For isothermal condition, Internal Friction measurements would provide significant informations on microstructure changes such as dissolution, recrystallization or precipitation [148]. It should be noted that the rate of temperature change dT/dt can have an impact on the measurements of Internal Friction [129] such as those presented in this work.

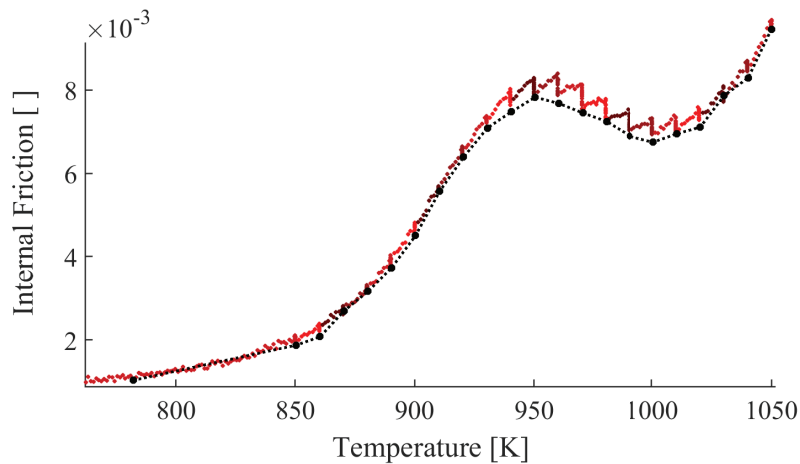


Figure 3.18: Influence of the heating speed on the relaxation peak P1 of WC-Co. The Internal Friction spectrum is interrupted by 20-minute steps at fixed temperature for each 10K steps between 850K and 1050K. The sample is a WC-10wt.%Co without PVD coating. The (●) markers connected by dotted lines represent the values obtained in isothermal conditions.

To test the influence of the rate of temperature change, an experiment consisting of 10K temperature steps followed by 20 minute annealings at constant temperature was carried out on a uncoated reference sample with WC-Co at 10 weight percent cobalt. The points in isothermal conditions obtained in this way can be linked to define an interpolated isothermal Internal Friction spectrum as a function of temperature. In the case of cemented carbides, it can be observed that the temperature rate increases the amplitude of internal friction. The conventional curve corresponds to a ramp of $1K/min$ and is to be compared with the curve under isothermal conditions, as presented in the Figure 3.18.

All of the internal friction spectra presented in this work are not performed under isothermal conditions. Due to the extreme sensitivity of the material to high-temperature annealing, a 20-minute annealing pause is most likely insufficient to ensure that the material finds isothermal equilibrium. In addition, these measuring conditions impact the test time excessively. However, it is important to keep in mind the influence of the temperature change rate when discussing the results, referred to as the T-point effect \dot{T} . This point will be particularly interesting to discuss the evolution of the thermodynamic equilibrium during the microstructural rearrangement.

3.3.4 Thermal activation of cobalt-related relaxation processes in the WC-Co

Internal friction measurements carried out as a function of temperature at different fixed frequencies allow to test the thermal activation of relaxation peaks. Note that thermal activation determines whether the relaxation time of an internal friction peak depends on temperature.

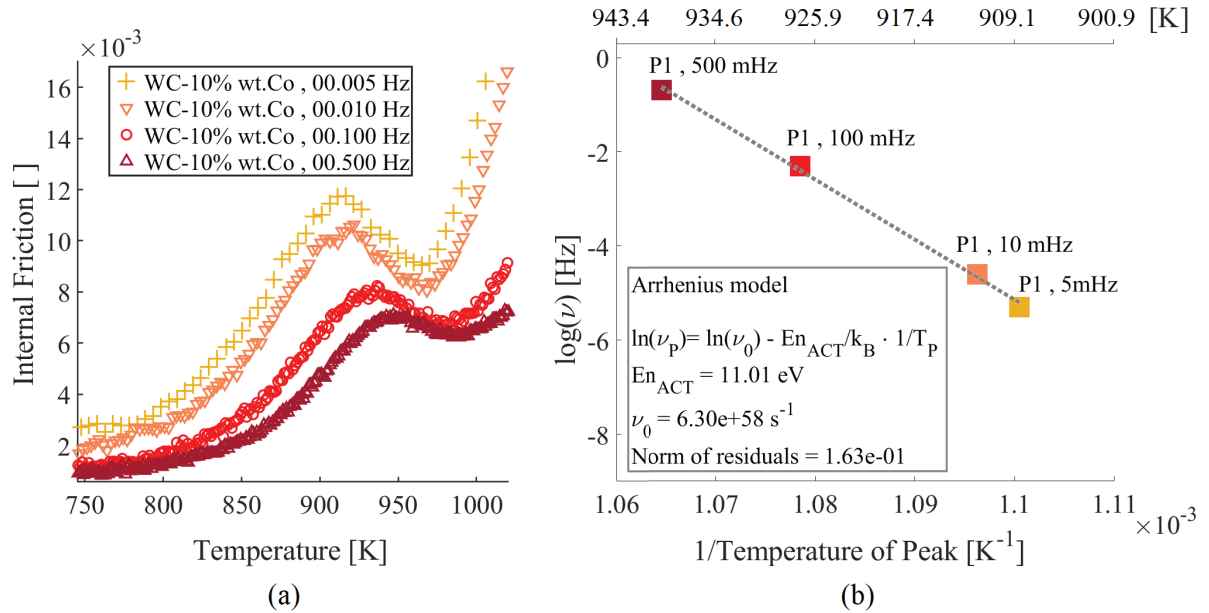


Figure 3.19: The internal friction peaks P1 is thermally activated. a) Evolution of the relaxation peak P1 related to the cobalt phase for a WC-10wt.%Co sample. The Internal Friction spectra are measured as function of the temperature for different fixed imposed stress frequencies. b) Arrhenius diagram corresponding to the frequency and temperature parameters of the relaxation peak P1.

Typically, the physical parameters of the limit relaxation time τ_0 and the activation energy of the relaxation phenomenon E_{act} describing a thermally activated peak are determined using an Arrhenius diagram by assuming an exponential temperature dependence of τ as denoted by the Equation 2.19.

Figure 3.19 reports some measurements taken for the relaxation peak P1 between 700K and 1050K for a cemented carbide with 10 weight percent cobalt. The peak activation is clearly visible and the same observations are found on samples with a 6 percent cobalt content. The parameters of the relaxation peak maxima in Figure 3.19(a) are reported in the Arrhenius Diagram in 3.19(b) relating the frequency to the inverse of the temperature of the peaks. The annealing effects can here be regarded as negligible since the temperature range used is that corresponding to the "stabilisation process" by annealings at 1050k.

In view of the results of the Arrhenius model for the analysis of the thermal activation of the relaxation peak P1 reported in 3.19(b), a clear conclusion is that the activation energy obtained has no physical meaning. Using the Arrhenius model, we obtain that the thermal activation energy corresponds to $E_{act} = 11.01 \text{ eV/atom}$. This exceeds any value that could have been expected as reported in the Table 3 in the Introduction Section of this work. It is also noticeable that the limit relaxation frequency is too high being of the order of $\nu_0 \approx 10^{58} \text{ 1/s}$, whereas in reference the Debye frequency is $\nu_D \approx 10^{13} \text{ 1/s}$. These are therefore apparent values and do not allow adequate conclusions to be drawn.

Similar investigations were carried out around the relaxation peak P2 between 800K and 1200K to test the thermal activation, as reported in Figure 3.20(a) and (b). To achieve this, the analyses had to be carried out at very low fixed frequencies (50 MHz to 500mHz) in order to ensure sufficient coverage of peak P2.

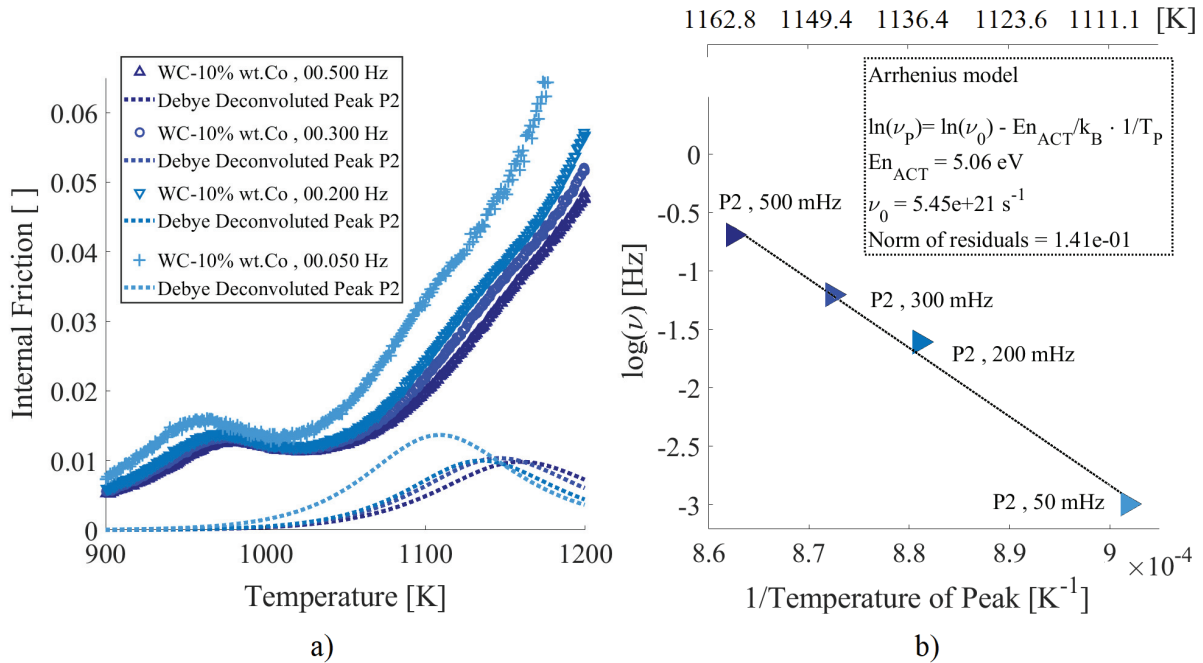


Figure 3.20: The internal friction peaks P2 is thermally activated. a) Evolution of the relaxation peak P2 related to the cobalt phase for a WC-10wt.%Co sample. The Internal Friction spectra are measured as function of the temperature for different fixed imposed stress frequencies. b) Arrhenius diagram corresponding to the frequency and temperature parameters of the relaxation peak P2.

Again for the relaxation peak P2, it can be seen from the Arrhenius diagram 3.20(b) that the activation energy and the relaxation time are only apparent values with no physical relevance. The activation energy of peak P2 of $E_{act} = 5.06 \text{ eV/atom}$ is more realistic than that of peak P1 but remains high. The relaxation frequency is also implausible with $\nu_0 \approx 5.45 \cdot 10^{21} \text{ 1/s}$.

These first non-conclusive analyses provide the motivation for further measurements on the thermal activation of the relaxation peaks P1 and P2. The best measurement strategies are as follows:

- For the cobalt related relaxation peak P1, and since its frequency-temperature range does not allow it to be analysed within the frequency scan range of the instrumentation (4 mHz to 15 Hz), several temperature scans at various frequencies had to be performed. One considerable drawback of such a process, is its time-consuming nature, which nevertheless represents several months of continuous measurements with no guarantee of conclusive results.
- For the cobalt related relaxation peak P2, the optimal method is to perform frequencies scan IF spectra at fixed temperature. A major disadvantage of such a technique is the fact that an anneal effect will certainly occur during the measurement due to the high temperature experienced.

These analyses are reported in the following sections.

3.3.5 Thermal activation of the Cobalt relaxation peak P1

Further analyses on the behaviour of the relaxation peak P1 as a function of temperature and frequency have been carried out and are reported in the Figure 3.21. The measurements were conducted at fixed frequencies between 5 mHz and 5 Hz upon cooling between 1050 K and 500 K . Due to these particular test conditions and due to the number of spectra obtained, the results represent more than 4 months of continuous measurements.

In the Figure 3.21, the evolution of the relative modulus and internal friction are reported. For the peak P1, a characteristic relaxation behaviour with an IF peak and a modulus defect is observed. It can be seen that the amplitude of the peak increases with the inverse of the frequency, which suggests a phase transition with amplitude $\approx 1/\omega$. It should be noted that each value obtained for low frequency spectra corresponds to longer integration times than those for high frequency spectra. Such parameters are necessary to ensure an average of at least 3 oscillations of the phase shift measurement between stress and strain. Specifically, an average over 3 oscillations is ensured for the measurement at 5 mHz , over 6 oscillations then for 10 mHz and 50 mHz and up to 150 oscillations for the measurement at 5 Hz . The increase in integration time on low frequency spectra has a visible effect on their amplitude. Low frequencies have more time allocated to establish the relaxation. This results in relaxation peaks being more sharp at low frequencies. This indicates that the relaxation peak P1 is time dependant, as already mentioned in the previous Section 3.3.3 on the T-point effect. During the deconvolution stages, it was therefore necessary to fit them with Lorentz peaks and not Debye peaks as usually. However, as only temperature and frequency parameters are used to determine the activation energy and the relaxation time, this has no impact on the final results.

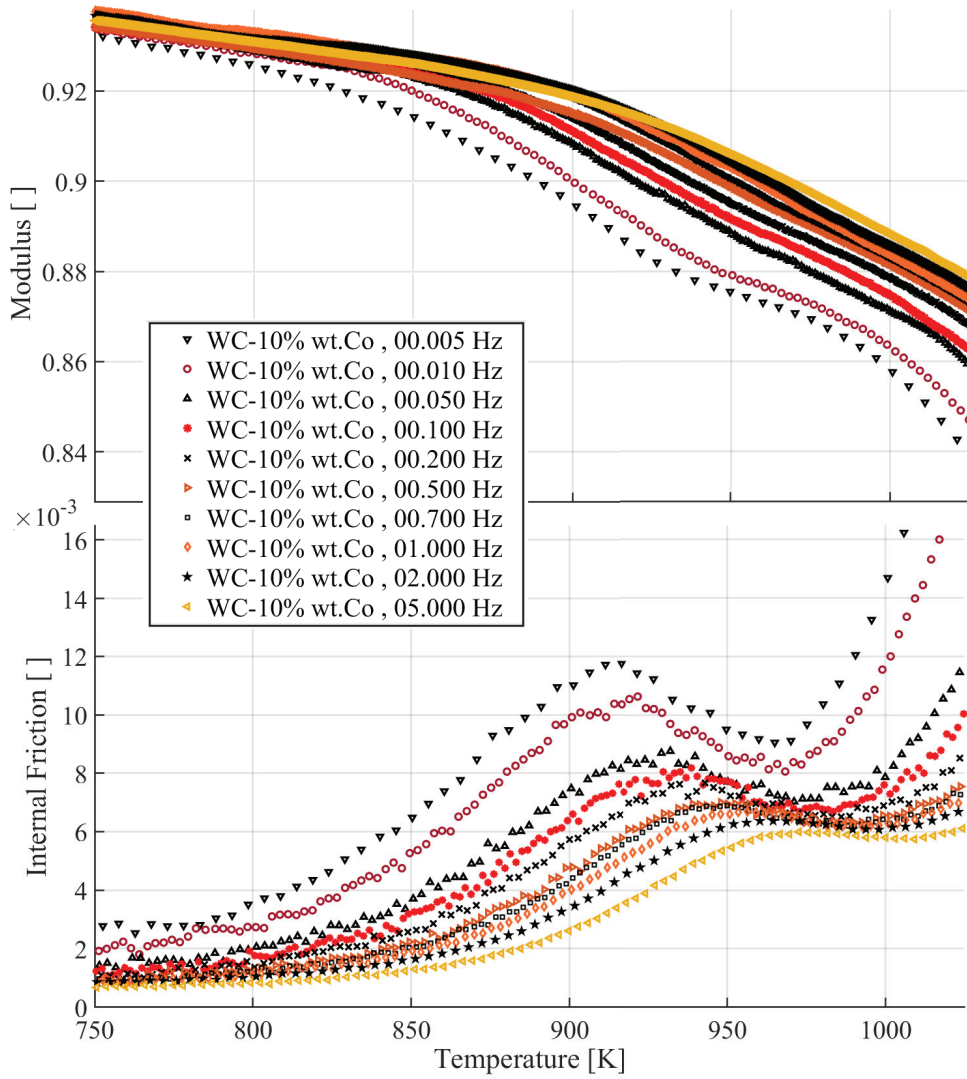


Figure 3.21: Observed relaxation process of the cobalt phase of WC-Co during cooling tests (a) Relative shear modulus as a function of temperature at various fixed frequencies. Low temperature hardening and high temperature softening are observed. (b) Internal Friction spectra as a function of temperature at various fixed frequencies. The IF peaks P1 are thermally activated, as indicated by their frequency-temperature evolution.

The analysis of thermal activation is made in Figure 3.22 by reporting the positions in temperature and frequency of the maxima of the P1 relaxation peaks obtained in Figure 3.21(b). It can be seen from the reported peak values that the temperature/frequency behaviour does not represent a purely Arrhenius behaviour as reported in the Equation 2.19:

$$\tau = \tau_0 \cdot \exp\left(\frac{\Delta E_{act}}{k_B T}\right)$$

By observing the behaviour of the maximum of the peak while decreasing the excitation frequency, one can notice an asymptotic behaviour for the displacement of this peak in temperature. Such a behaviour would induce a divergence in relaxation time by lowering the temperature. This explains why the Arrhenius model was not adapted to the behaviour of peak P1 and only provided non-physical values.

On Figure 3.22 it can be observed, on the other hand, that the law of Vogel-Fulcher-Tamman (VFT) 2.22, introduced in the Sections 1.2.1 and 2.7.2, correctly fits the experimental values. This empirical law states that :

$$\tau = \tau_0 \exp\left(\frac{E_{act}}{k_B(T - T_0)}\right)$$

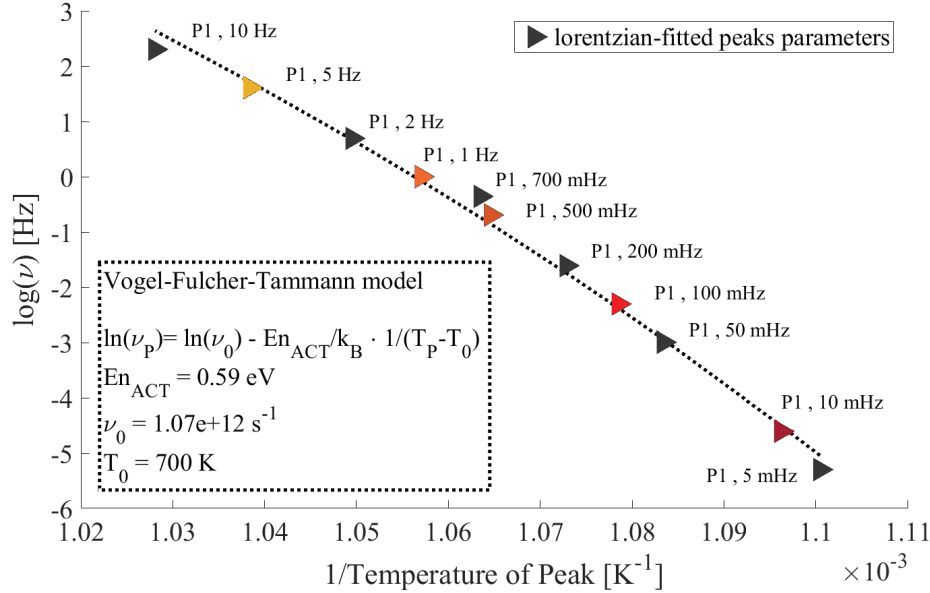


Figure 3.22: Diagram for the peak P1 measured in isochronal scans. The frequency-temperature evolution of the IF peak is fitted with the Vogel-Fulcher-Tamman law.

The Vogel temperature T_0 given here defines the point at which the relaxation time diverges. However, there is a very large uncertainty on the value T_0 . Several values between 675K and 825K were tested for fitting the observations by the VFT model and all provided suitable fits with low norm of residuals of the order of 10^{-1} . This can be explained by the fact that only the beginning of the asymptotic behaviour is visible on the VFT diagram. In order to obtain a better accuracy on the T_0 parameter, it would be necessary to work at lower frequencies in order to shift the relaxation peak P1 towards the lower temperatures. However, this is impossible given the capabilities of the instrumentation used. The exact range of the temperature where the relaxation time start to diverge is therefore unknown. But a possible lower limit would be the temperature of the hcp-fcc phase transition that occurs in pure cobalt at about 680-720 K. This phase transition has been measured in 99.98% pure cobalt polycrystal around 1 Hz by acoustic techniques [26]. Again, these observations could be confirmed as being well reproducible by equivalent measurements on another specimen.

3.3.6 Thermal activation of the Cobalt relaxation peak P2

The non-physical values obtained from the results in Figure 3.20 from an initial study of the relaxation peak P2 justify the need of further analysis. In order to widen the range of the peak P2 observations and to include the peak P3, Internal Friction measurements as a function of frequency in isothermal conditions are carried out. The frequency spectra for an uncoated sample of WC-6wt.%Co between temperatures of 1350K and 1000K are shown in Figure 3.23. A cooling process with a dwell of 20 minutes precedes each frequency spectrum.

In Figure 3.23, the presence of two peaks can be seen, the evolution of which is framed by dashed lines in the graph. These two peaks experience a decrease in their frequency position following the cooling process. This confirms the thermal activation of the peak P2 corresponding to the cobalt and the relaxation peak P3 corresponding to the WC carbide skeleton. The evolution of the peak P3 is clearly visible between the dotted lines. The evolution of the peak P2 is also clear for spectra at the lowest temperatures (1000K to 1100K) and above 1150K. However, a break in the evolution of peak P2 appears between 1120K and 1150K. The analysis of these frequency spectra is carried out by deconvolution of the peaks P2 and P3 with a low frequency exponential background and by arbitrarily setting a relaxation peak at very high frequencies corresponding to a peak P1. The Debye's model is used to fit the internal friction peaks. The deconvoluted spectra are reported in the Appendix 4.5.

Variations in the temperature and frequency positions of P2 and P3 peaks are reported in the Arrhenius plot in Figure 3.24. The shift of their positions serves to calculate their activation energy E_{act} and the inverse of the limit relaxation frequency τ_0 using linear regressions. For the relaxation phenomenon related to the WC-WC grain boundary sliding, values of physical meaning are obtained with an activation energy of approximately $4eV/atom$ and a limit relaxation time of about $1.5 \cdot 10^{-15} seconds$. For the relaxation peak P2 related to the cobalt phase, a remarkable fact is that the results of the measurements under isothermal conditions suggest a transition of the relaxation time associated with a cobalt defect between temperature ranges upper and lower of approximately 1140K. These two behaviours are clearly visible on the Arrhenius diagram in Figure 3.24.

By increasing the temperature above 1140K, the limit relaxation time τ_0 decreases from $5.68 \cdot 10^{-12} seconds$ to $4.26 \cdot 10^{-13} seconds$. However, the delimitation between these two behaviours is not necessarily as abrupt, the temperature steps between each spectrum being of 25 K. Analyses using the Arrhenius diagram indicate that the activation energy between these two behaviours of the P2 peak is equivalent. This is in good agreement with the fact that the observed relaxation corresponds to a single type of microstructure defect movement. An overall activation energy value close to $2.8eV/atom$ is obtained for the peak P2. This value is approaching the cobalt self-diffusion energy of $2.7eV/atom$ and does not seem to suggest a defect diffusion mechanism such as the diffusion of tungsten W in cobalt with a diffusion energy of $2.45eV/atom$. This would appear to be the first experimental demonstration of such a significant change in the relaxation parameters observed by mechanical spectroscopy. This finding explains the observation of non-physical values in the preliminary study of the thermal activation of the P2 peak in Figure 3.20.

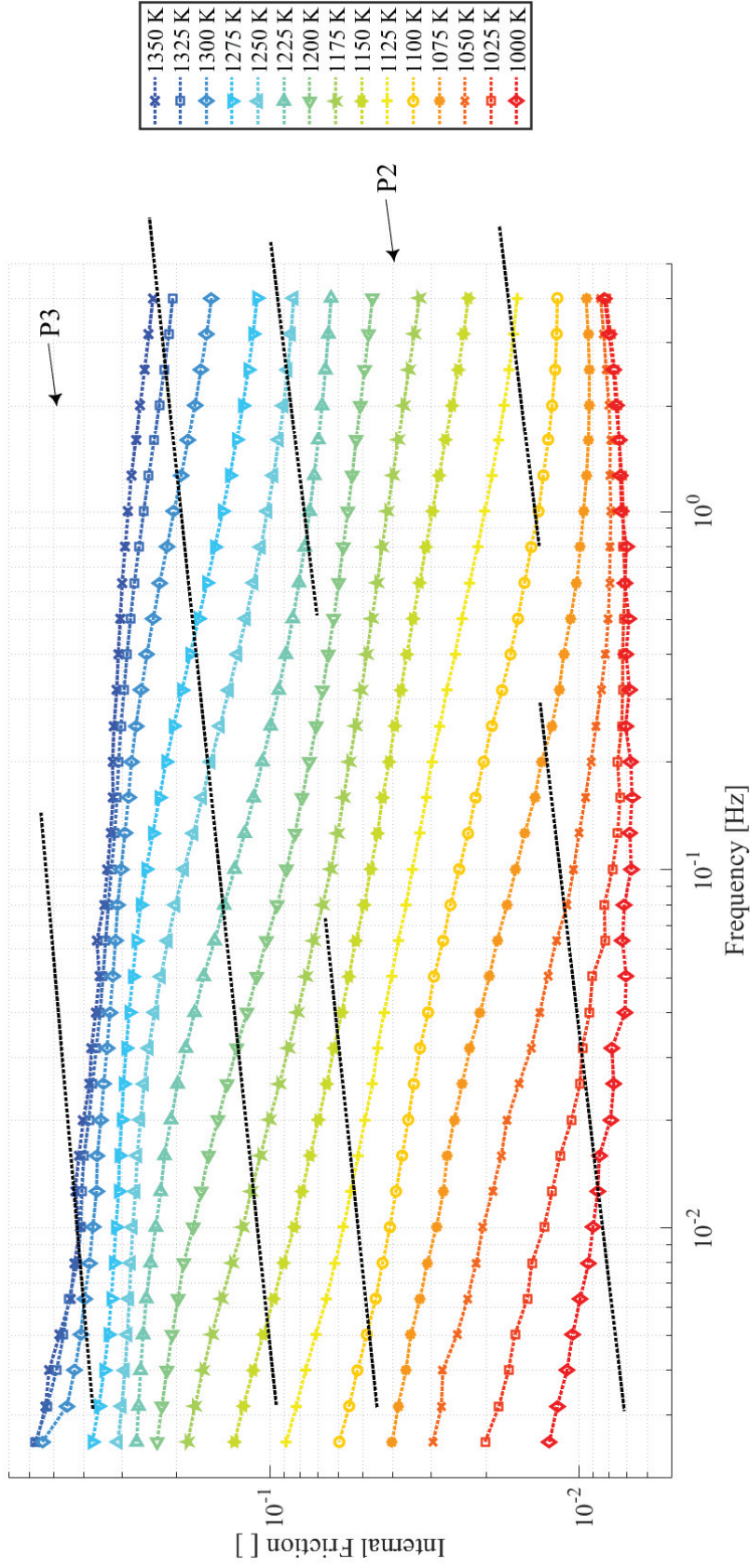


Figure 3.23: Internal Friction measurement as function of the frequency in isothermal conditions for WC-6wt.%Co. Measurements were performed between 4Hz and 3mHz starting from 1350K to 1000k each 25K, after a conventional thermomechanical stabilisation annealing process at 1050K.

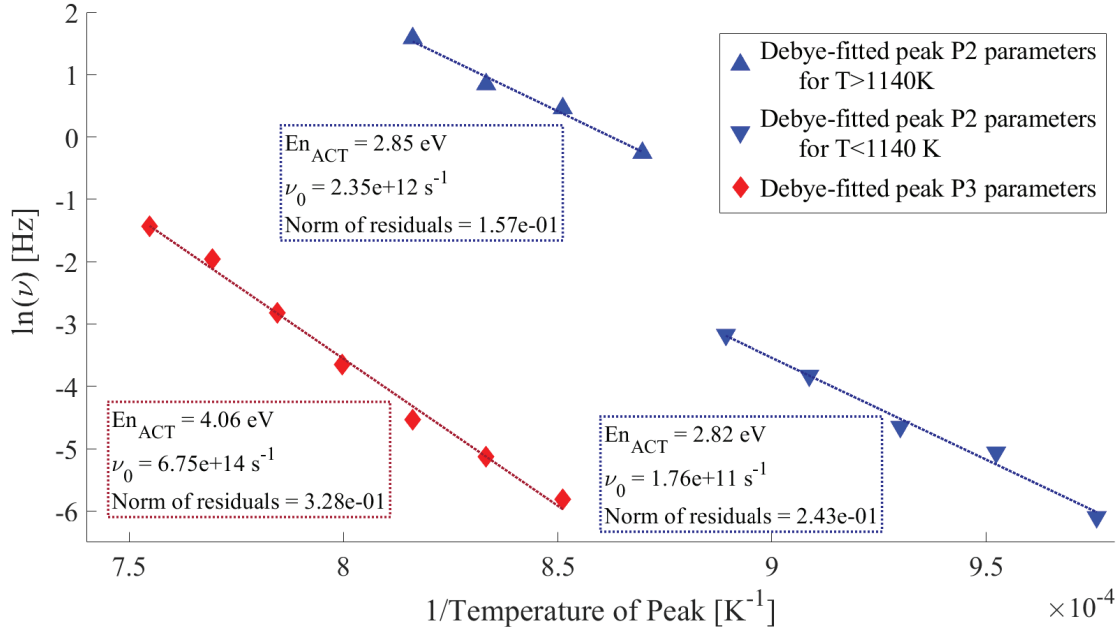


Figure 3.24: Arrhenius diagram plotting the fitted parameters of relaxation peaks P2 and P3. This diagram relates the logarithm of the frequency to the inverse of the temperature that corresponds to the internal friction spectra of a WC-6wt.%Co sample presented in Figure 3.23. The slope of the linear regressions indicates the activation energy E_{act} and the vertical axis intercept the relaxation limit frequency τ_0 .

3.4 Investigations on ergodicity

From the observations made on the microstructural stabilisation annealing processes (c.f. Sections 2.7.4 and 3.3.2) and on the strong T-point effect by Internal Friction (c.f. Section 3.3.3), it appears that the WC-Co microstructure has a important dependence on its thermomechanical history. It is therefore judicious to wonder whether this behaviour is linked to a fundamental thermodynamic property of materials, namely ergodicity. The hypothesis of ergodicity for a material would require, that during its transformation, the experimental time scale is sufficient for the system to visit all its possible states and thus rearrange itself into a thermodynamic equilibrium [65]. On the contrary, a non-equilibrium material (like a glass) would find its properties (like strain) and structure to be strongly dependent on its thermomechanical history [149].

A technique is widely recognised for experimentally testing an ergodicity break within a presumed glassy state by a historical dependence on a physical property; it is the so-called zero-field-cooling/field-cooling (ZFC-FH)/(FC-FH) test [65, 150].

The experimental protocol for such a test is shown in Figure 3.25. The measurement consists of transiting between the high-temperature disordered phase, which satisfies the ergodicity hypothesis, and the low-temperature disordered phase, which does not satisfy this hypothesis. By applying or not applying a stress field in several temperature cycles, it is possible to determine whether a test, with defined experimental conditions, is influenced by its preceding test, depending on whether the preceding test is under the influence of the external field or not. Concretely, by cycling over a temperature range containing the glass transition, a property is first tested without the effect of an external stress field.

On the Figure 3.25, these are the processes 0 and 1, called zero-field-heating (ZFH) and zero-field-cooling (ZFC) respectively. Then, when the sample is at low temperature in its glassy phase, an external field is applied, and the same temperature cycle is conducted while maintaining the external field. These cycles are processes 2 and 3, called field-heating (FH) and field-cooling (FC). Finally, a final test is carried out by raising the temperature, also under the influence of the external field. This last process 4 is called field-heating.

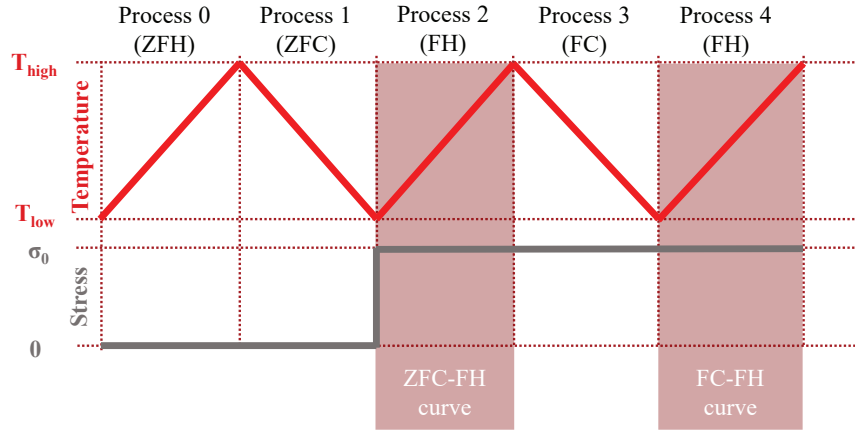


Figure 3.25: Diagram of the zero-field-cooling(ZFC-FH)/field-cooling(FC-FH) test protocol. This method is used to determine whether the ZFC-FH and FC-FH curves deviate from each other, demonstrating a dependence of the system on its history.

Processes 2 and 4 are thereby identical, but their histories differ. Since process 1 preceding process 2 is not under the effect of the external field, the system has no capacity to find an equilibrium at low temperature until the specimen passes above the glass transition temperature. On the contrary, the entire history of process 4 is under the influence of the external field. The physical property curves measured during processes 2 and 4, called ZFC-FH and FC-FH respectively, must therefore show a deviation from each other. If such a case occurs, a break of the ergodicity is demonstrated. On the contrary, for ergodic systems, no deviation would be detected [51].

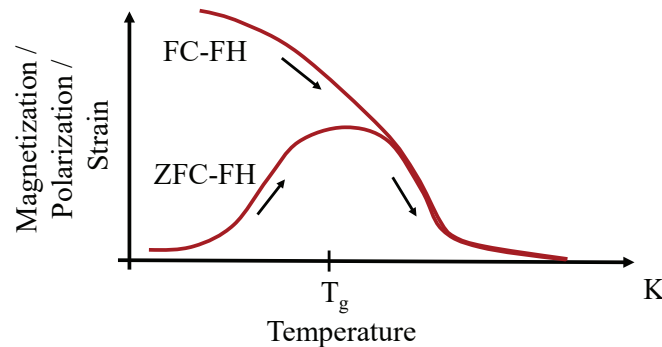


Figure 3.26: Typical (ZFC-FH)/(FC-FH) plot revealing ergodicity breaking, for systems such as cluster spin glass [151], ferroelectric relaxor [67] or strain glass [65]. It can be observed that the behaviour of the low-temperature frozen phase is dependent on the measurement history of the corresponding physical property (magnetization, polarization or strain). No deviation would be observed for ergodic systems [51].

The characteristic result of an ergodicity break observed by the zero-field-cooling/field-cooling (ZFC-FH)/(FC-FH) test is shown in Figure 3.26. Such measurements are, for example, obtained for ferromagnetic [151], ferroelectric [67] and ferroelastic systems [65], by measuring respectively the static strain curves for externally applied tensile stress, the magnetization for applied H-field, or the polarization with a tension bias field. For such systems showing a break in the ergodicity hypothesis, a deviation between the curves according to their history (ZFC-FH) or (FC-FH) is indeed found.

In the case of this study on WC-Co, the physical property to be tested is strain and the field applied according to the ZFC/FC test corresponds to mechanical stress. The investigations were carried out in a torsion pendulum by measuring the plastic torsional deformation (or drift on the deflection angle). The reader is invited to examine the Figure 2.20 illustrating the angle of deflection. A torsional bias applied by the magnetic excitation coils serves as an external stress field. Measurement conditions identical to internal friction measurements by mechanical spectroscopy are applied for this test, including an oscillation frequency of 1Hz, a heating ramp of 1 K/min, a maximum strain of $5.00 \cdot 10^{-5}$ and an integration time of 60 seconds for each measurement point. For the application of the external stress between processes 1 and 2 of the ZFC-FH/FC-FH protocol, a torsional stress of $4.96 \cdot 10^{-5}$ was set for the entire test with the help of a Kepco Bipolar Operational Power Supply connected to the magnetic excitation coils.

It should be noted here that the drift measurement of the deflection angle is extremely accurate (in the order of 10^{-7} radians). Particular attention was paid to stabilising this deflection drift before the ergodicity test. This step is a tedious process. WC-Co samples are composites with a unique morphology defined by the sintering process. Also each of their phases expand and transform in a way that is understandably complex. A zero deflection drift could thus never be observed despite numerous attempts. A null bias was therefore defined when the deflection drift remained as low as possible and was repeatable over five temperature cycles between 700K to 1050K. The reader may later refer to process 0 and 1 in Figure 3.28 (their curves have been shown to be perfectly repeatable).

A zero-field-cool/field-cool (ZFC/FC) curve measured on a WC-10wt.%Co is presented in Figure 3.27. One can clearly observe a deviation between the two curves which occurs around 800K. This behavior should be compared to that in Figure 3.26. Clearly, the shape is not the same, which can be justified by the presence of residual stresses in cobalt due to the composite nature of WC-Co. In the following Figure 3.28 all the deformation curves are presented, to better distinguish the evolution of the deformation between the moment when the deflection drift is stable and the moment when the external stress is applied. One should consider that the cobalt not only bears the external stress but also that of the carbide skeleton.

The processes 0 and 1 define perfectly repeatable reference curves of the deformation, without a stress field. These curves were then compared to curves where an external torsional stress is applied to the sample, in order to qualitatively characterize the evolution of the deformation curves. Figure 3.28 shows that the first response (Process 2) of the material to the external stress is to deform monotonously in the direction of the applied torsional stress.

Then, during the second heating (Process 4) the deformation goes first in the direction of the external applied stress and then, above 900-950K, starts to diverge from the external field direction and starts to follow the deformation observed on the WC-Co, which does not undergo external stress (Process 0). Thus, Processes 4 and 0 have similar behaviour at high temperature. Also we observe that the curves of Process 4 and 2 start to diverge from each other at around 800K.

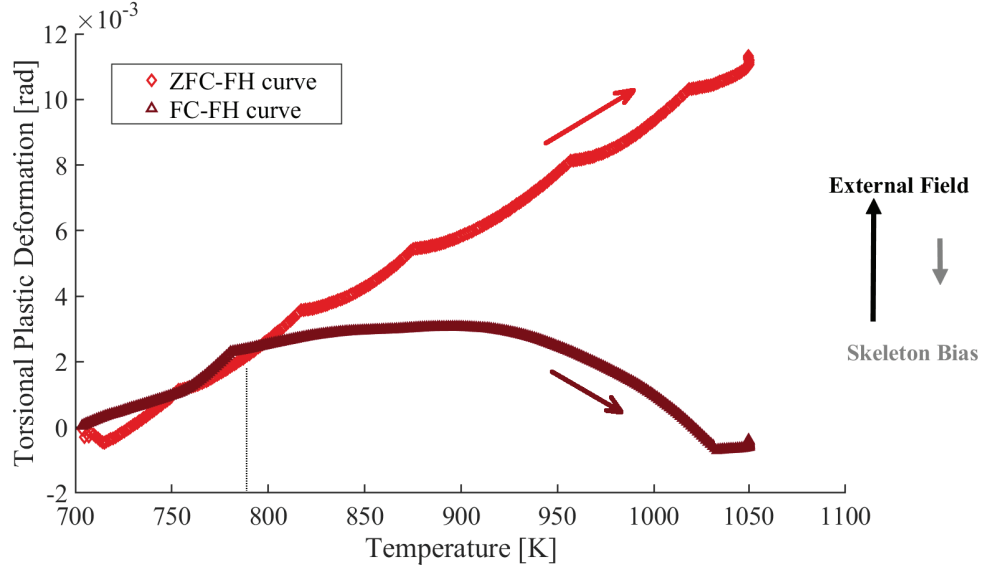


Figure 3.27: Evolution of the torsional deformation (or drift) of WC-10wt.%Co between 700K and 1050K. The corresponding measurement procotole is the (ZFC-FH)/(FC-FH) test illustrated in Figure 3.26. Due to the extreme sensitivity of the strain detection, the fluctuations are due to the temperature regulation fluctuations of the order of 10^{-1} degree.

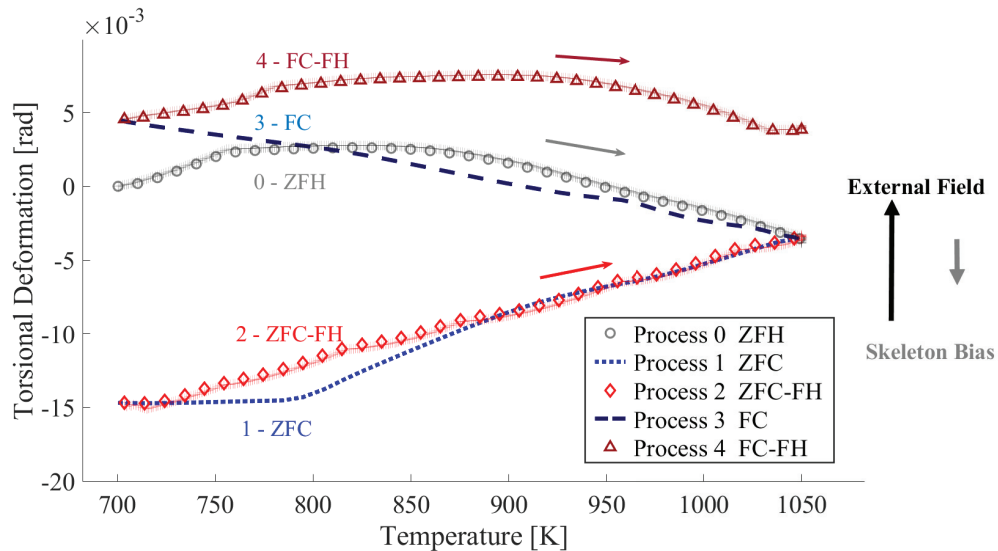


Figure 3.28: Evolution of the torsional deformation (or drift) of WC-10wt.%Co between 700K and 1050K. The corresponding measurement procotole is the (ZFC-FH)/(FC-FH) test illustrated in Figure 3.26.

The deviation temperature observed at approximately 800K varies greatly from the 945K observed by mechanical spectroscopy for the temperature position of the relaxation peak P1. However, it corresponds well to the temperature ranges proposed for the "Vogel temperature" in Section 3.3.5. This difference can be explained, according to the author, by the fact that for mechanical spectroscopy tests at 1Hz, only fluctuations faster than 1Hz would be frozen below the P1 peak temperature. The origin of this temperature difference for a glass phase transition would therefore be found in the kinetics of the applied stress. The situation observed during the zero-field-cooling/field-cooling test corresponds to a temperature below that of the relaxation peak P1 at 1Hz, since the external field is a static stress of zero frequency.

The continuous deformation experiments presented here do not correspond to the conventional curves of the zero-field-cooling/field-cooling (ZFC-FH)/(FC-FH) test illustrated in Figure 3.26. These are in fact direct susceptibility measures whose results would not be the composition of several phases influences. The approach proposed here is therefore not optimal, but it paves the way with promising results. However, several points remain unaddressed :

- Despite the care taken to stabilise the deflection drift, the microstructural origin of the deformation observed without and with the influence of the external stress field remains uncertain. It must be realised that, since torsional deformation measurements are conducted, the changes are not instantaneous and the material microstructure evolves to an equilibrium position with time. It is therefore possible that the observed deviation in 3.27 is only the incidental result of the deformation of the material over a very long interval of time.
- The time needed to stabilise the microstructure may be reasonably unreachable (but not impossible) even in a high temperature phase. During tests of the T-point effect (reported in Section 3.3.3), it was observed in particular that an isothermal pause of 20 minutes or more induced a stabilisation of the internal friction. And this for temperature steps of 10K. Implementing such a procedure in a ((ZFC-FH)/(FC-FH) test remains unachievable.

In spite of the limitations to verify the ergodicity breaking, the author remains convinced of the validity of the approach due to the observation of numerous indications of the material's dependence on its thermomechanical history.

3.5 Magnetic study

This section attempts to determine the experimental basis for a complete analysis of the P2 relaxation peak measured at 1130K and 1165K in the 1Hz frequency range for WC-6wt.%Co and WC-10wt.%Co respectively.

Previous mechanical spectroscopic analyses of WC-Co suggested that the relaxation peaks P1 and P2, also observed in this work, corresponded to the evolution of the same microstructural defect [128, 27, 129, 28]. This hypothesis was motivated by the observation of a transition from the relaxation peak P1 to peak P2 between a low temperature state (700K to 1000K) and a high temperature state (from 1000K to 1200k). In the latter studies, peak P1 appears in particular only after a long annealing at 1000K. However, this is not

observed in the cemented carbides of this study.

The observed transition from a low-temperature relaxation peak to a high-temperature relaxation peak was first attributed to a recombination of Schockley partial dislocations at low temperature into perfect dislocations at high temperature accompanied by a change in the concentration of tungsten solute in the cobalt binder [128, 27].

This vision was then completed by the proposal of a magnetic influence on the tungsten diffusion within the cobalt [28]. It was suggested that the relaxation peak P2 should be associated to a magnetic transition peak of cobalt at the Curie temperature. The length of the dislocations would be influenced by the presence of paramagnetic and ferromagnetic domains. An evaluation of the thermodynamic properties of Co-W-C systems using the CALPHAD calculation method predicts the existence of a miscibility gap that occurs at the Curie temperature between a tungsten-rich paramagnetic phase and a ferromagnetic phase where the cobalt is purer [152, 153]. A spinodal decomposition could then be confirmed experimentally in an indirect way by the observation of tungsten-rich compositional regions forming bands of 5nm to 10nm in width [153]. This measurement was carried out with an atomic probe technique in the cobalt phase of a cermet.

The magnetic interpretation of the origin of the relaxation peak P2 is thus adequately consistent with the observations of the studies described above of the requirement for long annealing to obtain a low temperature state (peak P1). The corresponding microstructure would therefore be obtained by the slow diffusion of tungsten solute into the cobalt phase. At low temperature, the presence of tungsten bands within the binder would thus constitute barriers limiting the dislocation free length. By increasing the temperature, the high-density tungsten bands dissolve and release the dislocations. Following the Lücke-Granato model [154], the increase in their free length thus leads to a shift of the relaxation peak towards higher temperatures.

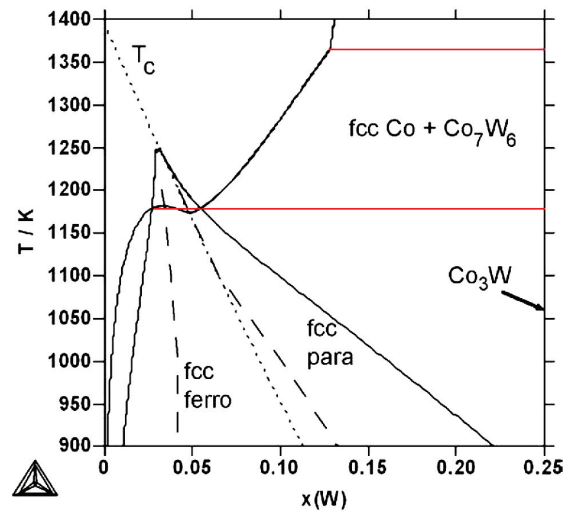


Figure 3.29: Co-W system phase diagram calculated with the thermodynamic CALPHAD method. A miscibility gap is visible. The extension of the miscibility gap is presented in full line. The dotted line gives the Curie temperature variation with the tungsten content. Spinodal lines are represented by the dashed lines. Reprinted from G. Ostberg et al. [153], with permission from Elsevier.

It is thus clear that the density of dissolved tungsten plays a determining role on the movement of dislocations and thus on the mechanical properties of the material. The paramagnetic phase of the tungsten-rich cobalt is favoured by a greater dissolution of the tungsten, which also has the effect of lowering the Curie temperature.

In this study it was decided to test two characteristics of the WC-Co material:

- The Curie temperature of the WC-10wt.%Co samples was measured to determine whether it actually corresponds to a temperature range close to the relaxation peak P1. This magnetic transition would thus confirm that it is related to a transition into a low-temperature ferromagnetic phase and a high-temperature paramagnetic phase which would release the movement of the dislocations.
- A further proof of a magnetic influence on the relaxation peak P2 was searched by internal friction measurements. Two approaches were explored: the influence of a constant external magnetic field on the internal friction, and the influence of WC-Co polarization on the internal friction.

3.5.1 Magnetization transition and Curie temperature of WC-Co

It was decided to measure the Curie temperature of the WC-Co using a thermogravimetric technique, which is capable of determining the mass variation of a sample as a function of the annealing temperature. A thermogravimeter combines a microbalance with a furnace. In order to study the magnetic susceptibility as a function of temperature, a powerful magnet of 0.5 T (centre value) was placed in the axis of the microbalance on the thermogravimeter outside the furnace. In order to carry out a magnetic transition investigation by this method, two measurements are necessary. A first measurement is used to define a reference behaviour and is carried out with the sample holders empty. A second measurement then takes the samples into account. The difference between these two measurements then defines a equivalence of magnetisation.

The equipment used for this analysis is a Labsys TG-DTA/DSC thermogravimeter from the manufacturer SETARAM. The measurements were carried out with 100 μ l alumina crucibles as sample holder and under nitrogen flow. The samples of WC-10wt.%Co were prepared by electroerosion cutting, 705.5 mg was thus mounted in the thermobalance. A rough estimate based on the phase diagram in Figure 3.29 would give the Curie temperature between 1100K and 1200K. It was therefore decided to test the magnetisation of the samples up to approximately 1300K.

Figure 3.30 reports the results obtained. Figure 3.30(a) shows the mass variation for the reference and for the cemented carbide obtained directly by thermogravimetric analysis during the heating phase. Figure 3.30(b) then reports the difference between these two behaviours defining the equivalence of the magnetic behaviour. A temperature is clearly observed above which the magnetic order disappears between a low temperature ferromagnetic state and a high temperature paramagnetic state. We can thus define the Curie temperature at $1130.0 \pm 10.0K$ for the WC-10wt.%Co sample. During cooling, a similar behaviour could be seen with a transition temperature of $1120.0 \pm 10.0K$. This temperature corresponds to the temperature range that would correspond to a transition of the relaxation time observed for the peak of Internal Friction P2 (see Figure 3.24). By looking at Figure 3.29, one could event extrapolate the W content in Cobalt:0.08.

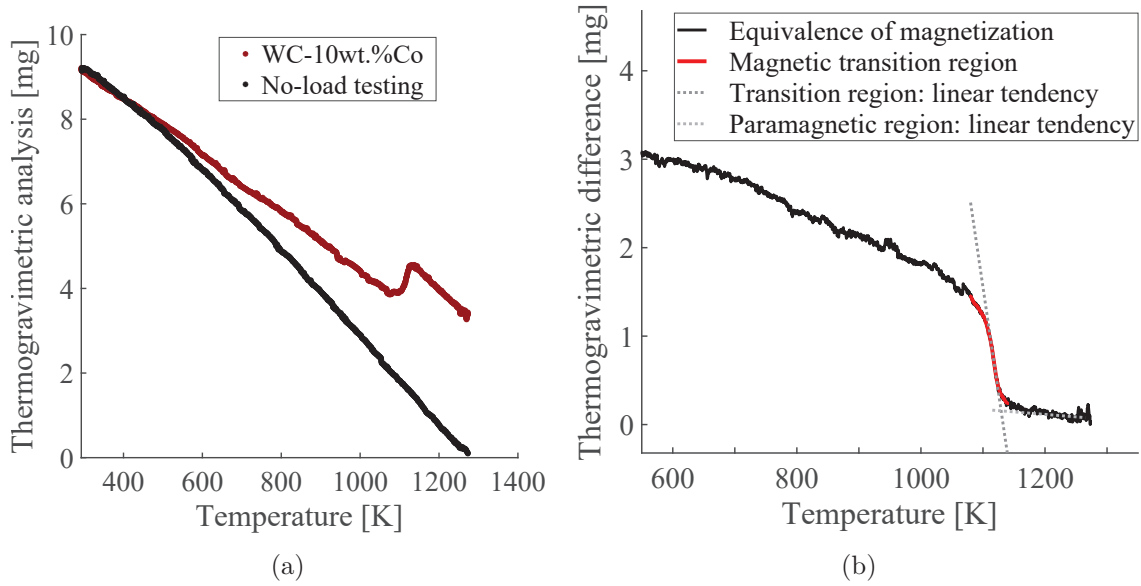


Figure 3.30: Thermogravimetric analysis of the magnetic behaviour of WC-10wt.%Co. (a) Mass variation with and without cemented carbide specimens measured on thermobalance. The result without specimens defines the reference. (b) Difference in mass variation between WC-Co and its reference defining a magnetisation equivalence. The intersection between the high-temperature paramagnetic behaviour and the transition zone determines the Curie temperature of $1130.0 \pm 10.0 K$. These results were not repeated.

3.5.2 Effect of magnetisation on microstructural relaxation

The magnetic origin of the relaxation peak P2 was investigated by a comparative study. Internal friction spectra were measured on a WC-10wt.% Co specimen between 700K and 1200K at a frequency of 50 mHz. This specimen was either or not under magnetic influence. The advantage of working at low frequency is twofold. It allows the relaxation peak to be observed in its integrality as its maximum is shifted towards low temperatures compared to measurements at 1Hz. The temperature position of the peak being therefore around 1090K, it finds itself below the Curie temperature observed by thermogravimetry.

Two cases were considered. Firstly, the influence of polarization on the material was tested. A specimen of WC-Co, polarised longitudinally (along the torsion axis) on a strong 0.5 T magnet, was mounted in the inverted torsion pendulum after polarization. The internal friction spectrum was then compared to a spectrum previously measured on the same non-polarised specimen. Secondly, the influence of an external magnetic field was tested by comparing measurements with and without an applied magnetic field. For this purpose two permanent magnets were mounted on the exterior furnace chamber containing the torsion rod (see Figure 2.20). The two magnets, each 0.35 T (centre value), induce a 0.015 ± 0.005 T field at the centre of the torsion pendulum. The resulting spectra comparisons are shown in Figure 3.31 and 3.32 respectively.

No noticeable difference for the Internal Friction peak P2 is found either for the polarized sample or for the sample under the influence of an external magnetic field. Some annealing effects were, however, observed. In Figure 3.31, annealing at 1200 K induces a marked increase in the peak maximum temperature from 901 K to 922 K. However, this change

was expected as explained in Section 3.3.2. In Figure 3.31 and 3.32, slight annealing effects are also visible on the relaxation peak P2 causing a shift to higher temperatures of the peak maximum (a few kelvins). There is therefore no visible magnetic effects on the cobalt relaxation at high temperature, even if the variation of the relaxation time corresponding to the Curie temperature seen in Figure 3.24 and 3.30(b) supports this hypothesis. It is likely that the field we could apply to the specimen was too low to produce an effect. It is also possible that the polarization could not introduce any effect either. In fact, when an external magnetic field is applied, it was expected to observe a change in the whole spectrum due to energy dissipation by Eddy currents. In fact, a perfect superimposition of the spectra was observed.

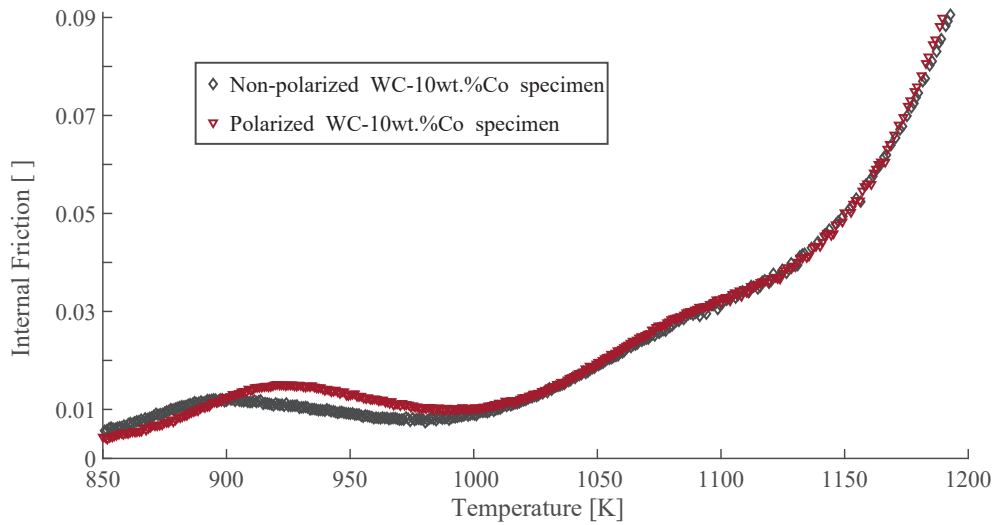


Figure 3.31: Comparative study of the effect of polarization by mechanical spectroscopy. The same sample is measured according to whether it has been polarised longitudinally or not. No effect on the relaxation peak P2 located at 1095K is visible.

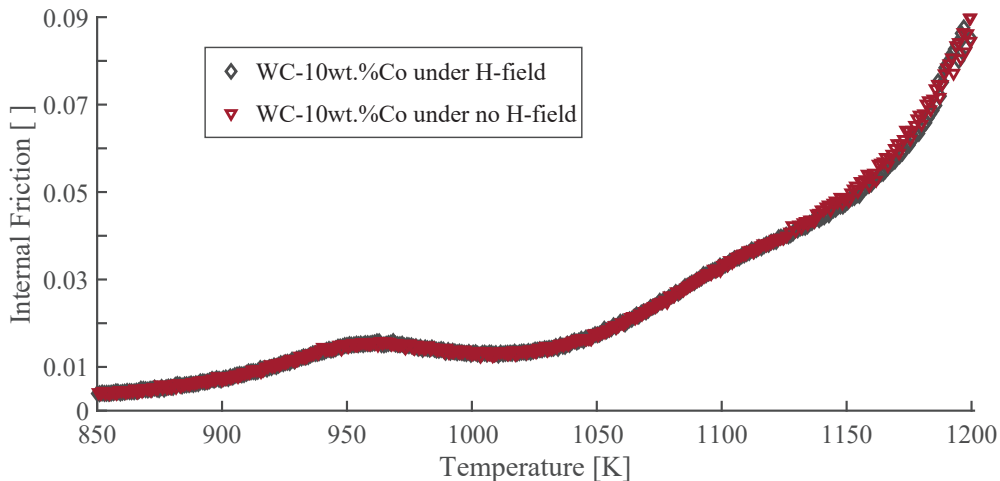


Figure 3.32: Comparative study conducted by mechanical spectroscopy of the effect of an external magnetic field of approximately 0.015 T on a WC-10wt% Co sample. The same specimen is measured according to whether it is under the influence of the magnetic field or not. No effect on the relaxation peak P2 located at 1095K is visible.

3.6 Transmission Electron Microscopy Study

This Section aims at identifying the microstructure of WC-Co by transmission electron microscopy. The aim is to understand the mechanisms which could be at the origin of the physical properties observed in the previous parts of this work. The interest is mainly focused on the cobalt phase, since initial observations show that it plays a preponderant role in the mechanical properties and performance of WC-Co.

It is well known that the possible crystalline structure of the cobalt are hcp and fcc. For pure cobalt, a transition from hcp to fcc is found at around 700K [26]. The difference between these crystalline structures can be represented by the formation of a stacking fault every three dense planes resulting in a hexagonal structure. The literature specifies well what could be the defects observed in the cobalt phase of cemented carbides [26, 130, 132, 36, 37, 27]. In WC-Co, cobalt with an fcc type structure is expected. The microstructure should contain stacking faults, areas of hexagonal structure, partial or perfect dislocations and twins.

Although the deformation mechanisms of fcc metals can sometimes be associated with twinning [155], previous studies on cemented carbides and cermets have highlighted the role played by dislocation movement in the binders and in the WC skeleton below 1050K [39]. In such previous study no areas of twins were found in the binder phase, but rather areas containing stacking faults bordered by partial dislocations before and after deformation. These stacking faults are the result of dissociation of perfect dislocations into partial dislocations. This dissociation is due to the low stacking fault energy of the fcc phase which is 13.5 mJ/m^2 around 800K and 18.5 mJ/m^2 around 1000K [156]. It therefore increases in fcc materials with the temperature and start to favor perfect dislocations. In hcp materials, this stacking fault energy is found to be 31 mJ/m^2 at room temperature [156]. This prevalence explains therefore the high stacking faults density observed so far in WC-Co materials.

On the basis of these considerations, two approaches were pursued. Firstly, TEM observations at ambient temperatures were carried out to establish the structural and microstructural origin of the variations observed by mechanical spectrometry on the specimens of this study. In particular, it was found that the internal friction peak P1 observed on these specimens showed perfect repeatability, whereas successive anneals tended to suppress this peak in previous studies [11, 131] (see Section 2.7.4). Secondly, a series of in-situ TEM observations between 550K and 1100K were carried out in order to determine the high-temperature dynamics of the defects contained in the cobalt phase. These results are reported in the following sections.

3.6.1 Microscopic study at room temperature

The samples used for TEM investigations at room temperature are WC-10wt.%Co cemented carbides previously tested by mechanical spectroscopy up to 1050K. A lamella of the material was cut and thinned using a Focused Ion Beam (FIB) technique, in a Zeta FIB column from Zeiss. As enormous residual stresses exist within the composite, the thinning of the FIB lamella was therefore stopped as soon as the first bending of the material appeared.

It is essential to maintain the state of internal stresses and to disturb to the least extent the microstructure present in the cobalt phase surrounded by the carbide grains. This methodology still ensured sufficient electron transparency for the TEM analysis on a FEI Talos with a 200 kV acceleration voltage. A standard double-tilt sample holder was used in the TEM.

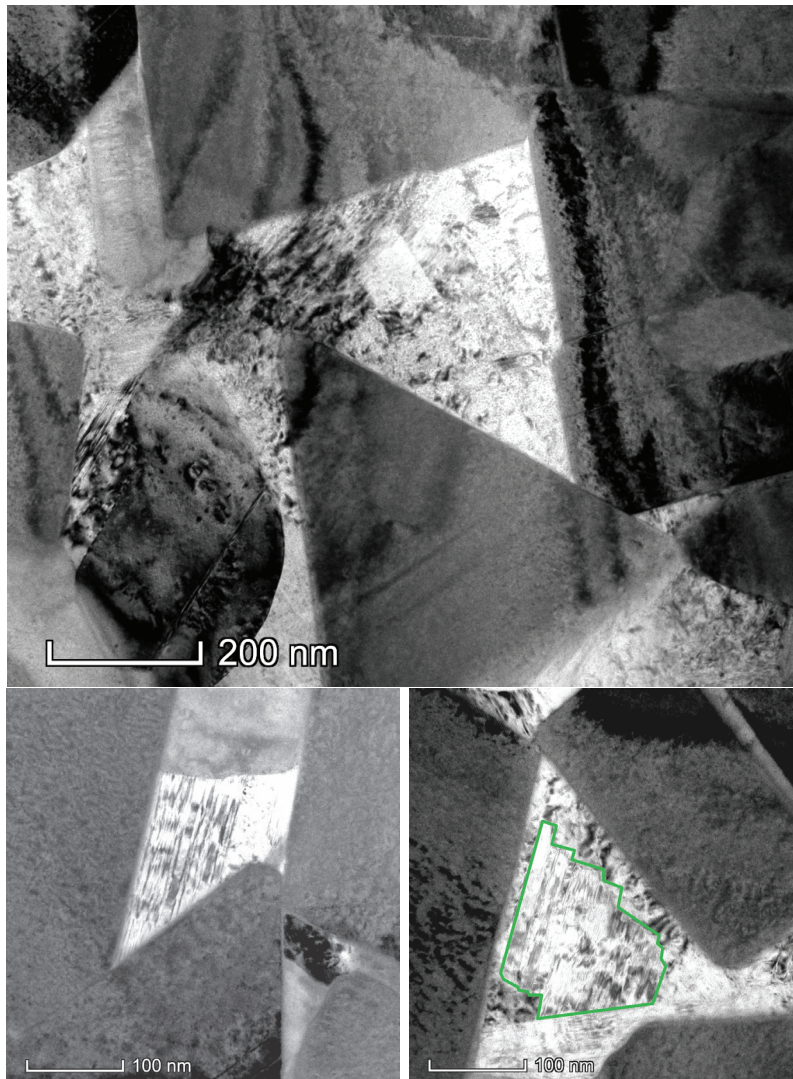


Figure 3.33: Examples of the microstructure of the cobalt phase in a WC-10wt.%Co observed by TEM in brightfield mode at room temperature. The specimen was previously tested by mechanical spectroscopy up to 1050K. The cobalt phase can be seen in light contrast and the WC phase in dark contrast. Cobalt nanodomains misaligned with respect to each other containing nano-twins are visible. The example of a nanodomain is highlighted in green in the third micrograph.

The Figure 3.33 presents representative micrographs of the cobalt phase in WC-10wt.%Co made at room temperature. Three micrographs of cobalt zones are shown in brightfield mode, with the cobalt phase in light contrast and the WC phase in dark contrast. These TEM observations reveal that the Co phase is not present in the crystalline form usually found in cemented carbides. While cobalt grains of several tens of micrometres in size with a long order fcc phase containing a dense network of stacking faults forming hcp monolayers

were expected, cobalt is here present in the form of polycrystalline nanodomains with an fcc structure. These nanodomains are twinned with respect to each other, which blocks this particular structure. The size of these nanodomains is comprised between 50 nm and 100 nm. In addition, a high density of nano-twins was observed. The cobalt twins are identifiable by contrast through the long, parallel streaking patterns formed within the nanodomains. The twins width is of the order of several nanometers. Those microstructural defects are present even if the specimen has been annealed at 1050 K. Their stability would therefore be ensured by the excessive energy required for their recombination.

The streaks observed in the cobalt phase of the Figure 3.33 could also have corresponded to stacking defects forming monolayers of hcp structure. However, their identification as twins in a fcc cobalt structure was confirmed by a Electron Diffraction Pattern (EDP) reported in Figure 3.34. In particular, double diffraction spots (encircled in the EDP) are the characteristic feature of twins in the crystalline structure.

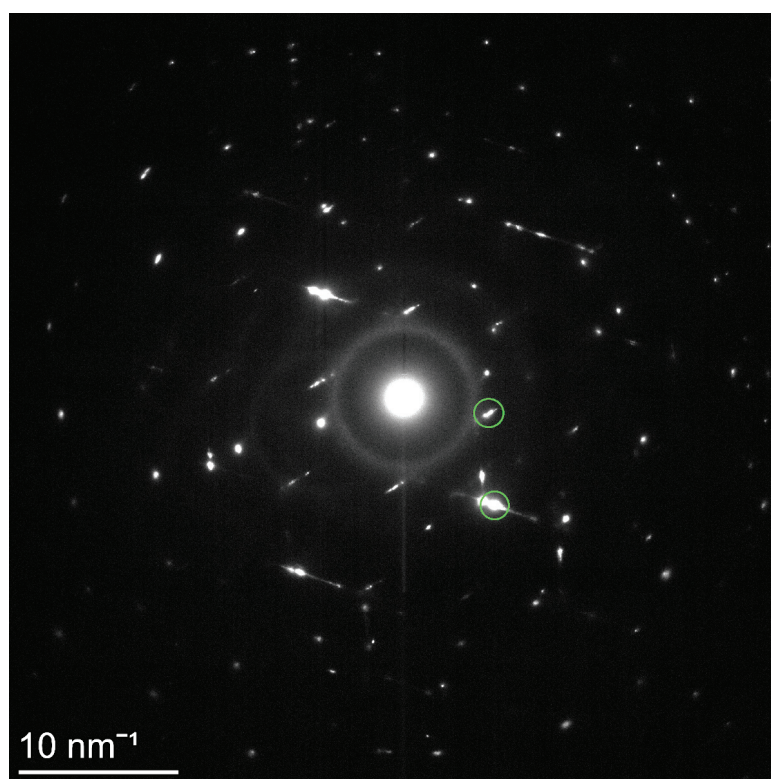


Figure 3.34: Electron Diffraction Pattern (EDP) of a cobalt grain. Diffraction spots corresponding to the fcc phase are observed with in particular a double diffraction spot characteristic of the presence of twins in the crystal structure. Double diffraction spots are encircled in the EDP.

A complete analysis of a Cobalt grain is presented in Figure 3.35. Observations in brightfield mode are presented in Figure 3.35(a) and with a weakbeam technique in (b) which allows a better distinction of the microstructure defects. In 3.35(c) and (e) the Electron Diffraction Pattern (EDP) of the cobalt grains is presented. The darkfield mode micrographs given in 3.35(d) and (f) are obtained from the encircled Selected Area of the corresponding Electron Diffraction Pattern (SAED), respectively (c) and (e). The selection of the diffraction spots thus highlights the twins defects by a strong contrast. The misorientation between the cobalt nanodomains is also clearly shown.

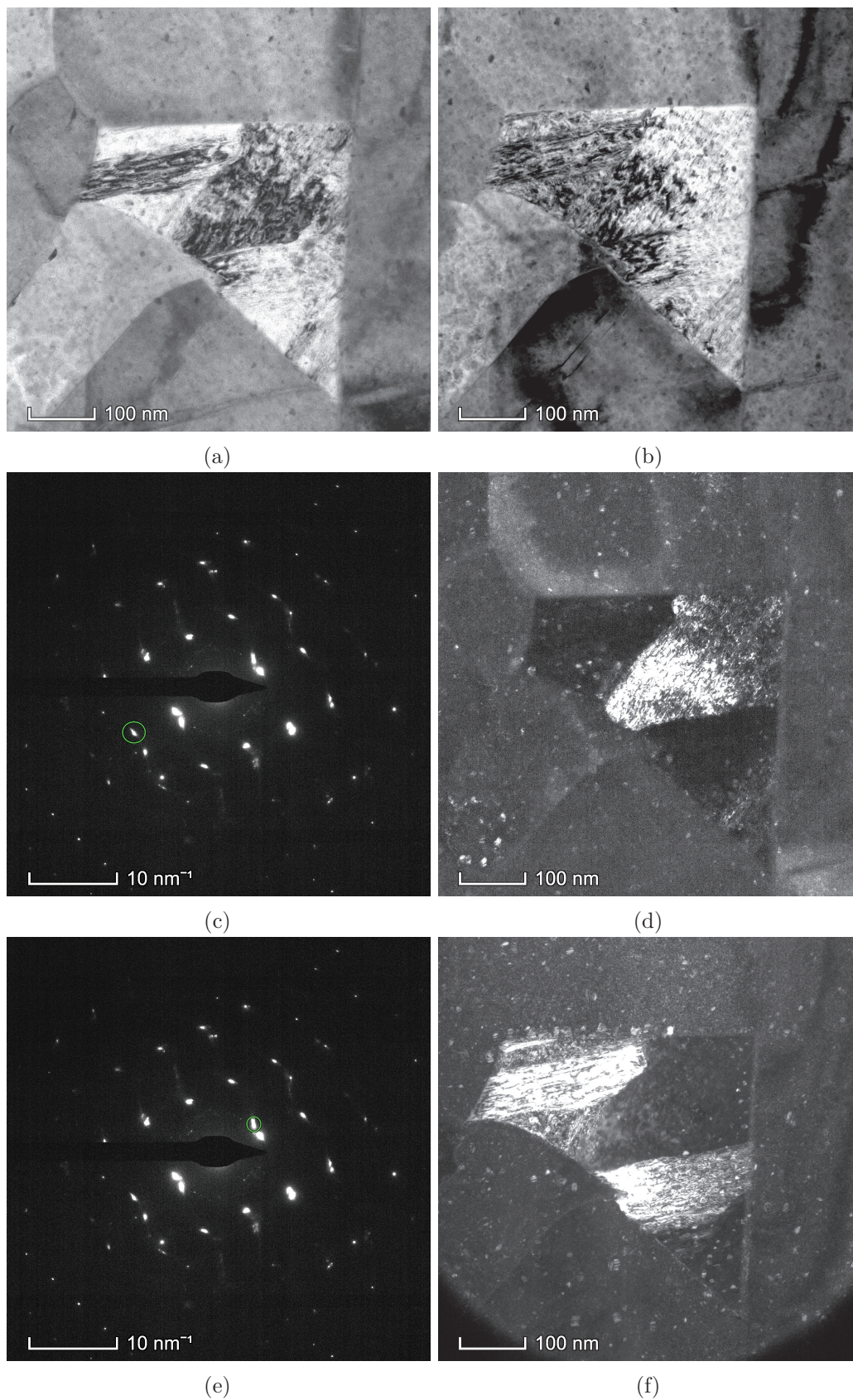


Figure 3.35: TEM analysis of the microstructure of a cobalt grain in a WC-10wt.%Co (a) Micrograph in brightfield mode (b) Micrograph in weakbeam mode (c)-(e) Electron Diffraction Pattern of the cobalt grain (d)-(f) Micrographs in darkfield mode corresponding to the encircled Selected Area Electron Diffraction Pattern (SAED) of (c) and (e) respectively.

3.6.2 In-situ microscopic study at high temperature

The high temperature in-situ TEM observations allow to track the movement of the microstructure defects in the cobalt phase when increasing (or decreasing) the temperature. The phenomena observed correspond to the detwinning in the cobalt nanodomains, and to the formation of a long order phase of fcc structure.

This experiment was performed with the help of a heating sample holder which, however, only incorporated a simple tilt. The observations were continuously recorded on the TEM computer program to produce videos of the microstructure evolution.

The micrographs of Figure 3.38 were generated by using one of the spots associated with a twin barrier in dark field. One of the twinning spots was selected for the entire in-situ experiment. The bright-dark contrast visible on the micrographs is associated with the internal twins of the cobalt grains corresponding with the diffraction spot.

The microstructure remains stable from 550K to approximately 700K. At 735K, the first detwinning processes at small scale were observed and continued to accumulate at low rate until the creation of detwinned zones clearly visible at 916K (see Figure 3.38(b)). No movement of wide detwinning fronts is so far observable, the detwinning process takes place by accumulation at fixed locations.

The detwinning can take place either by the formation of jogs or ledges since two different types of fcc twins exist: the (111) type or the (211) type [155, 157, 158]. The ledge corresponds to a (211) type twin in the cobalt of fcc structure, it is a semi-coherent twin. The jog corresponds to a (111) type cobalt fcc twin, it is a coherent twin. They are associated with different partial dislocations and different energies. The (211) semi-coherent twin have a higher associated energy, implying that ledges are of a more unstable and more mobile nature. A detwinning process associated with ledge formations is considered here. This is motivated by the observation of the detwinning angles. Abrupt angles of approximately 90 degrees are formed between the detwinning interface and the twin lines. It would therefore correspond to an interface that implies the presence of partial dislocations. For instance, perfect dislocations would not create such angles.

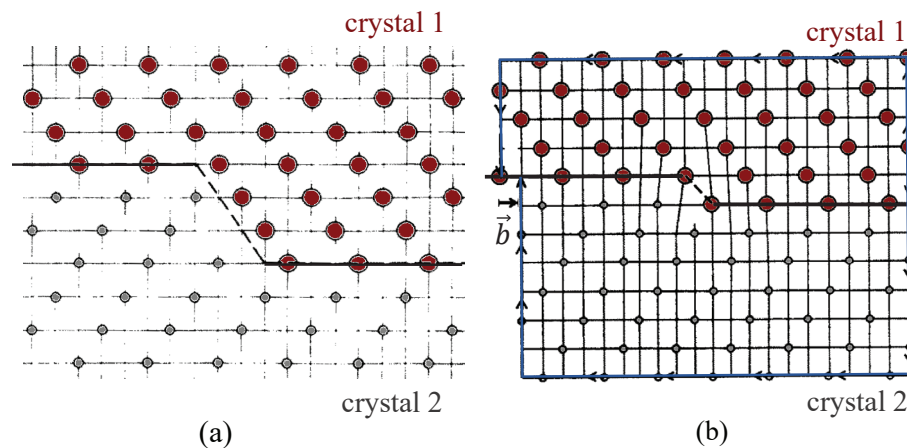


Figure 3.36: Schematic of ledge formation by a Schockley dislocation in a twin boundary. The burger vector \vec{b} is shown in black. A solid black line indicates the twin line and a dotted line indicates the ledge. (a) Close view of the ledge. (b) Nucleation of a ledge with a Schockley partial. Illustrations adapted from [159] with permission from Elsevier.

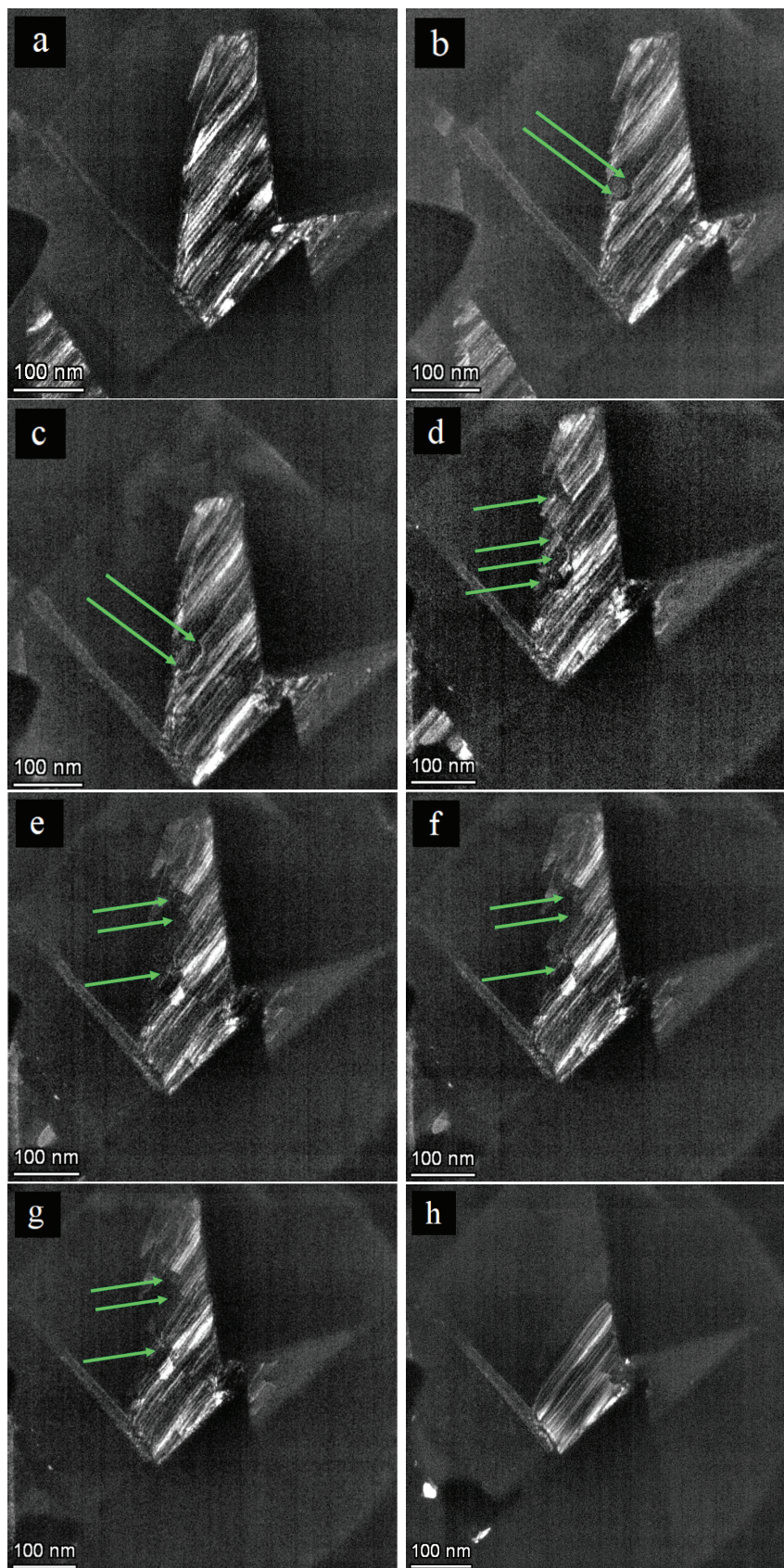


Figure 3.37: Evolution of a cobalt grain in a WC-10wt.%Co between 700K and 1020K showing a detwinning process. Darkfield mode micrographs obtained from a selected area aperture placed on the twinning diffraction spot at various temperature: (a) 695K (b) 916K (c) 950K (d) 984K (e) 1000K (f) 1001K (g) 1002K after a dwell of two minutes (h) 1017K. Detwinning fronts are highlighted by arrows in the micrographs.

At around 916K, small movements of the interfaces formed by the partial dislocations associated with ledges are visible. These ledge movements tend to accelerate around 950K (see Figure 3.38 (c)). The movement of the ledges then continues to accelerate and reveals entire zones of fcc cobalt without nano-twins, as can be seen at 1000K in Figure 3.38 (e). At this stage, the increase in temperature of the specimen was stopped for about ten minutes to allow the microstructure to rearrange and find a equilibrium. It appears that most of the cobalt zones were detwinned except for a visible nanodomain in Figure 3.38 (h). This nanodomain containing nanotwins thus remained stable up to approximately 1017K.

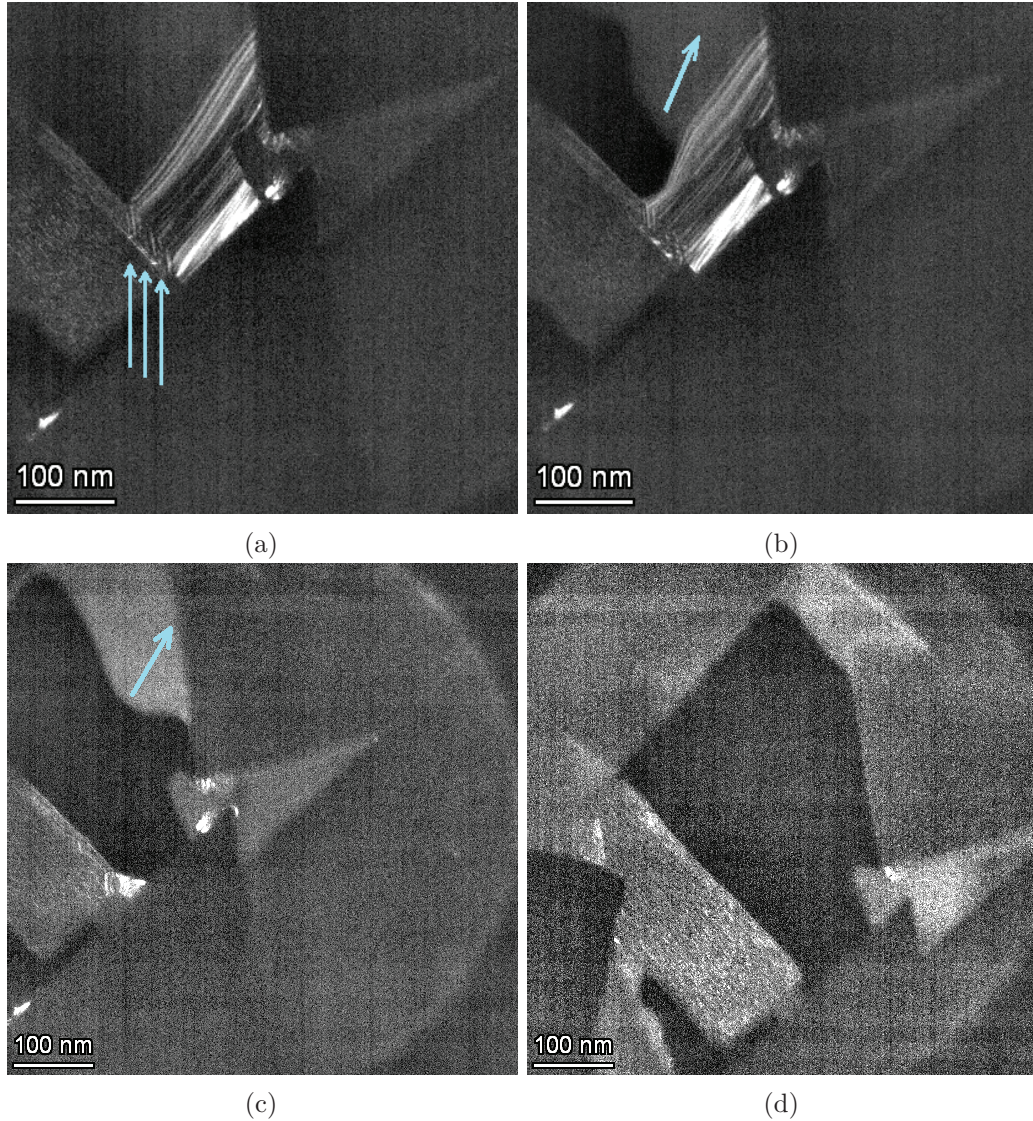


Figure 3.38: High temperature micrographs of a cobalt grain showing a microstructural rearrangement at the grain boundary and grain rotation. (a) Last cobalt nanodomain containing twins at 1040K, showing an accumulation of partial dislocations at the grain boundaries. The stacking of defects at the grain boundaries is indicated by arrows. (b) At 1041K, starting point of the cobalt grain reorientation originating from the grain boundary. (c) Further rotation of the cobalt grain at 1047K visible by the contrast change. The dynamics of the movement is shown by an arrow. (d) Fully fcc cobalt grain at 1090K.

Temperatures between 1020K and 1100K correspond to a microstructural rearrangement taking place at the grain boundary between cobalt and WC grain. This evolution is illustrated in the micrographs in Figure 3.38. Between 1020K and 1040K, it can be observed that defects are piling up and organising themselves at the grain boundary of the last cobalt nanodomain containing twins. As they accumulate, the defects are incorporated within the cobalt grain boundary. This accumulation of partial dislocations at the grain boundaries is made visible by arrows in the Figure 3.38(a). What we see here is an accumulation of partial dislocations at the grain boundaries along a specific glide plane.

At the grain boundary, there is free volume since it is a high angle grain boundary. Therefore the grain boundary can incorporate the partial dislocations, which would create a more stable structure. Even it is less stable than the coherent twin boundaries, the structure pumps partial dislocations at the grain boundary and lowers its energy. On the Figure 3.38(b) and (c), the cobalt grain is mainly detwinned and the defects are visibly organizing its boundary until it rotates completely the whole crystal by "remitting" dislocations from the boundary that form the most favorable orientation. Such dislocation emission causes a grain rotation. On the TEM, the reorientation is visible because of an abrupt contrast change and because of the change of the diffraction conditions. Energetically, this process can be explained by the accumulation of the partial dislocations at the grain boundary, which makes locally a higher strain energy. This strain energy is originating from the detwinning process, and accumulated at the grain boundary. It is similar to a recrystallisation. It is not proven by diffraction, but by a contrast change and by the change of the diffraction conditions.

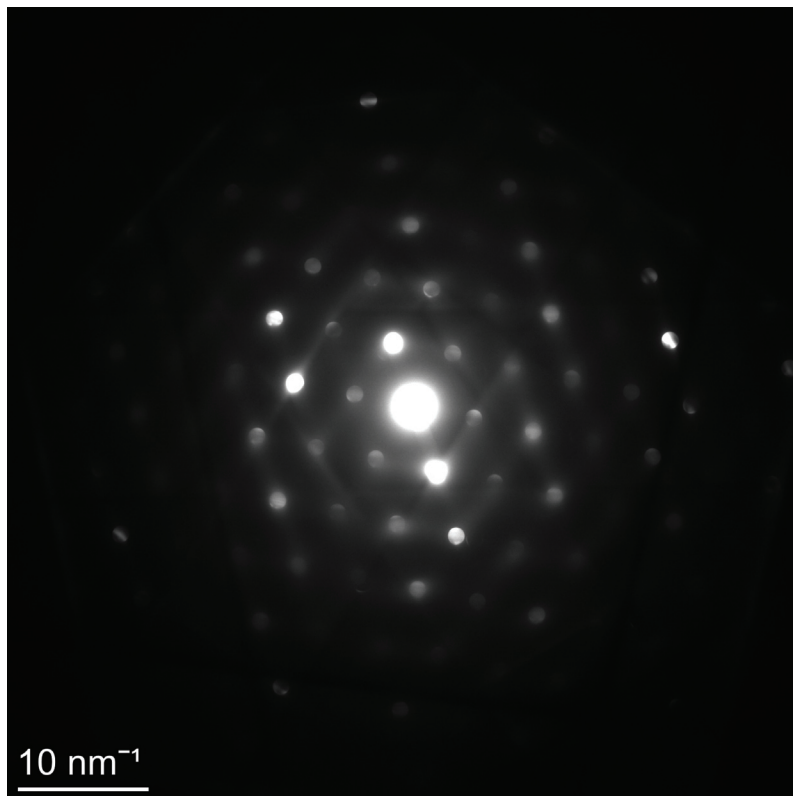


Figure 3.39: Nanodiffraction of a cobalt zone at 1100K. The diffraction discs are showing a fully fcc structure without double diffraction spots.

These observations could be reproduced on a second specimen of WC-10wt.%Co, and concordant results were obtained. These second observations were carried out with the aim of determining whether the motion of the defects created by detwinning was reversible as it seems to be indicated by mechanical spectroscopy. As a reminder, the relaxation peak P1, corresponding to cobalt structural defects, remains perfectly reproducible between 700K and 1050K (c.f. Section 3.3.2). During the in-situ TEM study, it was therefore decided to stop the temperature rise, stabilize the material at 850K and later decrease it back down to 700K. At 850K the first detwinning fronts had already started to move and were stabilised. When the temperature was lowered, it was possible to confirm that the detwinning process was indeed reversible on a significant number of detwinning fronts, although some of them remained stable despite the drop in temperature. These results are consistent with the repeatability of the relaxation peak P1 observed by mechanical spectroscopy.

In this second experiment, the temperature was finally also raised to 1100K, and the observations were consistent with the first experiment. Furthermore, at high temperature, the crystal structure of the cobalt zones proved to be completely fcc, as shown in the nanodiffraction pattern in Figure 3.39. TEM studies therefore do not reveal the usual long-range ordered fcc crystal structure of the cobalt in this specimen. Only short range order characterized by twinned cobalt domains containing nanotwins were observed. However, the diffraction observations exhibit the same average high-temperature fcc structure in the low temperature state.

4 Discussion

This chapter presents an overall analysis of the observations illustrated in Chapter 3. First of all, the mechanisms responsible for the mechanical behaviour of cemented carbides as a function of temperature, that are crucial for the performance and durability of cemented carbide cutting tools, are highlighted.

The changes in the microstructure of the material are evidenced by the various tests carried out on cemented carbides as a function of temperature: mechanical spectroscopy studies, microscopy and investigations of the magnetic properties of the material.

The highlight of this thesis is then discussed, i.e. the association of the internal friction peak P1 with a strain-glass transition linked to the formation of a peculiar structure determined by nano-twins. The influence of a disordered frozen state within the cobalt phase on the mechanical properties and on the wear resistance of WC-Co in cutting conditions is finally addressed.

To complete this work, generalities on some industrial development trials carried during this work will be presented as well as some research perspectives.

4.1 Essential concepts of this study

During machining processes, cutting tools are exposed to extreme temperatures. The rake face, which is subjected to severe friction (see Figure 2.2) sees the temperature of its cutting edge increase to values between approximately 920K and 1550K [79]. And even though only the first few tenths of a millimetre of the cutting edge reach such temperatures, more distant parts are also subjected to high temperatures between 570K and 700K [79].

The deformation behaviour and the mechanical properties of WC-Co cemented carbides are proven to be temperature dependent [9, 27, 37, 38, 160]. There are several evidences of a link between the evolution of mechanical properties and the tool life of the cutting tools [37]. In particular, it can be observed that the fracture of cemented carbides is linked and accompanied by plastic deformation [161]. A model of the origin of plastic deformation and microstructural dynamics is therefore essential to control the performance of cemented carbides for machining applications.

From the various works mentioned above [9, 27, 37, 38, 160], it can be inferred that the behaviour of cemented carbides is divided into three temperature ranges between 300 K and 1500 K :

- (I) Low temperature domain with approximately $T < 800K$. Elastic deformations followed by brittle fractures are observed.
- (II) Medium temperature domain with approximately $800K < T < 1100K - 1200K$. This region corresponds to a tough behaviour, while limited plastic deformation occurs.
- (III) High temperature domain with approximately $T > 1100K - 1200K$. In this region, increased plastic deformation is observed. It corresponds to creep.

This indicates that the medium temperature range is particularly suitable for machining with cemented carbides. In this temperature domain, brittle fracture caused by low temperatures is avoided and no severe plastic deformation is observed. These three domains of mechanical behaviour can be advantageously explained by the microstructure of the cobalt binder and by its evolution [132, 28, 39, 162]. These studies show that the cobalt microstructure consists at ambient temperature of long-range order fcc phase containing a large quantity of hcp stacking faults. These stacking faults are bordered by partial Shockley dislocations and constitute blocked networks, which drastically increase its yield strength [27]. At low temperatures up to 800K, the material thus becomes hard but brittle: no plastic deformation can be observed, only elastic deformation followed by fracture [9]. A model of crack propagation developed by Sigl and Fischmeister [82] shows the importance of cobalt in reducing crack propagation within cemented carbides. Due to the composite nature of the material, four fracture trajectories are to be considered: through the binder, near the binder/carbide interface, along the carbide grain boundaries, transgranular trajectory in the carbide [82]. It has been observed that cracks propagate within the ductile phase of the binder and along the carbide-binder interfaces, starting from brittle pre-cracking of the carbide phase. As with the tearing of glued parts, the voids generated by the crack are maintained by the formation of cobalt ligaments. These multiligaments thereby act as bridges, which support the traction acting between the crack faces. The ligaments are thus the last elements that hold the structure together before the crack propagates further. In this way, cobalt also makes a major contribution to the tensile strength of WC-Co.

In the 800K to 1100K-1200K range, as the temperature rises, the stacking fault energy increases [156] and some partial dislocations become mobile. Two internal friction peaks have been observed in the literature. The work of Ammann [129] reported the existence of an unstable peak, which shifted at higher temperatures. It would correspond to the relaxation peak P1 of this work. A peak located at around 1200 K is observed in several works [163, 131], and has been attributed to the dragging of W solute atoms by partial dislocations. This interpretation was justified by an activation energy corresponding to this IF peak of 2.5 eV/atom [28]. Effectively, such value corresponds to the diffusion energy of tungsten in cobalt (see table 3 in the Introduction Section). The mobility of these microstructure defects therefore explains the appearance of the plasticity of cemented carbides with temperature. This highlights the favourable development of the cobalt microstructure for the mechanical properties of WC-Co.

Three-point bending tests on the hard WC-Co skeleton were carried out on samples in

which the metal binder had been removed from the material by chemical etching. It was then possible to demonstrate that this temperature range corresponds to an elastic deformation for the hard skeleton. The mid-temperature range therefore corresponds to a material that is tough mainly due to the cobalt binder.

In the high temperature domain, the dislocations contained in the cobalt can move freely once the temperatures of the two internal friction peaks are overpassed. The metallic phase is thus characterised by a high ductility. However, the deformation of the cobalt phase is supplanted by that of the hard phase of cemented carbides. The high temperatures are in fact characterised by a decohesion of the WC grains and by grain boundary sliding [9, 39]. In particular, the formation of cobalt lamellae is observed at the WC-WC grain boundaries, with the notable exception of the WC-WC $\Sigma 2$ grain boundaries whose cohesion is maintained [39]. The presence of these lamellae proves that the grain boundary sliding is driven by cobalt infiltration. However, these mechanisms are harmful as they allow plastic behaviour for the overall composite. Therefore, creep is observed.

In addition, the dislocation pile-up also acts as a precursor for crack formation in WC-Co [83, 164]. These cracks can then lead to a critical failure of the material [83, 164]. The resistance to crack propagation is then designated by the critical stress intensity factor K_{IC} .

Two to three stages are generally considered in total: crack initiation on defects, followed in some cases by crack growth, and then finally catastrophic crack propagation [83, 165, 164, 82, 166]. This behaviour is also temperature sensitive. In particular, the growth of cracks can be observed with increasing temperature on creep tests [167].

The coatings also play a fundamental role for cutting applications [8, 84]. The properties of coatings for cemented carbides are mainly influenced by three factors: the chemical composition of the film, its structure, and its adhesion to the substrate core materials. These factors control the hardness at room and elevated temperatures of the coating, as well as its chemical and thermal stability. In this way, the coating prevents from failure mechanisms such as adhesion, oxidation, abrasion and diffusion [8].

4.1.1 Evidence from the initial comparative study

The comparative study of the performance of coated cutting tools yields an analysis of the influence of critical parameters on the tool-life of cutting tools measured under extreme conditions by shock tests:

- Nanoindentation tests, residual stress measurements of the different coatings, tribological tests were conducted. None of those values showed a direct correlation to the values of the tool-life. See Figures 3.4 to 3.6, 3.10, and 3.4 to 3.6, respectively.
- As shown in Figure 3.9, an indirect link can be drawn between the thickness of the coatings and the cutting tool-life. It turns out that - generally - the thinner the PVD layer is, the better is the machining performance. One can also observe that multilayered coatings have their performance that surpasses the bi-layered one. This demonstrates the importance of the architecture for coating materials.
- Another study was conducted by Mechanical Spectroscopy (MS). Coated and uncoated

cemented carbide with different cobalt concentrations WC-6wt.%Co and WC-10wt.%Co have been compared. In the 1 Hz frequency range, a mechanical damping peak related to the cobalt phase is detected at 925-950 K. It is observed (see Figure 3.11) that this damping peak is systematically shifted to lower temperature for samples where the thin film is deposited. Interestingly, this peak shift is correlated to the tool-life: the greater the peak shift, the longer the tool-life, demonstrating a direct link between the tool-life, a macroscopic property, and the damping capacity of the material, a microscopic property.

4.1.2 Overview

Based on the results of the comparative study and the general knowledge provided by the literature presented above, it appears that three main factors are responsible for the mechanical properties of cemented carbide cutting tools:

1. The coating of the cutting tool. In this study, it was observed that multilayer architectures induce longer tool lives than conventional bilayer material coatings.
2. The hard tungsten carbide skeleton. The creep limit of the material is controlled in particular by the decohesion of WC grains and by the infiltration of cobalt at the WC-WC grain boundaries in the form of lamellae. The WC-WC $\Sigma 2$ grain boundaries constitute, nevertheless, an exception. However, the formation of such orientation at the grain boundaries occurs during the sintering process. It was therefore not explored during this work.
3. The microstructure of the cobalt binder as well as its dynamics determines the microplasticity of WC-Co, which is shown to be essential for machining applications.

This thesis aims at establishing a model of the mechanical behaviour of the binder of cemented carbides, which is linked to the crystal structure and its dislocation and extended defect dynamics.

4.2 Cobalt microstructure in cemented carbides

The analyses of the microstructure and its evolution for WC-Co presented in previous studies (Section 4.1) could only be confirmed in part and new aspects of the cobalt behaviour appear in this study. The material used in this work revealed a cobalt microstructure in many points different from that presented in the literature. The essential characteristics of this microstructure are presented here.

The Electron Diffraction Pattern (EDP) of a cobalt grain shown in Figure 3.34 confirms that the cobalt phase has an fcc structure. Within WC-Co, the allotropic transition of pure cobalt from fcc to hcp at approximately 700K is prevented. Two hypotheses may explain the absence of transformation to hcp structure at room temperature: the effects of carbide-induced residual stresses on the cobalt [24] and the presence of solutes formed during sintering. However, the presence of double diffraction spots in the EDP of Figure 3.34 indicates the formation of twins within the cobalt fcc structure.

The cobalt zones identified on the micrographs in Figures 3.33, obtained by TEM in brightfield mode, reveal the presence of cobalt nanodomains. Their size ranges from 50 nm to 100 nm. These nanodomains show a conjugated twin structure.

4.3. Properties and characteristics of cemented carbides as a function of temperature

On the micrographs, it can be observed that these nanodomains contain streaks. These are identified as the nanotwins mentioned above. The presence of these nanotwins therefore indicates the trace of an unachieved or frustrated transformation of cobalt. It is important to note that this structure is characterised by a high thermal stability. The sample used for the TEM observations has been previously annealed at 1050 K in a torsion pendulum.

This particular microstructure, which is composed of nanotwins distributed in nanodomains, limits the deformation mode of the cobalt phase. In the microstructure observed in the above-mentioned work [132, 28, 39], the deformation could be assimilated to a stress-induced transformation from fcc to hcp. An hcp structure has 1 sliding plane whereas an fcc structure has 4. The local formation of hcp phases thus already reduces the possibility of deformation. In our case, the structure is even more blocked, resulting in an even greater deformation limitation. The low-temperature cobalt phase in cemented carbides becomes hard and brittle.

4.3 Properties and characteristics of cemented carbides as a function of temperature

This Section presents a discussion of the in-situ microscopic studies, the mechanical spectroscopic studies, and investigations of the magnetic properties carried out as a function of temperature.

4.3.1 Microscopic characteristics

The microstructural transformation between a low-temperature cobalt phase and a high-temperature phase could be examined by in-situ TEM observations between 500K and 1100K. Two processes could thereby be highlighted. The first one is the detwinning process starting from fixed locations in the material until the creation of detwinning fronts that enter in motion. The second process is the recrystallisation or rotation of the cobalt crystals. This process is related to the accumulation and "re-emission" of dislocations at and from the grain boundaries.

The detwinning process takes place between 735K and 1020-1040K. At 735K the first detwinings are observed. This process leads to the formation of twin free zones, where detwinning fronts are bordering the twinned zones. Such structures are clearly visible at 916K and the detwinning fronts are characterised by small movements. The detwinning process has been attributed to the formation of ledges corresponding to semi-coherent fcc twins of type (211). It is reasonable to interpret them as interfaces of ledge associated partial dislocations.

As the temperature rises up to 950K, there is an acceleration of the interface movements of the partial dislocations associated with ledges. This temperature range corresponds to the internal friction peak P1 observed by mechanical spectroscopy, as shown in Figures 3.13 and 3.19. The damping measured in WC-Co at around 945K for frequencies of 1Hz and 909K at 5mHz can thus be associated with the movement of partial dislocations and detwinning.

As the temperature increases, more and more areas become detwinned and fully fcc. At 1000K, it can be observed that the majority of the cobalt nanograins no longer contain nanotwins. Only certain particularly blocked grains still show some twins.

Between 1020K and 1100K, a second process of microstructural rearrangement is observed, which completes the detwinning. This process is initiated at the grain boundary between the cobalt and the WC grains. At these temperatures, partial dislocations accumulate and organise themselves at the grain boundaries until the strain energy at the grain boundaries is large enough to turn the whole cobalt crystal into a more favourable orientation.

Figure 3.38(c) shows that after 1050 K, the cobalt crystals recrystallize or rotate. This means that once the temperature has fallen back to 850 K, the microstructure has evolved from its initial state, and the state remains more stable for longer at high temperatures. It is indeed observed that annealing at 1050K lowers the internal friction peak P1 from 950K to 920K in Figure 3.16.

However, it has been established by in-situ TEM observations that the detwinning process is reversible. The structure of the cobalt grains therefore does not fall back into a long order fcc state at low temperature. The origin of the reversibility is probably to be found in the presence of high residual stresses within the sintered composite. But, more specifically, the presence of dislocations generated by the detwinning process is needed. This process is elucidated below.

The existence of a cobalt phase characterised by a long order fcc above 1050-1090K as proven by the electron nanodiffraction pattern is shown in Figure 3.39. The presence of this crystal structure thereby allows the dislocations to move more extensively. This region starts at 1050-1090K and continues until the observations of the decohesion of WC grains forming the hard skeleton and the infiltration of cobalt at the WC-WC grain boundaries. This region has been reported as starting at about 1200K-1300K [36, 168, 44].

The observations presented above finally make it possible to present a first redefinition of the domain (II) of mid-temperatures for the mechanical behaviour of the WC-Co in this study:

- IIa Temperature domain with approximately $800K < T < 1000K$ characterized by a reduced plasticity and preserved hardness, where detwinning occurs and where the cobalt nanodomains remain partially.
- IIb Temperature domain with approximately $1000K < T < 1200K$ characterized by a increased plasticity, where the mode of deformation corresponds movement of the dislocations in the fcc cobalt phase.

4.3.2 Microstructural defects dynamics

The dynamics of the cobalt phase microstructural defects could be studied between 300K and 1350K by means of mechanical spectroscopy.

In the Figure 3.16, the evolutions of the relative shear modulus and internal friction are reported for annealings between 500K and 1050K. Both the internal friction spectra and the modulus curves are fully repeatable after these stabilization thermal cycles.

By observing the modulus for the low temperature **domain I** of purely elastic behaviour at $T < 800K$, it can be seen that the modulus is higher at low temperature corresponding effectively to hard and possibly brittle behaviour.

In a first **sub-domain IIa** (between $800K$ and approx. $1000K$), a decrease in modulus is first observed until an inflection point at $920K$ or $930K$ (depending on whether the curve corresponds to the first annealing or not). It corresponds to a slight softening of the material. After this first inflection point, the modulus curve continues monotonically over a few dozen Kelvin before a second inflection point at $975 K$ or $1000K$ (whether the curve corresponds to the first annealing or not).

Then begins a second **sub-domain IIb** (between approx. $1000K$ and $1200K$) marked by a more consequent drop in the shear modulus, which becomes increasingly significant as the temperature rises. The material softening increases. This observations corresponds well for the Domain II to an overall increase in toughness and the beginning of plastic behaviour for the WC-Co material.

In Figure 3.21 showing also IF spectra and relative shear modulus curves between $500K$ and $1050K$, a separation of the spectra as a function of their torsional frequency is visible, corresponding to thermally activated relaxations at higher temperature. This is a clear indication that the observed softening mechanism is related to a relaxation mechanism.

For the **domain III**, the relative shear modulus decreases, which then continues at high temperature/low frequency. This trend is in good agreement with the high relaxation strength at high temperature and corresponds to the region of creep behaviour.

It was clear that both Internal Friction peaks P1 and P2 are related to the cobalt phase of the material as shown in Section 3.3.1. Examination of the in-situ TEM results clearly shows that the temperature domains of the detwinning processes first, and secondly of the appearance of a long range ordered fcc phase in the cobalt correspond to the damping peaks P1 and P2 respectively.

The relaxation peak P1 is therefore linked to the unusual microstructure of the low temperature cobalt phase. The damping corresponds to the movement of partial dislocations associated with ledges and forming detwinning fronts. The partial dislocations were not, however, observed directly by TEM, but represent prime potential candidates. The reversibility of the detwinning process observed by in-situ TEM explains the repeatability of the P1 peak, which has never been observed in previous work [129]. The relaxation peak P2 should be associated with the movement of partial Schockley dislocations in an fcc phase no longer forming nanodomains. The presence of this peak, instead of an exponential increase in internal friction, reveals the existence of pinning points interacting with the dislocations. These may possibly be precipitates within the cobalt. An increase in temperature would induce a depinning and a softening of the material.

In the temperature range of the peaks P1 and P2, the energy dissipation is still dominated by the amplitude of the internal friction peaks. This temperature domain is followed by an exponential increase of the damping background, which becomes dominant for the internal friction amplitude. In the mid-temperature range, the presence of the two damping peaks P1 and P2 increases the ability of the cobalt binder to relieve strain throughout the material. This improves the overall toughness of the material compared to its low-temperature state.

At $T < 800\text{K}$, the amplitude of internal friction, and therefore of energy dissipation through the motion of microstructural defects, remained very low. At $T > 1200\text{K}$, the ever-increasing internal friction leads to creep for the composite. In fact, this is the flank of the peak P3 related to WC-WC grain boundary sliding.

Further analysis of the peak parameters presented in this work have highlighted important features regarding the interpretation of the damping peak P1:

1. The internal friction peak P1 appears to be **thermally activated** as shown in Figure 3.19. However, its examination by the Arrhenius model does not provide physically interpretable results, for instance, a relaxation time limit far too low and an activation energy too high to correspond to any process possibly occurring in cobalt. A better description of the thermal activation of the relaxation process is given by the empirical **Vogel-Fulcher-Tammann model** in Figure 3.22 describing a divergence in the relaxation time. By means of this model, physical values can be obtained with, for example, a relaxation limit frequency close to the Debye frequency of $\nu_D \approx 10^{13} \text{ 1/s}$ of a structural defect jump. This model also introduces a Vogel temperature T_0 at which the relaxation time diverges and proves to be very suitable for describing transitions in glass-forming materials [51]. One should notice that a valid Vogel Temperature is close to the hcp-fcc transition temperature of cobalt.
2. It has also been described in the previous Sections 3.6 and 4.2 that the low temperature phase of cobalt below the relaxation peak P1 is characterised by the formation of polycrystals of cobalt forming nanodomains globally fcc, reciprocally twinned, and containing nanotwins. **The low-temperature state is therefore not characterised by a long range order structure.** At high temperature, however, a long-distance ordered fcc cobalt phase is found, certainly containing partial dislocations which can begin to move.
3. Several points highlight the great dependence of the low temperature phase on its thermomechanical history. In Section 3.3.2, the need for several anneals at the high temperature phase to stabilise the microstructure of the material is reported. In Section 3.3.3, the strong T-dot effect on the amplitude of the internal friction spectrum is shown, demonstrating an increase in the time required to establish thermodynamic equilibrium specifically at the relaxation peak.

The investigations reported in Section 3.4 therefore aimed at testing the non-ergodicity hypothesis related to the WC-Co composite. For this purpose the standard zero-field-cooling/field-cooling test (ZFC-FH)/(FC-FH) was applied by cycling from the low-temperature phase to the high-temperature phase. A deviation between two identical measures, but varying in their history, was thus revealed. This observation alone would suffice to demonstrate a break in ergodicity. However, it was pointed out that some caution in interpreting these results was required. The material being a composite formed of two phases under high residual stresses, the variation in the composite plasticity can be complex. Non-ergodicity is therefore not yet completely demonstrated.

These three characteristic points represent the features defining the behaviour of strain-glass materials (see Section 1.2.2). The low-temperature strain glass state would be characterized by polycrystalline cobalt nanodomains containing nanotwins. From a thermodynamic point of view, the low-temperature cobalt phase would therefore be interpreted as an out-of-

equilibrium glass-like state. The glass transition would thus be highlighted by the movement of the defects contained in the frozen cobalt phase observed by mechanical spectroscopy and in-situ microscopy. The detwinning process would allow the cobalt phase to be retransformed into a long range ordered phase enabling microstructural rearrangements at thermodynamic equilibrium. However, care must be taken when interpreting the peak P1 observed by Internal Friction. The damping peak P1 is not purely a transition peak but rather a relaxation peak corresponding to defects released above the transition temperature.

4.3.3 Magnetic properties

This work proposes that the deformation mode above 1050K becomes activated by defects in the fcc cobalt phase. The dynamics of the microstructure between 1050K and 1300K would be characterised by the movement of partial Shockley dislocations which would be able to recombine to form perfect dislocations at higher temperatures. A relaxation peak P2 is generated. Consequently, an increase in toughness and plasticity is expected.

Previous works [131] proposed that the cobalt relaxation peak P2 could be influenced by a para-ferro magnetic transition. According to [153] such magnetic transition would also be responsible for a spinodal decomposition in the tungsten rich cobalt phase. The peak P2 would therefore be associated with the dragging of W atoms by dislocations, the W atoms being in different concentrations in the paramagnetic or in the ferromagnetic phases. The temperature peak position observed would be determined by the associated dislocation free length, which would correspond to the cobalt mean free path in f.c.c. structures of the two phases.

The analysis of the Internal Friction peak P2 in Section 3.3.6 revealed a transition in the associated relaxation time τ . The study of the magnetic properties of cemented carbides showed a transition from a low-temperature ferromagnetic state to a high-temperature paramagnetic state at approximately 1130K: the Curie temperature. This temperature corresponds to that of the observed relaxation time transition. However, further studies by mechanical spectroscopy could not reveal any magnetic influence on the microstructural dynamics of cemented carbides. The intensity of the magnetic fields used was probably too weak.

4.4 Cobalt in cemented carbides as a strain glass

For glass, as for non-crystalline materials in general, the arrangement that characterises atoms, or other structural units, has a short distance order, but no long distance order. Moreover, the glassy states are outside of thermodynamic equilibrium. This has a major impact on their mechanical properties, as it can be observed in the domains of plastic behaviour or behaviour until material failure.

To consider the plastic responses of materials, tensile, compression or shear tests are generally used, restricted to the areas of plastic or viscoplastic deformation. As glassy states can be schematised as frozen liquids with particular thermodynamics, considerations of viscosity can provide valuable insights. For viscosity properties, the ideal Newtonian behaviour would follow Maxwell's model.

For this model, there is a relationship linking viscosity η , shear modulus G and a characteristic time related to molecular mobility τ : $\eta = G \cdot \tau$ [49]. As viscosity is proportional to $\sigma/(d\varepsilon/dt)$, a compression test can reveal its behaviour. Figure 4.1 illustrates the difference, in a compression test, between an ideal Newtonian behaviour and the behaviour observed on mineral or metallic type glasses (non-crystalline solids). There is a clear difference between their behaviour: the stress level at which viscoplastic flow is observed is much lower for non-crystalline materials. This is the result of time of structural rearrangement τ which diminishes when the stress level is high; and the time τ is related to viscosity. Another point that is also observed, for the glass materials, is that stress forms a peak before entering the viscoplastic flow regime. These behaviours are very sensitive to the deformation speed. At a sufficiently high deformation speed, the stress corresponding to the viscoplastic flow plateau for the glasses becomes lower than the conventional yield stress [49].

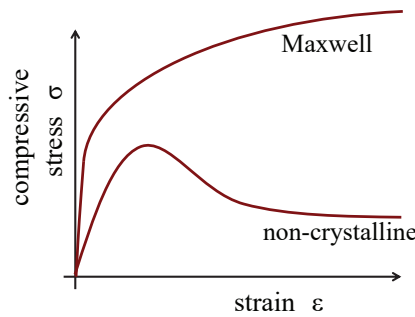


Figure 4.1: Comparison of an ideal Newtonian behaviour and that of mineral and metallic glasses in compression measurement. Arranged from [49].

Considering the case of a glassy material in the composition of a cutting tool, one could think that this characteristic could facilitate the deformation of the material at low temperature and thus increase its propensity to absorb shocks. Less stress being necessary for its deformation. However, this would have omitted the importance of experimental time for glassy materials. In a glassy state, a restoration linked to deformation takes place over a much longer time scale than the experimental time [49]. The presence of a glass state may have a catastrophic impact on cutting tools.

Another important point is the characteristic evolution of the elastic limit (yield stress) σ_e and the ultimate tensile strength σ_r . Perez reports [49] the deformation to failure curve as a function of temperature $\varepsilon_r - T$ for non-crystalline materials (see Figure 4.2). It can be seen that for these materials deformation to failure ε_r evolves rapidly around a transition temperature T_t , with a limit ε_r low at low temperature followed by a strong increase around T_t . Around this transition temperature, it can also be observed that the elastic limits σ_e and the ultimate tensile strength σ_r coincide, whereas below T_t plasticity is prevented by the fact that the ultimate tensile strength σ_r becomes lower the elastic limit σ_e would be.

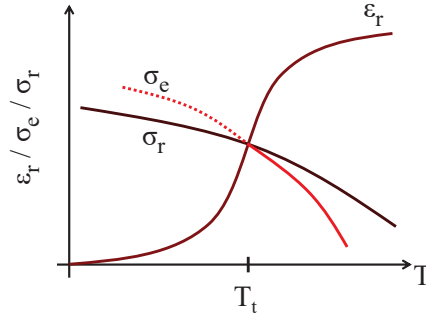


Figure 4.2: Deformation until failure ε_r as function of the temperature for a non-cristalline material. An evolution of the elastic limit (yield stress) σ_e and the ultimate tensile strength σ_r is visible. Arranged from [49].

This type of transition corresponds generally to a so-called ductile-to-brittle transition. This transition is well known for ferritic steels, and can cause many fracture accidents [169, 170]. These catastrophic fractures originate at the level of small cracks. While a material is in its brittle low-temperature state, only minor stresses are necessary to propagate the cracks throughout the material. Depending on whether the material is in its temperature phase, different behaviour will be exhibited when exposed to similar external thermal or mechanical stresses. The negative impact of such a ductile-to-brittle transition at machining temperatures on cutting tool materials is therefore self-evident. Moreover by cycling around this transition temperature, an ageing effect would be promoted. Such cutting materials would for instance be less performant with the use of coolants, which would enfavor the low-temperature brittle material state. Another bulk composite material may be suggested for such applications.

4.4.1 Coating effect

Studies on nanotwinned coppers and their deformation [171] allow us to draw a parallel with the observations made on the low-temperature cobalt binder phase. It is known that copper has an fcc structure similar to that of cobalt. It also has an high stacking fault energy as cobalt. Some interesting observations are reported hereafter.

Copper shows an unusual mechanism of strengthening through the presence of nanotwins. An increase of dislocations has been reported, which is accompanied by a sudden softening at about 180 C. It is inferred that the source of dislocations are the twin ledges. Partial dislocations are forming twin ledges but according to Morris Wang et al. [171] twin imperfections are also source of dislocations. This is highlighted by the fact that no strain hardening is observed but dislocations are well present. Therefore the dislocations source should lie in the twinning process.

Stress-strain behaviour for tensile tests associated with MD simulations show a hardening phenomenon for which twins act as dislocation blockers by forming Lower-Cottrell locks. However, a decrease in stress and a softening behaviour can be observed afterwards in the same experiment. This is explained by the detwinning process through the mouvement of kinks or ledges. This drains the partial dislocation to the grain boundaries. Further, a detwinning is observed after the kinks have been absorbed by the grain boundaries after

migration. It seems that coherent twin boundaries close to grains boundaries are more sensitive to detwinning, as suggested by the migration of coherent twin boundaries induced by the motion of kinks.

By considering the interface between a coating and the bulk material as a grain boundary, a parallel can be drawn between the work of Morris Wang et al. [171] and the behaviour observed for the cobalt microstructure. The presence of the coating would, in this regard, favour detwinning. This vision coincides with the observation of a lowering of the friction peak P1 for coated WC-Co (see Figure 3.11 in Section 3.2.3). A dislocation-based mechanism would induce the opposite behaviour. Indeed, dislocations are attracted to the material with the lowest modulus when an interface between two materials exists. For example, a ceramic coating should repel dislocations from the cobalt to the bulk.

By considering the presence of WC grains and thus additional grain joints, the processes of detwinning and twin absorption at the boundaries are accentuated. In other words the presence of defective twins (ledged) facilitates a mechanism of detwinning favoured by the presence of an interface. In cemented carbides, the partial dislocations standing at boundaries as a product of the detwinning are then the source of plastic yield of the cobalt and the relaxation peak P2 appears. Since these dislocations remain all the time (no dislocation recovery) the twinning mechanism can occur again with those dislocations as sources : therefore the peak P1 is reversible.

This interpretation is greatly interesting for its implications for cutting tools.

4.4.2 Origin of cobalt glassy state

Cobalt is characterized by frozen nanodomains, which contain a high density of nanotwins. The martensitic transformation observed for pure cobalt is replaced by a glassy transition from this disordered low temperature frozen state to a high temperature normal parent state. This transition is induced by the presence of local stresses (residual stresses or point defects) limiting a long-range ordering of strains.

This state would correspond to a brittle glassy state. The origin of this unfavourable material state is to be found in the sintering process, which induces enormous residual stresses from the WC grains and the dissolution of elements in the binder. A possible hypothesis regarding the influence of the metal powder size on the microstructure of cobalt can be formulated. Previous studies [9, 37, 11] carried out on materials of similar composition have not been able to reveal such characteristics, neither microscopically, nor on the properties of the internal friction peak P1. These studies were conducted on materials produced from fine powders (with grain size in the micron range). The one corresponding to this thesis work are finer. A study on the formation of hcp phase to the detriment of fcc phase within the cemented carbide binder also raises the possibility of an influence of the size of the sintering powders on the hcp phase formation [172].

4.5 Perspectives

This Section presents the industrial implementation of the results of this study. Few details of the strategies explored are presented in order to guarantee the confidentiality of the industrial developments belonging to the partner of this project.

On the basis of the cobalt phase defects observations, new binders were developed. The aim of these new alloys is to incorporate elements into the cobalt that stabilise the fcc phase and produce tougher binder alloys. These new materials offer excellent grain size, porosity, toughness and hardness.

Another approach has been explored and it concerns the sintering process. This process is a crucial step in the production of cemented carbides. It controls the characteristics and mechanical properties of the final bulk material through delicate processes such as solid state densification, WC grain growth, accidental development of vanadium or chromium carbide grains, or proliferation of porosities. Due to the complexity of the obstacles that a change in the sintering process can cause, only specific parameters have been changed. Two modifications were investigated, and the resulting samples have a grain size, porosity and hardness quality equivalent to that of the WC-Co usually produced.

Cemented carbides with new binders were also tested by mechanical spectroscopy. They showed the same peaks of internal friction as those reported previously in this work. However, the IF P1 peak corresponding to cobalt was shifted to lower temperatures. On the basis of the results presented in this study, this increased shift should thus correspond to a longer tool life in the machining shock tests. Indeed, tests carried out on the inserts with the new formula clearly demonstrated a longer tool life. Compared to the initial production batch, a relative improvement of 6 percent was achieved.

Conclusion

WC-Co cemented carbide cutting tools are composed of three main components, each of which will determine their performance and resistance to wear and deformation. The bulk composite consists of a hard skeleton of WC grains and a cobalt binder forming a skeleton around the WC grains. The whole material is coated with metal-ceramic composite thin films such as Al_2O_3 , TiAlN, TiCN, TiC, CrN, ZrN. The hard skeleton ensures high hardness at low and high temperature and a refractory character. This hard phase becomes critical at very high temperatures by the initiation of decohesion processes. The binder phase enables the composite to acquire ductility and toughness. Finally, the coatings provide the material with physical and chemical resistance to wear and a thermal protection.

This thesis develops a model of the microstructural behaviour of the binder phase of cemented carbides and the unsuspected influence of coatings on mechanical properties. It highlights the major role played by cobalt in these materials. Within the cobalt binder, a glass-like transition could be identified. This transition involves the formation at low temperature of a cobalt frozen state demonstrating only short-range order but no long-range order. The thermodynamics of this state is peculiar. A significant increase in the rearrangement time for the microstructure of the cobalt takes place until it becomes too long with respect to the experimental time.

The glassy phase transition for cobalt in WC-Co was evidenced by three features:

1. At low temperatures, the cobalt binder turns out to be composed of 50nm to 100nm frozen nanodomains. Each of these nanodomains then contains a second sub-structure of nanotwins. A detwinning process taking place between 735K and 1040K is related to the formation of ledges associated with partial dislocations associated with detwinning fronts. This reveals a long-range ordered cobalt fcc phase at higher temperatures. The presence of the dislocations needed for detwinning is key for the reversibility of the process when WC-Co is cooled again in the temperature region of the glass transition.
2. The glass-like transition was revealed by mechanical spectroscopy showing a characteristic relaxation peak P1. The relaxation time of the peak P1 is associated with the movement of nanotwins does not show the common Arrhenius behavior. The attempt frequency of the order of 10^{58} obtained in an Arrhenius plot is totally unphysical. Instead, a divergence of the relaxation time could be discovered and associated with the Vogel-Fulcher-Tammann model. The description of thermal activation seems to be more adequate in accordance with the thermodynamics of a glass transition.

3. Several observations support the proposition that the low-temperature state of cobalt is dependent on its thermomechanical history. By mechanical spectroscopy, it has been shown that the study of the peak P1 requires a stabilisation process by several anneals above the temperature of the relaxation peak. This relaxation peak also demonstrates the need for long isothermal rearrangement times by the T-point effect. Finally, plastic deformation studies were carried out by applying a stress field following the zero-field-cooling/field-cooling (ZFC-FH)/(FC-FH) protocol. A deviation in the behaviour of the material, between two identical processes with different histories, was demonstrated; although, this could not be fully attributed to the behaviour of the cobalt phase alone. In this sense, several evidences indicate a break in the ergodicity for the low-temperature state of the cobalt binder.

The in-depth study of a second relaxation peak (Internal Friction peak P2) revealed a relaxation time associated with defects in the cobalt phase. The second relaxation peak of cobalt would be associated with partial dislocations and the presence of tungsten solute in the cobalt binder. In the temperature region where the peak P2 is observed, the cobalt becomes ductile.

The glass transition of cobalt in cemented carbides thus corresponds to a transformation from a brittle low temperature phase composed of frozen nanodomains containing nanotwins to a more ductile high temperature phase fcc comprising 4 sliding planes. It can be assimilated to a brittle-to-ductile transition well known for in ferritic steel applications. Unfortunately for cutting applications, this transition often corresponds to the machining tool temperatures. The results obtained in this work, combined with the studies already carried out for cemented carbides, provide an overall description of the mechanical behaviour of WC-Co as a function of temperature. Three domains can be defined, which are mainly controlled by cobalt.

- I A low temperature domain starts from room temperature up to 800K. Hardmetals in this temperature range have a high hardness and are brittle. Mechanically, this domain corresponds to the elastic behaviour of the material. The special frozen microstructure of cobalt is responsible for the mechanical properties and in particular the brittle behaviour.
- IIa A first mid-temperature domain between approximately 800K and 1000K follows. This range corresponds to a slight softening of the composite and depends on the detwinning process observed in cobalt. It is the beginning of the plastic behaviour.
- IIb This is followed by a second mid-temperate domain between 1000K and 1200K, approximately. An increase in softening is observed here. The cobalt binder is in its long-range ordered fcc phase where movement of dislocations can take place and ensure deformation. This range corresponds to an increase in the plasticity of the composite and of its toughness. This is the most favourable temperature range to ensure the performance of WC-Co cutting tools.
- III A high temperature domain takes place from 1200K and above. From these temperatures, phenomena of infiltration of cobalt between the WC grains and decohesion of the hard composite skeleton are observed. This corresponds to important plastic behaviour and is harmful to the material. Creep is thus observed.

The study of cobalt phase transformations is an innovative basis for the development

of new grades of cemented carbides tools. Other informations such as the influence of the composition and dynamics of the microstructure would not be accessible through conventional techniques. Mechanical spectroscopy has thus proven to be a major asset for understanding the stakes of this project.

There are several essential points to consider for developing new grades of cemented carbides. The observed ductile-fragile transition must be suppressed or reduced at lower temperatures. A binder phase consisting of a long-range ordered structure is indeed necessary over a wider temperature range. This mid-temperature phase must thus ensure sufficient but moderate plasticity by increasing the mobility of the dislocations, as observed in domain (IIb). Transmission electron microscopy and mechanical spectroscopy techniques will prove to be essential assets for these developments. In addition, the interface between the coating and the substrate is critical to the performance of the cutting tools. This interface must depend on the coating and the structure of the cobalt binder at the interface. Further model development of the interaction between the coating and the cobalt microstructure is crucial.

This project paves the way for the design of prototypes of new binders for applications in the cutting tool industry ¹.

¹These developments are not disclosed for confidentiality purposes.

Bibliography

- [1] B. M. Kramer, “On Tool Materials for High Speed Machining,” *Journal of Engineering for Industry*, vol. 109, no. 2, pp. 87–91, 05 1987. URL <https://doi.org/10.1115/1.3187113>
- [2] (2020) Product presentation from lamina-tech. multi-mat inserts and tools. lamina technologies is a swiss manufacturer of cutting tools for machining. URL <https://www.youtube.com/watch?v=cUIcEwUUeeQ>
- [3] (2020) Product presentation from lamina-tech. magia-pro inserts and tools. lamina technologies is a swiss manufacturer of cutting tools for machining. URL https://www.youtube.com/watch?v=o_n0HdF4JGU
- [4] (2019) Lamina technologies, product catalog 2019-2020, lamina technologies is a swiss manufacturer of cutting tools for machining. Product Line Presentation. URL <https://www.lamina-tech.ch/downloads>
- [5] M. P. Groover, *Fundamentals of modern manufacturing: materials, processes and systems*, 4th ed. Wiley, 2010. URL <https://archive.org/details/FundamentalsOfModernManufacturing4thEditionMikellPGroover/page/n9/mode/2up>
- [6] S. Cooke, K. Ahmadi, S. Willerth, and R. Herring, “Metal additive manufacturing: Technology, metallurgy and modelling,” *Journal of Manufacturing Processes*, vol. 57, pp. 978 – 1003, 2020. URL <https://doi.org/10.1016/j.jmapro.2020.07.025>
- [7] Y. Naerheim and E. M. Trent, “Diffusion wear of cemented carbide tools when cutting steel at high speeds,” *Metals Technology*, vol. 4, no. 1, pp. 548–556, 1977. URL <https://doi.org/10.1179/030716977803292673>
- [8] K. Bobzin, “High-performance coatings for cutting tools,” *CIRP Journal of Manufacturing Science and Technology*, vol. 18, pp. 1 – 9, 2017. URL <https://doi.org/10.1016/j.cirpj.2016.11.004>
- [9] S. Bolognini, “Propriétés mécaniques à haute température de cermets ti(c,n)-wc-mo-co à gradient de composition pour outils de coupe,” p. 164, 2000. URL <http://infoscience.epfl.ch/record/32637>
- [10] K. Schröter, “Gesinterte harte metallegierung und verfahren zu ihrer herstellung,” Patent. URL <https://worldwide.espacenet.com/patent/search/family/007381421/publication/DE420689C?q=pn%3DDDE420689C>

Bibliography

- [11] J.-J. Ammann, “Etude des propriétés mécaniques du matériau composite wc-co par frottement intérieur,” p. 186, 1990. URL <http://infoscience.epfl.ch/record/31339>
- [12] V. Sarin, “Morphology of eta phase in cemented wc-co alloys,” in *Modern developments in powder metallurgy. Vol. 10*, 1977.
- [13] P. Gustafson, “Thermodynamic evaluation of c–w system,” *Materials Science and Technology*, vol. 2, no. 7, pp. 653–658, 1986. URL <https://doi.org/10.1179/mst.1986.2.7.653>
- [14] A. Markstroem, K. Frisk, and B. Sundman, “A revised thermodynamic description of the co-w-c system,” *Journal of Phase Equilibria and Diffusion*, vol. 26, no. 2, pp. 152–160, Apr 2005. URL <https://doi.org/10.1007/s11669-005-0133-1>
- [15] R. Warren and M. B. Waldron, “Microstructural development during the liquid-phase sintering of cemented carbides,” *Powder Metallurgy*, vol. 15, no. 30, pp. 166–201, 1972. URL <https://doi.org/10.1179/pom.1972.15.30.005>
- [16] I. Konyashin, A. Zaitsev, D. Sidorenko, E. Levashov, B. Ries, S. Konischev, M. Sorokin, A. Mazilkin, M. Herrmann, and A. Kaiser, “Wettability of tungsten carbide by liquid binders in wc–co cemented carbides: Is it complete for all carbon contents?” *International Journal of Refractory Metals and Hard Materials*, vol. 62, pp. 134 – 148, 2017. URL <https://doi.org/10.1016/j.ijrmhm.2016.06.006>
- [17] L. Prakash, “1.02 - fundamentals and general applications of hardmetals,” in *Comprehensive Hard Materials*, V. K. Sarin, Ed. Oxford: Elsevier, 2014, pp. 29 – 90. URL <https://doi.org/10.1016/B978-0-08-096527-7.00002-7>
- [18] V. Richter and M. Ruthendorf, “On hardness and toughness of ultrafine and nanocrystalline hard materials,” *International Journal of Refractory Metals and Hard Materials*, vol. 17, no. 1, pp. 141 – 152, 1999. URL [https://doi.org/10.1016/S0263-4368\(99\)00003-7](https://doi.org/10.1016/S0263-4368(99)00003-7)
- [19] B. Roebuck and E. A. Almond, “Deformation and fracture processes and the physical metallurgy of wc–co hardmetals,” *International Materials Reviews*, vol. 33, no. 1, pp. 90–112, 1988. URL <https://doi.org/10.1179/imr.1988.33.1.90>
- [20] A. Gant, R. Morrell, A. Wronski, and H. Jones, “Edge toughness of tungsten carbide based hardmetals,” *International Journal of Refractory Metals and Hard Materials*, vol. 75, pp. 262–278, 2018. URL <https://doi.org/10.1016/j.ijrmhm.2017.12.020>
- [21] R. Morrell and A. Gant, “Edge chipping of hard materials,” *International Journal of Refractory Metals and Hard Materials*, vol. 19, no. 4, pp. 293–301, 2001, 7th international conference on the science of hard materials. URL [https://doi.org/10.1016/S0263-4368\(01\)00030-0](https://doi.org/10.1016/S0263-4368(01)00030-0)
- [22] A. V. Shatov, S. Ponomarev, and S. Firstov, “1.09 - hardness and deformation of hardmetals at room temperature,” in *Comprehensive Hard Materials*, V. K. Sarin, Ed. Oxford: Elsevier, 2014, pp. 267 – 299. URL <https://doi.org/10.1016/B978-0-08-096527-7.00009-X>

-
- [23] K. Buss, “High temperature deformation mechanisms of cemented carbides and cermets,” p. 156, 2004. URL <http://infoscience.epfl.ch/record/33564>
- [24] D. Mari, B. Clausen, M. Bourke, and K. Buss, “Measurement of residual thermal stress in wc-co by neutron diffraction,” *International Journal of Refractory Metals and Hard Materials*, vol. 27, no. 2, pp. 282 – 287, 2009, international Conference on the Science of Hard Materials - 9. URL <https://doi.org/10.1016/j.ijrmhm.2008.11.015>
- [25] A. Krawitz and E. Drake, “Residual stresses in cemented carbides — an overview,” *International Journal of Refractory Metals and Hard Materials*, vol. 49, pp. 27 – 35, 2015, special Issue: International Conference on the Science of Hard Materials – 10. URL <https://doi.org/10.1016/j.ijrmhm.2014.07.018>
- [26] J.-E. Bidaux, R. Schaller, and W. Benoit, “Study of the h.c.p.-f.c.c. phase transition in cobalt by acoustic measurements,” *Acta Metallurgica*, vol. 37, no. 3, pp. 803 – 811, 1989. URL [https://doi.org/10.1016/0001-6160\(89\)90007-2](https://doi.org/10.1016/0001-6160(89)90007-2)
- [27] D. Mari, S. Bolognini, G. Feusier, T. Viatte, and W. Benoit, “Experimental strategy to study the mechanical behaviour of hardmetals for cutting tools,” *International Journal of Refractory Metals and Hard Materials*, vol. 17, no. 1, pp. 209 – 225, 1999. URL [https://doi.org/10.1016/S0263-4368\(98\)00078-X](https://doi.org/10.1016/S0263-4368(98)00078-X)
- [28] D. Mari, “Understanding the mechanical properties of hardmetals through mechanical spectroscopy,” *Materials Science and Engineering: A*, vol. 521-522, pp. 322 – 328, 2009, 15th International Conference on Internal Friction and Mechanical Spectroscopy. URL <https://doi.org/10.1016/j.msea.2008.10.064>
- [29] H.-O. André, “Microstructures of cemented carbides,” *Materials and Design*, vol. 22, no. 6, pp. 491 – 498, 2001. URL [https://doi.org/10.1016/S0261-3069\(01\)00006-1](https://doi.org/10.1016/S0261-3069(01)00006-1)
- [30] C. Smithells, “Metals reference book, edited by ea brandes,” 1983.
- [31] D. E. Gray, Ed., *American institute of physics handbook*. New York: McGraw-Hill, 1963, vol. 2nd edition.
- [32] C. Hauser, “Technologie et quelques problèmes liés au revêtement,” *Wear*, vol. 62, no. 1, pp. 59 – 82, 1980. URL [https://doi.org/10.1016/0043-1648\(80\)90037-X](https://doi.org/10.1016/0043-1648(80)90037-X)
- [33] B. Kramer and N. Suh, “Tool wear by solution : A quantitative understanding.” *Journal of engineering for industry*, vol. 102, no. 4, pp. 303–309, 1980, cited By 146. URL <https://doi.org/10.1115/1.3183869>
- [34] T. Kagnaya, C. Boher, L. Lambert, M. Lazard, and T. Cutard, “Wear mechanisms of WC-Co cutting tools from high-speed tribological tests,” *Wear*, vol. 267, no. 5-8, pp. 890–897, 2009. URL <https://doi.org/10.1016/j.wear.2008.12.035>
- [35] T. Kagnaya, “Identification of wear mechanisms of a WC-6%Co grade in machining by combining thermal and tribological approaches,” Theses, École Nationale Supérieure des Mines de Paris, Sep. 2009. URL <https://pastel.archives-ouvertes.fr/pastel-00005750>

- [36] L. Toller-Nordström, J. Östby, and S. Norgren, "Towards understanding plastic deformation in hardmetal turning inserts with different binders," *International Journal of Refractory Metals and Hard Materials*, vol. 94, p. 105309, 2021. URL <https://doi.org/10.1016/j.ijrmhm.2020.105309>
- [37] D. Mari and D. Gonseth, "A new look at carbide tool life," *Wear*, vol. 165, no. 1, pp. 9 – 17, 1993. URL [https://doi.org/10.1016/0043-1648\(93\)90366-T](https://doi.org/10.1016/0043-1648(93)90366-T)
- [38] T. Sakuma and H. Hondo, "Plastic flow in wc-13wt.%co at high temperatures," *Materials Science and Engineering: A*, vol. 156, no. 2, pp. 125 – 130, 1992. URL [https://doi.org/10.1016/0921-5093\(92\)90144-P](https://doi.org/10.1016/0921-5093(92)90144-P)
- [39] G. Östberg, K. Buss, M. Christensen, S. Norgren, H.-O. Andrén, D. Mari, G. Wahnström, and I. Reineck, "Mechanisms of plastic deformation of wc-co and ti(c, n)-wc-co," *International Journal of Refractory Metals and Hard Materials*, vol. 24, no. 1, pp. 135 – 144, 2006. URL <https://doi.org/10.1016/j.ijrmhm.2005.04.009>
- [40] K. Buss and D. Mari, "High temperature deformation mechanisms in cemented carbides and cermets studied by mechanical spectroscopy," *Materials Science and Engineering: A*, vol. 370, no. 1, pp. 163 – 167, 2004, 13th International Conference on Internal Friction and Ultrasonic Attenuation in Solids. URL <https://doi.org/10.1016/j.msea.2002.12.004>
- [41] R. Raj and M. F. Ashby, "On grain boundary sliding and diffusional creep," *Metallurgical Transactions*, vol. 2, no. 4, pp. 1113–1127, Apr 1971. URL <https://doi.org/10.1007/BF02664244>
- [42] S. Lay, J. Vicens, and F. Osterstock, "High temperature creep of wc-co alloys," *Journal of Materials Science*, vol. 22, no. 4, pp. 1310–1322, Apr 1987. URL <https://doi.org/10.1007/BF01233127>
- [43] G. Östberg and H.-O. Andrén, "Microstructural changes during wear by plastic deformation of cemented carbide and cermet cutting inserts," *Metallurgical and Materials Transactions A*, vol. 37, no. 5, p. 1495, May 2006. URL <https://doi.org/10.1007/s11661-006-0094-y>
- [44] M. Yousfi, J. Weidow, A. Nordgren, L. Falk, and H.-O. Andrén, "Deformation mechanisms in a wc-co based cemented carbide during creep," *International Journal of Refractory Metals and Hard Materials*, vol. 49, pp. 81 – 87, 2015, special Issue: International Conference on the Science of Hard Materials – 10. URL <https://doi.org/10.1016/j.ijrmhm.2014.07.016>
- [45] G. Östberg, M. Farooq, M. Christensen, H.-O. Andrén, U. Klement, and G. Wahnström, "Effect of sigma-2 grain boundaries on plastic deformation of wc-co cemented carbides," *Materials Science and Engineering: A*, vol. 416, no. 1, pp. 119 – 125, 2006. URL <https://doi.org/10.1016/j.msea.2005.09.095>
- [46] B. Uhrenius, H. Pastor, and E. Pauty, "On the composition of fe-ni-co-wc-based cemented carbides," *International Journal of Refractory Metals and Hard Materials*, vol. 15, no. 1, pp. 139 – 149, 1997, wear Resistant Materials for the South African Industry. URL [https://doi.org/10.1016/S0263-4368\(96\)00023-6](https://doi.org/10.1016/S0263-4368(96)00023-6)

- [47] W. Schubert, M. Fugger, B. Wittmann, and R. Useldinger, “Aspects of sintering of cemented carbides with fe-based binders,” *International Journal of Refractory Metals and Hard Materials*, vol. 49, pp. 110 – 123, 2015, special Issue: International Conference on the Science of Hard Materials – 10. URL <https://doi.org/10.1016/j.ijrmhm.2014.07.028>
- [48] V. Tracey, “Nickel in hardmetals,” *International Journal of Refractory Metals and Hard Materials*, vol. 11, no. 3, pp. 137 – 149, 1992. URL [https://doi.org/10.1016/0263-4368\(92\)90056-8](https://doi.org/10.1016/0263-4368(92)90056-8)
- [49] J. M. I. L. Perez, *Matériaux non cristallins et science du désordre*, ppur ed. Presses Polytechniques et Universitaires Romandes, 2001. URL <https://www.epflpress.org/produit/403/9782880744854/materiaux-non-cristallins-et-science-du-desordre>
- [50] D. A. Porter, K. E. Easterling, and M. Y. A. Sherif, *Phase Transformations in Metals and Alloys*, taylor and francis group ed. CRC Press, 2009. URL <https://doi.org/10.1201/9781439883570>
- [51] X. Ren, Y. Wang, Y. Zhou, Z. Zhang, D. Wang, G. Fan, K. Otsuka, T. Suzuki, Y. Ji, J. Zhang, Y. Tian, S. Hou, and X. Ding, “Strain glass in ferroelastic systems: Premartensitic tweed versus strain glass,” *Philosophical Magazine*, vol. 90, no. 1-4, pp. 141–157, 2010. URL <https://doi.org/10.1080/14786430903074771>
- [52] G. Jaeger, “The ehrenfest classification of phase transitions: Introduction and evolution,” *Archive for History of Exact Sciences*, vol. 53, no. 1, pp. 51–81, May 1998. URL <https://doi.org/10.1007/s004070050021>
- [53] T. V. Tropin, J. W. Schmelzer, and C. Schick, “On the dependence of the properties of glasses on cooling and heating rates: I. entropy, entropy production, and glass transition temperature,” *Journal of Non-Crystalline Solids*, vol. 357, no. 4, pp. 1291 – 1302, 2011. URL <https://doi.org/10.1016/j.jnoncrysol.2010.11.111>
- [54] H. Eyring, “The activated complex in chemical reactions,” *The Journal of Chemical Physics*, vol. 3, no. 2, pp. 107–115, 1935. URL <https://doi.org/10.1063/1.1749604>
- [55] H. Eyring, “Viscosity, plasticity, and diffusion as examples of absolute reaction rates,” *The Journal of Chemical Physics*, vol. 4, no. 4, pp. 283–291, 1936. URL <https://doi.org/10.1063/1.1749836>
- [56] H. Vogel, “Das temperaturabhaengigkeitsgesetz der viskositäet von fluessigkeiten,” *Phys. Z.*, vol. 22, pp. 645–646, 1921.
- [57] G. S. Fulcher, “Analysis of recent measurements of the viscosity of glasses,” *Journal of the American Ceramic Society*, vol. 8, no. 6, pp. 339–355, 1925. URL <https://doi.org/10.1111/j.1151-2916.1925.tb16731.x>
- [58] G. Tammann and W. Hesse, “Die abhängigkeit der viscosität von der temperatur bie unterkühlten flüssigkeiten,” *Zeitschrift für anorganische und allgemeine Chemie*, vol. 156, no. 1, pp. 245–257, 1926. URL <https://doi.org/10.1002/zaac.19261560121>

Bibliography

- [59] G. W. Scherer, “Editorial comments on a paper by gordon s. fulcher,” *Journal of the American Ceramic Society*, vol. 75, no. 5, pp. 1060–1062, 1992. URL <https://doi.org/10.1111/j.1151-2916.1992.tb05537.x>
- [60] S. R. Elliott, *Physics of Amorphous Materials*. New York: Longman, 1990, vol. 2nd Revised edition.
- [61] J. Zarzycki, *Glasses and Amorphous Materials*, ser. Materials science and technology : A comprehensive Treatment. Weinheim: VCH, 1991, vol. 9.
- [62] G. Tammann, “Der glaszustand [the glassy state] (in german),” no. A 5365, 1933, out of print. URL <http://d-nb.info/576624187>
- [63] S. Hechler, I. Gallino, M. Stolpe, F.-T. Lentes, and R. Busch, “Analysis of thermophysical properties of lead silicates in comparison to bulk metallic glasses,” *Journal of Non-Crystalline Solids*, vol. 485, pp. 66 – 73, 2018. URL <https://doi.org/10.1016/j.jnoncrysol.2018.01.041>
- [64] J. Y. Cavaille, J. Perez, and G. P. Johari, “Molecular theory for the rheology of glasses and polymers,” *Phys. Rev. B*, vol. 39, pp. 2411–2422, Feb 1989. URL <https://doi.org/10.1103/PhysRevB.39.2411>
- [65] Y. Wang, X. Ren, K. Otsuka, and A. Saxena, “Evidence for broken ergodicity in strain glass,” *Phys. Rev. B*, vol. 76, p. 132201, Oct 2007. URL <https://doi.org/10.1103/PhysRevB.76.132201>
- [66] R. Bhowmik and R. Ranganathan, “Anomaly in cluster glass behaviour of $\text{Co}_{0.2}\text{Zn}_{0.8}\text{Fe}_{2.0}\text{O}_4$ spinel oxide,” *Journal of Magnetism and Magnetic Materials*, vol. 248, no. 1, pp. 101 – 111, 2002. URL [https://doi.org/10.1016/S0304-8853\(02\)00190-7](https://doi.org/10.1016/S0304-8853(02)00190-7)
- [67] D. Viehland, J. F. Li, S. J. Jang, L. E. Cross, and M. Wuttig, “Glassy polarization behavior of relaxor ferroelectrics,” *Phys. Rev. B*, vol. 46, pp. 8013–8017, Oct 1992. URL <https://doi.org/10.1103/PhysRevB.46.8013>
- [68] S. Kartha, T. Castán, J. A. Krumhansl, and J. P. Sethna, “Spin-glass nature of tweed precursors in martensitic transformations,” *Phys. Rev. Lett.*, vol. 67, pp. 3630–3633, Dec 1991. URL <https://doi.org/10.1103/PhysRevLett.67.3630>
- [69] S. Kartha, J. A. Krumhansl, J. P. Sethna, and L. K. Wickham, “Disorder-driven pretransitional tweed pattern in martensitic transformations,” *Phys. Rev. B*, vol. 52, pp. 803–822, Jul 1995. URL <https://doi.org/10.1103/PhysRevB.52.803>
- [70] S. Semenovskaya and A. Khachaturyan, “Coherent structural transformations in random crystalline systems,” *Acta Materialia*, vol. 45, no. 10, pp. 4367 – 4384, 1997. URL [https://doi.org/10.1016/S1359-6454\(97\)00071-2](https://doi.org/10.1016/S1359-6454(97)00071-2)
- [71] Z. Zhou, J. Cui, and X. Ren, “Strain glass state as the boundary of two phase transitions,” *Scientific Reports*, vol. 5, no. 1, p. 13377, Aug 2015. URL <https://doi.org/10.1038/srep13377>

-
- [72] Y. Ji, D. Wang, Y. Wang, Y. Zhou, D. Xue, K. Otsuka, Y. Wang, and X. Ren, "Ferroic glasses," *npj Computational Materials*, vol. 3, no. 1, p. 43, Oct 2017. URL <https://doi.org/10.1038/s41524-017-0039-6>
- [73] Y. Wang, J. Gao, H. Wu, S. Yang, X. Ding, D. Wang, X. Ren, Y. Wang, X. Song, and J. Gao, "Strain glass transition in a multifunctional β -type ti alloy," *Scientific Reports*, vol. 4, no. 1, p. 3995, Feb 2014. URL <https://doi.org/10.1038/srep03995>
- [74] D. Wang, Z. Zhang, J. Zhang, Y. Zhou, Y. Wang, X. Ding, Y. Wang, and X. Ren, "Strain glass in Fe-doped Ti-Ni," *Acta Materialia*, vol. 58, no. 18, pp. 6206–6215, 2010. URL <https://doi.org/10.1016/j.actamat.2010.07.040>
- [75] A. Nowick and B. Berry, *Anelastic Relaxation in Crystalline Solids*. Academic Press, 1972. URL <https://doi.org/10.1016/B978-0-12-522650-9.50002-1>
- [76] R. Schaller, G. Fantozzi, and G. Gremaud, *Mechanical spectroscopy Q-1 2001 - With applications to materials science*, ser. Materials Science Forum. Trans Tech Publications, 2001, vol. 366-368. URL <https://doi.org/10.4028/www.scientific.net/MSF.366-368>
- [77] J. Meixner, "Thermodynamische Theorie der elastischen Relaxation," *Zeitschrift fur Naturforschung - Section A Journal of Physical Sciences*, vol. 9, no. 7-8, pp. 654–663, 1954. URL <https://doi.org/10.1515/zna-1954-7-812>
- [78] J. Meixner, "Thermodynamik und Relaxationserscheinungen," *Zeitschrift fur Naturforschung - Section A Journal of Physical Sciences*, vol. 4, no. 8, pp. 594–600, 1949. URL <https://doi.org/10.1515/zna-1949-0809>
- [79] T. Kagnaya, M. Lazard, L. Lambert, C. Boher, and T. Cutard, "Temperature evolution in a WC-6%Co cutting tool during turning machining: Experiment and finite element simulations," *WSEAS Transactions on Heat and Mass Transfer*, vol. 6, no. 3, pp. 71–80, jul 2011. URL <http://www.wseas.us/e-library/transactions/heat/2011/53-368.pdf>
- [80] J. Sheikh-Ahmad and J. Davim, "Tool wear in machining processes for composites," in *Machining Technology for Composite Materials*, ser. Woodhead Publishing Series in Composites Science and Engineering, H. Hocheng, Ed. Woodhead Publishing, 2012, pp. 116 – 153. URL <https://doi.org/10.1533/9780857095145.1.116>
- [81] M. Shaw, *Metal Cutting Principles*, ser. Oxford series on advanced manufacturing. Oxford University Press, 2005. URL <https://books.google.ch/books?id=VxNiQgAACAAJ>
- [82] L. Sigl and H. Fischmeister, "On the fracture toughness of cemented carbides," *Acta Metallurgica*, vol. 36, no. 4, pp. 887 – 897, 1988. URL [https://doi.org/10.1016/0001-6160\(88\)90143-5](https://doi.org/10.1016/0001-6160(88)90143-5)
- [83] A. V. Shatov, S. Ponomarev, and S. Firstov, "1.10 - fracture and strength of hardmetals at room temperature," in *Comprehensive Hard Materials*, V. K. Sarin, Ed. Oxford: Elsevier, 2014, pp. 301 – 343. URL <https://doi.org/10.1016/B978-0-08-096527-7.00010-6>

Bibliography

- [84] A. Inspektor and P. A. Salvador, "Architecture of pvd coatings for metalcutting applications: A review," *Surface and Coatings Technology*, vol. 257, pp. 138 – 153, 2014. URL <https://doi.org/10.1016/j.surfcoat.2014.08.068>
- [85] Y. X. Wang and S. Zhang, "Toward hard yet tough ceramic coatings," *Surface and Coatings Technology*, vol. 258, pp. 1 – 16, 2014. URL <https://doi.org/10.1016/j.surfcoat.2014.07.007>
- [86] D. Quinto, A. Santhanam, and P. Jindal, "Mechanical properties, structure and performance of chemically vapor-deposited and physically vapor-deposited coated carbide tools," *Materials Science and Engineering: A*, vol. 105-106, pp. 443 – 452, 1988. URL [https://doi.org/10.1016/0025-5416\(88\)90729-X](https://doi.org/10.1016/0025-5416(88)90729-X)
- [87] B. Breidenstein and B. Denkena, "Significance of residual stress in pvd-coated carbide cutting tools," *CIRP Annals*, vol. 62, no. 1, pp. 67 – 70, 2013. URL <https://doi.org/10.1016/j.cirp.2013.03.101>
- [88] L. Karlsson, L. Hultman, and J.-E. Sundgren, "Influence of residual stresses on the mechanical properties of TiCN_{1-x} ($x=0, 0.15, 0.45$) thin films deposited by arc evaporation," *Thin Solid Films*, vol. 371, no. 1, pp. 167 – 177, 2000. URL [https://doi.org/10.1016/S0040-6090\(00\)00996-2](https://doi.org/10.1016/S0040-6090(00)00996-2)
- [89] D. T. Quinto, "Mechanical property and structure relationships in hard coatings for cutting tools," *Journal of Vacuum Science & Technology A*, vol. 6, no. 3, pp. 2149–2157, 1988. URL <https://doi.org/10.1116/1.575206>
- [90] P. Ranjan and S. S. Hiremath, "Role of textured tool in improving machining performance: A review," *Journal of Manufacturing Processes*, vol. 43, pp. 47 – 73, 2019. URL <https://doi.org/10.1016/j.jmapro.2019.04.011>
- [91] W. Münz, "Titanium aluminum nitride films: A new alternative to tin coatings," *Journal of Vacuum Science & Technology A*, vol. 4, no. 6, pp. 2717–2725, 1986. URL <https://doi.org/10.1116/1.573713>
- [92] P. Jindal, A. Santhanam, U. Schleinkofer, and A. Shuster, "Performance of pvd tin, tcn, and tialn coated cemented carbide tools in turning," *International Journal of Refractory Metals and Hard Materials*, vol. 17, no. 1, pp. 163 – 170, 1999. URL [https://doi.org/10.1016/S0263-4368\(99\)00008-6](https://doi.org/10.1016/S0263-4368(99)00008-6)
- [93] B. Navinšek, P. Panjan, and I. Milošev, "Industrial applications of crn (pvd) coatings, deposited at high and low temperatures," *Surface and Coatings Technology*, vol. 97, no. 1, pp. 182 – 191, 1997. URL [https://doi.org/10.1016/S0257-8972\(97\)00393-9](https://doi.org/10.1016/S0257-8972(97)00393-9)
- [94] O. Knotek, F. Loeffler, and H.-J. Scholl, "Properties of arc-evaporated crn and (cr, al)n coatings," *Surface and Coatings Technology*, vol. 45, no. 1, pp. 53 – 58, 1991. URL [https://doi.org/10.1016/0257-8972\(91\)90205-B](https://doi.org/10.1016/0257-8972(91)90205-B)
- [95] H. Prengel, A. Santhanam, R. Penich, P. Jindal, and K. Wendt, "Advanced pvd-tialn coatings on carbide and cermet cutting tools," *Surface and Coatings Technology*, vol. 94-95, pp. 597 – 602, 1997, 24th International Conference on Metallurgical Coatings and Thin Films. URL [https://doi.org/10.1016/S0257-8972\(97\)00503-3](https://doi.org/10.1016/S0257-8972(97)00503-3)

-
- [96] O. Knotek, W. D. Münz, and T. Leyendecker, “Industrial deposition of binary, ternary, and quaternary nitrides of titanium, zirconium, and aluminum,” *Journal of Vacuum Science & Technology A*, vol. 5, no. 4, pp. 2173–2179, 1987. URL <https://doi.org/10.1116/1.574948>
- [97] G. Beensh-Marchwicka, L. Król-Stepniewska, and W. Posadowski, “Structure of thin films prepared by the cosputtering of titanium and aluminium or titanium and silicon,” *Thin Solid Films*, vol. 82, no. 4, pp. 313 – 320, 1981. URL [https://doi.org/10.1016/0040-6090\(81\)90474-0](https://doi.org/10.1016/0040-6090(81)90474-0)
- [98] H. A. Jehn, S. Hofmann, V. Rückborn, and W. Münz, “Morphology and properties of sputtered (ti,al)n layers on high speed steel substrates as a function of deposition temperature and sputtering atmosphere,” *Journal of Vacuum Science & Technology A*, vol. 4, no. 6, pp. 2701–2705, 1986. URL <https://doi.org/10.1116/1.573709>
- [99] I. A. Abrikosov, A. Knutsson, B. Alling, F. Tasnádi, H. Lind, L. Hultman, and M. Odén, “Phase stability and elasticity of tialn,” *Materials*, vol. 4, no. 9, pp. 1599–1618, 2011. URL <https://doi.org/10.3390/ma4091599>
- [100] (2020) Swiss-pvd sa is a company that is specialized in the construction of hard layers of coating machines of high range and pvd systems in general. URL <https://www.swiss-pvd.ch/cms/en/home>
- [101] Y. Deng, W. Chen, B. Li, C. Wang, T. Kuang, and Y. Li, “Physical vapor deposition technology for coated cutting tools: A review,” *Ceramics International*, vol. 46, no. 11, Part B, pp. 18 373 – 18 390, 2020. URL <https://doi.org/10.1016/j.ceramint.2020.04.168>
- [102] R. L. Smith and G. E. Sandly, “An accurate method of determining the hardness of metals, with particular reference to those of a high degree of hardness,” *Proceedings of the Institution of Mechanical Engineers*, vol. 102, no. 1, pp. 623–641, 1922. URL https://doi.org/10.1243/PIME_PROC_1922_102_033_02
- [103] “Standard Test Method for Knoop and Vickers Hardness of Materials.” ASTM International, West Conshohocken, PA, Standard, 2010. URL <https://doi.org/10.1520/E0384-10E02>
- [104] (2020) Shimadzu micro hardness testers performing vickers hardness measurements. URL <https://www.shimadzu.com.sg/an/sap/products/hard-visco/hmv-g21.html>
- [105] (2020) Keyence digital microscope : Vhx-5000 series. URL <https://www.keyence.com/products/microscope/digital-microscope/vhx-5000/>
- [106] J. B. Pethica, R. Hutchings, and W. C. Oliver, “Hardness measurement at penetration depths as small as 20 nm,” *Philosophical Magazine A*, vol. 48, no. 4, pp. 593–606, 1983. URL <https://doi.org/10.1080/01418618308234914>
- [107] M. Doerner and W. Nix, “A method for interpreting the data from depth-sensing indentation instruments,” *Journal of Materials Research*, vol. 1, no. 4, p. 601–609, 1986. URL <https://doi.org/10.1557/JMR.1986.0601>

Bibliography

- [108] W. Oliver and G. Pharr, “An improved technique for determining hardness and elastic modulus using load and displacement sensing indentation experiments,” *Journal of Materials Research*, vol. 7, no. 6, p. 1564–1583, 1992. URL <https://doi.org/10.1557/JMR.1992.1564>
- [109] W. Oliver and G. Pharr, “Measurement of hardness and elastic modulus by instrumented indentation: Advances in understanding and refinements to methodology,” *Journal of Materials Research*, vol. 19, no. 1, p. 3–20, 2004. URL <https://doi.org/10.1557/jmr.2004.19.1.3>
- [110] “Anton paar: H70ib100en-a indentation software manual,” p. 144/155. URL <https://www.anton-paar.com/corp-en/products/details/nanoindentation-tester-nht3/>
- [111] D. J. Shuman, A. L. Costa, and M. S. Andrade, “Calculating the elastic modulus from nanoindentation and microindentation reload curves,” *Materials Characterization*, vol. 58, no. 4, pp. 380 – 389, 2007. URL <https://doi.org/10.1016/j.matchar.2006.06.005>
- [112] J. Woirgard, J.-C. Dargenton, C. Tromas, and V. Audurier, “A new technology for nanohardness measurements: principle and applications,” *Surface and Coatings Technology*, vol. 100-101, pp. 103 – 109, 1998. URL [https://doi.org/10.1016/S0257-8972\(97\)00597-5](https://doi.org/10.1016/S0257-8972(97)00597-5)
- [113] V. L. Popov, *Contact Mechanics and Friction*. Springer Berlin Heidelberg, 2010. URL <https://doi.org/10.1007%2F978-3-642-10803-7>
- [114] (2020) Zeiss geminiseM : Field emission scanning electron microscope. URL <https://www.zeiss.com/microscopy/int/products/scanning-electron-microscopes/geminiseM.html>
- [115] (2020) Electron microscopy at cime epfl: instruments and facilities. presentation of the sem zeiss gemini 300. URL <https://www.epfl.ch/research/facilities/cime/electron-microscopy/microscopes/zeiss-gemini/>
- [116] S. Bonnamy and A. Oberlin, “Chapter 4 - transmission electron microscopy,” in *Materials Science and Engineering of Carbon*, M. Inagaki and F. Kang, Eds. Butterworth-Heinemann, 2016, pp. 45 – 70. URL <https://doi.org/10.1016/B978-0-12-805256-3.00004-0>
- [117] (2020) Talos f200s g2 : Tem and stem microscope for dynamic microscopy. URL <https://www.thermofisher.com/ch/en/home/electron-microscopy/products/transmission-electron-microscopes/talos-f200s-tem.html>
- [118] (2020) Electron microscopy at cime epfl: instruments and facilities. presentation of the talos f200s g2 tem and stem. URL <https://www.epfl.ch/research/facilities/cime/electron-microscopy/microscopes/talos/>
- [119] T. Tepperneegg, T. Klünsner, P. Angerer, C. Tritremmel, C. Czettl, J. Keckes, R. Ebner, and R. Pippan, “Evolution of residual stress and damage in coated hard metal milling inserts over the complete tool life,” *International Journal of Refractory Metals and Hard Materials*, vol. 47, pp. 80 – 85, 2014. URL <https://doi.org/10.1016/j.ijrmhm.2014.07.005>

-
- [120] E. Brinksmeier, J. Cammett, W. König, P. Leskovar, J. Peters, and H. Tönshoff, “Residual stresses — measurement and causes in machining processes,” *CIRP Annals*, vol. 31, no. 2, pp. 491 – 510, 1982. URL [https://doi.org/10.1016/S0007-8506\(07\)60172-3](https://doi.org/10.1016/S0007-8506(07)60172-3)
 - [121] E. Brinksmeier and H. Wobker, *Residual Stresses in Tool Ceramics and Their Influence on Tool Life*, ser. International Conference on Residual Stresses, G. Beck, S. Denis, and S. A., Eds. Dordrecht: Springer, 1989. URL https://doi.org/10.1007/978-94-009-1143-7_44
 - [122] U. Welzel, J. Ligot, P. Lamparter, A. C. Vermeulen, and E. J. Mittemeijer, “Stress analysis of polycrystalline thin films and surface regions by X-ray diffraction,” *Journal of Applied Crystallography*, vol. 38, no. 1, pp. 1–29, Feb 2005. URL <https://doi.org/10.1107/S0021889804029516>
 - [123] A. D. Krawitz, *Introduction to Diffraction in Materials Science and Engineering*. Wiley-VCH, 03 2001. URL <https://www.wiley.com/en-us/Introduction+to+Diffraction+in+Materials+Science+and+Engineering-p-9780471247241>
 - [124] (2020) Thermo scientific : Arl equinox 3000 x-ray diffractometer. URL <https://www.thermofisher.com/order/catalog/product/IQLAAHGABLFAQLMBIZ#/IQLAAHGABLFAQLMBIZ>
 - [125] R. M. Fuoss and J. G. Kirkwood, “Electrical Properties of Solids. VIII. Dipole Moments in Polyvinyl Chloride-Diphenyl Systems,” *Journal of the American Chemical Society*, vol. 63, no. 2, pp. 385–394, 1941. URL <https://doi.org/10.1021/ja01847a013>
 - [126] D. Hull and D. Bacon, “Chapter 3 - movement of dislocations,” in *Introduction to Dislocations (Fifth Edition)*, fifth edition ed., D. Hull and D. Bacon, Eds. Oxford: Butterworth-Heinemann, 2011, pp. 43 – 62. URL <https://doi.org/10.1016/B978-0-08-096672-4.00003-7>
 - [127] G. Feusier, “Etude des propriétés mécaniques à haute température des cermets ti(c,n)-mo-co par mesures de frottement intérieur et par essais de flexion trois points,” p. 186, 1997. URL <http://infoscience.epfl.ch/record/32136>
 - [128] R. Schaller, J. J. Ammann, and C. Bonjour, “Internal friction in WC-Co hard metals,” *Materials Science and Engineering*, vol. 105-106, no. PART 2, pp. 313–321, 1988. URL [https://doi.org/10.1016/0025-5416\(88\)90712-4](https://doi.org/10.1016/0025-5416(88)90712-4)
 - [129] J. J. Ammann and R. Schaller, “Influence of a changing microstructure on high temperature relaxation peaks, an example: WC11wt.%Co,” *Journal of Alloys and Compounds*, vol. 211-212, no. C, pp. 397–401, 1994. URL [https://doi.org/10.1016/0925-8388\(94\)90530-4](https://doi.org/10.1016/0925-8388(94)90530-4)
 - [130] D. Mari, “Déformation à haute température des composites wc-co,” p. 176, 1991. URL <http://infoscience.epfl.ch/record/31416>
 - [131] D. Mari, “Understanding the mechanical properties of hardmetals through mechanical spectroscopy,” *Materials Science and Engineering A*, vol. 521-522, pp. 322–328, 2009. URL <https://doi.org/10.1016/j.msea.2008.10.064>

Bibliography

- [132] R. Schaller, J. Ammann, D. Mari, and M. Maamouri, “Mechanical Properties of Tungsten Carbide-11 Cobalt (WC-11Co) Studied by Internal Friction,” *M3D: Mechanics and Mechanisms of Material Damping, ASTM International*, pp. 510–524, 2009. URL <https://doi.org/10.1520/STP17982S>
- [133] D. Jianxin and L. Aihua, “Dry sliding wear behavior of pvd tin, ti₅₅al₄₅n, and ti₃₅al₆₅n coatings at temperatures up to 600°C,” *International Journal of Refractory Metals and Hard Materials*, vol. 41, pp. 241 – 249, 2013. URL <https://doi.org/10.1016/j.ijrmhm.2013.04.008>
- [134] D. Jianxin, L. Jianhua, Z. Jinlong, S. Wenlong, and N. Ming, “Friction and wear behaviors of the pvd zrn coated carbide in sliding wear tests and in machining processes,” *Wear*, vol. 264, no. 3, pp. 298 – 307, 2008. URL <https://doi.org/10.1016/j.wear.2007.03.014>
- [135] H. Elmkhah, F. Attarzadeh, A. Fattah-alhosseini, and K. H. Kim, “Microstructural and electrochemical comparison between tin coatings deposited through hipims and dcms techniques,” *Journal of Alloys and Compounds*, vol. 735, pp. 422 – 429, 2018. URL <https://doi.org/10.1016/j.jallcom.2017.11.162>
- [136] Y. Purandare, A. Ehasarian, A. Santana, and P. Hovsepien, “Zrn coatings deposited by high power impulse magnetron sputtering and cathodic arc techniques,” *Journal of Vacuum Science & Technology A*, vol. 32, no. 3, p. 031507, 2014. URL <https://doi.org/10.1116/1.4869975>
- [137] M. Stueber, H. Holleck, H. Leiste, K. Seemann, S. Ulrich, and C. Ziebert, “Concepts for the design of advanced nanoscale pvd multilayer protective thin films,” *Journal of Alloys and Compounds*, vol. 483, no. 1, pp. 321 – 333, 2009, 14th International Symposium on Metastable and Nano-Materials (ISMANAM-2007). URL <https://doi.org/10.1016/j.jallcom.2008.08.133>
- [138] C. Subramanian and K. Strafford, “Review of multicomponent and multilayer coatings for tribological applications,” *Wear*, vol. 165, no. 1, pp. 85 – 95, 1993. URL [https://doi.org/10.1016/0043-1648\(93\)90376-W](https://doi.org/10.1016/0043-1648(93)90376-W)
- [139] O. Knotek, F. Löffler, and G. Krämer, “Multicomponent and multilayer physically vapour deposited coatings for cutting tools,” in *Metallurgical Coatings and Thin Films 1992*, B. SARTWELL, G. McGUIRE, and S. HOFMANN, Eds. Amsterdam: Elsevier, 1992, pp. 241 – 248. URL <https://doi.org/10.1016/B978-0-444-89900-2.50045-2>
- [140] K.-D. Bouzakis, S. Hadjiyiannis, G. Skordaris, J. Anastopoulos, I. Mirisidis, N. Michailidis, K. Efstathiou, O. Knotek, G. Erkens, R. Cremer, S. Rambadt, and I. Wirth, “The influence of the coating thickness on its strength properties and on the milling performance of pvd coated inserts,” *Surface and Coatings Technology*, vol. 174-175, pp. 393 – 401, 2003, proceedings of the Eight International Conference on Plasma Surface Engineering. URL [https://doi.org/10.1016/S0257-8972\(03\)00678-9](https://doi.org/10.1016/S0257-8972(03)00678-9)
- [141] K. Tuffy, G. Byrne, and D. Dowling, “Determination of the optimum tin coating thickness on wc inserts for machining carbon steels,” *Journal of Materials Processing Technology*, vol. 155-156, pp. 1861 – 1866, 2004, proceedings of the International

- Conference on Advances in Materials and Processing Technologies: Part 2. URL <https://doi.org/10.1016/j.jmatprotec.2004.04.277>
- [142] V. G. Sargade, S. Gangopadhyay, S. Paul, and A. K. Chattopadhyay, “Effect of coating thickness on the characteristics and dry machining performance of tin film deposited on cemented carbide inserts using cfubms,” *Materials and Manufacturing Processes*, vol. 26, no. 8, pp. 1028–1033, 2011. URL <https://doi.org/10.1080/10426914.2010.526978>
- [143] M. Abdoos, K. Yamamoto, B. Bose, G. Fox-Rabinovich, and S. Veldhuis, “Effect of coating thickness on the tool wear performance of low stress tialn pvd coating during turning of compacted graphite iron (cgi),” *Wear*, vol. 422-423, pp. 128 – 136, 2019. URL <https://doi.org/10.1016/j.wear.2019.01.062>
- [144] V. Teixeira, “Residual stress and cracking in thin pvd coatings,” *Vacuum*, vol. 64, no. 3, pp. 393 – 399, 2002, the Fouth Iberian Vacuum Meeting. URL [https://doi.org/10.1016/S0042-207X\(01\)00327-X](https://doi.org/10.1016/S0042-207X(01)00327-X)
- [145] B. Denkena and B. Breidenstein, “Residual stress distribution in pvd-coated carbide cutting tools - origin of cohesive damage,” *Tribology in Industry*, vol. 34, pp. 158–165, 2012. URL <https://doi.org/10.15488/1407>
- [146] M. Gelfi, E. Bontempi, R. Roberti, and L. Depero, “X-ray diffraction debye ring analysis for stress measurement (drast): a new method to evaluate residual stresses,” *Acta Materialia*, vol. 52, no. 3, pp. 583 – 589, 2004. URL <https://doi.org/10.1016/j.actamat.2003.09.041>
- [147] F. Klocke, C. Gorgels, A. Stuckenberg, and E. Bouzakis, “Qualification of coatings to predict wear behavior of micro blasted cutting tools,” in *The Coatings in Manufacturing Engineering*, ser. Key Engineering Materials, vol. 438. Trans Tech Publications Ltd, 9 2010, pp. 23–29. URL <https://doi.org/10.4028/www.scientific.net/KEM.438.23>
- [148] S. Kiss, R. Schaller, and W. Benoit, “Heating-rate dependent internal friction background in aluminium,” *physica status solidi (a)*, vol. 92, no. 2, pp. K109–K112, 1985. URL <https://doi.org/10.1002/pssa.2210920246>
- [149] J. C. Mauro and M. M. Smedskjaer, “Statistical mechanics of glass,” *Journal of Non-Crystalline Solids*, vol. 396-397, pp. 41 – 53, 2014. URL <https://doi.org/10.1016/j.jnoncrysol.2014.04.009>
- [150] S. Nagata, P. H. Keesom, and H. R. Harrison, “Low-dc-field susceptibility of CuMn spin glass,” *Phys. Rev. B*, vol. 19, pp. 1633–1638, Feb 1979. URL <https://doi.org/10.1103/PhysRevB.19.1633>
- [151] N. Gayathri, A. K. Raychaudhuri, S. K. Tiwary, R. Gundakaram, A. Arulraj, and C. N. R. Rao, “Electrical transport, magnetism, and magnetoresistance in ferromagnetic oxides with mixed exchange interactions: A study of the $\text{la}_{0.7}\text{ca}_{0.3}\text{mn}_{1-x}\text{co}_x\text{o}_3$ system,” *Phys. Rev. B*, vol. 56, pp. 1345–1353, Jul 1997. URL <https://doi.org/10.1103/PhysRevB.56.1345>

Bibliography

- [152] A. F. Guillermet, “Thermodynamic properties of the Co-W-C system,” *Metallurgical Transactions A*, vol. 20, no. 5, pp. 935–956, 1989. URL <https://doi.org/10.1007/BF02651660>
- [153] G. Östberg, B. Jansson, and H. O. Andrén, “On spinodal decomposition in the Co-W system,” *Scripta Materialia*, vol. 54, no. 4 SPEC. ISS., pp. 595–598, 2006. URL <https://doi.org/10.1016/j.scriptamat.2005.10.040>
- [154] K. Lücke and A. V. Granato, “Simplified theory of dislocation damping including point-defect drag. i. theory of drag by equidistant point defects,” *Phys. Rev. B*, vol. 24, pp. 6991–7006, Dec 1981. URL <https://doi.org/10.1103/PhysRevB.24.6991>
- [155] X. An, S. Ni, M. Song, and X. Liao, “Deformation twinning and detwinning in face-centered cubic metallic materials,” *Advanced Engineering Materials*, vol. 22, no. 1, p. 1900479, 2020. URL <https://doi.org/10.1002/adem.201900479>
- [156] T. Ericsson, “The temperature and concentration dependence of the stacking fault energy in the co-ni system,” *Acta Metallurgica*, vol. 14, no. 7, pp. 853 – 865, 1966. URL [https://doi.org/10.1016/0001-6160\(66\)90006-X](https://doi.org/10.1016/0001-6160(66)90006-X)
- [157] J. Wang, O. Anderoglu, J. P. Hirth, A. Misra, and X. Zhang, “Dislocation structures of sigma3 112 twin boundaries in face centered cubic metals,” *Applied Physics Letters*, vol. 95, no. 2, p. 021908, 2009. URL <https://doi.org/10.1063/1.3176979>
- [158] Y. Morris Wang, F. Sansoz, T. Lagrange, R. T. Ott, J. Marian, T. W. Barbee, and A. V. Hamza, “Defective twin boundaries in nanotwinned metals,” *Nature Materials*, vol. 12, no. 8, pp. 697–702, 2013. URL <https://doi.org/10.1038/nmat3646>
- [159] J. Hirth and R. Balluffi, “On grain boundary dislocations and ledges,” *Acta Metallurgica*, vol. 21, no. 7, pp. 929 – 942, 1973. URL [https://doi.org/10.1016/0001-6160\(73\)90150-8](https://doi.org/10.1016/0001-6160(73)90150-8)
- [160] X. Han, N. Sacks, Y. Milman, and S. Luyckx, “On plastic deformation mechanisms of wc–15wt% co alloys at 1000c,” *International Journal of Refractory Metals and Hard Materials*, vol. 27, no. 2, pp. 274 – 281, 2009, international Conference on the Science of Hard Materials - 9. URL <https://doi.org/10.1016/j.ijrmhm.2008.09.021>
- [161] S. B. Luyckx, “Microscopic aspects of fracture in wc-co alloys,” *Acta Metallurgica*, vol. 16, no. 4, pp. 535 – 544, 1968. URL [https://doi.org/10.1016/0001-6160\(68\)90128-4](https://doi.org/10.1016/0001-6160(68)90128-4)
- [162] H. S. Mohand, G. Fantozzi, G. Orange, and J. Dubois, “Comportement mécanique à haute température des carbures cémentes wc-co,” *Rev Int Hautes Tempér Refract*, vol. 19, pp. 311–323, 1982.
- [163] D. Mari, S. Bolognini, T. Viatte, and W. Benoit, “Study of the mechanical properties of ticn–wc–co hardmetals by the interpretation of internal friction spectra,” *International Journal of Refractory Metals and Hard Materials*, vol. 19, no. 4, pp. 257 – 265, 2001. URL [https://doi.org/10.1016/S0263-4368\(01\)00037-3](https://doi.org/10.1016/S0263-4368(01)00037-3)
- [164] J. L. Chermant and F. Osterstock, “Fracture toughness and fracture of wc-co composites,” *Journal of Materials Science*, vol. 11, no. 10, pp. 1939–1951, Oct 1976. URL <https://doi.org/10.1007/BF00708272>

-
- [165] F. Osterstock and J.-L. Chermant, *Some Aspects of the Fracture of WC-Co Composites*. Boston, MA: Springer US, 1983, pp. 615–629. URL https://doi.org/10.1007/978-1-4684-4319-6_33
- [166] H. Exner, L. Sigl, M. Fripan, and O. Pompe, “Fractography of critical and subcritical cracks in hard materials,” *International Journal of Refractory Metals and Hard Materials*, vol. 19, no. 4, pp. 329 – 334, 2001. URL [https://doi.org/10.1016/S0263-4368\(01\)00035-X](https://doi.org/10.1016/S0263-4368(01)00035-X)
- [167] H. Schmid, D. Mari, W. Benoit, and C. Bonjour, “The mechanical behaviour of cemented carbides at high temperatures,” *Materials Science and Engineering: A*, vol. 105-106, pp. 343 – 351, 1988. URL [https://doi.org/10.1016/0025-5416\(88\)90716-1](https://doi.org/10.1016/0025-5416(88)90716-1)
- [168] D. Mari, U. Marti, and P. Silva, “A new photolithographic technique to detect the local deformation of materials: application to wc-co composites,” *Materials Science and Engineering: A*, vol. 158, no. 2, pp. 203 – 206, 1992. URL [https://doi.org/10.1016/0921-5093\(92\)90009-P](https://doi.org/10.1016/0921-5093(92)90009-P)
- [169] L. E. Steele, *Neutron irradiation embrittlement of reactor pressure vessel steels*. International Atomic Energy Agency (IAEA): IAEA, 1975. URL http://inis.iaea.org/search/search.aspx?orig_q=RN:07222068
- [170] A. Munier, “Frottement intérieur et transition fragile-ductile dans les aciers ferritiques de cuves de réacteurs nucléaires,” p. 184, 1991. URL <http://infoscience.epfl.ch/record/31429>
- [171] Y. M. Wang, F. Sansoz, T. LaGrange, R. T. Ott, J. Marian, T. W. Barbee, and A. V. Hamza, “Defective twin boundaries in nanotwinned metals,” *Nature Materials*, vol. 12, pp. 697–702, 2013. URL <https://doi.org/10.1038/nmat3646>
- [172] M. Eizadjou, H. Chen, C. Czettl, J. Pachlhofer, S. Primig, and S. P. Ringer, “An observation of the binder microstructure in wc-(co+ru) cemented carbides using transmission kikuchi diffraction,” *Scripta Materialia*, vol. 183, pp. 55 – 60, 2020. URL <http://www.sciencedirect.com/science/article/pii/S1359646220301421>
- [173] A. Guillermet, “Use of phase-diagram calculations in selecting the composition of fe-ni bonded wc tools,” *International Journal of Refractory Metals and Hard Materials*, vol. 6, no. 1, pp. 24–27, 1987. URL <https://www.scopus.com/inward/record.uri?eid=2-s2.0-0023314487&partnerID=40&md5=a7696cc9da72e2bc41b1193cbd4a70d6>
- [174] D. T. Quinto, G. J. Wolfe, and P. C. Jindal, “High temperature microhardness of hard coatings produced by physical and chemical vapor deposition,” *Thin Solid Films*, vol. 153, no. 1, pp. 19 – 36, 1987. URL [https://doi.org/10.1016/0040-6090\(87\)90166-0](https://doi.org/10.1016/0040-6090(87)90166-0)
- [175] S. PalDey and S. Deevi, “Single layer and multilayer wear resistant coatings of (ti,al)n: a review,” *Materials Science and Engineering: A*, vol. 342, no. 1, pp. 58 – 79, 2003. URL [https://doi.org/10.1016/S0921-5093\(02\)00259-9](https://doi.org/10.1016/S0921-5093(02)00259-9)
- [176] R. Schaller, “Applications Of Mechanical Spectroscopy To Industrial Materials,” *Archives of Metallurgy and Materials*, vol. 60, no. 2, pp. 1085–1089, 2015. URL <https://doi.org/10.1515/amm-2015-0264>

Bibliography

- [177] S. Bolognini, D. Mari, T. Viatte, and W. Benoit, “Fracture toughness of coated TiCN-WC-Co cermets with graded composition,” *International Journal of Refractory Metals and Hard Materials*, vol. 19, no. 4-6, pp. 285–292, 2001. URL [https://doi.org/10.1016/S0263-4368\(01\)00025-7](https://doi.org/10.1016/S0263-4368(01)00025-7)
- [178] R. Bhowmik and R. Ranganathan, ““super-ferromagnetic” clusters in spinel oxide,” *Journal of Magnetism and Magnetic Materials*, vol. 247, no. 1, pp. 83 – 91, 2002. URL [https://doi.org/10.1016/S0304-8853\(02\)00158-0](https://doi.org/10.1016/S0304-8853(02)00158-0)
- [179] R. Zhang, J. F. Li, and D. Viehland, “Effect of aliovalent substituents on the ferroelectric properties of modified barium titanate ceramics - relaxor ferroelectric behavior,” *Journal of the American Ceramic Society*, vol. 87, no. 5, pp. 864–870, 2004. URL <https://doi.org/10.1111/j.1551-2916.2004.00864.x>
- [180] D. Viehland, S. J. Jang, L. E. Cross, and M. Wuttig, “Freezing of the polarization fluctuations in lead magnesium niobate relaxors,” *Journal of Applied Physics*, vol. 68, no. 6, pp. 2916–2921, 1990. URL <https://doi.org/10.1063/1.346425>

Appendices

Appendix A: Shock test

In this appendix, images are given of the machining performance over time of various coated cemented carbide inserts produced by Lamina-tech SA. These images correspond to some of the impact durability tests reported in Figure 3.1 of Chapter 3.1 of the results. The presentation of the impact durability test can be found in paragraph 2.1.2 of the Experimental Techniques Chapter.

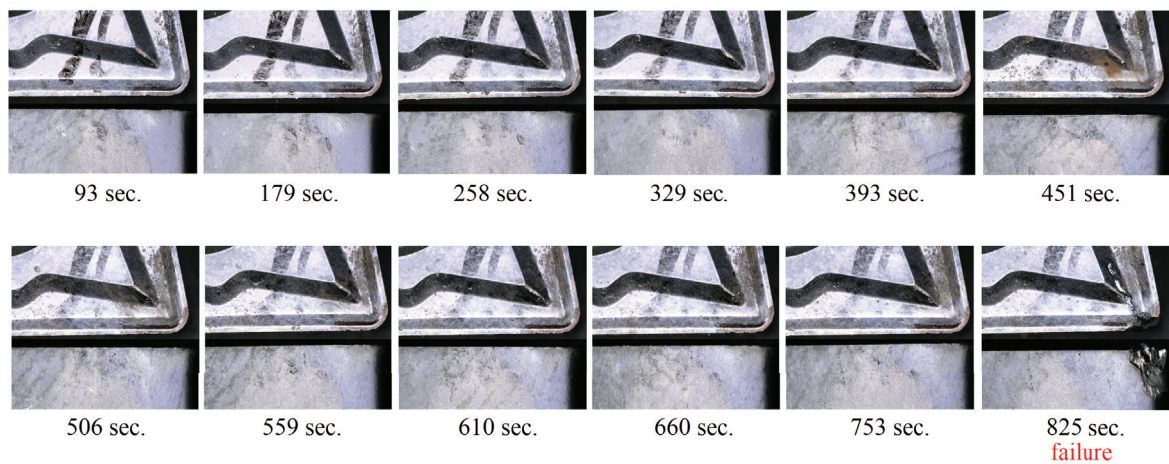


Figure 4.3: Machining performance in shock test for a tungsten cemented carbide insert coated with the multilayer coating 2. The indicated times correspond to the test duration for each observation. The upper part of each image is the top view (face) of the inserts and the lower part is a side view (flank). The failure mechanisms observed on this insert is breakage.

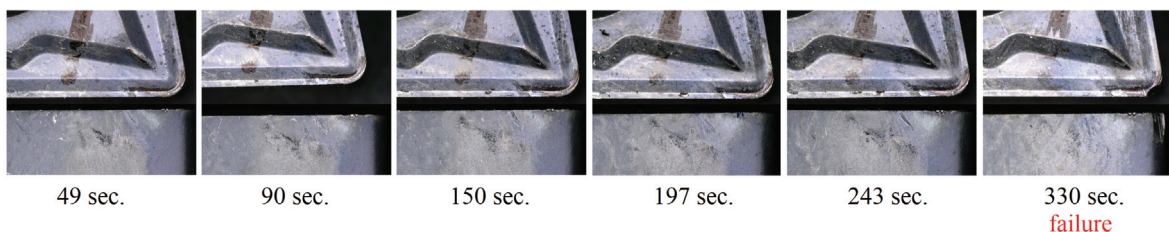


Figure 4.4: Machining performance in shock test for a tungsten cemented carbide insert coated with the bilayer coating 1. The indicated times correspond to the test duration for each observation. The upper part of each image is the top view (face) of the inserts and the lower part is a side view (flank). The failure mechanisms observed on this insert is edge chipping.

Appendix B: Facing until the center test

In this appendix, images are given of the machining performance over the number of passes of various coated cemented carbide inserts produced by Lamina-tech SA. These images correspond to some of the rapid wear tests reported in Figure 3.2 of Chapter 3.1 of the results. The presentation of the rapid wear test can be found in paragraph 2.1.3 of the Experimental Technics Chapter.

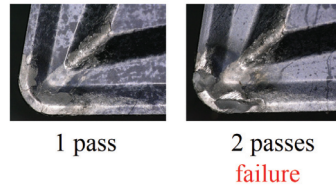


Figure 4.5: Rapid Wear test (Facing until the center) for a tungsten cemented carbide insert coated with the multilayer coating 1, as function of the passes. Each image is the top view (face) of the inserts. The failure mechanisms observed on this insert is edge chipping and coating flaking.

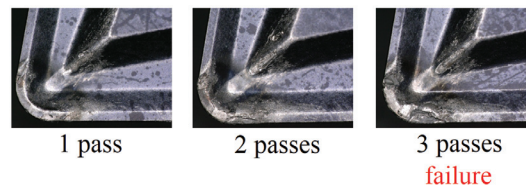


Figure 4.6: Rapid Wear test (Facing until the center) for a tungsten cemented carbide insert coated with the multilayer coating 2, as function of the passes. Each image is the top view (face) of the inserts. The failure mechanisms observed on this insert is edge chipping and coating flaking.

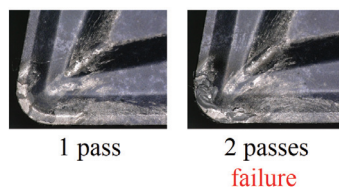


Figure 4.7: Rapid Wear test (Facing until the center) for a tungsten cemented carbide insert coated with the bilayer coating 1, as function of the passes. Each image is the top view (face) of the inserts. The failure mechanisms observed on this insert is edge chipping and coating flaking.

Appendix C: Friction test

This Appendix reports some of the tribological study of the Coefficient Of Friction (COF) behaviours of coated cutting tools. The corresponding analysis is given in the Chapter 3.2.1. The curves for the evolution of COF are presented.

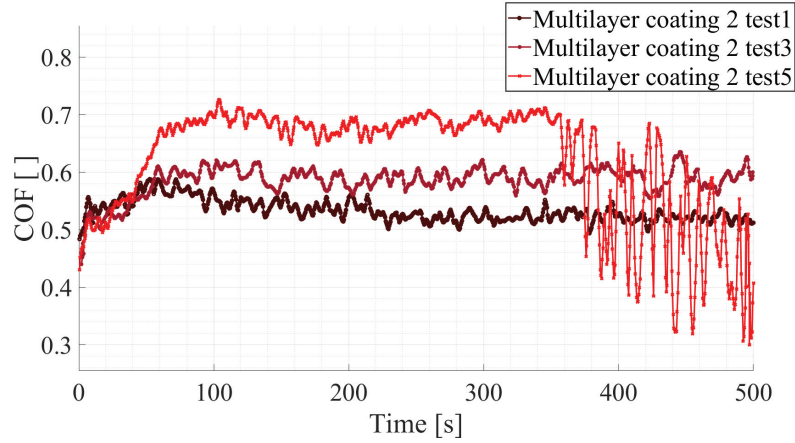


Figure 4.8: Evolution of the friction coefficient as a function of time measured on a linear tribometer. The ball used as sliding material is a 3 mm diameter 100Cr6 steel ball. The applied force is 2N. The sample is a cutting insert with WC-6wt.%Co and submicron WC grains, coated with a multilayer coating of type TiAlN.

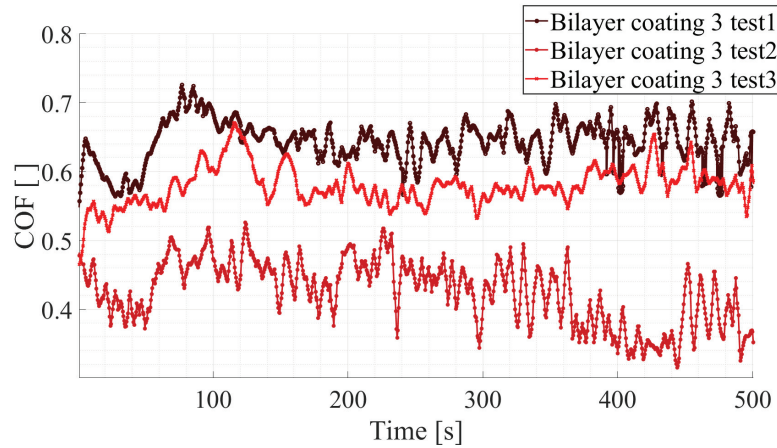


Figure 4.9: Evolution of the friction coefficient as a function of time measured on a linear tribometer. The ball used as sliding material is a 3 mm diameter 100Cr6 steel ball. The applied force is 2N. The sample is a cutting insert with WC-6wt.%Co and submicron WC grains, coated with a bilayer coating of type TiAlN.

Appendix D: Nanoindentation test

Hereafter are reported some representative surface states marked by Berkovich indentation imprints and the corresponding nano-indentation curves. These elements serve as a basis for the determination of nano-hardness values and elastic moduli according to the Oliver and Pharr model (c.f. Section 2.3.2).

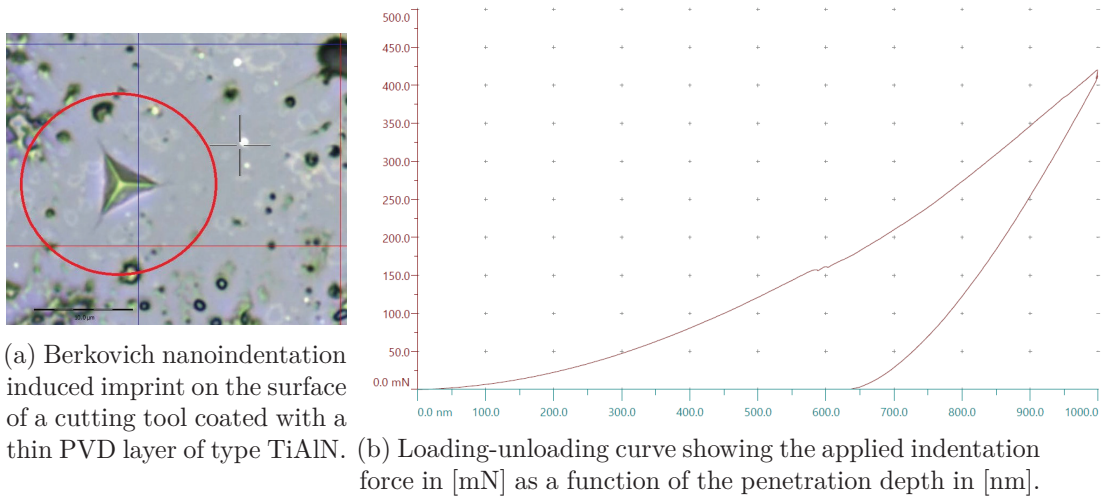


Figure 4.10: Indentation for the evaluation of the nano-hardness and elastic modulus of the Multilayer Coating 1 of type TiAlN.

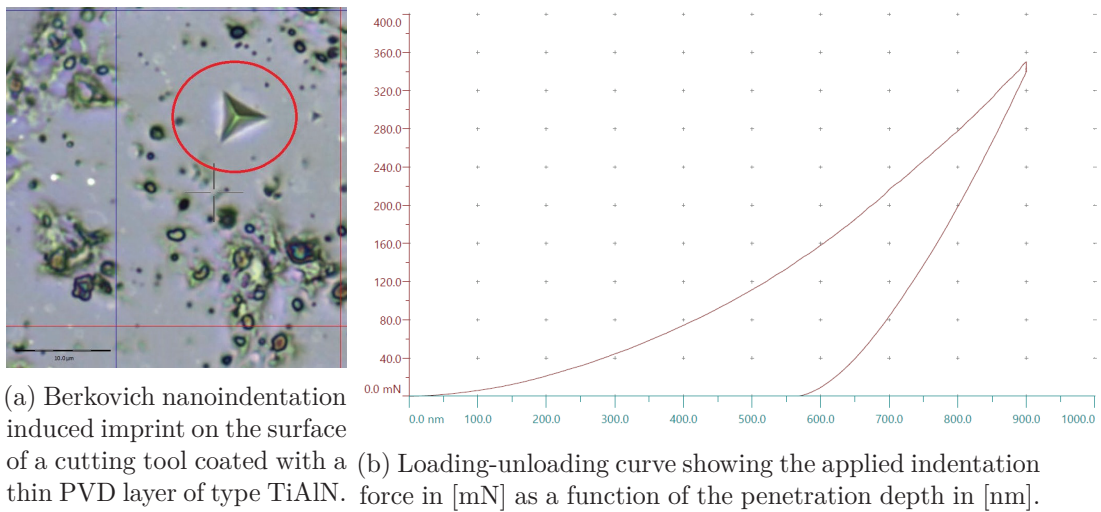


Figure 4.11: Indentation for the evaluation of the nano-hardness and elastic modulus of the Multilayer Coating 2 of type TiAlN.

Appendix E: Frequency internal friction spectra

Hereafter are reported the deconvoluted spectra measured on a WC-6wt.%Co at fixed frequency in isothermal condition. All spectra are reported in the Figure 3.23 and the parameters of the deconvoluted peaks are reported in the Arrhenius diagram 3.24. The internal friction spectra are deconvoluted with three Debye peaks and a low frequency background (c.f. Section 3.3.6).

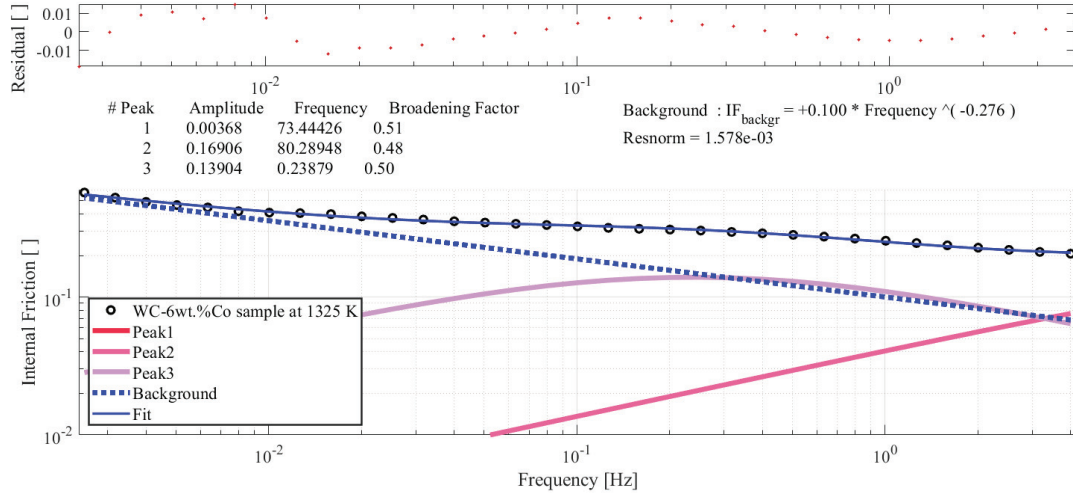


Figure 4.12: Deconvoluted spectrum of internal friction as a function of the frequency of a WC-6wt.%Co sample measured at 1325 K.

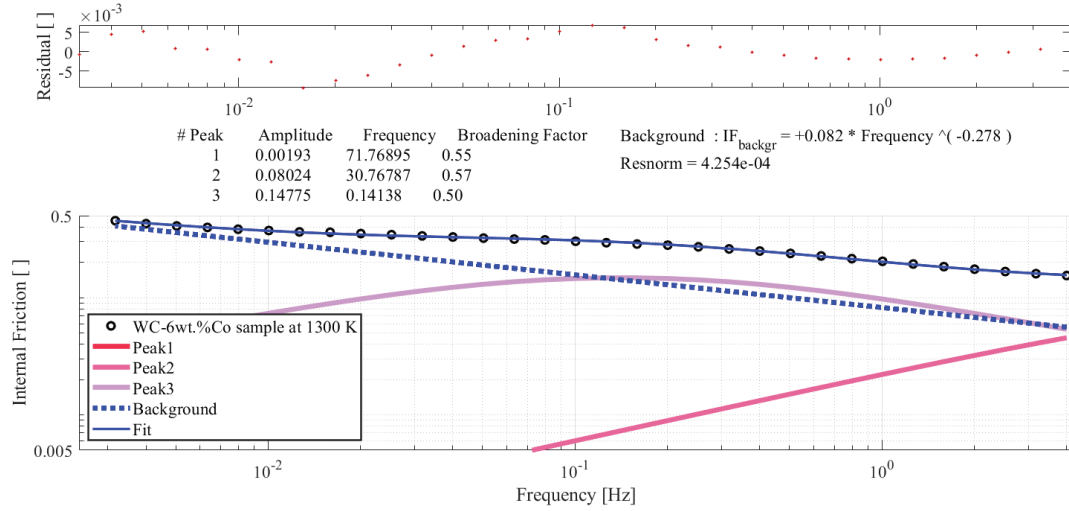


Figure 4.13: Deconvoluted spectrum of internal friction as a function of the frequency of a WC-6wt.%Co sample measured at 1300 K.

Remerciements

C'est avec beaucoup d'humilité que je profite de l'aboutissement de ce travail pour exprimer mes profonds remerciements et toute mon affection pour celles et ceux qui m'ont accompagné, épaulé, conseillé, aidé ou qui ont simplement partagé avec moi des rêves et des passions durant ces quatre dernières années.

Ce travail est l'initiative de Daniele Mari, le capitaine de notre groupe, qui de par sa bienveillance et son dynamisme m'a très rapidement convaincu à m'engager dans ce projet de recherche qu'il montait en 2016 avec l'équipe de Lamina Technologies. Il aurait été difficile de tomber sur un meilleur directeur de thèse. Ses qualités humaines, l'étendue de ses connaissances et de ses passions, son intégrité et son engagement en recherche et en enseignement forcent l'admiration. J'aimerais le remercier pour m'avoir fait rapidement confiance, pour s'être toujours montré disponible et pour m'avoir apporté de judicieux conseils tout au long de ces quatre années.

Je veux exprimer mes remerciements à toute l'équipe de notre partenaire sur ce travail, Lamina Technologies à Yverdon-les-Bains. Merci aux instigateurs de ce projet : à Peleg Amir, le directeur général de Lamina Technologies, à Tomer Gershtein pour sa rigueur et sa volonté d'aller de l'avant, et à Ligia Colina pour sa grande générosité tant personnelle que professionnelle. Merci surtout à ceux qui ont géré et développé ce projet avec nous: Johan Böhlmark et Emerson Cardoso De Campos. J'admire leurs connaissances, tant du point de vue industriel que technique et technologique, et leur belle personnalité. Mes remerciements également à l'équipe des polymécaniciens de Lamina Technologies pour m'avoir montré leurs tests de performances mécaniques.

Une thèse est un travail personnel à mener en bonne autonomie, mais la vie de chercheur reste remplie de belles rencontres et de nombreuses collaborations. Du fond du cœur, j'aimerais tout d'abord remercier le groupe que j'ai intégré. A Iva Tkalc̃ec, précise et dévouée qui accueille le monde entier par son sourire. A Raffaele Cosimati, bienveillant et généreux qui m'a accompagné sur le début de mon travail. A Patrick Mayor, brillant et rieur pour les mots fléchés de midi. A Loïc Favre, grand joueur et aventurier à l'esprit affuté. Au nouvel arrivant, Lucas Degenève pour son travail assidu et sa belle personnalité. Egalement, un grand merci à tous les membres du LPMC et du LQM. Ils sont malheureusement trop nombreux pour tous être cités, mais j'espère qu'ils se reconnaîtront.

J'aimerais aussi exprimer ma profonde gratitude à toutes celles et ceux qui ont contribué à la bonne réussite de ce projet par leur collaboration et pour avoir embelli le quotidien par leurs qualités personnelles. Au groupe des travaux pratiques et à leur soutien infailible : Antonio Gentile et Nicolas Turin. A Arnaud Magrez et à Wen Hua David Bi, grands et sympathiques experts de la caractérisation des matériaux par rayon-X, et à Julien Chauvet

Acknowledgements

pour en avoir effectué certaines. A Gérard Beney, Gilles Grandjean et à toute l'équipe des mécaniciens de l'institut de physique. C'est un vrai bonheur d'avoir pu travailler avec eux. A Thomas La Grange, à Grégoire Baroz et à Danièle Laub du Centre Interdisciplinaire de Microscopie Electronique pour leurs conseils, leur aide et leur expertise. J'ai été très heureux et chanceux de pouvoir collaborer avec eux. Je tiens à remercier Valentine Agnès Magnin et le Dr. Stefano Mischler du groupe de Tribologie et de Chimie Interfaciale (TIC) de l'EPFL pour leur précieux soutien à nos tests tribologiques.

La vie quotidienne sur le campus n'aurait pas été la même sans eux. J'exprime donc ma plus profonde amitié à Antoine, Félix, Francisco, Samuel, Luc, Justin et Virgile. J'aurais aimé pouvoir célébrer ce moment avec eux, mais les circonstances actuelles nous forcent à la patience. Ce sera fait aussi rapidement que possible, et aussi lentement que nécessaire.

Il m'est impossible de ne pas penser à mes amis proches qui ont et qui continuent de forger ma personnalité et mes aspirations. Merci à mes amis d'enfance, Joakim et Morgan pour leur soutien durant nos jeunes années. Un immense merci à Alex et Mahsa, et à l'ensemble de nos amis iraniens de St. Gall pour leur passion et leur joie de vivre.

En particulier, je voudrais exprimer ma profonde gratitude à quelques-uns de mes amis qui ont incontestablement marqué ces années de thèse. A Antoine pour ses valeurs et sa droiture, pour son intelligence et ses passions, et pour son goût immense de la lecture et de l'échange. A Bryan pour sa rigueur et sa générosité, pour son goût du travail et du progrès, et pour sa loyauté et sa bienveillance. A Francisco pour ses passions, son intellect et son ouverture d'esprit, et surtout pour son humanité et sa bonne humeur.

Surtout, je tiens à remercier chaleureusement ma famille. Je suis infiniment reconnaissant envers ma sœur et mes parents pour ce qu'ils sont et pour ce qu'ils m'ont apporté. A ma sœur, Maïmouna, belle comme un soleil, j'aimerais lui exprimer tout mon amour et mon indéfectible soutien. A mon père que j'aimerais remercier pour la droiture, pour les valeurs et pour l'éducation qui m'ont été transmises. A ma mère pour son soutien et sa confiance, pour sa douceur et son goût des choses bien faites, et pour le pilier qu'elle représente pour tant de monde. J'ai une pensée pleine d'affection pour l'ensemble de ma famille, qu'ils soient de Genève, de Zürich ou de Tunisie, pour ceux encore à nos côtés ou ceux déjà partis.

J'exprime enfin le message le plus tendre et ma plus profonde gratitude à mon femme, Neda, pour son soutien, pour sa douceur et sa générosité, pour les rêves que nous partageons et pour ce nous construisons ensemble. J'espère grandir infiniment avec toi à mes côtés, continuer à prospérer et à partager ce bonheur ensemble. Du fond du cœur.

Eshgh e lab e shirinat sad shour barangizad.

Scientific publications and conferences contributions

The scientific aspects of the studies conducted during this doctoral thesis were presented at three key conferences on hard materials and ceramic:

- The "International Conference on Internal Friction and Mechanical Spectroscopy" (ICIFMS-18) was held in September 2017, with the presentation of a poster entitled "High temperature mechanical spectroscopy of PVD coated cutting tools".
- The "European Inter-Regional Conference on Ceramics CIEC-16" was held in September 2018, and a poster entitled "A link between tool-life of WC-Co cutting tools coated by PVD TiAlN and the damping capacity spectra" was presented.
- Attended to the conference "ICSHM11 - 11th International Conference on the Science of Hard Materials 2019", with presentation as registered speaker and presentation of a poster.

This work has also been the subject of two publications in specialized journals:





- Publication 1: S. Adjam, D. Mari, A link between durability of WC-co coated cutting tools and mechanical damping spectra, *Int. J. Refract. Met. Hard Mater.* 85 (2019), Article 105068, doi.org/10.1016/j.ijrmhm.2019.105068
- Publication 2: S. Adjam, D. Mari, T. La Grange, Strain glass transition of cobalt phase in a cemented carbide, *Int. J. Refract. Met. Hard Mater.* (2019), doi.org/10.1016/j.ijrmhm.2019.105161

Contact informations

<p>Samy ADJAM PhD Student and Doctoral Assistant</p> <p>Ecole Polytechnique Fédérale de Lausanne EPFL SB IPHYS LQM PH D2 494 (Bâtiment PH), Station 3 CH-1015 Lausanne</p> <p>tel : +41 (0)21 693 33 93 fax: none email: samy.adjam@epfl.ch</p>	<p>Emerson CARDOSO DE CAMPOS R&D Design Supervisor and Project Leader</p> <p>Lamina Technologies SA Rue Pythagore 2 CH-1400 Yverdon-les-Bains</p> <p>tel : +41 (0)24 423 54 32 fax: +41 (0)24 423 54 44 email: e.cardoso@lamina-tech.ch</p>
<p>Daniele MARI Deputy Director School of Physics</p> <p>Ecole Polytechnique Fédérale de Lausanne EPFL SB IPHYS LQM PH D1 325 (Bâtiment PH), Station 3 CH-1015 Lausanne</p> <p>tel : +41 (0)21 693 44 73 fax: +41 (0)21 693 44 70 email: daniele.mari@epfl.ch</p>	<p>Johan BOHLMARK R&D Group Manager</p> <p>Lamina Technologies SA Rue Pythagore 2 CH-1400 Yverdon-les-Bains</p> <p>tel : +41 (0)24 423 54 32 fax: +41 (0)24 423 54 44 email: j.bohlmark@lamina-tech.ch</p>

Samy ADJAM

Curriculum vitae

 [linkedin.com/in/samy-adjam](https://www.linkedin.com/in/samy-adjam)
 Born June 22, 1989
 Swiss citizenship
 Married

Profile

- Meticulous, pragmatic, caring
- Enjoy building, developing, automating experimental facilities and devices
- Develop a good understanding of the underlying processes
- Interest not only in solving technical problems but also in people, environment and society
- Passionate about pioneer engineering and innovative technologies

Education

10.2016 – (01.2021)	EPFL, Lausanne, Ph.D. candidate , in collaboration with Lamina-tech SA, Physics and Applied Physics Department, Optimizing Structures and Interfaces in Cutting Tools , Director: Dr. Daniele Mari
02.2014 – 09.2016	EPFL, Lausanne, Master's degree , Physics and Applied Physics Department.
09.2011 – 02.2014	EPFL, Lausanne, Bachelor's degree, 2nd and 3rd year , Physics Department.
09.2010 – 09.2011	ETHZ, Zürich, Bachelor's degree, 1st year , Physics Department.

Experiences

Professional

02.2016 – 08.2016	Engineering project , Master Project, Manufactures des montres Rolex, Bienne, <i>Concept and Technologies Group</i> <ul style="list-style-type: none">• Development and characterization• Organic / organometallic layers• Thin-film processes (Atomic Layer Deposition / Molecular Layer Deposition)
08.2015 – 01.2016	Engineering internship , Manufactures des montres Rolex, Bienne, <i>Tribology and Lubricant Group</i> <ul style="list-style-type: none">• Watchmaking lubricant evaluation of relevance for applications• Design of experiments• Various experimental and numerical statistical methods

Miscellaneous

10.2012 – 02.2016	Student employment , <i>Société Coopérative Migros Genève</i> , Activity rate : 20 %, During my university studies, every weekend as well as during the inter-semester periods
07.2008 – 05.2009	Military service , <i>Military Disaster Relief</i> . All military obligations completed in service without interruption.

Competences

Language Skills

French	Mother tongue
German	Level C1
Swiss German	Good comprehension
English	Level C1

Computer Skills

General	Numerical Modelling, Data analysis, processing, and visualization L ^A T _E X , Microsoft Office
Programming	Matlab, C++ (essential knowledge), Python (essential knowledge)

Technical and Laboratory Skills

Technique & Technology	<ul style="list-style-type: none"> • Development and engineering • Automation • Mechanical Maintenance • Troubleshooting
Material & Mechanical Characterizations	<ul style="list-style-type: none"> • Investigations of relaxation processes and dynamic properties of structural defects by Mechanical Spectroscopy (MS) • Micro- and Nano-indentation (resp. by standard and the Oliver and Pharr method) • Thin Films characterizations (Profilometry, Ellipsometry (Cauchy layer model), Electrical Resistivity (Van der Pauw, Drude-Lorentz model) • X-ray diffraction (Basic crystallographic phases identification and Residual Stress assessment) • Basic optical spectroscopy and spectroscopic ellipsometry • Thermogravimetric analysis (TGA-DSC) • Basic wear and friction tribology (Tribometer) • Optical tweezers / trap: from setup to observation, manipulation and statistical analysis
Thin Films Deposition	<ul style="list-style-type: none"> • Evaporation techniques by Joule effect • Physical vapor deposition (PVD) <ul style="list-style-type: none"> ◦ Cathodic sputtering (Deposition and studies of thin layers of transparent conductive oxides (TCO) ZNO:Al) ◦ High Power Impulse Magnetron Sputtering (HiPIMS) and DC (direct current) sputtering (deposition, studies, and optimization of thin layers of NbTiN with industrial partnership) • Atomic Layer Deposition (ALD)
Cleanroom	<ul style="list-style-type: none"> • Training "Safety and behavior in cleanroom" Experiments performed in a clean room of "ISO 6 / class 1'000" level

Academia

Teaching Experience

2016 – 2017	Physics lab III , <i>Physics Department</i> , Installation and development of Practical Laboratory for Physics students, " <i>Vibrated granular matter studied with a torsion oscillator</i> ", Dr. Tkalec Văju Iva
2016 – 2017	Physics lab III , <i>Physics Department</i> , Installation and development of Practical Laboratory for Physics students, " <i>Electronic properties in solids and thin films</i> ", Dr. Tkalec Văju Iva
2016 – 2020	Assistant for Physics lab III , <i>Physics Department</i> : <ul style="list-style-type: none"> • Vibrated granular matter studied with a torsion oscillator • Electronic properties in solids and thin films • Optical Trapping: Optical tweezers, Brownian motion and single particle tracking • Thin Film Physics • Optical Spectroscopy Dr. Oberli Daniel, Dr. Tkalec Văju Iva, Dr. MER. Magrez Arnaud
2014 – 2015	Assistant for General Physics IV , <i>Life Sciences Engineering Department</i> , Prof. Dietler Giovanni
2014 – 2015	Assistant for General Physics , <i>Faculty of Biology and Medicine</i> , Prof. László Forró

Publications

NbTiN thin films deposited by hybrid HiPIMS/DC magnetron co-sputtering,
Del Giudice, S. Adjam, D. Dumitriu La Grange, O. Banakh, A. Karimi, R. Sanjines,
Surface and Coatings Technology, Volume 295, 15 June 2016, Pages 99–106,
doi.org/10.1016/j.surfcoat.2015.10.007

A link between durability of WC-Co coated cutting tools and mechanical damping spectra, *S. Adjam, D. Mari*, *International Journal of Refractory Metals & Hard Materials*, Volume 85, December 2019, 105068, doi.org/10.1016/j.ijrmhm.2019.105068

Strain glass transition of cobalt phase in a cemented carbide, *S. Adjam, D. Mari, T. La Grange*, *International Journal of Refractory Metals & Hard Materials*, Volume 87, February 2020, 105161, doi.org/10.1016/j.ijrmhm.2019.105161

Awards

JECS Trust Poster Competition Award, September 2018, Poster entitled :
"A link between tool-life of WC-Co cutting tools coated by PVD TiAlN and the damping capacity spectra", at the European Inter-Regional Conference on Ceramics CIEC-16

ICSHM11 Committee Poster Competition Award, March 2019, Poster entitled :
"Damping capacity spectra and the durability of WC-Co coated cutting tools",
at the International Conference on the Science of Hard Materials ICSHM11